Doctoral Dissertation
Doctoral Program in Mechanical Engineering (35th Cycle)

Development of numerical and experimental tools for the simulation of train braking operations

By

Matteo Magelli

******

Supervisor(s):
Prof. Nicola Bosso ,Supervisor

Doctoral Examination Committee:
Prof. A.B. , Referee, University of….
Prof. C.D. , Referee, University of…
Prof. E.F. , Referee, University of….
Prof. G.H. , Referee, University of…
Prof. I.J. , Referee, University of….

Politecnico di Torino
February, 2023

Declaration

I hereby declare that, the contents and organization of this dissertation constitute my own original work and does not compromise in any way the rights of third parties, including those relating to the security of personal data.

Matteo Magelli

2023

* This dissertation is presented in partial fulfillment of the requirements for **Ph.D. degree** in the Graduate School of Politecnico di Torino (ScuDo).

Dedico questa tesi a mio papà, che spero possa vedermi ogni giorno, e a mio nonno, la "roccia" della nostra famiglia.

Acknowledgment

I would like to express my gratitude to my tutor, Prof. Nicola Bosso, for his support throughout these years and for his great suggestions, that always lit a light when I could not find the right way. I also wish to acknowledge Nicolò (Prof. Nicolò Zampieri), for his friendship and for his continuous helpfulness, that always led to a straight road even when I had been stuck for a bit. I really appreciate how both Prof. Bosso and Prof. Zampieri warmly welcomed me as a part of the research group: we worked really hard, but we often found moments to enjoy our time together.

I would like to acknowledge Prof. Luciano Cantone, from Università di Roma Tor Vergata, for his kindness and for his help in many topics related to the simulation of longitudinal train dynamics.

I wish to sincerely thank Prof. Riccardo Trinchero, from Department of Electronics and Telecommunications at Politecnico di Torino, for his great contribution in the development of digital twins of multibody simulations, for always kindly clearing up my doubts and for his advice on my thesis.

I would like to express my gratitude to Ing. Andrea Ottati, from Trenitalia, for his great help in the activities dealing with tread braking thermal effects. I also sincerely thank Giovanni Falcitelli, from EnginSoft S.p.a., for patiently describing many details of the ANSYS finite element code.

The support of Dr. Qing Wu, from Central Queensland University, who provided useful data and fruitfully collaborated with the research group on many topics, is greatly acknowledged, and I hope we can soon meet after a long time of remote collaboration.

Many thanks to Ignazio, a train engineer and friend of my whole family, for giving me useful information that I could never have found on books and papers.

I wish to express my sincere gratitude to Eng. Ben Altman, from Rail Safety and Standards Board, for kindly providing useful reports of experimental activities carried out over the years in the UK. I also acknowledge Prof. Mats Berg and Prof. Ulf Olofsson, from Royal Institute of Technology, for their insights into railway wear laws.

Finally, I wish to thank all the students that over these years have been working on their master's degree thesis with the research group. They worked hard and gave a big contribution to many activities that are shown in my thesis.

Abstract

Despite being a mature and reliable technology, the traditional railway braking system is not exempt from critical issues and limits, that require further investigations and analyses. Since on-track tests feature high costs, low repeatability, and often lead to traffic interruptions, the simulation of braking operations with numerical codes, enabled by the high power of modern computers, and with laboratory devices is often the best compromise solution. Therefore, this thesis deals with the development of numerical and experimental tools for the investigation, simulation and optimization of railway braking operations.

Because of the large in-train forces that can arise on long trains, which increase the derailment risk, one of the goals of the present thesis was the implementation of an efficient and accurate longitudinal train dynamics (LTD) code. In previous activities, the research group had developed an LTD model implemented within the Simpack multibody (MB) code, but the model produced numerical instabilities and divergences in the simulation of freight trains with many vehicles. The new code, named LTDPoliTo, was written in MATLAB, making use of vectorization programming strategies and built-in functions for the management of large arrays, storing the main input data of the simulations. The code was validated in the simulation scenarios suggested in an international benchmarking activity. The final version of LTDPoliTo can estimate the air brake forces generated on common European freight vehicles, using a simplified

approach which only requires the knowledge of the wagon braked weight. Moreover, because typical LTD codes cannot calculate the wheel-rail contact forces, that are needed for the estimation of the safety indexes, including the derailment coefficient, this thesis shows a possible approach to compute these indexes from the outputs of LTD simulators. The proposed method relies on training closed-form surrogate models, working as digital twins of computationally expensive and long-lasting MB simulations.

The air brake system adopted on trains is based on the friction forces that are generated at the wheel-rail contact patch, which are strongly dependent on the possible presence of contaminants at the contact interface. Contaminants are known to reduce the friction coefficient and to modify the adhesion curve shape, thus affecting safety and performances of braking operations. Therefore, a second goal of the thesis was the setup of an innovative multi-axle roller-rig, previously designed by the research group. The configuration of the test bench allows to simulate the adhesion recovery phenomena activated by the friction forces, which partially remove the contaminant layer sticking to wheel and rails. The bench setup required the calibration of the sensors installed on the rig and the implementation of a bench control software. In a subsequent activity, the original bench configuration was modified, and a new motor control strategy was designed, to simulate the vehicle inertia on the bench.

Finally, the thesis shows the development of a numerical tool for the computation of the worn profile of railway wheels and of a numerical tool allowing to estimate the wheel temperature during tread braking operations. These tools are essential to estimate the damage of the railway wheel running surface, and their outputs can be used to tune innovative monitoring systems. The wear tool is based on dynamic simulations run in Simpack, while the wheel thermal model relies on finite element (FE) modules for the solution of the wheel-shoe

conformal contact problem and for the subsequent estimation of the temperature field in the wheel during drag and stop braking operations.

Contents

List of Figures

List of Tables

Chapter 1

Railway braking system

The present chapter gives an overview of the air brake system installed on railway vehicles, describing its most important components, and highlighting the major differences between passenger coaches and freight wagons. Then, focus is given to the notions of braked weight and braked weight percentage, which are used to describe the railway vehicles running on European lines. Finally, the primary issues related to the traditional air brake system are discussed and the main activities carried out in the context of the present thesis are briefly listed.

1.1 Introduction to railway braking

Braking is one of the most critical operations for railway vehicles as it affects the performances, punctuality, and safety of the whole railway system. Braking operations are required when the train has to decelerate until stop (stop braking), when the train speed must be kept constant on a downhill track section (drag braking), when the train speed must be reduced to a lower value and finally when a vehicle stopped on a line must be prevented from running (parking brake).

During braking operations, the kinetic energy of the vehicle is converted into a different energy form. Therefore, braking systems can be classified according to the energy form into which the vehicle kinetic energy is converted or according to the dependency of the braking system on adhesion at the wheel-rail interface. A comprehensive review of different braking systems adopted in railway vehicles can be found in the recent work by Günay et al. [1].

The typical solution adopted in railway braking systems is based on brake shoes or pads pressed against the surface of the wheels (tread braking) or brake

discs (disc braking), respectively. This kind of friction brakes clearly converts the kinetic energy of the vehicle into heat, which heats up the surfaces of the friction elements and is eventually dissipated to the ambient air. The main drawback of this solution is linked to the wear of brake shoes/pads, but also to the heating of the wheel surface in case of tread braking. For vehicles provided with electric traction units, a possible braking strategy is the transformation of the vehicle kinetic energy into electricity, with the electric motors acting as generators. The amount of converted energy is not negligible, so several feasibility studies investigated the possibility of implementing regenerative braking strategies to recover the kinetic energy through on-board batteries or by powering the electric network [2,3]. Nevertheless, in Italian lines and in many other countries, the kinetic energy is typically dissipated though rheostatic banks, to avoid voltage fluctuations on the network. Examples of regenerative braking strategies are implemented in special lines where the operations of two trains running in opposite directions is synchronized so that the kinetic energy of the train decelerating on a downhill section is immediately used to power the other vehicle which is facing an uphill grade [4]. Clearly, the efficiency of dynamic braking is strongly dependent on the vehicle speed, therefore this system usually acts as a support or back-up to friction brake systems. Other types of brake systems that rely on adhesion at the wheel-rail interface include rotating eddy current brakes, based on magnetic discs mounted on the wheelset and spinning inside the magnetic field generated by permanent magnets, and hydrodynamic brakes, used in vehicles powered by hydraulic motors.

As the adhesion at the wheel-rail interface drops to extremely low values at large speeds, concept designs for adhesion independent brakes include aerodynamic brakes as well as linear eddy current brakes based on an electromagnetic repulsion between the wheels and the rails.

Nonetheless, the most common brake system installed on all types of railway vehicles still relies on friction elements, namely brake pads and brake shoes, pressed against brake discs or against the wheel tread surface. The pressing force is typically obtained using compressed air thanks to a dedicated pneumatic plant which is installed along the whole length of the train. Despite the wear of the brake friction elements and the heating of tread braked wheels, this system ensures an excellent reliability which makes it the best option for emergency operations. Furthermore, brake shoes are used in parking brake systems to prevent the vehicle from moving. However, for such applications the pressing force is typically obtained through manual screw systems, as the pressure in the air brake

plant can drop to atmospheric pressure after long stops because of the leakages in the sealing elements.

1.2 UIC air brake system

The UIC 540 leaflet [5] sets the main conditions that the air brake system installed on European railway trains must fulfil. According to the prescriptions of the standard, the air brake system must be:

- *Automatic*. The braking action must be automatically produced in emergency conditions, for instance in case of breakage of the train composition.
- *Continuous*. A single air brake plant must connect all the vehicles in the train composition and the braking command can be provided from any vehicle, at least in emergency conditions.
- *Adjustable*. The braking force must be adjustable in both braking and releasing operations.
- *Inexhaustible*. The braking system must always ensure a new application of the braking force even immediately after a braking operation.

The conceptually simplest way to obtain a braking action through a fluid is the use of a direct braking system, like the one installed on automotive cars, which moves a brake cylinder when the pressure in the plant is increased. Nevertheless, such a solution does not comply with the requirement of an automatic brake system, therefore nowadays it is limited to service brake operations on locomotives. A first step towards the fulfilment of the automaticity constraint was the design of vacuum brakes, in which vacuum is obtained on a brake pipe running along the train using ejectors, and the braking action occurs when the atmospheric pressure is restored in the plant. This system is automatic, since in case of breakage of the train composition, the atmospheric pressure is automatically restored in the brake pipe. However, the main drawback of the vacuum brake system is related to the need for brake cylinders with large diameters and to the long times required to create vacuum conditions on all the brake cylinders installed on the vehicles.

Therefore, the air brake system commonly installed nowadays on railway freight vehicles is an evolution of the solution that George Westinghouse had already proposed in 1896. The air brake system, sketched in Figure 1, relies on a brake pipe, connecting all vehicles in the train, which in normal running operations is kept at a constant pressure equal to 5 bar. The compressed air is

obtained thanks to a compressor C installed in the head locomotive and stored in a main reservoir MR at a pressure of 8-10 bar. The train driver in the head locomotive can command a brake operation by means of a dedicated brake valve V. When a braking operation is commanded, the pressure in the brake pipe running along the train is reduced and a sensing valve D (distributor valve or triple valve) opens the communication between an auxiliary reservoir AR and the brake cylinder installed in each vehicle. As can be seen in Figure 1, the head locomotive differs from the other wagons as it includes the compressor and the main reservoir, as well as the brake valve. The core of the system is the distributor valve installed on each vehicle. The distributor manages the communication among the auxiliary reservoir AR, the command reservoir CR, and the brake cylinder. The command reservoir CR acts as a *memory* element because it is kept at a constant pressure of approximately 5 bar, corresponding to the nominal pressure of the brake pipe in running conditions. The auxiliary reservoir is the *lung* of the system, as it is filled with the air that flows to the brake cylinder during braking operations, up to a maximum pressure of 3.8 bar. Finally, the force produced at the brake cylinder level is magnified and transferred to the brake shoes through a system of mechanical levers, i.e., the brake rigging. Please note that the system shown in Figure 1 includes a single brake cylinder per each wagon, which is the typical configuration for freight trains, nonetheless other solutions are possible.

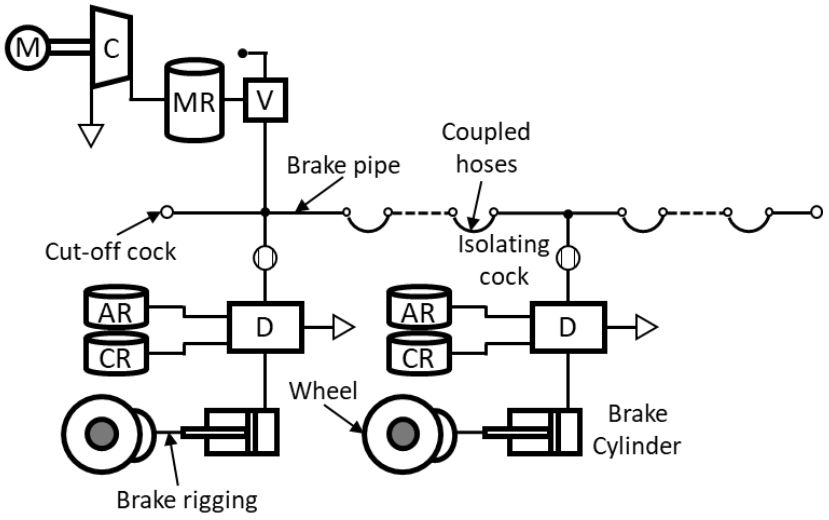

Figure 1: Single-pipe air brake system typically installed on freight wagons.

As mentioned above, the core of the UIC braking system is the distributor, which allows to fill the brake cylinder with compressed air when the pressure in

the main brake pipe decreases. Figure 2 shows a sketch of the distributor valve. The working principle of the valve depends on the pressure in volumes C and D, and on the corresponding position of the main piston (3). In normal running conditions, when braking is not applied, the pressure in volumes C and D, connected to the main brake pipe and to the command reservoir respectively, is equal to 5 bar. Therefore, the main piston (3) is at its lowest position and the volume A, which is always connected to the brake cylinder, is in communication with volume B and ultimately with the atmosphere. If the pressure in the auxiliary reservoir is below the nominal value of 3.8 bar, air flows from volume C to volume E through the check valve (7), so that a refill of the auxiliary reservoir occurs.

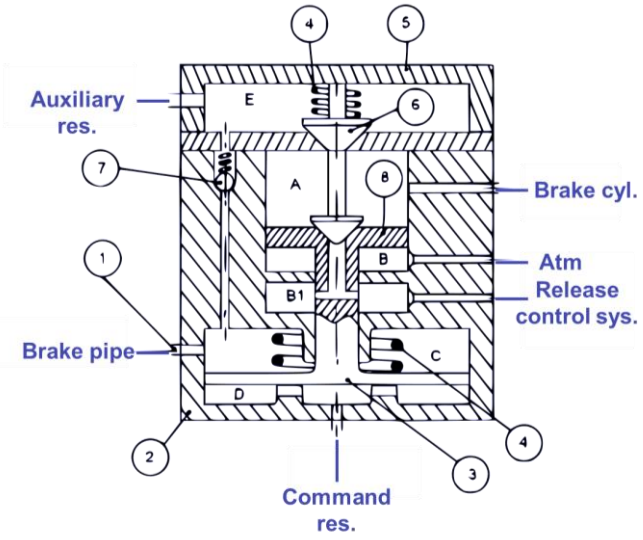

Figure 2: Simplified drawing of the brake distributor.

During a braking operation, the pressure in the brake pipe and hence in volume C decreases below the nominal value of 5 bar, while the pressure in the command reservoir is always kept at 5 bar. Therefore, the main piston (3) moves upwards and comes into contact with the double piston (6). In this position, air in volume A is prevented from flowing into volume B, while an air flow streams from volume E to volume A. As a consequence, the auxiliary reservoir is supplying the brake cylinder, and a braking force is being applied.

Finally, in release operations, the pressure in the brake pipe is gradually increasing up to 5 bar and therefore the main piston moves downwards. The lower piston of the double piston is not in contact with the main piston (3), so air can

flow from the brake cylinder to the atmosphere, and the brake cylinder pressure can be gradually released.

The braking system described so far and sketched in Figure 1 is typically adopted on freight trains. On passenger trains, due to the requirements for quicker release operations, a slightly different system is used, based on two pipes running along the whole length of the train consist, namely a train brake pipe, like the one adopted in the freight train brake system, and a main reservoir pipe, which directly connects the main reservoir to the auxiliar reservoir, see Figure 3. The main pipe is the same pipe used to feed the pneumatic on-board auxiliary devices, e.g., doors. Air in the main pipe downstream the main reservoir is at a pressure of approximately 8 bar, therefore a pressure reducer is necessary to ensure that pressure in the auxiliary reservoir never overcomes the maximum value of 3.8 bar. The check valve installed between the main reservoir and the auxiliary reservoir is essential to prevent air from flowing from the auxiliary reservoir to the main reservoir in case of breakage of the main pipe.

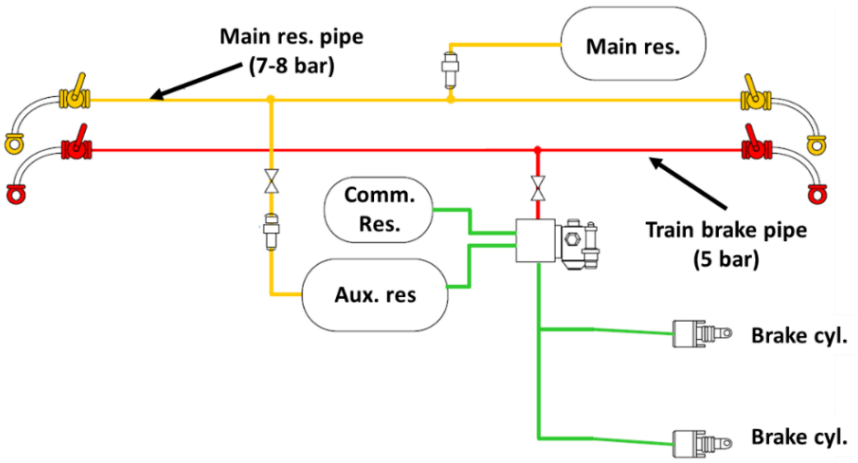

Figure 3: Sketch of the double pipe air brake system.

Apart from being supplied by the brake system running along the whole train length, the brake cylinders installed on the head locomotive can be directly supplied by the main reservoir, thanks to a direct brake installed in the locomotive and commanded via a dedicated brake valve, see Figure 4. The locomotive brake is typically used as a direct brake during operations between the train depot and the railway station, however it can also be applied at the train stop to prevent the train from moving. The working principle of the locomotive direct brake relies on a two-way selector valve acting as a logic “or” (8). When the train driver activates

the locomotive brake via the dedicated valve (2), air flows from the main reservoir to the selector valve, and the passage towards the brake cylinder is open, so that the brake cylinders are fed to brake the locomotive wheels. The air pressure flowing to the brake cylinder is proportional to the rotation of the locomotive brake valve handle, and this is essential to limit the brake pressure so that wheel locking is prevented.

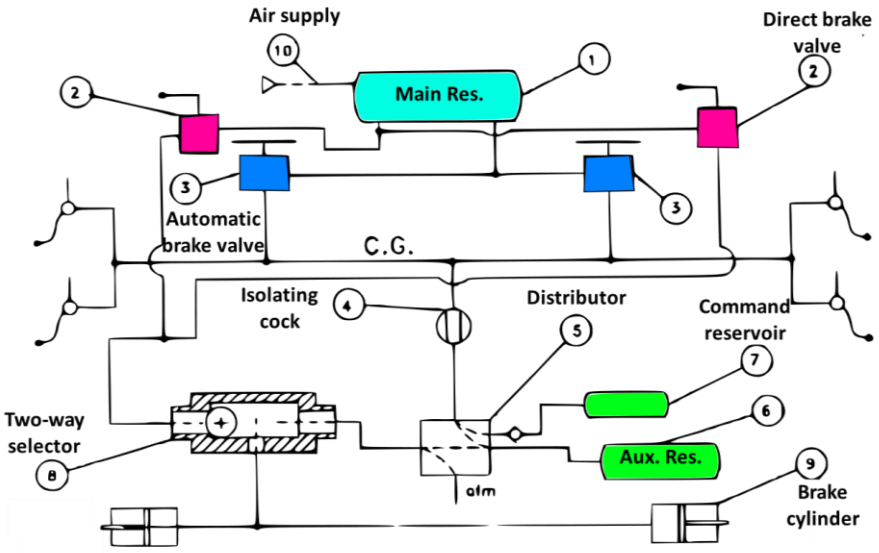

Figure 4: Direct brake installed on locomotives.

1.2.1 Additional equipment

The present subsection provides further details about the additional components included in the railway brake system to improve the braking performance. Before listing and describing such devices, it is essential to briefly show the mechanics of the braked wheel to highlight the main issues related to braking operations, see Figure 5, which sketches the main forces acting on the wheelset during braking operations.

The sum of all pressing forces pushing the friction elements $\Sigma_{ax}F_{b,N}$ acts at a braking radius r_b. In tread braked wheels, the braking radius is equal to the wheel radius r_w, while in systems relying on brake discs, the braking radius has a different value, lower than the wheel radius and depending on the position and size of the brake pads. Due to the application of a braking torque on the wheelset, a reaction force ΣF_x is generated at the wheel-rail interface, which opposes the wheel motion. The value of the longitudinal force is limited by the maximum friction coefficient at the wheel-rail interface. In case adhesion is saturated, the

wheels lock and the braking performance drops, causing negative effects, like the generation of wheel flats and a severe wear of the wheel rolling surface. The adhesion limit condition is expressed by the inequality in equation (1.1), where $\Sigma_{ax}F_{N,b}$ is the sum of all pressing forces acting on the friction elements installed on the wheelset, Q_{ax} is the axle-load, f_{wr} is the wheel-rail friction coefficient and μ_b is the friction coefficient related to the braking friction surface.

$$\Sigma_{ax}F_{b,N} \leq Q_{ax}\frac{f_{wr}}{\mu_b}\frac{r_b}{r_w} \tag{1.1}$$

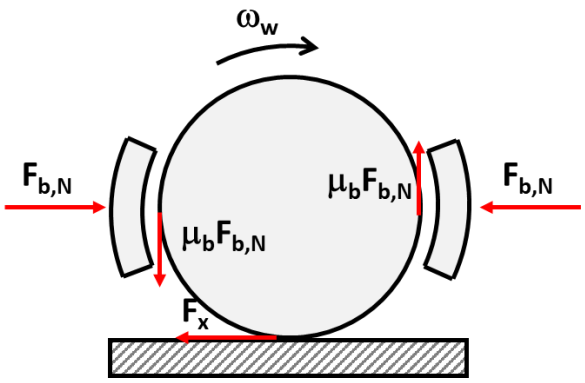

Figure 5: Forces acting on a braked wheelset.

As the ratio between the braking radius and the wheel radius is constant, equation (1.1) states that the pressing force must be limited as a function of the axle-load, which may vary significantly in empty and loaded conditions, especially on freight wagons. Therefore, the braking force should be adjusted as a function of the axle-load, to maximize the braking performance while at the same time preventing the wheels form locking. Furthermore, the ratio between the wheel-rail adhesion coefficient and the friction coefficient at the brake friction surface is not constant as both coefficients show a dependency on the wheel speed [6,7], see Figure 6. The ratio f_{wr}/μ_b increases at larger speed, hence a higher pressing force can be applied at the beginning of a braking operation, whereby the speed value is maximum.

In conclusion, the pressing force should be adjusted as a function of both the axle-load and the current speed, to improve the braking performance. To comply with these requirements, modern railway vehicles are provided with proper on-board systems.

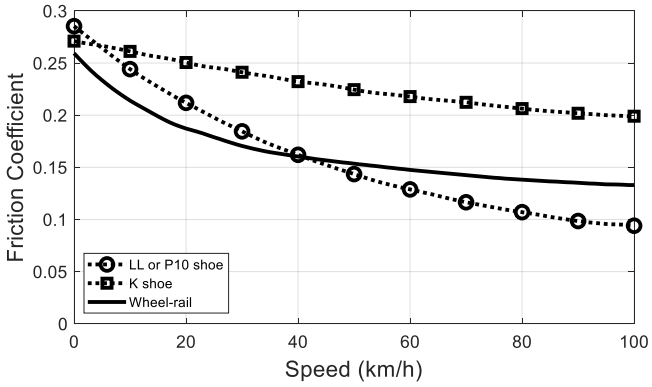

Figure 6: Dependency of wheel-rail and wheel-shoe friction coefficient on speed.

The first kind of systems adopted to adjust the braking effort includes empty-loaded devices that modify the pressing force according to the weight of the vehicle on the rails. These devices can be either mechanical or pneumatical. In the first case, the pressing force is adjusted through a change in the rigging ratio, while with pneumatical devices, the reduction of the pressing force in empty conditions is obtained by decreasing the maximum brake cylinder pressure. Regardless of the basic principle exploited to adjust the normal pressing force, these devices can be classified into systems that are able to continuously adjust the normal force [8] and systems that only adjust the force in a two-stage way [9], i.e., adopting two separate values for empty and laden conditions. For the latter type of systems, the variation of the force level can be obtained either manually, by means of a proper cranked lever that is typically installed on both wagon sides, or automatically, i.e., with an additional system that is able to sense whether the vehicle weight on rails is above a threshold value (changeover weight).

As previously mentioned, equation (1.1) states that the sum of all normal forces is limited by the ratio between the wheel-rail maximum adhesion coefficient and the friction coefficient at the interface between the brake friction element pair (wheel-shoe for tread braked wheels and disc-pad for disc brakes). Both coefficients are a function of the wheel speed, and Figure 6 shows that at high speeds, the wheel-rail friction coefficient is greater than the brake friction coefficient of cast iron shoes, while at lower speeds the situation is reversed. For this reason, the ratio between the two friction coefficients decreases with decreasing speed. To adjust the braking effort with speed, freight vehicles equipped with tread brakes running at speeds above 120 km/h are provided with a dedicated device (high-speed valve), which is a pressure transformer that reduces the braking pressure at low speed. The system is sketched in Figure 7. At higher

speed values, the coil of the selector valve on the right opens the connection between the distributor and the C1 volume, so that the dummy cylinder moves upwards and the connection between the auxiliary reservoir and the brake cylinder is established. In such condition, due to the vertical equilibrium of the dummy cylinder, equation (1.2) holds, in which S_1 is the upper surface of the dummy cylinder, p_d is the pressure signal from the distributor and p_{out} is the outlet pressure flowing towards the brake cylinder. Therefore, the output pressure is equal to the pressure of the signal coming from the distributor. On the other hand, when speed is below a threshold value (60 km/h), the coil of the selector valve opens the connection between volume C1 and the atmosphere. In this condition, the equilibrium of the dummy cylinder is expressed by equation (1.3), in which S_2 is the lower surface of the dummy cylinder. Consequently, since $S_2<S_1$, the output pressure is lower compared to the control signal coming from the distributor.

$$p_d S_1 = p_{out} S_1 \rightarrow p_{out} = p_d \tag{1.2}$$

$$p_d S_2 = p_{out} S_1 \rightarrow p_{out} = p_d \frac{S_2}{S_1} \tag{1.3}$$

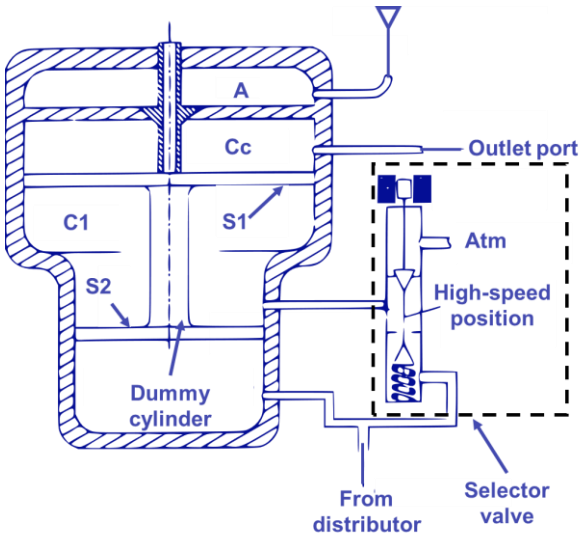

Figure 7: High-speed valve.

Apart from the previously described high-speed valve, modern passenger vehicles can include a more complex system, referred to as the wheel slide protection (WSP) system, which is a mechatronic device including a wheel speed sensor, a control unit, and a group of electro-pneumatic valves, which can be grouped into a single valve unit. The algorithms implemented in the WSP control

unit can detect locking, unlocking and re-adhesion conditions [10]. When wheel locking is detected, the brake cylinder pressure is released, until the wheel unlocks. Then, pressure at the brake cylinder is kept constant, and finally, when re-adhesion takes place, the brake cylinder is supplied again, and pressure increases. The main benefits related to the WSP system include the minimization of the braking distance and the reduction of the wheel damages due to wheel flats and wear.

One of the main drawbacks of the air brake system is the delay of the braking action along the train. In fact, the brake pipe is discharged at the head locomotive, and the pression drop wave propagates along the train with a limited speed, in the range of 250 m/s-300 m/s. Consequently, while the front vehicles are already applying braking forces, the vehicles at the back of the train are unbraked and still tend to push the train forward. Therefore, large compressive in-train forces are generated on the coupling systems, which can increase the derailment risk. This issue is accentuated on long freight trains, especially those operating outside Europe, which can feature total lengths of several kilometres. A possible mitigation is represented by electro-pneumatic brakes, which include additional valves in each vehicle to synchronize the braking operation of all vehicles in the train consist. Nonetheless, since these additional valves are activated using electrical signals, this system is mainly adopted on passenger vehicles, as freight wagons typically lack electrification.

Since the electro-pneumatic brake system cannot be applied on all vehicles because it requires an on-board electrical power supply, simpler systems exist to partially mitigate the issues related to the delays in the air brake system. One of these systems is the first-stroke device, which is commonly integrated in the distributor. The first-stroke device is used to ensure a quick growth of the pressure in the brake cylinder to a value of 0.6 bar, which allows to push the brake shoes or pads against the wheel or disc. After reaching the braking pressure value of 0.6 bar on a specific vehicle, the pressure growth rate is decreased, so that a more homogeneous braking effort is produced on the train.

Moreover, to avoid the generation of large dynamic forces on the coupling systems, the braking and releasing times of freight wagons are increased with respect to passenger vehicles. Two brake regimes (or positions) exist, namely the P (passenger) and G (goods) regimes. According to the UIC 540 leaflet, the brake cylinder filling time in G position must be in the range 18-30 s, while in P regime, the filling time must be between 3 and 5 s, with a maximum value of 6 s if a load-

braking system is installed on the vehicle. On the other hand, the draining time of the brake cylinder in release operations must be between 45 and 60 s in G regime and between 15 and 20 s for the P regime. Figure 8 shows the brake cylinder pressure rise in braking operations for the two regimes. The selection of the brake regime can be performed using a dedicated cranked lever, installed on both wagon lateral sides, which changes the diameter of the calibrated orifices of the distributors. The difference between the filling time of the two regimes can be exploited to obtain a better synchronization of the braking effort along the train, by setting the braking regime to G for the head locomotive and a few vehicles at the head of the train, while keeping all other vehicles braked in P position. This strategy is commonly referred to as "long locomotive" [11].

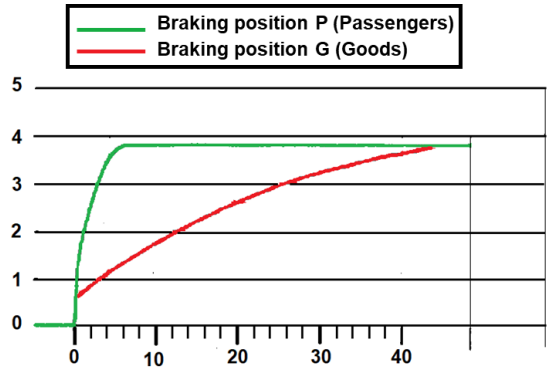

Figure 8: Brake cylinder pressure in filling operations for P and G braking positions.

1.3 Braked weight (UIC 544-1)

The efficiency and performances of the braking system of a railway vehicle equipped with the UIC air brake system are described in terms of its braked weight and braked weight percentage as defined in the UIC 544-1 leaflet [12]. The braked weight percentage λ of a single railway vehicle is calculated according to equation (1.4), where M is the vehicle mass (tonnes), and B is the braked weight (tonnes). The braked weight of a passenger coach corresponds to the braked weight of the vehicle when it is part of a train with a length of 400 m, while for freight wagons, the braked weight is defined as the braked weight of the vehicle when it is included in a 500 m long train. For a whole train, the braked weight percentage is calculated as the ratio between the sum of all braked weights of the braked vehicles $\sum_b$ B and the sum of the masses of all individual wagons $\sum$ M, see equation (1.5).

$$\lambda = \frac{B}{M} \cdot 100 \tag{1.4}$$

$$\lambda = \frac{\sum_b B}{\sum M} \cdot 100 \tag{1.5}$$

The notion of braked weight was first introduced in France in 1938, as a result of the experimental tests carried out by Pedeluc, an engineer working for the French railways [13]. To assess the braking performances of trains, Pedeluc ran tests of emergency braking operations on a reference train including 15 identical passenger coaches, equipped with brake shoes made of low phosphorus cast iron. The stopping distances recorded on the reference train when all vehicles were braked corresponded to a braked weight of 100%, while different values of the braked weight were obtained by leaving some of the coaches unbraked. Thanks to this experimental campaign, Pedeluc was able to find an experimental relationship between braked weight and stopping distance. The indication of the braked weight on modern vehicles is thus related to the ratio between the stopping distance of the vehicle and the stopping distance obtained on Pedeluc's reference train.

According to the UIC 544-1 leaflet, the braked weight of a vehicle can be determined via experimental tests or by calculation. The experimental tests suggested in the leaflet require to run emergency braking operations for different values of the initial speed and to record the braking distance for each test. The UIC 544-1 relates the braking distance S (m) to the braked weight percentage according to the expression stated by equation (1.6), where C and D are constants depending on the initial speed. The relationship between braking distance and braked weight percentage can also be expressed by means of equation (1.7), which gives results close to the ones calculated by equation (1.6) and in which V is the initial speed (km/h), i_g is the track slope, and φ(V) is tabulated as a function of the initial speed. Therefore, after running emergency braking tests from different initial speeds, the braked weight of the tested vehicle is defined as the minimum braked weight among those obtained at the different investigated speed values.

$$S = \frac{C}{\lambda + D} \tag{1.6}$$

$$S = \frac{V^2}{\frac{1.094\lambda}{100\varphi(V)} + \frac{0.127}{\varphi(V)} + 0.253 i_g} \tag{1.7}$$

The UIC 544-1 also provides a simpler calculation method for the determination of the braked weight of freight wagons meeting the following requirements:

- Maximum speed below 120 km/h.
- Maximum axle-load of 22.5 tonnes.
- Brake blocks applied on both sides of the wheel, in either Bg or Bgu configurations. The Bg configuration refers to blocks with one shoe per holder, while the Bgu configuration features two shoes per brake holder.
- Wheel diameter in the range 920-1000 mm.
- Maximum force on the block in the range 5-40 kN for Bg configuration and in the range 5-55 kN for Bgu configuration.

For this kind of wagons, the braked weight can be calculated according to equation (1.8), in which B is the braked weight (tonnes), $\sum F_{dyn}$ is the sum of all brake block forces (kN), g is the acceleration of gravity and k is an assessment factor provided by the leaflet as a function of the block force and depending on the block configuration, see Figure 9.

$$B = \frac{k \sum F_{dyn}}{g} \tag{1.8}$$

The sum of all brake block forces is computed according to equation (1.9), where F_t is the force at the brake cylinder (kN), i_G is the total rigging ratio, i^* is the rigging ratio after the central rigging (commonly equal to 4 for two-axled wagons and to 8 for bogie wagons), F_R is the counteracting force of the brake rigging regulator (suggested equal to 2 kN) and finally η_{dyn} is the rigging efficiency, which commonly lies in a range between 0.83 and 0.91. The brake cylinder force is calculated according to equation (1.10), where p_{cyl} is the brake cylinder pressure (bar) D_{cyl} is the brake cylinder diameter (mm) and $F_{s,cyl}$ is the brake cylinder spring return force, suggested equal to 1.5 kN. The calculation of the braked weight percentage in all loading conditions is an essential information for the train engineer, as the railway infrastructure managers typically provide tables that relate the maximum allowed speed on the line as a function of the braked weight percentage and of the line slope.

$$\sum F_{dyn} = (i_G F_t - i^* F_R)\eta_{dyn} \tag{1.9}$$

$$F_t = \frac{p_{cyl}}{1000} \cdot \pi \frac{{D_{cyl}}^2}{4} - F_{s,cyl} \tag{1.10}$$

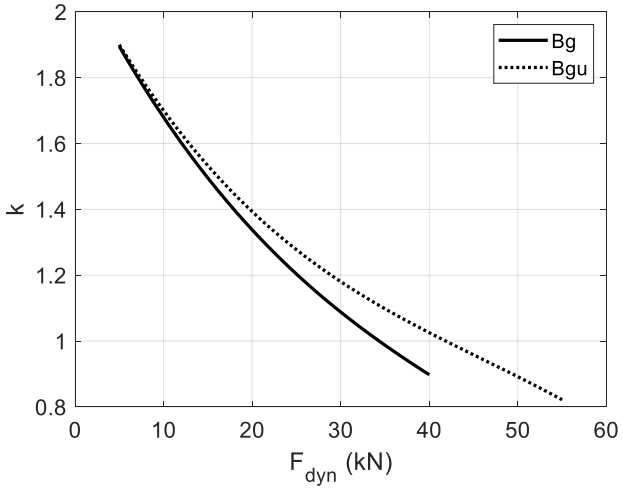

Figure 9: k factor (defined by the UIC 544-1 leaflet) for the assessment of the braked weight of freight wagons.

1.4 Main issues related to braking operations and scope of the thesis

The air brake system adopted on railway vehicles, shown in the previous sections, is still affected by several issues that need to be tackled to maximize the safety and the performances of braking operations.

As already pointed out, the main drawback of the traditional air brake system is the delay of the brake application along the vehicles in the train consist, which is related to the limited propagation speed of the pressure drop wave along the train brake pipe. Due to this delay, the vehicles at the front of the train consist generate a braking action while the vehicles at the rear are still unbraked and push the train forward. This condition generates compressive forces on the coupling elements connecting the adjacent vehicles (buff forces). Large values of buff forces are correlated to an increase of the derailment risk [14-17]. Since modern freight trains must ensure higher speeds and loads, it is obvious that great focus must be paid to the composition of full trains to minimize the values of the in-train forces during braking operations. To reach this goal, the simulation of the dynamic behaviour of isolated vehicles is not enough, as the dynamics of the whole train strongly influences the values of the in-train forces that may eventually cause derailment. In fact, the optimization of the dynamic behaviour of

a whole train is the key to turn into reality the possibility of having longer freight trains running on the European railways. Among the activities described in the present thesis was indeed the development of an in-house longitudinal train dynamics (LTD) code, which must be able to compute the in-train forces for different operating conditions of the train with a good computational efficiency.

Another big issue of railway braking operations concerns the friction conditions at the contact interface. In fact, the braking efforts produced by the air brake system ultimately lead to the generation of longitudinal forces at the wheel-rail contact patch. The value of these forces is limited by the friction coefficient at the wheel-rail interface. It is clear that in degraded adhesion conditions, the braking distances increase, and the braking performances are worsened. At the same time, if the wheels lock during a braking operation, local defects can arise on the wheel surface, such as the well-known *wheel flats*. Although modern passenger vehicles are provided with WSP systems, there is still a lack of knowledge in the literature for what concerns braking operations in degraded adhesion conditions. In fact, when the leading wheelsets of the train face a contaminated section, high creepage values arise and the work of the friction forces can partially remove the contaminant from both the wheels and rails, thus restoring higher adhesion levels for the rear wheelsets. Nonetheless, modern WSP systems and algorithms neglect these adhesion recovery phenomena due to the limited knowledge in the field. As part of the activities carried out in the context of the present thesis, a laboratory test rig (the *multi-axle roller-rig*) was set up for the investigation of the adhesion recovery phenomena.

As previously pointed out, freight wagons are still commonly equipped with block brakes. The main downside of this system is understandably the frictional heating of the wheel surface. Traditional cast iron shoes with phosphorus (P10 cast iron shoes) were responsible of thermo-elastic instability (TEI) phenomena which eventually led to squeal noise, so they are being gradually replaced by shoes made of composite materials. Nonetheless, composite shoes can have different mechanical, thermal and even frictional properties compared to P10 shoes, and they eventually proved to lead to a higher wheel surface heating. Thermal stresses in the wheel can cause several kinds of wheel surface damage, like shelling, spalling, the generation of local hot spots and even crack initiation. At the same time, thermal stress can lead to local phase transformations, which drastically change the mechanical properties of the rail wheel steel. Damages to the wheel surface are not only due to tread braking operations, since the transmission of longitudinal forces at the wheel-rail contact interface inevitably

generates local contact stresses, that ultimately cause the wear of the wheel profile. As the wheel profile shape is commonly optimized to improve the dynamic behaviour of railway vehicles, changes in the profile shape are totally undesired and must be kept under control. To address wheel damage phenomena, the research group recently started implementing a finite-element model for the computation of the wheel temperature in braking operations, as well as a new tool for the calculation of the wheel worn profile, due to the material removal linked to the dynamic behaviour of the vehicle.

The present thesis aims at developing numerical and experimental techniques for the investigation of the main issues related to braking operations of both isolated vehicles and trains. The main topic faced in the present thesis is clearly the investigation of the longitudinal train dynamics during braking operations, which is the activity that has been most thoroughly investigated. Further investigations concerned other aspects related to braking operations, such as the setup of experimental test rigs to study adhesion at the wheel-rail contact even under degraded conditions. Moreover, this thesis focused on aspects related to the wear of wheel profiles and to the thermal balance of the wheel-shoe pair. These last aspects, unlike the first ones, can be considered as preliminary activities that can thrust the development of an integrated approach for the investigation of all issues related to braking operations.

The thesis is organized as follows. Chapter 2 shows the new specifically built LTD code, focusing on its implementation, its validation and on the recent upgrades made to extend its modelling capabilities. Chapter 3 deals with the description of the new multi-axle roller-rig, first highlighting the calibration of the bench sensors and the development of the bench control software, and then outlining the results of preliminary experimental campaign for the investigation of degraded adhesion conditions and adhesion recovery phenomena. Then, the chapter shows changes made to the bench configuration allowing to carry out activities for testing and validation of monitoring systems. Chapter 4 presents the last works carried out by the research group, dealing with the development of numerical codes for the calculation of wheel profile wear and wheel temperature. Finally, chapter 5 summarizes the main conclusion of the activities performed in the frame of the present thesis.

Chapter 2

Longitudinal train dynamics

The simulation of longitudinal train dynamics (LTD) is indispensable to evaluate the in-train forces which can arise on the wagon connection systems. In fact, large values of compressive in-train forces generated during braking operations are known to increase the derailment risk. At the same time, the determination of the longitudinal dynamics of a long train is often the first step for further analyses, such as the estimation of the wheel/shoe temperature or the prediction of the wheel/shoe wear. Several examples of LTD simulators can be found in the literature, however they are typically in-house codes rather than commercial software packages. Therefore, the research group needed to develop an in-house LTD code able to produce reliable results, to be integrated in the framework of the main activities of interest, including the investigation of the wheel-rail contact and the simulation of the wheel-shoe thermo-mechanical behaviour, which are shown in the next chapters. Prior to the works shown in the present thesis, the research group had tried to implement a Simpack multibody (MB) model for LTD simulations of long freight trains, but this strategy led to numerical inefficiencies. Next, the group started implementing a MATLAB code at a very early stage of development. Nonetheless, the MATLAB code produced unreliable output results, and the computational efficiency was poor.

Therefore, the main contribution of the present thesis for what concerns the works of the research group on LTD modelling is represented by the full design and implementation of the new MATLAB LTDPoliTo code, able to calculate reliable output results with a low computational effort. Apart from validating the new in-house code and optimizing its computational performances, the present thesis aimed at expanding the modelling capabilities of the code. In fact, as the literature witnesses many different expressions for the calculation of the running

resistances, the LTDPoliTo code was upgraded to enable the user to set and test different laws, and simulations were launched to assess the influence of such equations on the main output results. Furthermore, as the LTDPoliTo code was initially validated in the frame of an international benchmark neglecting the air brake forces, this thesis aimed at providing the newly built in-house LTD simulator with a module for the fast computation of the air brake forces acting on typical European freight wagons. In fact, the estimation of the air brake forces is essential to adopt the LTDPoliTo code for the new activity on which the research group is currently working, dealing with the simulation of the temperature of tread braked wheels. Finally, since common LTD codes are not able to compute the values of the wheel-rail contact forces, this thesis shows a possible strategy to derive the running safety indexes directly from the outputs of an LTD simulator, by means of digital twins replacing computationally demanding multibody simulations. The development of the new strategy required the introduction of the LTDPoliTo code into a wider computational framework, including a MB model of a reference wagon and MATLAB routines for the derivation of surrogate models. This computational framework was totally conceived as a part of the present thesis, however the wagon MB model had already been developed by the research group in past activities, while the derivation of the surrogate models was performed by the EMC group of Politecnico di Torino, with a great expertise in the field of machine learning techniques.

This chapter is organized as follows. Firstly, the chapter provides an overview of the typical modelling strategy for LTD simulation, and then it highlights the implementation and validation of the LTDPoliTo code. Finally, the main recent code upgrades are presented and discussed.

2.1 Introduction to LTD models

LTD refers to the longitudinal motion of the train as a whole as well as to the relative motions between adjacent vehicles (slack actions), that are allowed by clearances in the coupling elements and by their flexibility [18]. LTD simulations are the key to predict the values of the in-train forces during train operations. In fact, large tensile forces (draft forces), can lead to a breakage of the train composition, while large buff forces increase the derailment risk. The main applications of LTD modelling include [19]:

- Calculation of the in-train forces to assess the safety of train operations.
- Design and testing of innovative coupling and braking systems.

- Prediction of speed and position of each vehicle during a specific mission of the train.
- Choice of the best driving strategy to comply with the mission requirements and possibly to minimize the energy consumption.

Commonly, LTD simulators model the train as a system composed by concentrated point masses, corresponding to the vehicles, connected to each other by means of springers and dampers, that represent the coupling elements and thus feature a strongly nonlinear mechanical impedance characteristic. Each point mass in the system only has a single degree of freedom (dof) along the longitudinal direction. Track slopes and curves are simply considered in terms of their effect on the longitudinal motion of the vehicles, through the definition of equivalent resistant forces. Figure 10 shows the forces acting on a generic vehicle in the train consist, while equation (2.1) states the equilibrium condition along the longitudinal direction x. In equation (2.1), m is the vehicle mass (kg), ρ_{in} is the inertia factor, accounting for the equivalent mass of the rotating elements, F_{cf} and F_{cr} are the forces on the front (f) and rear (r) couplers, $F_{t/db}$ is the force due to traction or dynamic braking generated by the motors, F_{air} is the air brake force, F_{ord} is the resistant force due to the ordinary resistances (propulsion resistances), namely rolling resistances and aerodynamic drag, F_g is the force due to track slope and finally F_{crv} is the curving resistance. Please note that while the propulsion and curving resistances always oppose the vehicle motion, the track grade forces can be regarded as propelling forces in downhill sections, whereby they tend to accelerate the vehicle. The track grade force is calculated according to equation (2.2), in which i_g is the track slope in ‰ and g is the acceleration of gravity (9.81 m/s^2).

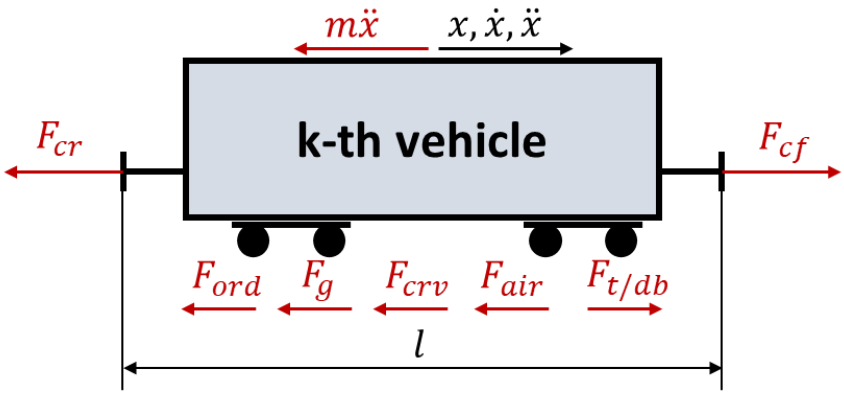

Figure 10: Longitudinal forces on a single vehicle in the train composition.

$$\rho_{in} m\ddot{x} = F_{cf} - F_{cr} + F_{t/db} - F_{air} - F_{ord} - F_g - F_{crv} \quad (2.1)$$

$$F_g = \frac{mgi_g}{1000} \quad (2.2)$$

The propulsion resistant forces and the curving resistances are commonly modelled using simplified expressions. More in detail, the propulsion resistant forces are usually estimated as a function of the vehicle speed via second-order polynomial equations in the form of equation (2.3), in which the coefficients A, B and C are obtained from experimental tests [20]. Several expressions can be found in the literature for different types of vehicles [21]. On the other hand, the curving resistances are typically estimated via analytical expressions as a function of the curve radius only, mainly via expressions in the form of equation (2.4), where r_{crv} is the specific curving resistance (N/tonne), R_c is the curve radius (m) and k_{crv} is a factor which assumes different values worldwide, see Table 1 [22]. Nonetheless, other equations can be found in the literature, such as the expression suggested in the former Soviet Union which accounted for the curve superelevation [23].

$$F_{ord} = A + BV + CV^2 \quad (2.3)$$

$$r_{crv} = 9.81 \frac{k_{crv}}{R_c} \quad (2.4)$$

Table 1: Coefficient for the calculation of curving resistances.

Country	**Equation coefficient**
Italy/Japan	800
USA	446
UK	600
China	573
Spain	900

Conversely, the locomotive traction/dynamic braking forces are calculated by introducing the mechanical characteristics of the locomotive motors, which relate the traction/braking forces to the locomotive speed. The calculation can be carried out using simple look-up tables (LUTs), analytical expressions or even complex models that require co-simulation techniques [21,24].

For what concerns the air brake forces, according to a recent review paper [25], the calculation in LTD codes is performed with three main modelling strategies, namely empirical, fluid-dynamics and fluid-empirical models. The first kind of models is based on simple analytical expressions or LUTs to directly obtain the brake cylinder pressure or the brake cylinder force on each vehicle in the train consist. On the other hand, fluid-dynamics approaches model in detail the air flow along the train brake pipe and the valves installed in the air brake system, using the classical fluid-dynamics equations (continuity, momentum and in some cases energy balance equation). Typically, fluid-dynamics models only consider a single dof for the air flow in the brake pipe. To reduce the simulation times with a limited loss of accuracy, the fluid-empirical approach models in detail the air flow along the brake pipe, but then the valves that convert the air brake pipe pressure into a brake cylinder pressure are modelled by means of simplified expressions or LUTs [26].

Finally, the computation of the in-train forces is often the bottleneck of LTD simulations, due to the nonlinear hysteretic behaviour of coupling elements. Due to the major role played by the type of coupling system in LTD and LTD simulations, the following subsection gives an overview on the two main types of coupling systems currently adopted (the American automatic coupler and the European buffer-hook system) and the modelling strategies to calculate the coupling forces.

2.1.1 Modelling of wagon coupling systems

Two distinct types of coupling elements are nowadays installed on railway vehicles, namely the European buffer-hook system and the automatic coupler used in the rest of the world [27]. The European system relies on two separate elements for the transmission of tensile and compressive loads: a central hook transmits the load in draft conditions, while two side buffers act in compressive states. On the other hand, the automatic coupler is able to transmit both types of forces.

The European draw gear system [28], shown in Figure 11, includes the hook, a screw adjustable link and an elastic device for the connection to the vehicle

frame, which is intended to damp the load acting on the frame itself. The buffer [29], sketched in Figure 12, comprises a moveable part (plunger) and a fixed part (base), with a spring-damper element (elastic group) in between, which is used for energy dissipation during impacts and to control the plunger stroke. The elastic group can be a rubber elastomer, a group of friction springs or a hydrodynamic/hydrostatic system in which the elastic and damping forces are obtained through a viscous fluid.

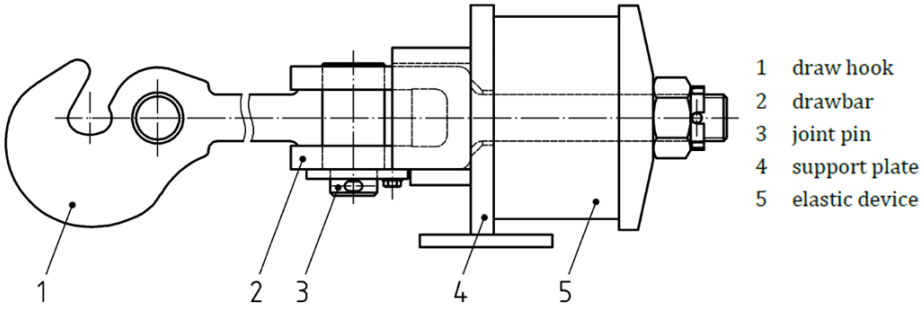

Figure 11: Scheme of the European draw gear system [28].

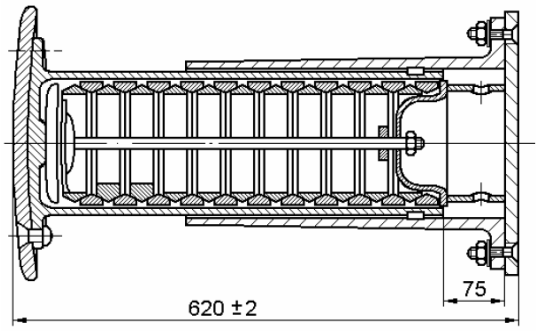

Figure 12: European buffer [30].

The coupling system adopted outside Europe includes a coupler, based on the original Janney coupler shown in Figure 13, which is connected to the vehicle frame by means of an elastic group named draft gear. The draft gear dissipates energy during traction and braking operations. Several draft gears based on different energy dissipation principles exist, ranging from friction draft gears to polymer draft gears and even hydraulic draft gears, but also devices relying on a combination of different mechanism can be found in operation [31]. Please note that both the European hook and the automatic coupler are connected to the

drawbars with cylindrical joints that allow the coupling elements of adjacent vehicle to rotate in curves in order to ensure a correct orientation.

The main advantages of the automatic coupler over the European system include the higher loads that can be transmitted, the automatic coupling of the vehicles with no need for the intervention of an operator and the use of a single element installed in the middle of the vehicle, with no drawbacks related to the load transfers in lateral direction between the two side buffers in curves. Nonetheless, the buffer-hook system is still the most widespread system in Europe, mainly because of economic reasons, as a shift towards the automatic coupler would require the replacement of the coupling systems traditionally installed on whole vehicle fleets.

Figure 13: Janney coupler.

Due to the presence of slacks and friction elements in their mechanical structure, coupling systems feature a strongly nonlinear hysteretic behaviour [14,32]. In spite of the aforementioned serious differences between the European buffer-hook system and the automatic coupler, similar modelling strategies can be used to calculate the in-train forces of the two systems in LTD simulations. According to the review paper by Wu et al. [33], LTD simulators commonly compute the in-train forces with three main strategies, namely LUT approach, fitting equations and white-box models. The LUT approach is based on fixed tables that store the loading and unloading characteristics of the coupling system, as a function of deflection and in some cases speed. If the dependency on speed is not considered, and the in-train force is calculated as a function of deflection only, the modelling strategy may miss some dynamic behaviours of the coupling element. Fitting equation models rely instead on nonlinear expressions that

describe the hysteretic behaviour of the coupling elements, through the identification of nonlinear stiffness and damping terms. The main issue of LUTs and fitting equations is related to the definition of a strategy to smooth the transition between the loading and unloading curves, in order to avoid numerical instabilities in the computation. Finally, white-box models describe in detail the dynamic behaviour of the coupling elements, and they rely on equations with a direct dependency on the main mechanical and physical parameters of the coupling system, like friction coefficients, wedge angles, spring stiffnesses, etc. Clearly, ranging from LUT models to fitting equations towards white-box models leads to a higher computational demand, but also to a higher accuracy.

2.2 LTDPoliTo code

2.2.1 The international benchmark of LTD simulators

Due to the big role played by LTD as regards the running safety of railway vehicles and to the growing interest in LTD simulations, in 2017 the research group from Central Queensland University (CQU) proposed a benchmarking activity (*the benchmark* in the rest of this thesis) to compare the outputs computed by different simulators for the same input dataset, with great focus on the maximum tensile and compressive in-train forces and deflections [34,35].

Initially, the Politecnico di Torino railway research group joined the benchmark with an LTD model implemented in the Simpack commercial MB software. The MB model only considered the longitudinal dof of the model bodies, with no detailed calculation of the wheel-rail contact forces. Nevertheless, the implementation of an LTD model in a MB software platform proved to be computationally inefficient and numerically unstable. Hence, the development of a new dedicated LTD simulator, ensuring fast computational times with high numerical accuracy, became one of the main goals of the activities shown in the present thesis. The new code, named LTDPoliTo, was built in MATLAB and initially validated on the simulation scenarios suggested in the international benchmark.

The main goal of the benchmark was the comparison of the force and deflection values computed by different simulators, each one using a different approach for the simulation of the mechanical behaviour of the coupling elements, in the same simulation scenarios. For this reason, air brake forces were neglected in the simulation scenarios proposed in the international benchmark, as different modelling approaches for the simulation of pneumatic braking may strongly affect

the outputs of the LTD simulation. The main inputs provided in the benchmarking questions paper [34] are given in the following bulleted list.

1. *Train configuration*. Four train configurations were considered, built from two types of wagons and two types of diesel-electric locomotives. Table 2 presents the main parameters of the reference vehicles, while Table 3 shows the composition of the four trains, highlighting the total hauled load. The large axle-load values indicated in Table 2 clearly suggest that the considered vehicles are vehicles from outside Europe, as data were indeed extracted from typical Australian freight trains. As noticeable from Table 3, the trailed mass increases from train 1 to train 3, while train 4 has the same number of vehicles and trailed mass as train 3, but it features a distributed power configuration, with a locomotive placed in the middle of the train composition.
2. *Track data*. All four trains run over the same track. Figure 14 shows the track slope and curvature as a function of the location along the track. In all simulations, the train journey starts with the head locomotive placed at the 3rd km position and with an initial speed of all vehicles equal to zero.
3. *Locomotive mechanical characteristics*. The traction and dynamic braking characteristics of the two diesel-electric locomotives, shown in Figure 15, were provided in the form of analytical expressions for eight notch levels.
4. *Driving control*. The notch level value as a function of time was provided as a spreadsheet for all four configurations. The driving controls given in the benchmark refer to the head locomotive, and on all remote locomotives a 3 second delay was considered. According to the benchmark rule, negative notch values referred to dynamic braking operations, while positive values corresponded to traction operations.
5. *Draft gear characteristic*. An experimental draft gear impedance characteristic was provided in graphical form, see Figure 16, but all participants could select the desired modelling approach, as long as the experimental input characteristic was fairly reproduced. In all four train compositions, pair of wagons are connected to each other using automatic couplers with a 10 mm slack. The wagons belonging to the same wagon pair are connected using a rigid drawbar with no slack. The coupler connection is also used for the connection between adjacent locomotives and between each locomotive and the adjacent wagon pairs.
6. *Resistant forces*. Ordinary resistant forces are computed using the modified Davis's expression, see equation (2.5), in which M_v is the

vehicle mass (tonnes), V is the vehicle speed (km/h), n_{ax} is the number of axles, M_{ax} is the axle-load (tonnes), and Q_{ad} is an aerodynamic factor, which is equal to 3.2 on the head locomotive and equal to 1 for all other vehicles. The curving resistance is calculated as a function of the curve radius only, using an expression in the form of equation (2.4), see equation (2.6), in which R_c is the curve radius.

Table 2: Main data of the reference vehicles considered in the international benchmark.

Vehicle	Length over couplers (m)	Axle-load (tonnes)	Number of axles
Loco #1	22.95	22.33	6
Loco #2	24.35	32.50	6
Wagon #1	15.00	32.00	4
Wagon #2	11.00	40.00	4

Table 3: Train compositions considered in the international benchmark.

Train	Configuration	Hauled load (tonnes)
Train 1	2x Loco #1 + 50x Wagon #1	6400
Train 2	2x Loco #1 + 50x Wagon #1 + 2x Loco #1 + 50x Wagon #1	12800
Train 3	3x Loco #2 + 240x Wagon #2	38400
Train 4	2x Loco #2 + 120x Wagon #2 + 1x Loco #1 + 120x Wagon #2	38400

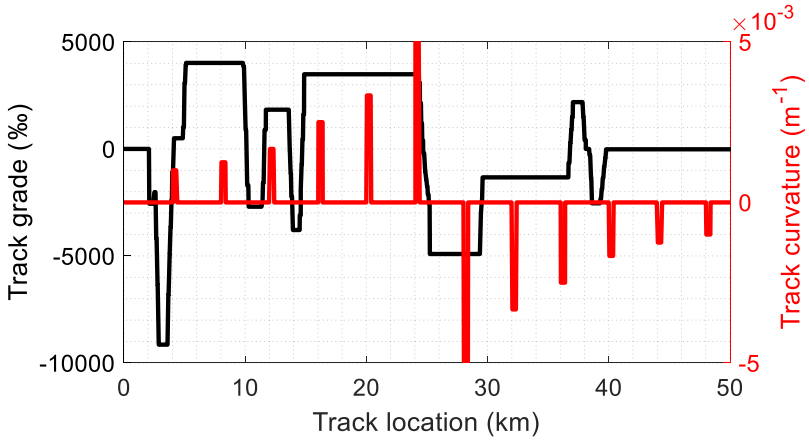

Figure 14: Reference track layout considered in the international benchmark.

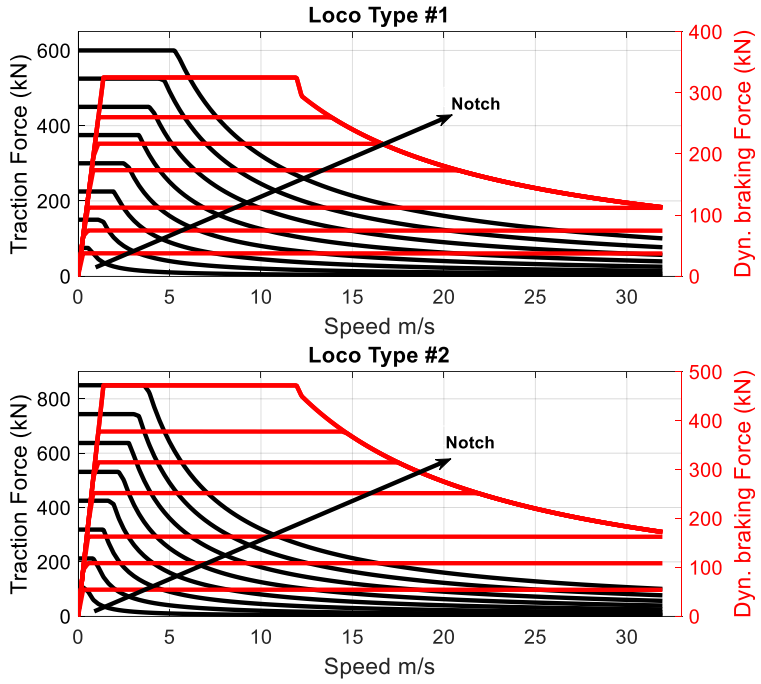

Figure 15: Locomotive mechanical characteristics provided in the international benchmark [36].

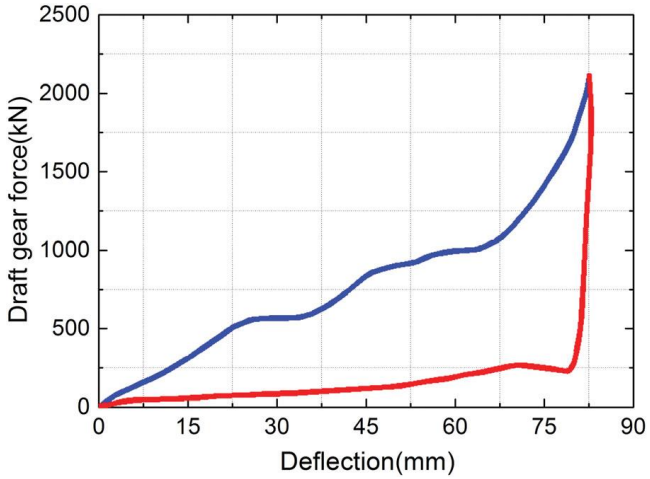

Figure 16: Draft gear experimental characteristics provided in the international benchmark [34].

$$F_{ord} = Q_{ad} M_v \cdot \left(2.943 + \frac{89.2}{M_{ax}} + 0.0306V + \frac{0.122V^2}{M_{ax} n_{ax}}\right) \tag{2.5}$$

$$F_{crv} = M_v \cdot \frac{6116}{R_c} \tag{2.6}$$

Nine simulators from 6 countries joined the benchmark, see Table 4. The research group from Politecnico di Torino launched the simulations with the original LTD code developed in Simpack (PoliTo Simpack), which however led to numerical instabilities in the simulations. The results of the benchmarking activity [35] showed that all simulators calculate similar results in terms of speed profile along the track, as indeed they were all forced to adopt the same expressions for the determination of the resistant forces. The biggest differences were identified in the calculation of the in-train forces, with the PoliTo Simpack and VOCO codes, implemented in MB software packages, featuring numerical instabilities. More in detail, the original PoliTo Simpack code proved to be numerically unstable in simulation scenarios 3 and 4, corresponding to trains with a huge number of wagons, while the VOCO code was unstable in the first simulation scenario, and did not complete the simulations on the other train configurations.

Therefore, since the PoliTo code implemented in Simpack was not able to guarantee stable results and good computational efficiency, the research group

decided to develop a new dedicated in-house code to be implemented in MATLAB and to be validated against the results of the international benchmark.

Table 4: Simulators joining the benchmark.

Simulator	Institution	Country
CRE-LTS	Central Queensland University	Australia
CARS	China Academy of Railway Sciences	China
UM	Bryansk State Technical University, Monash University	Russia, Australia
TABLDSS	Dalian Jiaotong University	China
BODYSIM	DEKRA Rail, Delft University of Technology	Netherlands
VOCO	Institut Français des Sciences et Technologies des Transports et de l'Aménagement des Réseaux, Université de Technologie de Compiègne	France
TsDyn	Politecnico di Milano	Italy
PoliTo Simpack	Politecnico di Torino	Italy
TDEAS	Southwest Jiaotong University	China

2.2.2 LTDPoliTo code implementation

The LTDPoliTo code is a dedicated in-house code for LTD simulations implemented in MATLAB. Since the need for a new LTD code arose as a consequence of the numerical inefficiency of the previous Simpack LTD code in the simulation scenarios proposed in the frame of the international benchmark, the LTDPoliTo code was initially written specifically to deal with the benchmark inputs. Nonetheless, the code can be easily modified to consider any kind of train configuration and track layout.

Figure 17 shows the flow chart of the developed code, which includes four main blocks:

- *Input data generation*. Loading of text files describing the simulation inputs (track layout, driving control, mechanical characteristic of the locomotives).
- *Pre-processing*. Definition of train configuration, processing on input data and definition of the main solver parameters.
- *Solver*. Numerical integration of the LTD equations.
- *Post-processing*. Calculation of coupler displacements, speeds and forces, with possible generation of text files to save and store the simulation outputs.

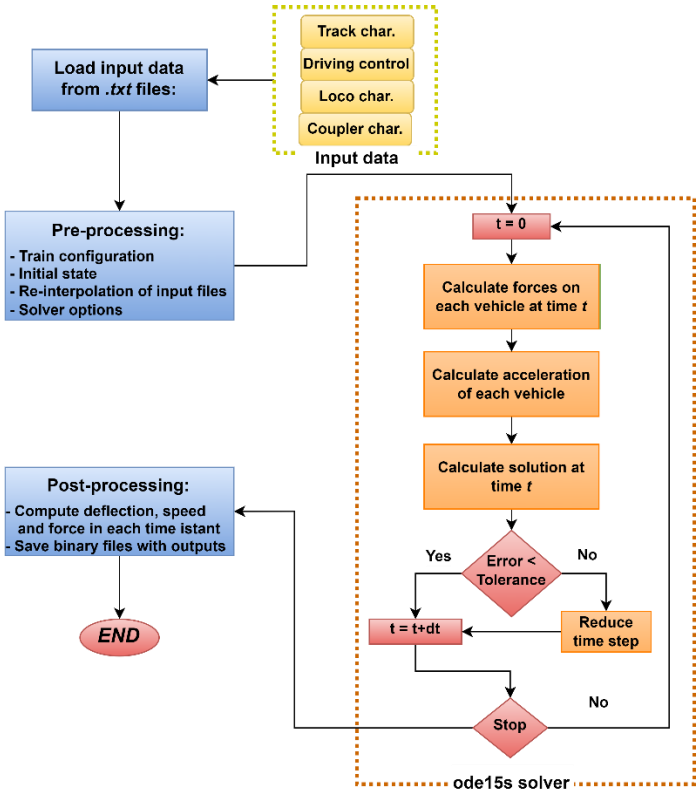

Figure 17: Flow chart of the LTDPoliTo code.

As already mentioned, one of the main requirements that the new code had to fulfil was a good computational efficiency. For this reason, all main input data, such as track layout (grade and curvatures), driving cycle, locomotive mechanical characteristics and draft gear impedance characteristics are defined in text files

and loaded as arrays in the pre-processing stage. This strategy allows the code to be easily adapted to several different sets of input data. All these arrays are then re-interpolated using a constant discretization step, in order to speed up indexing operations in the later stages of the computation. To ensure fast computational times, the LTDPoliTo code relies on several LUTs to efficiently compute the locomotive traction/braking forces as well as the coupler forces. In fact, the MATLAB code includes several optimized built-in functions for an efficient manipulation of large arrays. Different steps are used to interpolate the arrays: track characteristics are interpolated with a fixed track length step, the driving cycle is interpolated with a user defined time step, which can differ from the time step adopted by the numerical solver, the mechanical characteristics of the locomotives are interpolated by defining a proper speed step and finally the impedance characteristics of the coupler is interpolated with a fixed step for the coupler deflection.

More in detail, the track grade and curvature are stored in 2D matrixes: the first column is filled with the track position values and the second column is filled with the grade/curvature values. Similarly, the driving control is stored in a 2D matrix with the first column filled with time values and the second column filled with driving control values, using positive values for traction notch levels and negative values for dynamic braking notch positions. Drawbar and coupler impedance characteristics are stored in 2D matrixes, with the first column storing the coupling system deflection and the second one filled with force values. Different matrixes are defined for loading and unloading curves. The impedance characteristics stored in the 2D matrixes correspond to the characteristics of the series of two draft gears, see Figure 18, in which negative values are used for tensile states according to the benchmark rule and where the difference between the coupler and drawbar due to the coupler slack is highlighted.

Shifting focus to the locomotive forces, the benchmark considers two kinds of locomotives with eight notch values for both traction and dynamic braking operations. Hence, the locomotive mechanical characteristics are saved in a 3D array with eight *pages*, corresponding to the eight notch values. The 3D array can be seen as a collection of eight 2D matrixes. Each page, corresponding to a 2D matrix, includes five columns: the first column stores uniformly spaced speed values, columns 2 and 3 are filled with the traction forces of the locomotives 1 and 2, respectively, and finally columns 4 and 5 store the dynamic braking forces of the two locomotives.

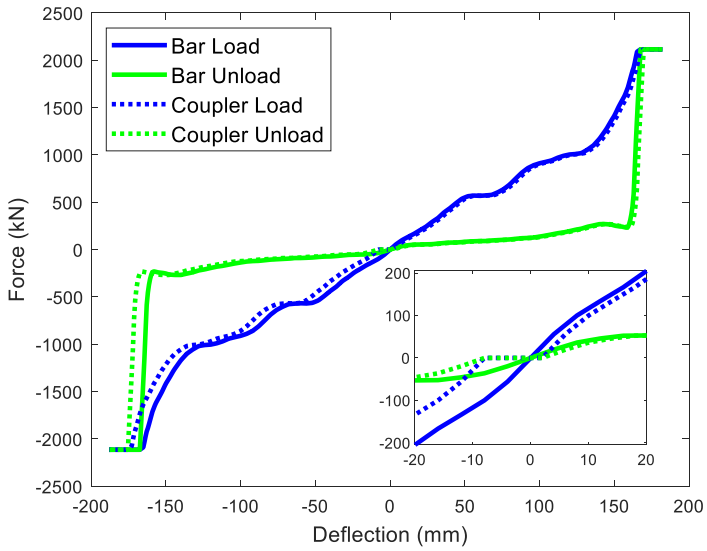

Figure 18: LUTs implemented in the LTDPoliTo code to compute draft gear forces.

The train configuration is defined in the pre-processing block. Since originally the code was implemented to be validated in the frame of the international benchmark, considering four different vehicles described in Table 2, the train configuration was initially identified by means of a 1D array, storing in each position an integer in the range 1-4, with 1 and 2 corresponding to the two wagons, and 3 and 4 corresponding to the two locomotives. Similarly, other 1D arrays were used to store the length, mass and number of axles of each vehicle in the train consist. As shown in Figure 19, LTDPoliTo numbers the vehicles in ascending order starting from the tail end wagon, so that in a train configuration with N vehicles, data corresponding to the head locomotive is stored in the N-th position of the arrays. Accordingly, coupler positions are numbered in ascending order from the front coupler of the tail-end vehicle, so that the j-th coupler is the one connecting vehicles j and j+1. In each time step, the deflection and relative speed on each coupling element are computed according to equation (2.7) and (2.8), in which subscript j is used to refer to coupler and vehicle positions, Δx is the coupler deflection, Δv is the coupler deflection speed, x is the vehicle position, l is the vehicle length, δ is the distance between the wagon centre and the coupling system mounting point, and d_N is the coupler initial length, see again Figure 19. For the simulation scenarios suggested in the international benchmark, an initial length of 1.3589 m was selected, corresponding to the initial length of a coupling system including two Australian couplers type EF1447AE. In the train configurations proposed in the international benchmark, vehicles are connected to

each other using either couplers or drawbars. To differentiate the two kinds of element, a 1D Boolean array is defined, in which a true value means that the corresponding element is a coupler, while a false value refers to a drawbar.

$$\Delta x_j = (x_{j+1} - x_j) - (\delta_j + \delta_{j+1}) - d_N$$
$$\delta_j = \frac{l_j - d_N}{2} \tag{2.7}$$

$$\Delta v_j = \dot{x}_{j+1} - \dot{x}_j \tag{2.8}$$

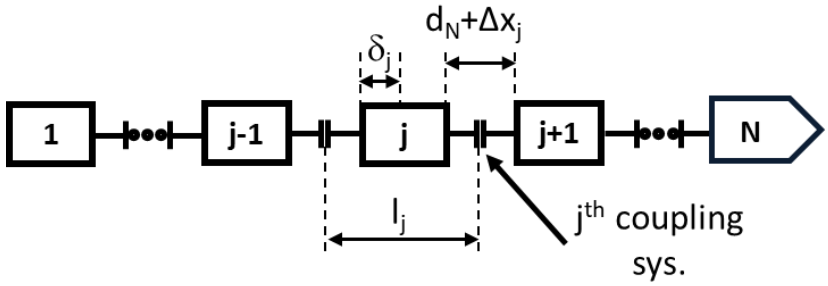

Figure 19: Numbering rule used in the new LTDPoliTo code and main quantities related to vehicle length.

After loading the main input text files, creating the input data arrays and defining the train configuration, the solution of the system of ordinary differential equations (odes) describing the LTD, see equation (2.1), can be performed using a proper numerical integrator. In the LTDPoliTo code, the variable step-size MATLAB built-in ode15s stiff solver is adopted, which was selected after a fine tuning [37,38]. The solver uses a predictor-corrector approach, so that when the error on the solution is above a prescribed threshold, the solution is discarded, the solver jumps back to the last stable solution and the numerical integration is repeated with a reduced time step. At each iteration, the ode15s MATLAB function calls a user-written function that computes the derivative of the solution. The LTD problem is described by second-order odes, but commonly most numerical integrators deal with first-order differential equations. Therefore, the LTD ode system is written and solved as a first-order ode system in the form of equation (2.9), in which t is time, **y** is the array storing the solution, **y'** is the array of the solution derivative, **[M_{LTD}]** is the mass matrix of the system and **f_{LTD}** is the function relating the state derivatives to the independent variables. Therefore, with this strategy, the vehicle speed becomes an additional unknown of the system. For a train with N vehicles, the solution vector **y** is a column vector with 2N elements:

elements in positions 1-N refer to the vehicle positions, while elements (N+1)-(2N) correspond to the speed of each vehicle, see equation (2.10). Accordingly, the vector of the solution derivatives **y'** is still a column vector with elements in positions 1-N corresponding to the vehicle speed and elements in positions (N+1)-(2N) storing the vehicle accelerations, see equation (2.11). The function $\mathbf{f_{LTD}}$ is a column vector with elements in position 1-N corresponding to vehicle speeds, while elements in positions (N+1)-(2N) are filled with the resultant force acting on each vehicle, see equation (2.12), in which F_{Res} accounts for the sum of propulsion, curving and track grade resistances. Finally, the system mass matrix is a diagonal matrix with the first N diagonal elements all equal to 1, while diagonal elements (N+1)-(2N) are equal to the mass of the corresponding vehicle, see equation (2.13). As stated by equation (2.13), the mass matrix of the system is constant, i.e., it does not depend on the values of the states of the system, and it is independent from time. Therefore, it is passed to the MATLAB ode15s function as an additional parameter.

$$[\boldsymbol{M_{LTD}}]\boldsymbol{y}'(t) = \boldsymbol{f_{LTD}}(t, \boldsymbol{y}, \boldsymbol{y}') \tag{2.9}$$

$$\boldsymbol{y} = \{x_1 \cdots x_N \dot{x}_1 \cdots \dot{x}_N\}^t \tag{2.10}$$

$$\boldsymbol{y}' = \{\dot{x}_1 \cdots \dot{x}_N \ddot{x}_1 \cdots \ddot{x}_N\}^t \tag{2.11}$$

$$\boldsymbol{f_{LTD}} = \begin{Bmatrix} \dot{x}_1 \\ \vdots \\ \dot{x}_N \\ F_{t/db,1} - F_{Res,1} + F_{c,1} \\ \vdots \\ F_{t/db,j} - F_{Res,j} + F_{C,j} - F_{c,j-1} \\ \vdots \\ F_{t/db,N} - F_{Res,N} - F_{c,N-1} \end{Bmatrix} \tag{2.12}$$

$$[\boldsymbol{M_{LTD}}] = \begin{bmatrix} 1 & & & & & \\ & \ddots & & & & \\ & & 1 & & & \\ & & & m_1 & & \\ & & & & \ddots & \\ & & & & & m_N \end{bmatrix} \tag{2.13}$$

In each time step, the user-written function called by the ode solver is demanded to calculate the forces acting on each vehicle and on each coupling element. As already mentioned, to speed up the computation, the LTDPoliTo code

relies on several LUTs that store the main input parameters, so that indexing during the simulation can be simplified. The forces on each coupling element are interpolated from the LUTs storing the loading and unloading impedance curves of the drawbars and couplers, which are indexed as a function of the deflection value. To avoid the numerical instabilities due to an abrupt transition between loading and unloading conditions, the smoothing approach suggested by Zhang et al. [39] is adopted. When the absolute value of the coupler deflection speed is below a user-defined threshold, the force value lies between the loading and unloading curves, and it is proportional to the speed value, see equation (2.14), in which F_c is the force on the coupling element, F_L is the loading force, F_U is the unloading force, Δv is the relative speed on the coupling element, and v_ε is the threshold speed. Figure 20 graphically shows the working principle of the smoothing approach in draft state: if the deflection speed absolute value is below the user-defined threshold value, a transition between the loading and unloading values occurs. Please note that the loading and unloading force for each coupling element are calculated starting from the Boolean variable which is equal to 1 for couplers and to 0 for drawbars, see equations (2.15) and (2.16), in which B is the Boolean variable, F is force, the superscripts L and U refer to loading and unloading states and finally subscripts B and C refer to drawbar and coupler, respectively.

$$F_c(\Delta x, \Delta v) = \begin{cases} F_L(\Delta x), & |\Delta v| \geq v_\varepsilon \wedge \Delta x \cdot \Delta v \geq 0 \\ F_U(\Delta x), & |\delta v| \geq v_\varepsilon \wedge \Delta x \cdot \Delta v < 0 \\ F_M(\Delta x) + |F_A(\Delta x)| \dfrac{\Delta v}{v_\varepsilon}, & |\delta v| < v_\varepsilon \end{cases}$$

$$F_M(\Delta x) = \frac{F_L(\Delta x) + F_U(\Delta x)}{2} \qquad (2.14)$$

$$F_A(\Delta x) = \frac{|F_L(\Delta x) - F_U(\Delta x)|}{2}$$

$$F_L(\Delta x, \Delta v) = F_{LC}(\Delta x) \cdot \mathrm{B} + F_{LB}(\Delta x) \cdot (1 - \mathrm{B}) \qquad (2.15)$$

$$F_U(\Delta x, \Delta v) = F_{UC}(\Delta x) \cdot \mathrm{B} + F_{UB}(\Delta x) \cdot (1 - \mathrm{B}) \qquad (2.16)$$

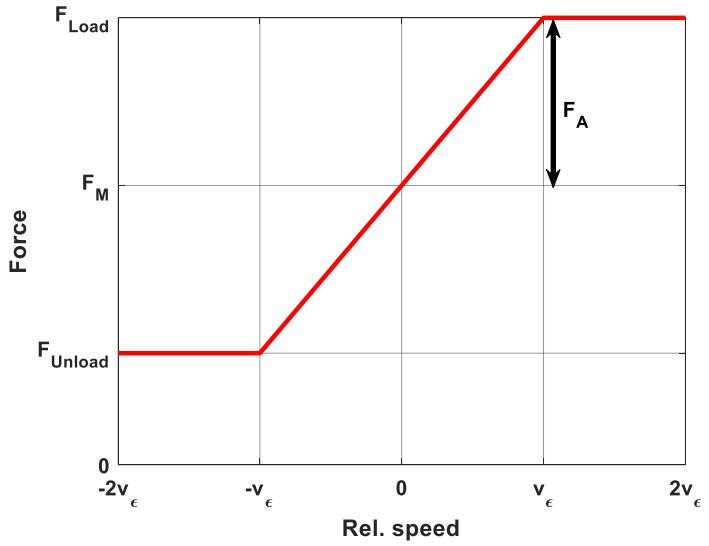

Figure 20: Smoothing approach for the calculation of the in-train forces.

The ordinary resistant forces are calculated using the polynomial equation suggested in the international benchmark, see equation (2.5), starting from the values of axle-load and vehicle mass stored in the 1D arrays built to describe the train configuration. The curving resistance and the track grade resistance are calculated using equations (2. 6) and (2.2), respectively, and a similar strategy is implemented to obtain the values of curvature and slope in each time step for each vehicle. In fact, the track grade and curvature characteristics are stored in LUTs as a function of the track position, which is discretized with a constant step. The corresponding index J for each wagon in each time step can be calculated according to equation (2.17), in which x is the vehicle position, x_0 is the first element in the track position array, δ_l is the step for track length discretization and $[\cdot]$ is the floor function, which outputs the integer part of a number. Once the index J is obtained, the LUTs can be directly indexed to obtain the corresponding track grade and curvature values.

$$J = \left[\frac{x - x_0}{\delta_l}\right] + 1 \tag{2.17}$$

Shifting focus to the locomotive forces, the computation starts from the LUT storing the driving cycle characteristic, which stores the notch position on the head locomotive as a function of time. The notch position on the other locomotives are shifted with a delay of 3 s. The LUT is indexed with a strategy identical to the one shown above for the LUTs storing the track data, see equation

(2.18), in which t is time, t_0 is the first time value stored in the driving cycle LUT, t_d is the time delay, equal to 0 for the head locomotive and to 3 s for all other remote locomotives, and δ_t is the time step used in the LUT. After indexing the driving cycle LUT, it is easy to obtain the notch position. The notch level is used to index the 3D array storing the locomotive mechanical characteristics, so that the correct page of the array can be obtained. As previously stated, each page of the 3D array is a 2D matrix, which can be regarded as a 2D LUT, storing the locomotive force as a function of speed. The index K related to the speed value can be easily obtained using the same approach shown above, see equation (2.19), in which v is speed, v_0 is the first speed value in the LUT and δ_v is the step used to discretize the locomotive speed values. After identifying the index K, the proper locomotive force value is obtained, depending on the operation type (braking/traction) and on the locomotive type (1 or 2).

$$J = \left[\frac{t - t_d - t_0}{\delta_t}\right] + 1 \tag{2.18}$$

$$K = \left[\frac{v - v_0}{\delta_v}\right] + 1 \tag{2.19}$$

Once the numerical integration of the LTD ode system is completed, the ode15s solver only outputs a 2D matrix storing the solution states in each time step, i.e., the position and speed of each vehicle in each time step. Hence, in the post-processing stage, deflections and relative speed on each coupling element in each time step are calculated again starting from the solution states, so that the in-train forces can be obtained. Finally, the user can store and save the main results of the simulation by activating one or more of the following options:

- Generation of binary files saving the solution, the in-train forces and the deflections and relative speeds on each time step.
- Storage of plots of the main quantities of interest.
- Generation of a table, saved as a spreadsheet file, filled with the main outputs considered in the international benchmark result paper [35].

The following subsection shows in detail the code validation, focusing on the numerical results obtained in the simulation scenarios of the international benchmark and on the computational efficiency.

2.2.3 LTDPoliTo code validation

The LTDPoliTo code was validated on the input dataset of the international benchmark, comparing the main simulation outputs with the results computed by the other simulator joining the benchmarking activity. The LTD differential equations were numerically integrated with the ode15s variable step-size stiff solver, which proved to ensure the lowest computational time among several numerical integrators tested. The relative and absolute tolerances of the solver were set to 1e-6 and 1e-7, respectively, however, the LTDPoliTo code allows the user to set the solver parameters as desired. Initially, the code was developed with a traditional programming strategy, strongly based on conditional loops (*for* and *while* loops) and on Boolean statements. The code computed results in good agreement with the other simulators, but the computational efficiency of the first version of the LTDPoliTo code was poor. In fact, the MATLAB language is not the best option for dealing with this kind of programming structures. Nonetheless, MATLAB can help speed up calculations on big arrays using operations in vector form by means of highly efficient built-in functions. Therefore, the code was optimized, and the final version strongly relies on vectorization, which is a programming strategy that replaces Boolean statements and conditional loops based on simple operations on single array elements with vector operations that work on the array as a whole. The code optimization was carried out with the help of the MATLAB profiler, which allows to identify the most time-consuming operations of the computation.

The computational performance of the LTDPoliTo code was evaluated by means of two quantities, namely the real-time factor and the normalized real-time factor, see equations (2.20) and (2.21). The real-time factor is defined as the ratio between the wall time, i.e., the time required to run the simulation, and the operational time, which corresponds to the time duration of the simulated trip. Since the wall time is expressed in ms in equation (2.20), a real-time factor below 1000 means that the simulation is faster than real-time. Please note that the real-time factor computed according to equation (2.20) was used as an indicator of the computational performance of the simulators in the international benchmark result paper [35], too, and defined as *Speed 1*. The normalized real-time factor is calculated as the ratio between the real-time factor and the number of dofs in the LTD ode system N_{dof}: for a train with N vehicles, the number of dofs is 2N, see equations (2.9)-(2.13). The normalized real-time factor allows to carry out a fair comparison of the computational performances of LTDPoliTo in the four train configurations, regardless of the number of vehicles in the train.

$$Real - time\ factor = \frac{Wall\ time\ (ms)}{Operational\ time\ (s)} \tag{2.20}$$

$$Normalized\ real-time\ factor = \frac{Real-time\ factor}{N_{dof}} \tag{2.21}$$

Figure 21 shows the normalized real-time factor calculated on the four train configurations of the international benchmark for three different version of the code, labelled "Original", "Vectorized" and "Jacobian". The original version of the code is the first working version of LTDPoliTo, which used conditional loops. The "Vectorized" version is an intermediate version of the code, in which all explicit loops and Boolean statements were replaced by vectorization. Finally, the "Jacobian" version is the ultimate version of the code, in which the Jacobian sparsity pattern is specified and defined as a parameter of the ode15s solver. In fact, the MATLAB profiler highlighted that most of the computation was spent by the ode15s solver in the evaluation of the system Jacobian matrix in rejected time steps. The Jacobian matrix of the LTD ode system is state-dependent, but it has a constant sparsity pattern, which can be specified as an additional solver property as a Boolean matrix where false values correspond to elements of the matrix always equal to zero. Figure 22 shows a map of the Jacobian sparsity pattern, where asterisks refer to non-zero elements. It is not difficult to demonstrate that for a train with N vehicles, the total number of elements in the Jacobian matrix is equal to $4N^2$, but the number of non-zero elements is limited to 7N-4. Hence, if the position of the non-zero elements is specified, the MATLAB internal routine for the evaluation of the Jacobian matrix has a lower number of elements to estimate, with a big saving of the computational time. As can be seen from Figure 21, the upgraded versions of the code always guarantee a speed up of the computation in all four simulation scenarios. The final version of the code, in which the Jacobian sparsity pater is pre-defined, guarantees an approximately constant normalized real-time factor for all four train configurations. This means that the computational time tends to increase linearly with the number of vehicles in the train composition, which is reasonable.

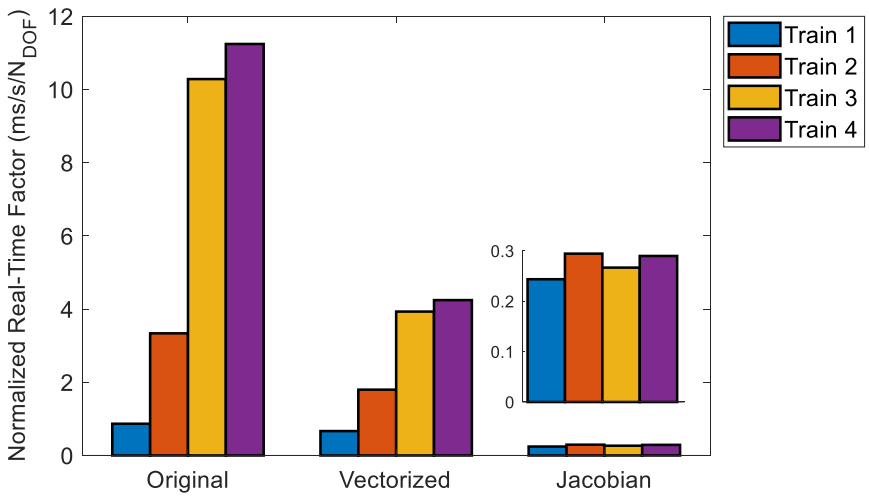

Figure 21: Computational performances of different LTDPoliTo code versions.

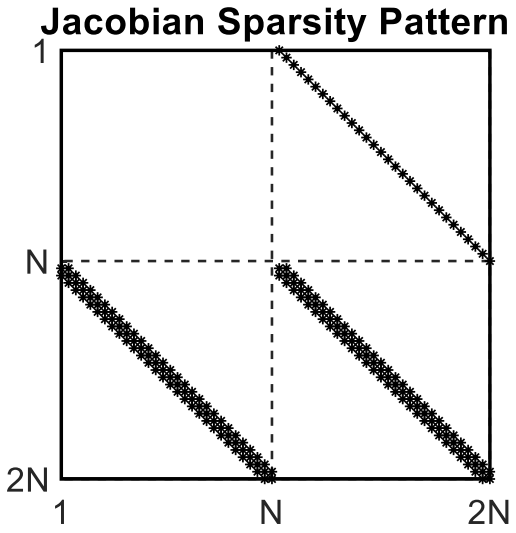

Figure 22: Sparsity pattern of the system Jacobian.

Figure 23 shows the real-time factor of all simulators joining the benchmark in the four simulation scenarios. All participants ran their simulators on their own computer, while a fair comparison would require all codes to be launched on the same hardware platform. Nonetheless, it can be observed that the original LTD code implemented in Simpack was the least efficient one in simulation scenarios 3 and 4, while currently the LTDPoliTo code in its final version with specification of the Jacobian sparsity pattern is the second fastest simulator for all four train configurations, only slower than the TABLDSS code.

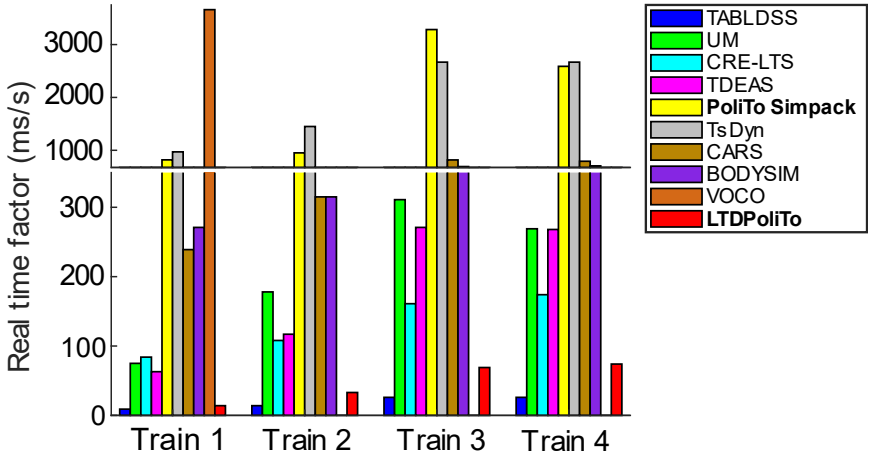

Figure 23: Comparison of computational performance of the simulators joining the international benchmark.

Shifting focus to the numerical outputs obtained with the LTDPoliTo code, in all simulations the threshold speed for the management of the smoothing transition between the loading and unloading curves was set to 1e-3 m/s. Table 5 shows the main results obtained by the simulators joining the benchmark in the third simulation scenario, in which the original LTD model implemented in Simpack produced numerical divergences. Similar tables for the other train configurations are shown in Annex A. The main results considered in the paper and reported in the tables are the following:

- Maximum and mean speed values calculated considering all time steps and all vehicles.
- Largest in-train force and corresponding coupler position for tensile (draft) and compressive (buff) states: the largest in-train force is obtained as the maximum value among all vehicles and all time steps.
- Mean value of the maximum in-train force for both draft and buff conditions: the mean force is taken as the mean of the maximum values recorded on each coupling elements.
- Maximum deflection in both draft and buff conditions on a specific coupling element, selected by the benchmark promoters, for each simulation scenario. For the third simulation scenario, the selected coupler is coupler 147, with counting started in ascending order from the first coupler behind the leading locomotive.

Table 5: Results of the simulators joining the international benchmark of LTD simulators in the third simulation scenario.

Code	Speed (km/h)		Largest in-train force* (kN)		Mean in-train force* (kN)		Max. deflection on coupler 147	
	Max.	Mean	Draft	Buff	Draft	Buff	Draft	Buff
TABLDSS	81.47	43.95	1636@3	1090@142	1179	688	145.57	120.65
UM	82.13	44.22	1626@3	930@142	1173	602	134.05	94.67
CRE-LTS	81.49	43.99	1802@71	800@150	1200	519	30.54	21.25
TDEAS	81.74	44.10	1639@3	1045@142	1174	710	124.80	56.26
PoliTo Simpack	81.57	43.85	2114@87	2114@141	1654	705	302.53	195.45
TsDyn	80.67	44.04	1630@3	826@140	1186	486	148.61	102.17
CARS	80.49	44.09	1625@3	959@136	1157	626	147.43	124.31
BODYSIM	81.20	44.08	1808@37	624@144	1240	395	87.29	50.50
LTDPoliTo	81.84	44.79	1636@3	1008@144	1166	620	169.56	129.00

* Couplers numbered in ascending order from train head to tail, starting from the first coupler behind leading locomotive

As can be seen from Table 5, due to the numerical instabilities in the computation, the PoliTo Simpack model predicted a huge value of the largest tensile in-train force, which was recorded on the 87th coupling element, while most simulators recorded the largest in-train force on the third coupling element. On the other hand, the new LTDPoliTo code gives results closer to the other simulators for what concerns the largest tensile in-train force. At the same time, the PoliTo Simpack model predicted a high value of the mean in-train tensile force, far from the outputs of the other simulators, while the new LTDPoliTo MATLAB code ensures a better agreement with the outputs of the other participants. Compared to the other simulators, the LTDPoliTo code tends to

compute the highest values of deflection in both tensile and compressive states, thus being the "softest" model. Nonetheless, Table 5 and tables in Annex A clearly highlight that a high variability exists in terms of the maximum deflections, with for instance CRE-LTS always being the "stiffest" model by far. Furthermore, the main goal of LTD simulations is the calculation of the in-train forces rather than the determination of deflections on coupling elements. Therefore, the tuning of the main LTDPoliTo model parameters was performed with the aim to achieve a good agreement in terms of in-train forces rather than in terms of deflections.

Figure 24 shows the time-history of the in-train force on the specific coupling element selected for train 3 (147^{th} coupler position), computed by the original Simpack model, by the new LTDPoliTo code and by two of the participants of the benchmark, namely TABLDSS and CRE-LTS. TABLDSS proved to be the most efficient simulator with a high numerical accuracy, while CRE-LTS is the LTD simulator adopted by the research group from Central Queensland University, which promoted the benchmarking activity. The new LTDPoliTo code avoids the numerical instabilities that were produced by the Simpack model, and its results are now in good agreement with the outputs from the other simulators. Furthermore, due to the numerical divergence in the simulation, the Simpack model predicted buff conditions in the time interval between approximately 500 and 900 s, while the other simulators calculated draft conditions. The new LTDPoliTo code shows again a better agreement with the other simulators, as it calculates tensile forces in this time interval. Figure 25 shows instead the cross plots of the force-deflection characteristics on the coupling elements chosen in the international benchmark computed by the two models developed by the Politecnico di Torino research group. Both the LTDPoliTo code and the previous Simpack model feature a velocity-dependent smoothing transition between the loading and unloading curves. Nonetheless, the new LTDPoliTo code always guarantees a stable behaviour of the coupling element, while the Simpack model led to a force saturation caused by the divergences in the solution.

As noticeable from the paragraphs above, compared to the previous Simpack model, the new MATLAB LTDPoliTo code ensures a higher numerical accuracy, without instabilities in simulation scenarios characterized by a large number of vehicles, and a close agreement with the outputs computed by the other simulators joining the international benchmark. At the same time, the code optimization, based on vectorization and on the help of the MATLAB profiler, allowed to achieve a high computational efficiency, with the final version of the code

ensuring a computational effort approximately proportional to the number of vehicles in the train composition. In conclusion, it can be stated the work carried out in the frame of the present PhD thesis and shown in this section led to the implementation of an accurate and computationally efficient in-house LTD code, that the research group can use in future activities.

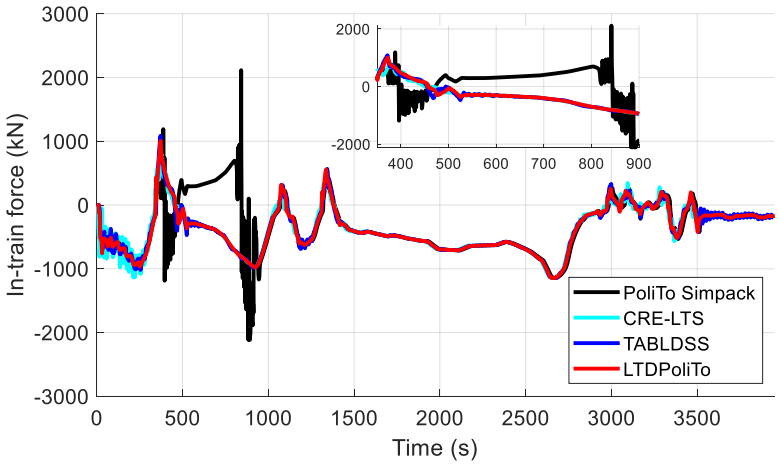

Figure 24: Time-history of the in-train force on the reference coupling element chosen for train 3.

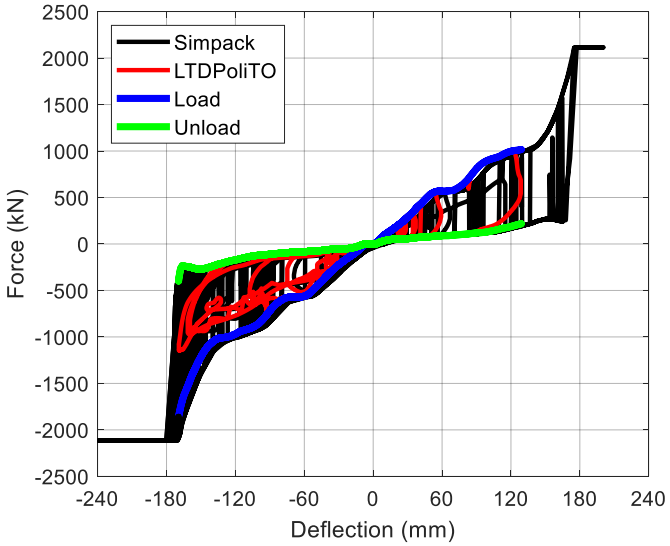

Figure 25: Force-deflection cross-plot on the reference coupling element for the third simulation scenario.

2.3 Upgrades to the LTDPoliTo code

After implementing and validating the new LTDPoliTo MATLAB code on the simulation scenarios defined in the framework of the international benchmark, the work done in the frame of the present thesis dealt with the implementation of different upgrades to enhance its modelling capabilities and to overcome its main limits. Since different expressions are witnessed in the literature for the evaluation of the running and curve resistances, the code was upgraded so that the user can choose among several laws for the calculation of such resistances, and the effects of the selected laws on the main simulation outputs were investigated [40]. The main drawback of the LTDPoliTo code developed for the international benchmark simulation scenarios is that it was not provided with a module for the calculation of the air brake forces, as the benchmark only considered dynamic braking operations. Therefore, the present thesis aimed at providing the newly built LTDPoliTo code with a dedicated module able to efficiently evaluate the air brake forces for European railway freight wagons, based on the knowledge of the braked weight percentage, and emergency braking simulations were run to assess the accuracy of the method [41]. Finally, since the main safety criteria defined in the EN 14363 standard [42] are based on the evaluation the wheel-rail contact forces, that are neglected by common LTD simulators like the LTDPoliTo code, an activity was carried out to show the feasibility of building digital twins of complex multibody models to estimate such safety criteria starting from the main outputs of an LTD simulation [43]. The latter work required the integration of the LTDPoliTo code within a more complex computational framework, including a multibody simulation module.

2.3.1 Influence of resistant force expressions

The running resistances and the curving resistance forces can be calculated according to several expressions described in the literature. For what concerns propulsion resistances, several examples of polynomial expressions can be found in the literature, for both locomotives and wagons, and some of these equations were tuned on experimental data of specific vehicles. On the other hand, for what concerns curving resistances, different expressions exist, which compute the resistant force as inversely proportional to the curve radius. The code was upgraded so that the user can chose different expressions of curving and propulsion resistant force expressions.

Although several expressions can be adopted to calculate the ordinary and accidental resistances, there is little knowledge about the influence of these expressions on the outputs of LTD simulations, in terms of speeds and in-train forces. Therefore, simulations were run on train 1 of the international benchmark dataset [34], considering different equations for the calculation of the resistant

forces. Obviously, when the resistant force expression is modified, it may be expected that at the same time instant of the simulation, the train location is different. Because of this reason, the notch control cannot be provided as a function of time, but it must be given as a function of the train position along the track. Therefore, from the results of the simulations run during the code validation stage, the notch characteristic was modified to build a LUT as a function of the location of the head locomotive, see Figure 26.

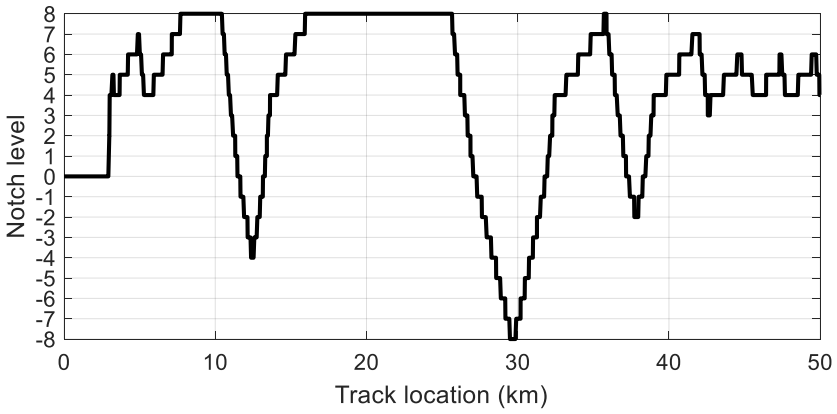

Figure 26: Driving control as a function of track location (train 1 of the international benchmark).

For what concerns the propulsion resistances, four simulations were run, using different types of laws for wagons and locomotives, as summarized in Table 6 and Table 7. Please note that in Table 6, r_{ord} is the specific ordinary resistance (N/tonne), V is the vehicle speed in km/h, n_{ax} is the number of axles and M_{ax} is the axle-load in tonnes. Figure 27 shows the speed of the head locomotive obtained with the four combinations of rolling resistance expressions, while Figure 28 presents the time history of the in-train force on the coupler behind the second locomotive. As can be seen from the plots, the results of simulations 2 and 4 are extremely similar to the outputs computed when using the reference expression provided in the benchmark. On the other hand, in simulation 3, the speed of the head locomotive is far lower compared to the other cases, while the forces on the reference coupler tend to increase during the whole trip.

Table 6: Expressions for the calculation of the rolling resistances.

Law name	Equation
Benchmark	$r_{ord} = 2.943 + \frac{89.2}{M_{ax}} + 0.0306V + \frac{0.122V^2}{M_{ax}n_{ax}}$
China full freight	$r_{ord} = 9.81 \cdot (0.92 + 0.0048V + 0.000126V^2)$
Russian	$r_{ord} = 9.81 \cdot \left(0.7 + \frac{3 + 0.1V + 0.0025V^2}{M_{ax}}\right)$
China HXD2 loco	$r_{ord} = 9.81 \cdot (0.84 + 0.0012V + 0.000313V^2)$

Table 7: Simulations for different expressions for the calculation of propulsion resistances.

Simulation #	Wagon expression	Loco expression
1	Benchmark	Benchmark
2	Russian	Russian
3	China full freight	China HXD2 loco
4	Benchmark	China HXD2

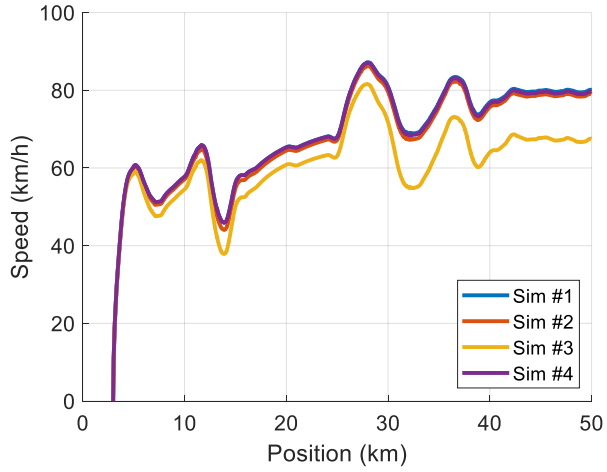

Figure 27: Speed of the head locomotive when different expressions for the computation of the propulsion resistances are considered.

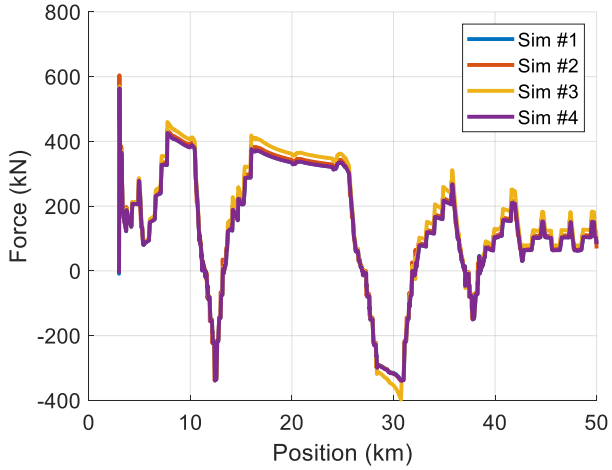

Figure 28: In-train force on the coupler behind the second locomotive when different expressions for the computation of the propulsion resistances are considered.

The explanation to this behaviour is that the Chinese laws calculate a higher resistance compared to the other equations investigated, see Figure 29, which plots the resistant force on the wagon behind the two locomotives at the head of the train for the four simulations listed in Table 7. As can be observed in Figure 29, the expression suggested by Chinese railways computes the highest values, so the speed profile when this law is adopted is strongly different compared to the one obtained when using the benchmark expression. The Russian law computes a higher value of the resistant force compared to the benchmark expression,

nonetheless the increase is limited, so the global results in terms of speed and in-train forces are not drastically affected. A big point of merit of the Russian and benchmark equations is that they consider several parameters of the vehicle in the computation of the resistant force, such as the axle-load and number of axles, so that they can adapt to several kinds of vehicles. On the other hand, the laws from Chinese railways were obtained for specific wagons and locomotives, so they can be misleading when applied to different vehicles. Thus, when launching an LTD simulation, the best option for the computation of the resistant forces is using an equation fitted on the specific kinds of vehicles included in the train composition. However, if such law is not available, a good solution can be the adoption of a law accounting for the main vehicle parameters, like the benchmark and Russian equations.

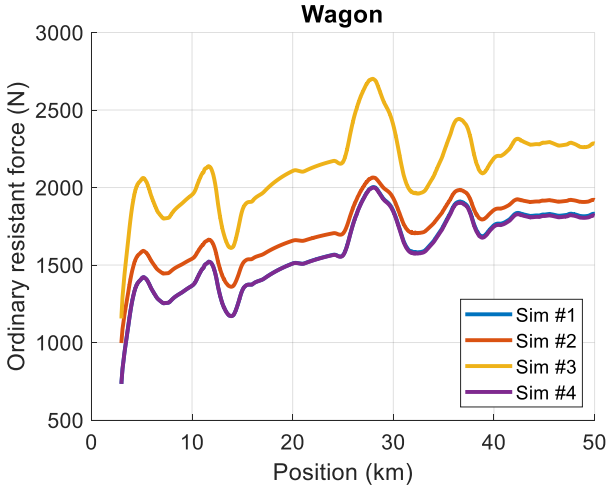

Figure 29: Ordinary resistant force on the leading wagon in train 1 of the benchmark simulation scenarios.

Shifting focus to the expressions for the calculation of the curving resistances, three expressions were tested, namely the benchmark equation (2.6), the Roeckl equation (2.22) and an expression depending on the wheelbase, see equation (2.23). Please note that in equations (2.22) and (2.23), r_{crv} is the specific curving resistance (N/tonne), R_c is the curve radius and a_b is the vehicle wheelbase (m). The value of the wheelbase was set according to typical values for Australian freight vehicles, i.e., 1.95 m for wagons and 2.03 m for locomotives. Figure 30 shows the curving resistance calculated by the laws considered in the present activity for different values of the curve radius. For large curve radii, all the

expressions compute similar values of the curving resistance, while differences among the equations are noticeable only for tight curves.

$$r_{crv} = \begin{cases} \dfrac{6500}{R_c - 55} & R_c > 350m \\ \dfrac{5300}{R_c - 35} & 250m < R_c < 350m \\ \dfrac{5000}{R_c - 30} & R_c < 250m \end{cases} \tag{2.22}$$

$$r_{crv} = \frac{1600 a_b + 1620}{R_c} \tag{2.23}$$

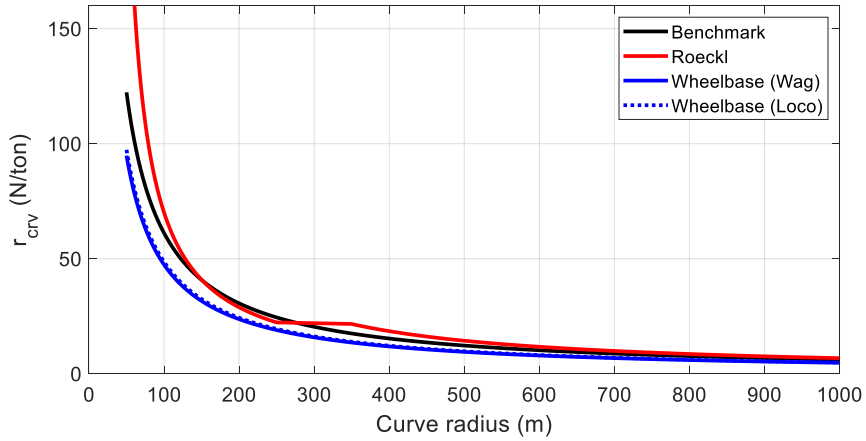

Figure 30: Comparison of curving resistance laws.

The expression adopted for the computation of the curving resistance has very little influence on the outputs of the simulation, as noticeable from Figure 31 and Figure 32, which show the speed of the head locomotive and the force on the coupler behind the second locomotive along the track, respectively. As a matter of facts, in the simulation scenarios considered in the international benchmark, the tightest curve has a radius of 200 m. For curve radii above 200 m, the expressions considered in the present activity compute close values of the curving resistances, see Figure 30. Obviously, larger differences could arise if a track with tighter curves was considered. Nonetheless, long freight trains do not commonly face very tight curves in normal operating conditions. Therefore, concerning freight train LTD simulations, the expression adopted to calculate the curving resistances has a very little influence on the main simulation outputs.

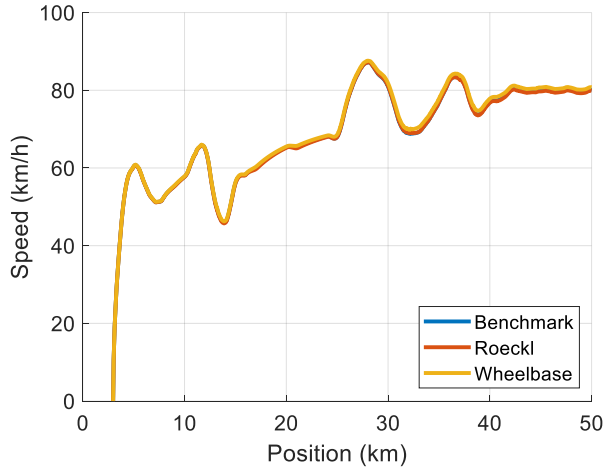

Figure 31: Speed of the head locomotive when different expressions for the computation of the curving resistances are considered.

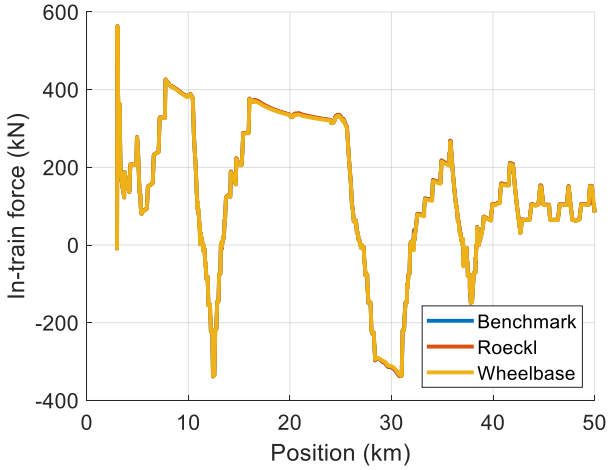

Figure 32: In-train force on the coupler behind the second locomotive when different expressions for the computation of the curving resistances are considered.

In conclusion, the activity performed in the frame of the present thesis and shown in this subsection highlights that a reliable LTD code should include a library for the selection of different possible expressions for the computation of the propulsion resistances or allow the user to set a custom equation. In fact, the outputs of the LTD simulation are strongly dependent on the expression adopted, as many different equations can be used for different kinds of vehicles. When expressions tuned on the specific vehicles to be simulated are missing, the best option is relying on equations that explicitly consider the main vehicle parameters,

such as axle-load and number of axles. On the other hand, concerning LTD simulations of long freight trains, the different expressions used to compute the curving resistances have a little influence on the main simulation outputs.

2.3.2 Estimation of the air brake forces

The main limitation of the LTDPoliTo code developed for the validation on the simulation scenarios proposed in the framework of the international benchmark is that it was not able to consider the effect of the air brake forces. To enhance the modelling capabilities of the LTDPoliTo code, it is essential to provide it with a module for the computation of the air brake forces. Since one of the biggest benefits of the LTDPoliTo code is its high computational efficiency, fluid-dynamics and fluid-empirical models were discarded, as the solution of the fluid-dynamics equations describing the air flow in the brake pipe may require co-simulation and parallel computing techniques [44] to ensure reasonable computational speeds. Therefore, the implementation of an empirical model was regarded as the most effective solution. Nonetheless, a big issue in the modelling of the air brake forces is that even empirical approaches require the knowledge of the main properties of the air brake plant installed on each vehicle (brake cylinder diameter, rigging ratios, presence of high-speed and/or empty-loaded devices, etc.), that may change from one vehicle to another. However, as long as European freight wagons are considered, their braking performance can be simply described in terms of their braked weight and braked weight percentage, see §1.3. Therefore, in a first attempt to include the air brake forces in the calculation of the LTD of long freight wagons, a method based only on the indication of the braked weight was developed.

The starting point of the method is equation (1.8), which relates the braked weight of railway wagons with maximum speed below 120 km/h and equipped with P10 cast iron blocks to the sum of all brake block forces. Therefore, if the braked weight of such a wagon is known, the sum of the brake block forces can be calculated by rearranging equation (1.8) in the form of equation (2.24), where again B is the braked weight (tonnes), $\sum F_{dyn}$ is the sum of all brake block forces (kN), g is the acceleration of gravity and k is an assessment factor provided by the UIC 544-1 leaflet.

$$\sum F_{dyn} = \frac{Bg}{k\left(F_{dyn}\right)} \tag{2.24}$$

Figure 33 shows the values of the k factor and of the braked weight for a typical two-bogie wagon equipped with a total of 16 brake blocks, as a function of the pressing force on each block. The idea behind the proposed method is

therefore to estimate the brake block forces starting from the knowledge of the braked weight through equation (2.24). Since the k factor is a function of the brake block force, equation (2.24) cannot be solved in closed form and a numerical scheme, like the Newton-Raphson method, is required.

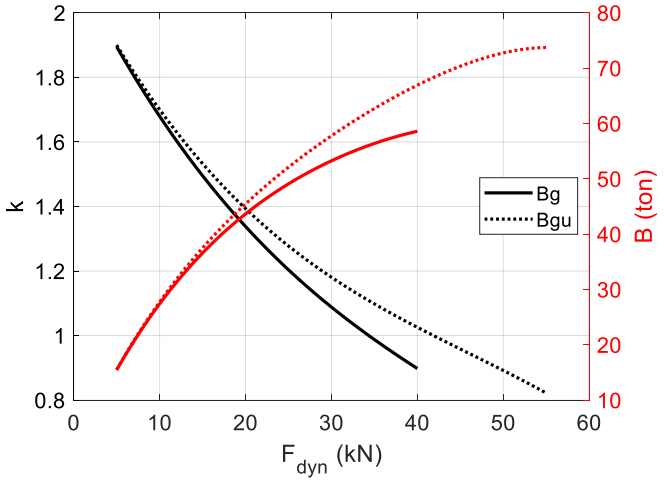

Figure 33: k factor and braked weight as a function of the force on each brake block.

The force computed with this approach corresponds to the maximum value of the total brake block force, which however is not immediately applied on all wagons at the same time, due to delays related to the pressure wave propagation speed along the brake pipe and to the time required to fill the brake cylinders. To consider these delays, the total force on all brake blocks $F_{b,tot}$ during the simulation is calculated according to an exponential heuristic function, see equation (2.25), where t is time, e is the Euler's number, t_{app} is the time delay between the braking command and the pressure drop in the brake pipe, t_{del} is the time delay between the head locomotives and the remote wagons, and τ is the parameter that adjusts the gradient of the exponential function. The time delay due to the pressure drop propagation wave speed is related to the air speed v_{air} in the brake pipe as stated by equation (2.26), where x_L is the position of the head locomotive and x_j is the position of the j-th vehicle in the train consist. On the other hand, the model time constant τ is related to the time required to fill the brake cylinder t_{fill}, defined as the time required to reach 95% of the target brake cylinder pressure, see equation (2.27). Finally, when the total brake block force on each wagon is obtained, the air brake force F_{air} can be calculated with equation (2.28), where the brake block friction coefficient μ_b is introduced. For cast iron brake shoes, the friction coefficient is not constant, and it is a function of the

vehicle speed and of the brake block force. The brake block friction coefficient can be estimated using the well-known Karwatzki's formula, see equation (2.29), where V is the vehicle speed (km/h), and Figure 34, which highlights that the brake block friction coefficient decreases at low speed and force values.

$$F_{b,tot}(t) = \begin{cases} 0, & t < t_{app} + t_{del} \\ 1000 \sum F_{dyn} \cdot \left[1 - e^{-\frac{(t - t_{app} - t_{del})}{\tau}}\right], & t \geq t_{app} + t_{del} \end{cases} \quad (2.25)$$

$$t_{del} = \frac{x_L - x_j}{v_{air}} \quad (2.26)$$

$$\tau = \frac{t_{fill}}{\ln 20} \quad (2.27)$$

$$F_{air} = \mu_b(V, F_{dyn}) F_{b,tot} \quad (2.28)$$

$$\mu_b = 0.6 \frac{V + 100}{5V + 100} \frac{16/g\, F_{dyn} + 100}{80/g\, F_{dyn} + 100} \quad (2.29)$$

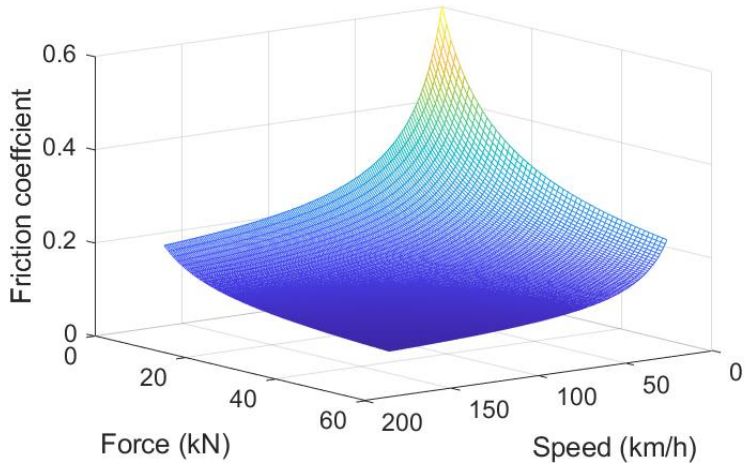

Figure 34: Friction coefficient for cast iron brake shoes according to Karwatzki's formula.

The approach shown above can be only adopted for railway wagons, as the k factor is defined for tread braked wagons fitted with 2Bg or 2Bgu P10 cast iron shoes. Nonetheless, to evaluate the air brake forces on the locomotives in the train composition, the aforementioned strategy is slightly modified and extended to this

kind of vehicles, too. For locomotives, Equation (2.24) is still applied by considering a constant value of the k factor, which is determined from the indications of Annex A of the UIC 544-1 leaflet, which provides the values of the braking distance for isolated locomotives as a function of the braked weight. The constant k factor for locomotives is determined via an optimization algorithm that minimizes the differences between the braking distances prescribed by the UIC 544-1 leaflet and the simulated ones. Since locomotives are commonly equipped with disc brakes, that feature an approximately constant friction coefficient, the air brake force acting on the locomotives is calculated according to Equation (2.30), where μ_d is the brake disc friction coefficient, while r_w and r_b are the wheel and braking radii.

$$F_{air} = \mu_d \frac{r_b}{r_w} F_{b,tot} = \mu_{eff} F_{b,tot} \tag{2.30}$$

The model described in the lines above was tuned and validated in the simulation scenarios of emergency braking operations considered in a reference paper by Pugi et al. [45]. The simulation scenarios deal with different compositions of European freight trains, including a variable number of Shimmns wagons trailed by a head E402B locomotive, all braked in P position starting from an initial speed of 100 km/h or 50 km/h. The model parameters were tuned on the simulations run from an initial speed of 100 km/h in order to obtain braking distance values close to the ones prescribed by the UIC 544-1 rule. The Shimmns wagon has a maximum axle-load of 22.5 tonnes (maximum weight on rails equal to 90 tonnes) and it is equipped with a double-stage empty-loaded device, so that the braked weight percentage is a function of the weight on rails, see Figure 35. On the other hand, the E402B locomotive has a weight on rails equal to 89 tonnes and a braked weight of 79 tonnes (braked weight percentage equal to 90%). Since the proposed method is mainly developed for European freight wagons, the in-train forces were calculated with LUTs storing experimental impedance characteristics of the European buffer-hook system, see Figure 36, in which positive values of force and deflection refer to draft states.

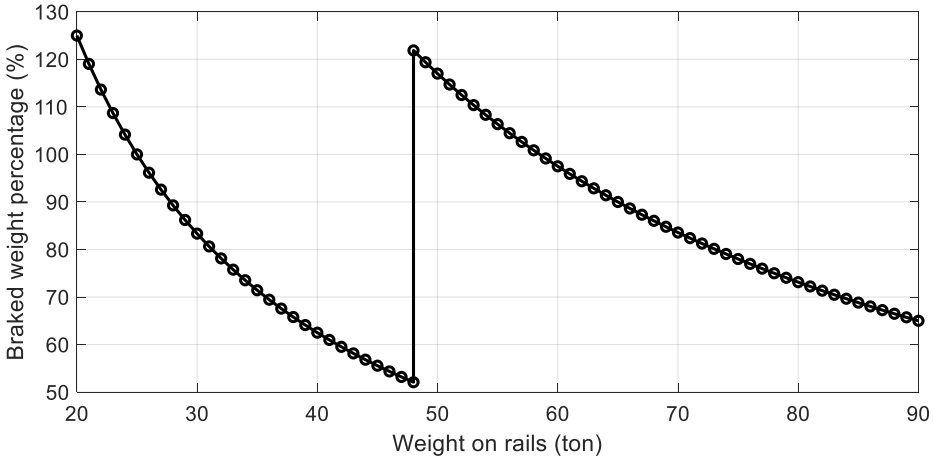

Figure 35: Braked weight percentage as a function of the wagon weight on rails for the reference Shimmns wagon.

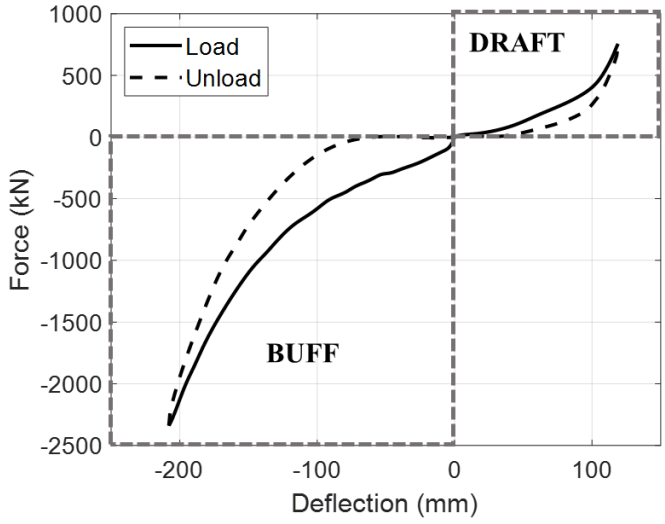

Figure 36: LUT storing the characteristics of the European buffer-hook system built from data shown in reference [45].

To run the simulations for the validation of the proposed strategy for the computation of the air brake forces, the architecture of the LTDPoliTo code was slightly modified, and the train configuration was defined with structures rather than simple arrays. This is a first step towards the possible implementation of a code based on object-oriented programming (OOP) strategies, which would guarantee the maximum flexibility to deal with any kind of input dataset. Table 8 shows the values obtained for the main model parameters derived with a trial-and-

error tuning operation intended to obtain braking distances close to the values prescribed by the UIC 544-1 leaflet. Details about the preliminary simulations launched to tune and validate the proposed model are given in Table 9, which provides the value of the train braked weight percentage λ_{train}, the braking distance prescribed by the UIC 544-1 leaflet S_{UIC}, the braking distance obtained by Pugi et al. with the fluid-dynamics model developed at Università degli Studi di Firenze (UniFi) S_{Pugi} and the braking distance calculated with the proposed method S_{Poli}. Please note that in Table 9 the train composition is described by a string in the form "N w (W ton) VY", where N is the number of wagons trailed by the head locomotive, W is the weight on rails of each wagon and Y is the initial speed in km/h. In each simulation, the double stage empty-loaded device is in loaded position, and the track is always a straight track with no curves and grades.

Table 8: Main parameters of simplified air brake force model.

Symbol	Description	Value
t_{app}	Delay between braking command and braking pressure rise in brake cylinders	1 s
v_{air}	Speed of pressure wave	200 m/s
t_{fill}	Brake cylinder filling time	5 s
k_{loco}	k factor for E402B head locomotive	3.54
μ_{eff}	Brake disc effective friction coefficient	0.264

As shown in Table 9, in simulations 1-6, whereby the initial speed is equal to 100 km/h, the results of the PoliTo air brake code are closer to the braking distances prescribed by the UIC leaflet rather than to the values provided by Pugi et al., since the tuning operation intended to minimize the differences between the simulated values and the values suggested in the UIC leaflet. In simulations 7-12, the UIC value cannot be calculated, as the braking distance curves are only given for minimum speeds above 100 km/h, and it is represented with "NA" in the corresponding cells. The braking distances provided by Pugi et al. are always far lower compared to the values prescribed by the UIC 544-1 leaflet, hence in

simulations 7-12, the PoliTo model predicts braking distance about 1.2 times higher compared to the values calculated by UniFi researchers.

Table 9: Results of simulations from initial speeds of 100 and 50 km/h.

Sim. #	Train composition	λ_{train} (%)	S_{UIC} (m)	S_{Pugi} (m)	S_{Poli} (m)
1	10 w (80 ton) V100	74.8	732.3	617	698.5
2	16 w (50 ton) V100	114.3	497.6	437	484.4
3	15 w (80 ton) V100	74.3	736.9	625	701.7
4	24 w (50 ton) V100	117.4	494.2	449	485.4
5	20 w (80 ton) V100	74	739.3	635	705.3
6	32 w (50 ton) V100	115.6	492.5	465	489.1
7	10 w (80 ton) V50	74.8	NA	136	162
8	16 w (50 ton) V50	114.3	NA	100	119
9	15 w (80 ton) V50	74.3	NA	138	163
10	24 w (50 ton) V50	117.4	NA	106	121.2
11	20 w (80 ton) V50	74	NA	143	164.5
12	32 w (50 ton) V50	115.6	NA	115	124

To further validate the model for initial speeds ranges considered by the UIC 544-1 leaflet, simulations were launched for an initial speed of 120 km/h considering the same train compositions as in simulations 1-6, see Table 10. A good agreement between the UIC prescribed values and the braking distances calculated by the PoliTo model is observed even in this simulation set on which the previously tuned model parameters were left unchanged.

Table 10: Results of simulations from initial speed of 120 km/h.

Train composition	λ_{train} (%)	S_{UIC} (m)	S_{Poli} (m)
10 w (80 ton) V120	74.8	1060.4	1033.3
16 w (50 ton) V120	114.3	727.8	709.9
15 w (80 ton) V120	74.3	1070	1038.7
24 w (50 ton) V120	117.4	723	710
20 w (80 ton) V120	74	1070.3	1044
32 w (50 ton) V120	115.6	720.5	713.8

In conclusion, the new method based on the indication of the braked weight percentage of freight wagons can provide braking distance values in good agreement with the prescriptions of the UIC leaflet. Therefore, the proposed strategy can be regarded as promising to upgrade the modelling capabilities of the LTDPoliTo code, allowing it to consider air brake operations. In this initial stage of the model development, only emergency braking operations with the vehicles braked in P position were considered. Nonetheless, the approach can be adapted to consider other types of braking operations, like service braking operations in G regime. Of course, for this purpose, the model parameters should be tuned again and adjusted to take into account different brake cylinder filling times and air brake pipe discharge rates. The development of the module for the calculation of the air brake forces is essential for the research group to simulate air brake operations and to keep on working on new activities, including for instance the simulation of the wheel-shoe thermal and mechanical behaviour. The module developed in the frame of the present thesis can be effectively used for the calculation of the main inputs required to compute the temperature of tread braked wheels in emergency and drag braking operations, which are believed to be the most harmful for the wheel surface. Further details about the application of the LTDPoliTo code in the simulation of the temperature of tread braked wheels are given in chapter 4.

2.3.3 Digital twins for LTD simulations

Since typical LTD models like the in-house LTDPoliTo code only consider the longitudinal dof of the vehicles in the train composition, they can effectively compute the in-train forces, but they cannot estimate the values of the wheel-rail forces. Nonetheless, the main assessment parameters defined in the EN 14363 standard [42] for the evaluation of the safety and running behaviour of railway vehicles are based on the values of the wheel-rail contact forces. These forces can be easily obtained from dynamics simulations launched on commercial MB software packages. However, as shown from the comparison between the original PoliTo Simpack LTD model and the new LTDPoliTo code, MB simulations struggle in the simulation of a huge number of elements, each one with few dofs. Consequently, MB simulations often consider isolated vehicles or small groups of vehicles, neglecting the in-train forces exchanged with the adjacent vehicles. Nonetheless, the in-train forces affect the vehicle dynamic behaviour and can cause an increase in the derailment risk, as already shown in previous sections.

A possible strategy to calculate the safety indexes accounting for the effect of the in-train forces can be launching an LTD simulation of the whole train to evaluate the in-train forces and then launching MB simulations of individual vehicles (or small groups of vehicles), with application of the in-train forces previously obtained from the LTD simulator [46]. However, if the train includes a large number of vehicles, many MB simulations should be run to calculate the assessment quantities of interest on each wagon, and the computational times may become huge even if co-simulation and parallel computing techniques are implemented.

Therefore, to enhance the modelling capabilities of the previously shown LTDPoliTo code, an add-on module was developed, which allows to estimate the main safety indexes defined in the international standards with simpler closed-form fast-to-evaluate surrogate models. These models act as digital twins of complex MB simulations, and they are built via machine learning (ML)-based kernel regressions. This strategy allows to drastically cut down the simulation efforts, as the computationally expensive MB simulations are replaced by fast and efficient evaluations of closed-form models. The work was carried out in collaboration with the EMC group of Politecnico di Torino, Department of Electronics and Telecommunications (DET), in order to combine the expertise in ML methods of the DET research group and the expertise in MB simulations of the railway research group. Precisely, the goal of the activity was to derive several surrogate models to estimate the following safety indexes: i) the derailment

coefficient Y/Q for each wheel, ii) the unloading ratio DQ/Q for each wheel and iii) the sum of the lateral forces ∑Y on each wheelset.

From a general perspective, the simpler closed-form surrogate models are trained from the results of a more complex model, which is usually referred to as the computational model. Therefore, in the present application, the surrogate models were derived from the results of dynamic simulations run with a Simpack MB model of a reference European railway wagon. A typical two-bogie freight wagon equipped with the Y25 bogie and with an axle-load of 22.5 tonnes was selected as the reference vehicle, see Figure 37. The Simpack MB model of the railway wagon had already been implemented by the research group the activities described in the present thesis took place, and further details can be found in [43].

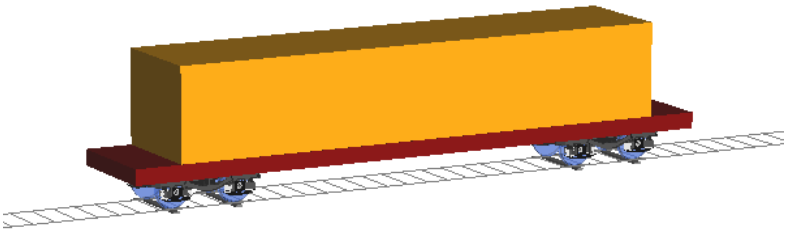

Figure 37: Simpack MB model of the reference wagon with Y25 bogie (snapshot).

The strategy adopted to derive the surrogate models is based on the following main steps, see the flow chart in Figure 38:

1. *Sampling*. A number L of simulation scenarios is identified via Latin hypercube sampling (LHS).
2. *LTD simulation*. Cascade of LTD simulations run with the MATLAB LTDPoliTo code.
3. *Wagon selection*. Random selection of a reference vehicle among the wagons in the train. A different vehicle is selected for each of the L simulation scenarios.
4. *MB simulation*. Simpack MB simulations of the dynamic behaviour of the reference wagon, with application of the in-train forces determined by the LTD code.
5. *Output calculation*. Calculation of the main safety indexes extracted from the EN 14363 standard.
6. *Training*. Building of the surrogate models performed by the DET research group with dedicated MATLAB routines.

Steps 1-6 can be repeated several times for a different number L of input configurations. The surrogate models are built by using the information available in the training set consisting of L_{Train}-samples, and then the derived surrogate models are tested on the test set including L_{Test}-samples. The testing stage is essential to assess the modelling capabilities of the surrogate models on input configurations that differ from the ones explored by the training set. Commonly, several training sets with an increasing number of samples are considered to assess the accuracy of the resulting surrogate models.

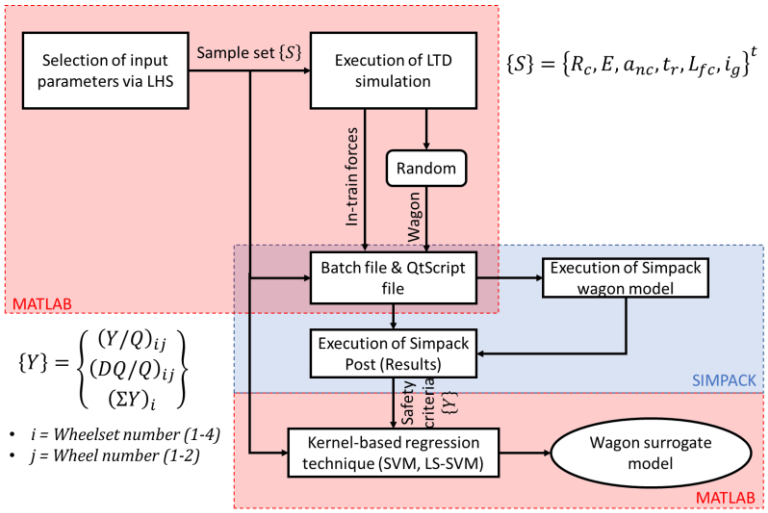

Figure 38: Flow chart of the strategy for the derivation of the digital twin models [43].

As previously mentioned, the MB model of the railway wagon with Y25 bogie had already been built by the research group before the beginning of the work described in this thesis. Nonetheless, deriving digital twins of MB simulations to be integrated into the newly built LTDPoliTo code required the implementation of dedicated scripts to run many dynamic simulations with different inputs. A cascade of dynamic simulations is needed to collect the main output results and store them in proper text files for a further processing aiming at obtaining the surrogate models. Therefore, the activities carried out during the present PhD thesis dealt with the design of the computational framework and with the development of dedicated MATLAB scripts for the sampling of the input configurations and for launching both the LTD simulations and the Simpack MB dynamic simulations. More in detail, the Simpack MB simulations are launched by calling dedicated scripts implemented in the QtScript language, which allow to modify the model parameters with low-level commands and to open the Simpack

output results binary file, in order to extract the main running safety indexes and to store them in text files for the subsequent derivation of the surrogate models, performed by the DET research group. The QtScript files are called for each simulation scenario from a batch file generated by a proper MATLAB script.

In this initial stage of the activity, the safety parameters defined in the EN standards were obtained in simple operating conditions characterized by a constant speed along a track including a straight section followed by a single right-handed curve with inlet and outlet clothoid transitions and a final straight section with constant track grade. Therefore, to define different track conditions, the inputs drawn via LHS included curve radius R_c and superelevation E, unbalanced acceleration a_{nc}, rail twist t_r, length of the full curve section L_{fc} and track slope i_g, see Table 11, which shows the lower and upper bounds of each parameter.

Table 11: Quantities drawn via LHS with corresponding variation range.

Parameter	**Symbol**	**Lower bound**	**Upper bound**
Curve radius	R_c	30 m	3000 m
Superelevation	E	0 m	0.16 m
Unbalanced acceleration	a_{nc}	0.1 m/s^2	0.6 m/s^2
Rail twist	t_r	0.1‰	4‰
Full-curve length	L_{fc}	30 m	500 m
Track slope	i_g	-15‰	15‰

The constant speed along the track $\dot{x}_{set}$ can be calculated with equation (2.31), in which g is the gravity acceleration and d_{cp} is the nominal distance between the contact points on the left and right rails, which is assumed equal to 1.5 m for a standard gauge of 1435 mm. On the other hand, the length of the clothoid entry and exit transitions L_{cl} can be determined from the curve superelevation E and rail twist t_r according to equation (2.32).

$$\dot{x}_{set} = \sqrt{R_c \cdot \left(a_{nc} + g \frac{E}{d_{cp}} \right)} \tag{2.31}$$

$$L_{cl} = \frac{E}{t_r} \tag{2.32}$$

The LTD simulations are launched with the new version of the LTDPoliTo code, in which the train composition is described with a user-defined structure variable. The dynamics of each vehicle in the train composition is described by equation (2.1), neglecting the effect of the air brake forces. In fact, although it is well known in the literature that the derailment risk increases during air brake operations in tight curves, whereby lateral in-train forces can be generated on the coupling elements, in this initial stage of the activity the air brake forces were neglected for the sake of simplicity, as the goal of the work was to simply prove the feasibility of building fast-to-evaluate digital twin models replacing the computationally demanding MB simulations in the estimation of the safety indexes.

The simulated train compositions include a head locomotive followed by 18 wagons with an axle-load of 22.5 tonnes. To ensure a constant speed along the track, an equivalent traction/dynamic braking force $F_{t/db}$ is provided by the head locomotive and calculated with a proportional-integral (PI) controller, see equation (2.33), in which x_{set} and x_{loco} are the target and feedback positions, respectively, $\dot{x}_{set}$ and $\dot{x}_{loco}$ are the reference and feedback speed values and finally K_{pos} and K_{velo} are the PI controller constants. The traction/dynamic braking force calculated on the head locomotive counteracts in each time step the resistant forces due to the rolling, curving and track grade resistances. The track grade resistance is calculated on each vehicle with equation (2.2), while the curving resistance is calculated with the benchmark expression, see equation (2.6). On the other hand, the rolling resistances are calculated on the locomotive with the expression proposed by British railways, see equation (2.34), while the rolling resistances on the wagons are evaluated with an expression suggested by Deutsche Bahn, see equation (2.35). Please note that once again in equations (2.34) and (2.35), V is the running speed in km/h and M_v is the vehicle mass in tonnes.

$$F_{t/db} = K_{pos}(x_{loco} - x_{set}) + K_{velo}(\dot{x}_{loco} - \dot{x}_{set}) \tag{2.33}$$

$$F_{ord} = M_v g \cdot [4.587 + 0.0245V + 3.6697 \cdot 10^{-4} \cdot V^2] \tag{2.34}$$

$$F_{ord} = M_v g \cdot \left[1 + 0.02 \cdot \left(\frac{V}{10}\right)^2\right] \tag{2.35}$$

Since the work deals with European freight trains, the vehicles are connected with the European buffer-hook device, which is described in LTDPoliTo code with a LUT storing the characteristics plotted in Figure 39. In each time step, the force on each coupling element is calculated according to equation (2.14), setting the speed threshold value for the smoothing transition between the loading and unloading curves to a value of 0.5 mm/s.

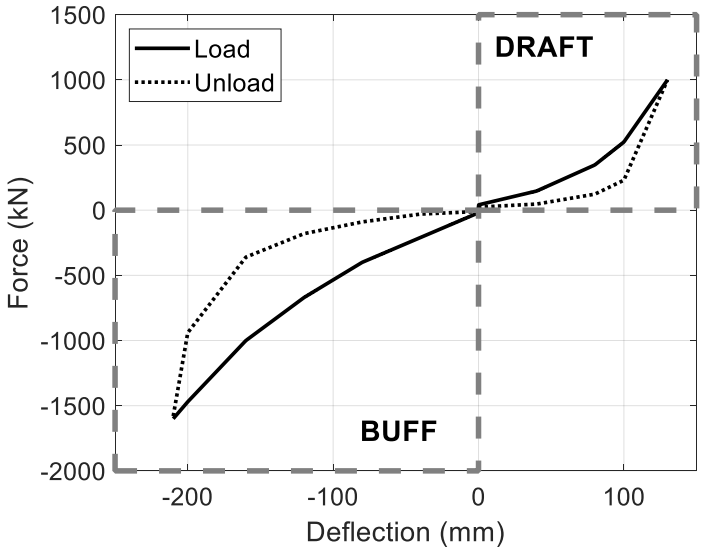

Figure 39: LUT storing the mechanical impedance characteristics of the European buffer-hook system.

After running each LTD simulation with the LTDPoliTo code, a random wagon in the train composition is selected as the reference wagon, for which a detailed MB simulation in Simpack is launched. The Simpack simulation is managed with the QtScript file, which receives the main simulation input parameters from a batch file. The simulation inputs include the values of the in-train forces as a function of the wagon position along the track. Such forces are calculated in the MB simulation using the Simpack built-in input function tool, which works similarly to LUTs. The front and rear in-train forces are applied between a marker defined on the carbody and a “Follow Track” marker, which

moves along the track. The simulated track is modelled without irregularities, but future works are planned to account for this effect on the derivation of the surrogate models. After the MB simulation with measurements is completed, a second QtScript file is called to collect the main simulation outputs, which include the maximum value of the derailment ratio Y/Q on each wheel, the maximum value of the DQ/Q coefficient on each wheel and the maximum value of the sum of the train-forces on each wheelset ∑Y. Therefore, a total number of 20 outputs is collected as the main result of the Simpack simulation. Please note that the maximum values of the safety quantities are calculated by applying the filtering operations defined in the EN 14363 standard.

After launching the LTD and MB simulations and collecting the main outputs in terms of the safety indexes prescribed by the EN 14363 standard for each simulation scenario, the surrogate models were trained. The inputs to the surrogate models can be classified in two groups, namely i) inputs obtained from the LHS sampling, that are related to the track layout, and ii) inputs calculated from the LTD simulation, that depend on the vehicle dynamics. More in detail, the inputs related to the simulation scenario include:

- Curve radius.
- Superelevation.
- Rail twist.
- Length of full curve section.

On the other hand, the following inputs for model training are extracted from the results of the LTD simulations:

- Average wagon speed along the track.
- Median of front and rear in-train forces.
- Maximum value of the rear and front in-train forces.

The DET research group built the surrogate models evaluating two different kernel-based regression techniques, namely the support vector machine (SVM) [47] and the least squares support vector machine (LS-SVM) [48]. Figure 40 shows the mean and standard deviation of the R^2 score for both regression techniques evaluated on a test sample of L_{Test} = 500 elements considering an increasing number of training samples L_{Train}. As noticeable from Figure 40, the R^2 score increases with the number of training samples, until a saturation of the curve is obtained for both techniques. The average R^2 score saturation value is

approximately equal to 0.8, which means that the digital twin surrogate models can predict accurately the variations of the outputs caused by changes in the model inputs.

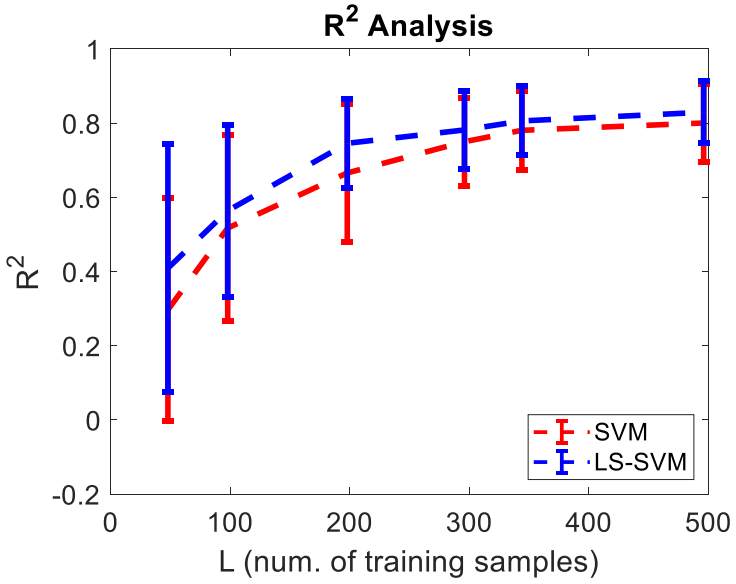

Figure 40: R^2 score for increasing number of training samples [43].

More in detail, Table 12 shows the mean value of the R^2 score according to the surrogate model predicted outputs for a number of training samples L_{Train} = 496. The LS-SVM ensures a slightly higher accuracy compared to the SVM technique, and for both methods, the surrogate models for the prediction of the ΣY safety index feature the lowest score. Figure 41 shows the scatter plots for the key surrogate models, confirming that the surrogate models for the Y/Q index feature the highest accuracy, while the lowest accuracy is obtained in the calculation of the ΣY parameter.

Concerning the computational performance, the time required to evaluate all 20 surrogate models on 500 test samples requires less than 1 s for both regression techniques. On the other hand, the estimation of the same quantities via MB simulations requires about 1 day on a commercial PC. The evaluation of the surrogate models from the outputs of the LTD simulation has a very low impact on the computational efficiency of the LTDPoliTo code. In fact, the additional post-processing operations to prepare data for the surrogate model evaluation and the evaluation itself of the models require an increase of the computational time of the LTDPoliTo code below 10%.

Table 12: Average R^2 score for SVM and LS-SVM surrogate models.

Model output	Average R^2	
	SVM	**LS-SVM**
Y/Q	0.889	0.901
DQ/Q	0.780	0.804
ΣY	0.663	0.737

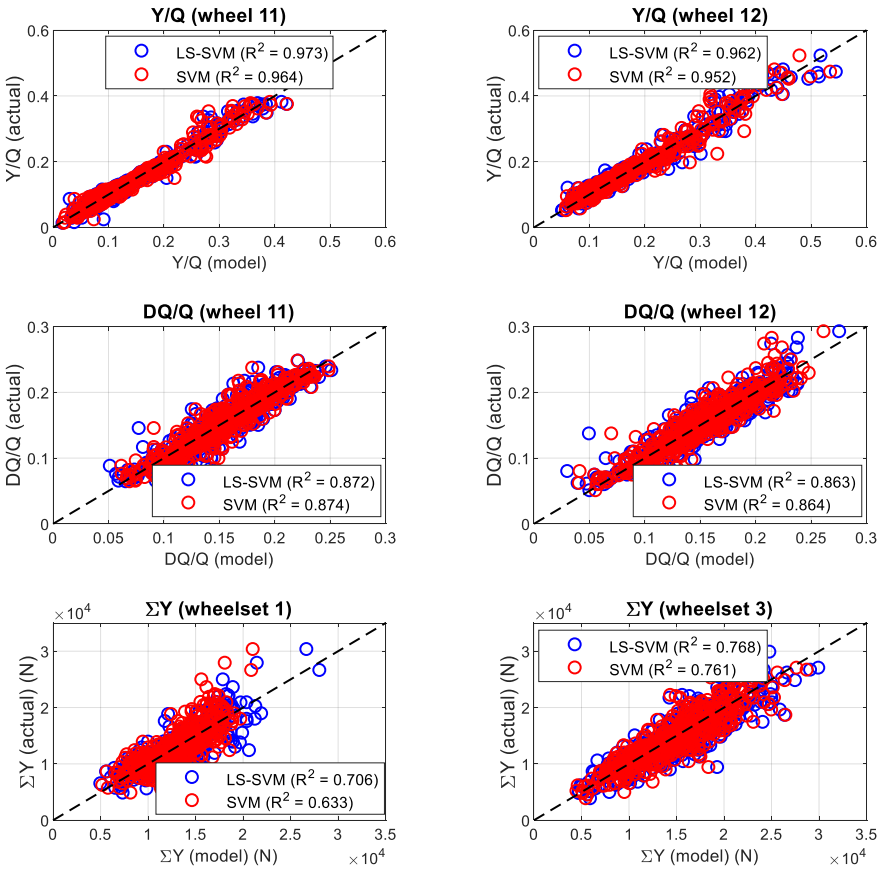

Figure 41: Scatter plots for the main safety indexes.

In conclusion, the proposed approach of building digital twin models to replace the time-consuming MB simulations proved to be feasible. The digital-twin models can be effectively integrated as add-ons in the LTDPoliTo code to estimate the main safety indexes on all vehicles of the train directly from the outputs of the LTD simulation with a simple call to the fast-to-evaluate closed-form regression models. The approach proposed in the frame of the present thesis is clearly not restricted to the LTDPoliTo code only, and such add-ons can be implemented in any LTD code, thus enhancing the modelling capabilities of basic LTD codes. Future works are planned to consider the effect of the air brake forces and of the track irregularities when building the digital twin models, as the delays due to the freight train air brake system can increase the values of the compressive in-train forces, especially for emergency operations.

Chapter 3

Experimental investigation of degraded adhesion

The braking torque produced by tread and disc braking systems is balanced by longitudinal forces generated at the wheel-rail contact patch. The value of these forces is limited by the available friction at the wheel-rail interface. A good knowledge of the wheel-rail contact conditions in both dry and contaminated conditions is thus essential to maximize the safety and performances of braking operations. As experimental tests can be extremely demanding in terms of costs and time, test rigs are often the best option to investigate phenomena involved in the wheel-rail contact. The present chapter mainly deals with the presentation of experimental activities performed by means of an innovative roller-rig that the research group had already designed and built in past activities, before the beginning of the works performed as a part of the present thesis. The bench innovative configuration was conceived to obtain a laboratory device able to simulate the mutual influence among the following wheelsets of a vehicle, which is not reproduced by traditional systems. This can enable the laboratory testing of braking torque control systems and air brake monitoring systems, thus replacing the long-lasting and expensive on-field tests, at least at the preliminary stages of development. Since the bench mechanical configuration had already been defined at the moment when this thesis started, the main activities carried out in the frame of this thesis included the bench setup, the calibration of the sensors installed on the test rig, the implementation of a LabVIEW bench control software and the development of MATLAB routines for the post-processing of raw data extracted

from the sensors. Furthermore, preliminary experimental tests to assess the repeatability and reliability of the bench were performed in the frame of this thesis.

During the activities of this thesis, after the setup of the bench was completed, the original layout of the bench was modified to reproduce the air brake system of freight wagons in laboratory conditions. This change was needed to make the roller-rig a reliable bench for the validation of air brake monitoring systems that the research group has been developing outside the frame of the present thesis for many years. The main contribution of the thesis to these activities of the group included the development of a new bench control software and a new motor control strategy for the simulation of the vehicle inertia on the roller-rig.

This chapter first provides a background on adhesion and on the effects of contaminants on the adhesion coefficient, next it describes the typical experimental devices adopted to investigate adhesion phenomena. Then, the chapter provides a quick overview of adhesion models for both dry and contaminated conditions. Finally, great focus is given to the presentation of the new innovative multi-axle roller-rig designed by the railway research group to study adhesion recovery phenomena, focusing on its mechanical layout, designed by the group in past activities, and on the bench setup, which was performed in the frame of the present thesis. The chapter ends with the description of the possible application of the new multi-axle roller-rig in the validation of air brake monitoring systems, describing in detail the new LabVIEW control software and the motor control strategy implemented as a part of the activities of the present PhD thesis.

3.1 Adhesion and friction

In the simple case of a block placed over a plane surface, see Figure 42, it is a common experience that a certain value of tangential force F_T must be applied to start moving the block in tangential direction. This force must be such that the static friction is overcome, as stated by equation (3.1), in which f_s is the static friction coefficient, N is the normal load and F_T is the tangential force. After sliding is initiated, a lower value of force is required to obtain a constant speed of the moving block. In fact, this force must balance the force due to the dynamic (or kinetic) friction, as stated by equation (3.2), in which f_k is the dynamic friction coefficient. Since the static friction coefficient is commonly larger than the dynamic friction coefficient, the force required to initiate sliding is always greater than the force needed to maintain sliding at a constant speed.

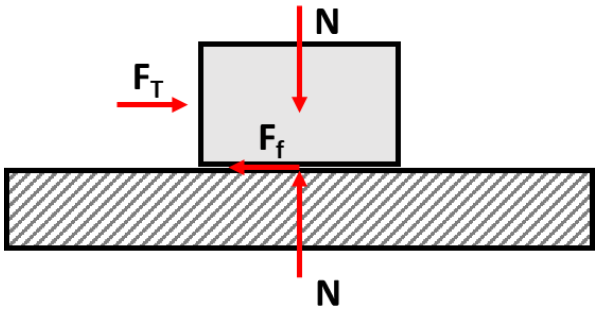

Figure 42: Definition of static and kinematic friction coefficient (F_f is the friction force).

$$F_T \geq f_s N \tag{3.1}$$

$$F_T = f_k N \tag{3.2}$$

In the case of a wheel running over a rail, the situation is more complicated, because the motion of the wheel is not a simple sliding motion, as the wheel is free to spin along its revolution axis. Theoretically, the wheel and rail surfaces would feature a single contact point, which would lead to pure rolling conditions, but due to the elasticity of the two bodies, the contact lies on a small contact patch, so that a combination of rolling and sliding is obtained. Therefore, when a braking or traction torque is applied to the wheel, a difference between the running speed of the wheel and its peripheral speed is obtained, which is usually referred to as slip or sliding speed, see equation (3.3), in which v_s is the slip speed, v_0 is the wheel running speed, ω_w is the wheel rotational speed and finally r_w is the wheel radius. The ratio between the sliding speed and the wheel running speed is referred to as creepage ξ, see equation (3.4), which refers to braking operations. According to equation (3.4), a creepage value of 0 corresponds to pure rolling conditions, while when the creepage is equal to 1, the wheel is locked.

$$v_s = v_0 - \omega_w r_w \tag{3.3}$$

$$\xi = \frac{v_s}{v_0} = \frac{v_0 - \omega_w r_w}{v_0} \tag{3.4}$$

The tangential force at the wheel-rail contact interface is a function of creepage, see Figure 43. As shown in Figure 43, the tangential force increases until the friction level is saturated. The ratio between the transmitted tangential

force at the wheel-rail contact interface and the normal load on the wheel is defined as the *adhesion coefficient*. Therefore, the adhesion coefficient can be regarded as the *used* friction and its value is always less than the static friction coefficient. As noticeable from Figure 43, as the creepage value increases, a larger portion of the contact area is in sliding conditions, until friction is saturated, and gross slip occurs.

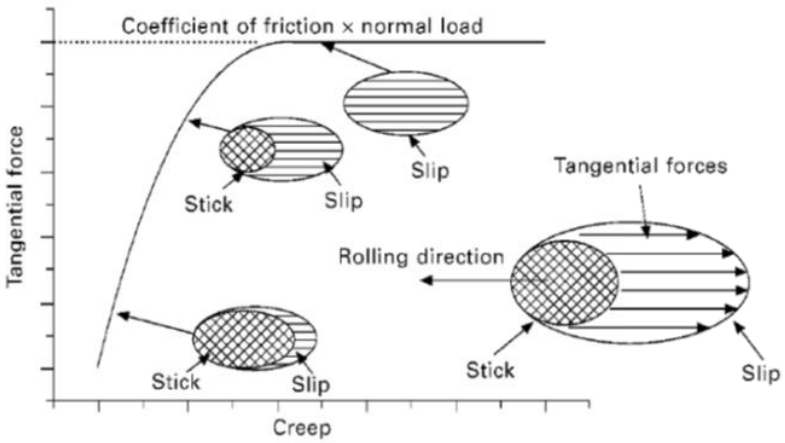

Figure 43: Adhesion curve with saturation of friction coefficient [49].

A first look at Figure 43 would suggest that very large creepage values should be achieved to maximize the tangential forces and thus increase the performances in traction and braking operations. Nonetheless, after the adhesion limit is overcome, the friction coefficient shifts from the static value towards the kinetic one, which is lower. Furthermore, both the static and dynamic friction coefficients tend to decrease as the relative speed (and hence creepage) increases [7], so that eventually the adhesion curve features a shape as depicted in Figure 44. As noticeable from Figure 44, the adhesion curve first features a linear region, followed by a nonlinear transition until the maximum adhesion coefficient is achieved. Finally, a decreasing trend can be observed beyond the maximum of the curve, corresponding to an unstable nonlinear region. In fact, in the first part of the curve, if creepage increases (i.e., the traction/braking torque increases), the adhesion coefficient (and hence the tangential force) increase, too. On the other hand, in the unstable part of the adhesion curve, if the torque increases, the adhesion coefficient decreases, and the wheel quickly reaches locking conditions. When the wheel is locked, it behaves like a block sliding over a plane, and this leads to several drawbacks, such as longer braking distances, increased wear rates,

generation of local hot spots, with possible transformation of the wheel steel microstructure, etc.

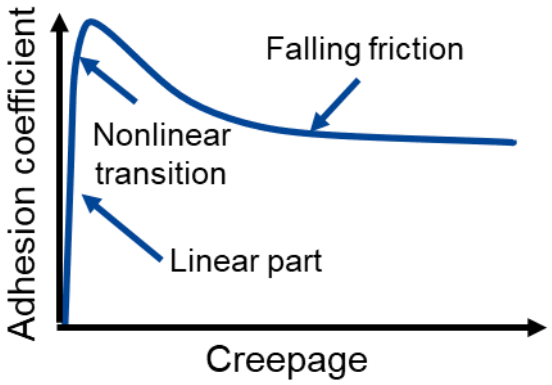

Figure 44: Adhesion curve with falling friction effect.

3.2 Degraded adhesion

The wheel-rail contact interface is an open interface, hence external substances can lie on the contact patch, thus changing the friction conditions as well as the shape of the adhesion curve. The external substances lying at the wheel-rail contact interface can be distinguished into *contaminants* and *applied substances*.

Contaminants refer to all possible natural substances that can be trapped between the wheel and the rail, e.g., water, due to rain and moist, leaves and snow. Contaminants typically lead to a big drop of the friction coefficient and to a strong modification of the adhesion curve shape, as shown in Figure 45. Figure 45, which is extracted from a technical document by Knorr-Bremse [50], highlights that all contaminants typically lead to adhesion levels below the minimum adhesion required to obtain good performances and acceptable braking distances. Furthermore, the adhesion curve for water contamination (wet conditions) shows a maximum peak at large creepage values, while leaves lead to an adhesion peak at a lower creepage value followed by a sharp adhesion reduction. Other contaminants can have behaviour in between water and leaves curves.

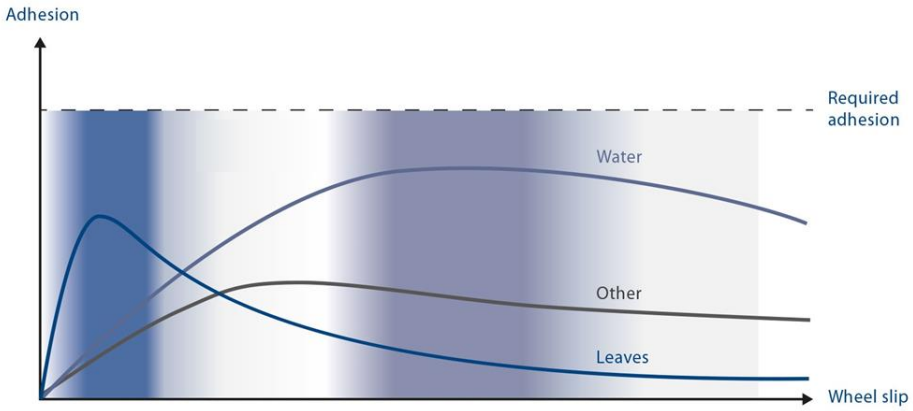

Figure 45: Adhesion curves for different contamination conditions [50].

On the other hand, applied substances are substances that are deliberately used to manage friction at the wheel-rail interface, like sand, friction modifiers and lubricants. Sand has been traditionally spread on the rail surface with sanders installed in the locomotives to restore dry adhesion levels on contaminated track sections, with the aim to achieve better traction performances. Oil lubricants are typically spread in tight curves to reduce friction thus lowering the derailment risk. Oil lubricants should act between the wheel flange and the rail gauge, see Figure 46, however, if they are accidentally spread towards the wheel tread-rail head contact zone, they can seriously affect the traction/braking operations. Finally, friction modifiers are engineered products that are intentionally spread at the wheel tread-rail head contact to manage friction, so that an optimum adhesion coefficient is attained, which optimizes the traction/braking performances whilst ensuring lower wear rates, lower energy consumption during traction operations, lower risk of crack initiation (rolling contact fatigue, RCF) and lower noise. Please note that while friction modifiers are deliberately used at the wheel tread-rail head interface, lubricants are applied at the wheel flange-rail gauge interface, and their presence at the wheel tread-rail head contact zone is totally undesired.

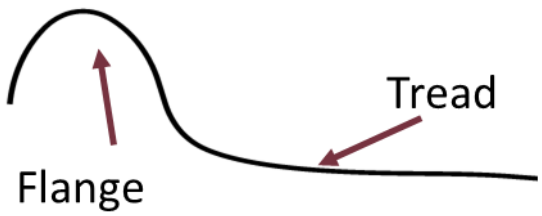

Figure 46: Wheel-rail profile: tread and flange contact zones.

All external substances that can possibly lie at the wheel-rail interface strongly modify the shape of the adhesion curve and the available friction. Therefore, to maximize the performances during traction and braking operations in all conditions, it is essential to gain a deep knowledge of adhesion in degraded conditions. In fact, modern railway passenger vehicles are equipped with dedicated systems that control the applied braking/traction torques to avoid gross slip and to ensure that the working point on the adhesion curve always fall into the stable region. Mechatronic systems that control the traction torque are commonly referred to as *antiskid* systems, while systems for the control of the applied braking torque are known as *wheel slide protection* (WSP) systems, see §1.2.1. Although commercial WSP systems already exist and are mounted on circulating passenger vehicles, a huge research effort is still ongoing to develop efficient and effective algorithms, able to immediately detect dangerous conditions and to adapt to all possible contamination conditions to minimize the braking distance whilst maximizing safety in the widest range of operating conditions.

The main limitation of current WSP algorithms is that they are not able to consider the effects of re-adhesion phenomena. In fact, when a vehicle is facing a contaminated track section, see Figure 47(a), the front wheelsets are clearly affected by the highest increase in creepage, and thus a partial sliding occurs. However, the energy dissipated at the contact patch because of the work done by the friction forces is able to partially destroy the contaminant layer sticking on the rails, thus restoring better adhesion conditions on the following wheels. Therefore, one can expect that the rear wheelsets of the train will be slightly affected by the track contamination, because of the cleaning action performed by the front wheelsets, as qualitatively depicted in Figure 47(b). This phenomenon is referred to in this thesis as *rail adhesion recovery* (RAR) phenomenon. Furthermore, focusing on any wheelset that is running over the track, a contaminant layer will be sticking on the wheel surface. Nonetheless, the wheel-rail contact forces generated for large creepage values will produce a partial removal of this contaminant layer, too, thus improving the adhesion conditions on the contaminated wheelset. The removal of the contaminant layer from the wheel surface can be classified as a *wheel adhesion recovery* (WAR) phenomenon. The two phenomena (RAR and WAR) cannot be easily distinguished in normal operating conditions, nonetheless they both produce a similar effect, i.e., a partial restoration of good adhesion levels as a consequence of the work done by the friction forces generated at large creepage values. Due to the aforementioned reasons, a partial slip on the front wheelsets could be tolerated since it may lead to

better adhesion levels on the rear wheelsets, that could eventually turn into a lower braking distance for the whole train.

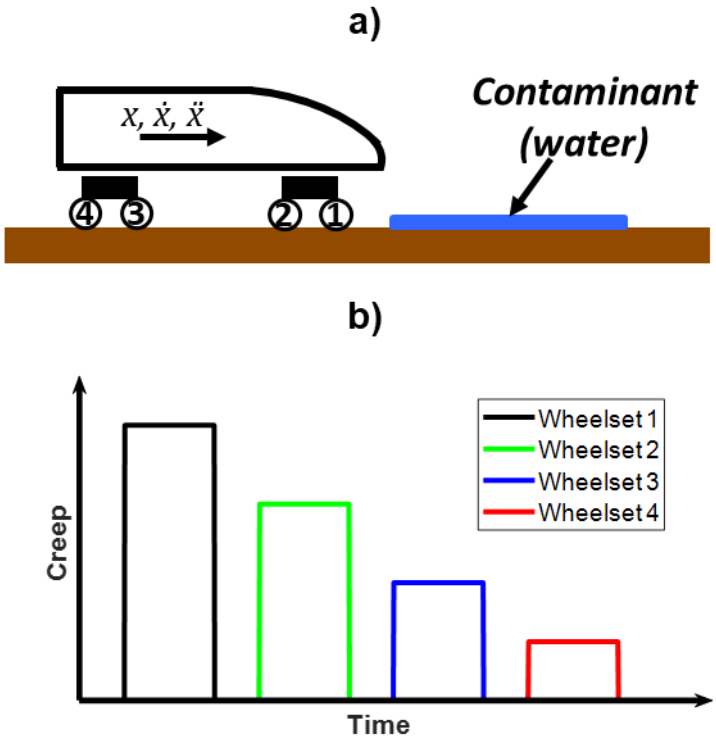

Figure 47: Re-adhesion phenomena, modified from [51].

The adhesion recovery phenomena due to the cleaning action of the friction forces have been known for a long time, as witnessed in the paper by Malvezzi et al. [52], which references works by ORE researchers that observed a second maximum of the adhesion curve for large values of creepage, probably related to a change in the surface condition. In the context of a wide experimental campaign, Logston and Itami [53] found that if the creepage value was allowed to overcome the limit values commonly adopted by traction control system, better adhesion conditions could be reached on the following wheels. This improvement of the adhesion conditions on the rear wheelsets of the test locomotive proved to be strongly affected by the contamination of the line. The adhesion recovery phenomena were also observed by Zhang et al. [54] during roller-rig tests that simulated a machine oil contamination. Zhou et al. [55] caried out a comprehensive experimental campaign by means of a full-scale roller-rig to investigate the effect of large slip values in wet conditions and found indeed a second adhesion peak for large slip values, as a result of an adhesion

improvement. Greater attention has been paid to the adhesion recovery phenomena in the last few years, as the review paper by Vollebregt et al. [56] clearly states that the knowledge of the adhesion phenomena connected to changes in the surface conditions during traction and braking operations is starting to be investigated more deeply and applied in antiskid and WSP systems to improve traction and braking performances.

3.3 Experimental devices for adhesion investigation

To deepen the knowledge of degraded adhesion, it is essential to carry out experimental campaigns to measure the adhesion and friction coefficients in different conditions. Several systems exist for the measurement of the friction at the wheel-rail interface, ranging from the estimation of adhesion by using on-board collected data, to the availability of on-track tribometers and to laboratory devices.

The calculation of the adhesion coefficient from on-board data is based on the estimation of the wheel-rail contact forces starting from data collected on-board the vehicle. In a collaboration with Faiveley, the Politecnico di Torino railway research group was able to estimate the adhesion coefficient during braking operations of passenger trains, starting from the measurements of wheelset speed, vehicle speed and brake cylinder pressure [57], obtained from conventional sensors installed on passenger vehicles. A similar campaign was carried out by Malvezzi et al. [52] from UniFi. However, this strategy clearly features a low repeatability and a low accuracy, unless dedicated additional sensors are installed on the vehicle, with a big rise of the costs required by the experimental campaign. Nonetheless, the estimation of wheel-rail contact forces from on-board data can enable the development of algorithms that can be implemented in WSP and antiskid systems to detect the adhesion conditions in real-time. A comprehensive review on the topic was carried out by Shresta et al. [58], who surveyed the typical methods adopted to estimate the adhesion coefficient with model-based approaches, which rely on the calculation of the adhesion coefficient starting from a numerical model that relates the response of a system (vehicle, bogie, wheelset or wheel) to the external excitations.

A possible solution to increase the repeatability of the experimental measurements is the adoption of tribometers, able to estimate the adhesion coefficient on rail sections of limited length. The rail section can be contaminated with a controlled amount of different substances before each measurement run, and then the tribometer is used to measure the adhesion and/or friction coefficient.

Harrison et al. [59] developed an upgraded version of an existing hand-pushed tribometer, based on small wheel connected to a magnetic clutch and pressed against the rail by means of a spring, that could be adjusted to ensure the required preload at the contact interface. By increasing the resisting torque of the magnetic clutch, higher creepage values could be achieved at the wheel-rail interface, and the corresponding friction force values were recorded. Areiza et al. [60] designed a similar device, in which the resisting torque was provided by an electromagnetic brake, see the sketch in Figure 48(a). The hand-pushed tribometers are commonly controlled manually by an operator, who walks along the track while holding a lever arm connected to the measuring wheel, so that as the operator walks along the track, the measuring wheel rolls on the rail. To achieve higher speeds, the SalientSystem company developed the TriboRailer commercial tribometer [59], which consists of a four-wheeled chassis that can be moved by a companion high-rail vehicle. An alternative tool to measure friction at the wheel-rail interface is the pendulum rig adopted by Lewis et al. [61], which relies on a working principle similar to the Charpy's pendulum, see Figure 48(b). The swing arm (c) is released from its horizontal configuration, and it starts swinging. When the swing angle approaches 90°, a rubber pad (d) contacts with the rail, and because of friction, a portion of energy is lost. The energy loss can be finally correlated to the friction coefficient.

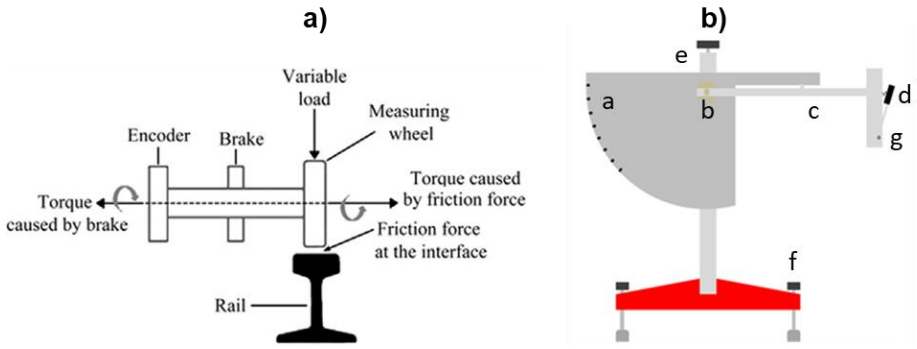

Figure 48: (a) Hand-pushed tribometer developed by Areiza et al. [60] and (b) pendulum tester used by Lewis et al. [61].

The tribometers relying on a measuring wheel are able to derive the adhesion curve, since the measuring wheel rolls on the rail just like a railway vehicle wheel, while the pendulum rig is only able to estimate a constant value of friction coefficient, since it reproduces pure sliding conditions. The greatest point of merit of both systems is that they can obtain the friction properties considering a real rail, but they are not able to reproduce the vehicle dynamics, which plays a big

role in the wheel-rail adhesion phenomena. Furthermore, although the hand-pushed tribometers can be used to derive the adhesion curve in different conditions, a scaling effect exists that can modify the values of adhesion coefficient with respect to the values observed in the operation of real vehicles [59].

To further improve the repeatability of experimental measurements, several laboratory test rigs exist, that allow to perform adhesion investigations in controlled environments. The greatest advantage of all laboratory devices is the big repeatability of the experimental tests as well as the reduction of costs related to instrumentation of real vehicles and interruption of railway traffic, which are often the main drawback of on-track tests. The simplest laboratory device for the measurement of the wheel-rail friction coefficient is the pin-on-disc system, in which a pin specimen is pressed against a rotating disc [62], see Figure 49(a). The pin-on-disc device can simply reproduce sliding friction conditions, hence it does not allow to obtain adhesion curves. Furthermore, it does not consider the vehicle dynamic behaviour and the real geometry of the contacting bodies. Nonetheless, the pin-on-disc device can be a reliable system to quickly assess the influence of several contaminants on the friction coefficient, as indeed done by Swedish researchers [63,64].

An evolution of the pin-on-disc system is the mini-traction-machine (MTM), in which the pin is replaced by a ball, able to spin around a fixed axis, see Figure 49(b). Since the ball and the disc can be powered with two independent motors, a controlled slip can be obtained at the contact patch, which is calculated according to equation (3.5), where ξ_{MTM} is the slip, ω is the angular speed, r is the radius and finally subscripts ball and disc are self-explaining. With the MTM device, both adhesion and Stribeck curves can be obtained. For adhesion curves, slip is increased while keeping a constant average speed, while to derive Stribeck curves, the slip is kept constant while increasing the average speed. The MTM can be used to reproduce the rolling-sliding motion of steel materials for different friction conditions, by properly contaminating the contact interface [65-67].

$$\xi_{MTM} = \frac{\omega_{ball} r_{ball} - \omega_{disc} r_{disc}}{0.5(\omega_{ball} r_{ball} + \omega_{disc} r_{disc})} \tag{3.5}$$

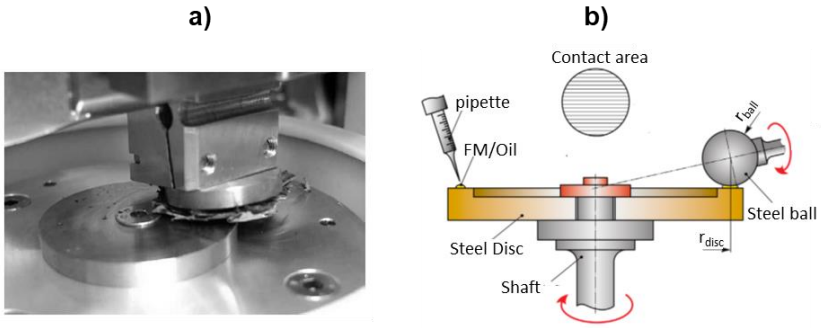

Figure 49: (a) Pin on disc used by Swedish researchers [63] and (b) example of mini-traction-machine [67].

A better simulation of the real rolling-sliding kinematics of the wheel-rail system can be achieved by means of twin-disc machines, in which two rotating discs are pressed against each other. The two discs are usually referred to as *wheel* and *rail* discs in experiments carried out in the railway field. A precursor of modern twin-disc machines is the Amlser's machine, in which two discs with a fixed gear ratio rotate over each other, and different creepage conditions ca be simulated by applying disc pairs with different radius. Figure 50 shows the layout of the twin-disc machine adopted by the research group from Sheffield University (USFD), named SUROS roller-rig [68]. As noticeable from Figure 50, the normal contact force pressing the two discs against each other is obtained by means of a hydraulic piston and measured with a dedicated load cell. Please note that in the SUROS roller-rig, the upper disc is the rail disc, while the lower disc is the wheel disc. Both discs are powered, and the speed of each shaft is recorded during the tests with two encoders. By properly controlling the two motors, steady-state creepage conditions can be achieved. The creepage value can be calculated according to equation (3.6), in which ω is the rotational speed, r is the disc radius, and subscripts r and w refer to the rail (upper) and wheel (lower) discs, respectively. The rail disc shaft is equipped with a torque transducer, that is able to evaluate the torque on the shaft during the test. Since the motors are controlled to achieve steady-state speed conditions, the inertia terms can be neglected, and the adhesion coefficient μ in each time instant can be calculated according to equation (3.7), in which T_r is the torque measured on the rail disc shaft, N is the applied normal force, measured by the load cell, and r_r is the rail disc radius. Over the last two decades, the SUROS roller-rig has been intensively used by the research group from USFD to investigate the tribological behaviour at the wheel-rail contact interface in different contamination conditions [69-72]. A big point of

merit of the experimental tests performed at USFD is that the two discs were cut from real wheels and rails, thus studying the tribological behaviour of real wheel and rail steels.

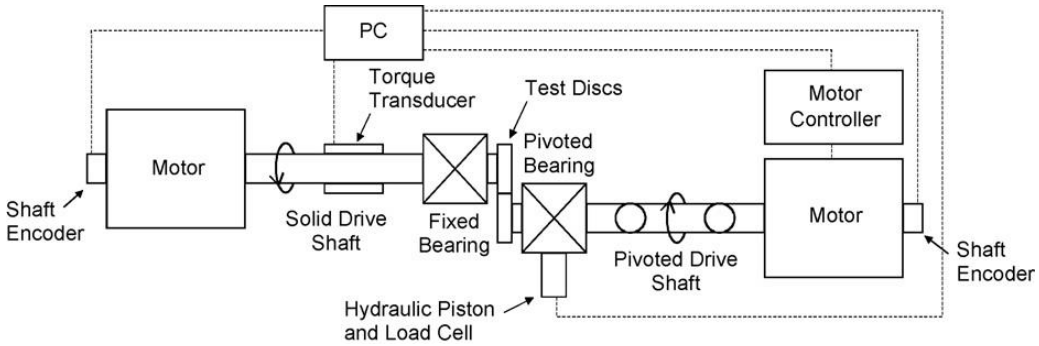

Figure 50: SUROS roller-rig [70].

$$\xi = \frac{\omega_w r_w - \omega_r r_r}{0.5(\omega_w r_w + \omega_r r_r)} \tag{3.6}$$

$$\mu = \frac{T_r}{N r_r} \tag{3.7}$$

A twin-disc similar to the configuration of the SUROS roller-rig was used by Omasta et al. [73] to investigate the effects of sanding in different conditions. To obtain an elliptical patch rather than the typical rectangular contact patch derived from the Hertzian contact between cylinders, the rail disc was machined to feature a constant transversal curve radius. A similar strategy was adopted by Chen et al. [74], who developed a twin-disc machine with a different configuration for the application of slip at the contact interface. In fact, with the twin-disc developed by Chen et al., the adhesion curves can be obtained by setting a constant speed of the wheel disc motor, disconnecting the rail disc shaft motor and then applying a braking torque on the rail disc shaft through an eddy current brake. Therefore, with this configuration, the inertia terms cannot be neglected, and the adhesion coefficient can be calculated according to equation (3.8), in which the same symbols as in the previous equations are used, while $I_{w,yy}$ is the inertia of the wheel disc shaft and $\dot{\omega}_w$ is the wheel disc rotational deceleration. Please note that conversely to the solution adopted on the SUROS roller-rig, the twin-disc developed by Chen et al. mounted the torque sensor on the wheel disc shaft.

$$\mu = \frac{T_w + I_{w,yy}\dot{\omega}_w}{F_N r_w} \tag{3.8}$$

All systems shown above for the investigation of adhesion at the wheel-rail interface share the same major drawback, i.e., they do not consider the real dynamic behaviour of the vehicle, thus not reproducing the interaction among geometry, kinematics and vehicle dynamics. Therefore, an excellent solution to simulate the dynamics of railway vehicles in a laboratory environment is the adoption of roller-rigs. Roller-rigs are test benches in which the rail is replaced by a roller with a finite value of curvature in the longitudinal direction. While twin-disc machines can only reproduce longitudinal creepage conditions, roller-rigs can have a more complex configuration, that allows to apply lateral creepages as well as a lateral shift of the contact point position. Obviously, because of their capability of reproducing the dynamic behaviour of railway vehicles with good accuracy, roller-rigs are not only limited to the investigation of tribological phenomena, but they are used in a broad range of applications in place of expensive and long-lasting on-field tests. More in detail, roller-rigs can be regarded as the most effective solution in the initial stages of prototyping, whereby a large number of tests must be carried out in short times. According to Allen et al. [75], who recently described in detail the configuration of 12 roller-rigs used all over the world, the main fields of applications of roller-rigs include wheel-rail contact, adhesion phenomena, traction and braking operations, wear and rolling contact fatigue, derailment and curving, noise and vibration issues, testing of component performances (e.g., suspensions) and finally investigation of the effects of different environmental conditions. As an example, Figure 51 shows the half-car full-scale roller-rig used by Zhang et al. for the investigation of degraded adhesion phenomena [54].

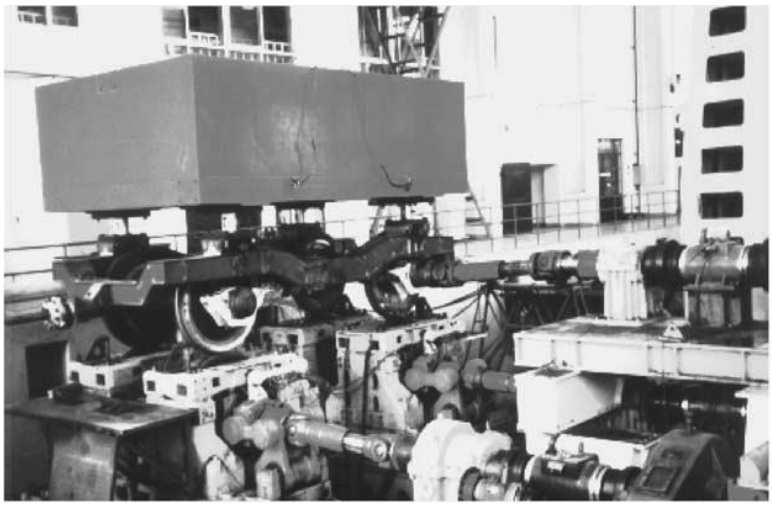

Figure 51: Full-scale roller-rig used by Zhang et al. [54].

Depending on the main phenomena that need to be investigated, different roller-rig configurations exist, which can be classified according to the element placed above the rotating rollers [76], ranging from a single wheel to a wheelset, to a single bogie and even to a whole vehicle. Obviously, a roller-rig with a single wheel rotating over a roller can be only adopted to investigate wheel-rail contact phenomena, while a roller-rig in which a whole vehicle is rotating over several pairs of rollers enables the investigation of a wide range of vehicle dynamics phenomena, but it clearly requires a more complex and more expensive design. Roller-rigs are typically classified according to their size, as either full-scale or scaled benches. Full-scale benches clearly allow to simulate with the greatest accuracy the vehicle dynamics of real railway vehicles, but they are expensive and cumbersome, so that their handling and maintenance can be complex. On the other hand, a scaled rig ensures lower costs for the construction of the bench itself and of the prototypes to be tested, and thanks to its smaller size, it can be installed in a larger number of research centres including universities [77]. As an example, Figure 52 shows the two-axle bogie roller-rig designed by the Politecnico di Torino railway research group in past activities.

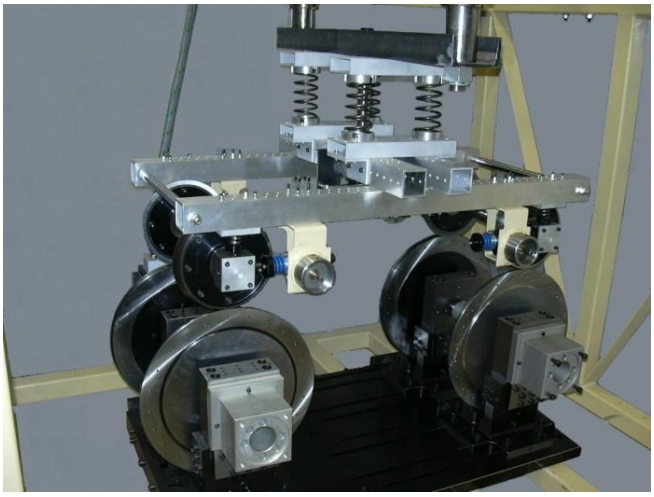

Figure 52: Scaled roller-rig installed at Politecnico di Torino [78].

Scaled roller-rigs require the definition of a scaling strategy, or similitude model, to correlate the results collected on the scaled bench to the real-life full-scale system. In fact, both full-scale and scaled roller-rigs feature some differences with respect to the operating scenario of the real system, which are mainly due to the different geometry between the rail and the roller, with the latter featuring a non-zero curvature in longitudinal direction, and to the longitudinal

constraint that prevents the wheels mounted on roller-rigs from translating [79,80]. Moreover, for scaled roller-rigs, the size scaling implies a scaling of all other quantities to ensure compatibility between the scaled system and the full-scale real system. The investigation of scaling strategies able to guarantee a similitude between a scaled and a full-scale system started with the pioneering works by Reynolds in the field of fluid-dynamics. The similitude between the two systems is ensured if three conditions are fulfilled, namely geometrical, kinematic and dynamic similitude. The definition of the scaling approach starts with the choice of the length scaling factor φ_l, which is the ratio between a length of the full-scale system l_1 and the corresponding length of the scaled system l_0, see equation (3.9).

$$\varphi_l = \frac{l_1}{l_0} \tag{3.9}$$

Obviously, it is not possible to independently set the scaling factor for each quantity since physical relationships, described by mathematical equations, exist between different quantities. As a simple example, if the length and time scaling factor are defined, the speed scaling factor cannot be arbitrarily defined, as from a unit of measurement point of view, speed is the ratio between length and time. Therefore, the typical approach adopted to define a scaling strategy is to choose some scaling factors for the main quantities of interest, and then all other scaling factors are identified to ensure the compatibility of the equations of motion for the full-scale and scaled system. In the following lines, the main similitude models currently adopted on roller-rigs are briefly described, highlighting the benefits and drawbacks of each solution. A formal mathematical derivation of the scaling factors for railway roller-rigs according to the different similitude models can be found in the work by Jaschinski et al. [79] and in the recent review by Bosso et al. [77]. Essentially, four scaling strategies can be adapted, deriving from the works of Iwnicki, Pascal and Jaschinski.

The scaling strategy proposed by Iwnicki is adopted on the scaled roller-rig of the Manchester and Huddersfield universities, and it is based on the definition of a unitary scaling factor for time $\varphi_t = 1$, so that the scaled and full-scale system feature the same natural frequencies. Therefore, the speed and acceleration scaling factors are equal to the length scaling factor, while the scaling factor for forces is $\varphi_F = {\varphi_l}^4$. Nonetheless, since the scaled roller-rig features the same material as the real wheel steel, the scaling factor for weight is $\varphi_w = {\varphi_l}^3$. Therefore, a conflict exists between the scaling factor for constraint and inertial forces and the

scaling factor for weight. To obtain a wheel-roller normal force scaled by a factor $\varphi_l{}^4$, a system of support wires and ropes is required to virtually scale down gravity on the scaled roller-rig.

Shifting focus to the scaling strategy developed by Pascal, which is used in the French INRETS (Institut National de Recherche sur les Transports et leur Securite) scaled roller-rig, it is based on a unitary scaling factor for stresses $\varphi_\sigma = 1$, to ensure the same values of contact pressure on the scaled and full-scale systems. Therefore, forces are scaled by a factor $\varphi_F = \varphi_l{}^2$, and since the scaling factors for all material properties, including density, are unitary, the scaling factor of stiffness is $\varphi_c = \varphi_l$, while the scaling factor for frequency is derived as $\varphi_\omega = \sqrt{\frac{\varphi_c}{\varphi_m}} = \frac{1}{\varphi_l}$. As a consequence, gravity on the scaled system is scaled by a factor $\varphi_g = \frac{1}{\varphi_l}$, which means that gravity on the scaled system must be virtually magnified to ensure a coherent value of the normal contact force. Therefore, if Pascal's scaling strategy is adopted, external normal forces must be applied at the contact interface to ensure the similitude with the full-scale system.

Finally, the last possible scaling strategy is the one derived from the work carried out by Jaschinski to design the scaled roller-rig installed in the DLR laboratories in Germany. The bench was designed with great focus on the investigation of hunting nonlinear instability, hence the scaling strategy was developed with the goal to ensure the similarity of the equations of motions describing this phenomenon. To obtain the similitude, accelerations must be scaled by a unitary factor $\varphi_a = 1$, while speed is scaled by a factor $\varphi_v = \sqrt{\varphi_l}$. However, to ensure a similitude for the wheel-rail forces, density should be scaled by a factor $\varphi_\rho = \frac{1}{\varphi_l}$, which is not easy to achieve. Therefore, Jaschinski proposed to set an arbitrary value for the density scaling factor, thus accepting a lack of similitude for the creep forces in the linear part of the adhesion curve. For instance, the DLR scaled rig was designed with a value of the density factor $\varphi_\rho = \frac{1}{2}$, while the theoretical value should be equal to $\varphi_\rho = \frac{1}{5}$.

As noticeable from the previous lines, the scaling strategy should be selected according to the main phenomena that the planned experimental campaign aims to investigate. Iwnicki's similitude model was especially developed to maintain the same natural frequencies for the scaled and full-scale system, however, the need to scale down gravity on the scaled model requires the design of a complex

mechanism to virtually reduce the mass of each body. On the other hand, Pascal's strategy is probably the best option to simulate contact phenomena, but gravity is reduced on the scaled system, so that additional external forces must be applied. Finally, the greatest advantage of Jaschinski's approach is that weight forces are scaled just like all other forces, and gravity is not modified. However, achieving a perfect similitude also for linear creep forces would require a different material density on the scale system. Table 13 shows the similitude factors for the main quantities of interest for a scaled system with length scaling factor equal to 5. For the Jashinski's similitude model, two columns are given in the table, corresponding to two values of the density scaling factor, namely 1, which is the value adopted on the new multi-axle roller-rig designed at Politecnico di Torino, and 1/5, which is the theoretical exact value for similitude of the creep forces in the linear stable part of the adhesion curve.

Table 13: Similitude models (length scaling factor equal to 5).

Quantity	Iwnicki	Pascal	Jashinski (ρ=1)	Jashinski (ρ=1/5)
Length	5	5	5	5
Time	1	5	$\sqrt{5}$	$\sqrt{5}$
Speed	5	1	$\sqrt{5}$	$\sqrt{5}$
Acceleration	5	1/5	1	1
Mass	125	125	125	25
Force	625	25	125	25
Density	1	1	1	1/5
Weight	125	125	125	25
Young's modulus	1	1	1	1
Stiffness	125	5	25	5
Torsional stiffness	3125	125	625	125
Creep force	625	25	125	25
Damping	125	25	$25\sqrt{5}$	$5\sqrt{5}$
Torsional damping	3125	625	$625\sqrt{5}$	$125\sqrt{5}$
Inertia	3125	3125	3125	625

3.4 Adhesion models

3.4.1 Generalities

The forces exchanged at wheel-rail interface strongly affect the railway vehicle dynamics, because they perform the functions of supporting and driving the vehicle, as well as of transmitting the efforts needed for acceleration and deceleration during traction and braking operations. The calculation of the contact forces acting at the wheel-rail interface is a complex task that requires the solution of the following four main problems:

1. *Geometrical problem*. Identification of the contact point position.
2. *Normal problem*. Determination of normal load, contact patch shape and size and contact pressure distribution.
3. *Kinematic problem*. Calculation of the relative motion between the wheel and the rail at the contact point, which allows to define longitudinal, lateral and spin creepage coefficients.
4. *Tangential problem*. Calculation of the tangential pressure distribution and hence of the tangential forces, as a function of normal contact pressure, contact patch shape, creepage values and friction conditions.

Obviously, the calculation of the contact forces cannot be easily obtained with a straightforward approach, as the four problems listed above feature strong mutual interactions. The tangential problem is strictly related to the development of adhesion models, that must relate the contact patch quantities and the friction conditions to the tangential forces generated at the contact patch. Since the main focus of the present chapter is on adhesion at the wheel-rail contact interface, this section will pay great attention to the adhesion models, while the methods adopted for the solution of geometrical, normal and kinematic problems will be briefly mentioned and the interested reader can refer to the dedicated works in the literature [81].

Concerning the solution of the contact problem, the identification of the contact point on the wheel and rail profile can be performed with two main methods, namely the rigid and elastic approaches. The rigid approach [82] is based on the solution of the constraint equations, that relate the translation along the vertical direction and the roll angle to the other states of the wheelset. For complex and irregular profiles, the solution of the constraint equations cannot be obtained in closed form, and numerical methods must be introduced. The rigid method does not allow the penetration of the contacting bodies, and it is only able

to detect single contact points. Therefore, the rigid approach struggles in the simulation of curve negotiation, whereby multiple contact points can be present, because of the contact in both the tread and flange zones of the wheel profile. On the other hand, the elastic approach considers the elastic deformations of the contacting bodies and allows a small penetration of the profiles. The normal force is calculated as the product of a nonlinear contact stiffness times the penetration value. Since the contact stiffness value is a function of the applied normal load, a closed-form solution is difficult to achieve without strong approximations, hence commonly an iterative numerical scheme is required. The elastic approach can more easily deal with multiple contact point situations, and it can straightforwardly determine the value of the normal load on each contact patch. This is why nowadays this method is the preferred one and available in all MB commercial software packages.

If the location of the contact points is known, the subsequent step is the determination of the contact patch shape and size. Currently, algorithms that guarantee acceptable computational times for MB dynamic simulations treat the wheel and rail as elastic half-spaces, thus assuming that the contact patch is planar. Advanced models able to deal with conformal contact exist [83,84], however they are commonly not available in commercial MB software packages. Furthermore, to decouple the tangential and normal problems, i.e., to neglect the mutual influence between the normal and tangential stresses, most models are based on the quasi-identity hypothesis, as the wheel and rail steels indeed feature similar elastic properties. According to the adopted algorithm, the contact patch can be either Hertzian or non-Hertzian. The Hertzian model predicts an elliptical contact patch and an ellipsoidal contact pressure distribution [85]. On the other hand, non-Hertzian models predict complex contact patch shapes, however they can be regarded as evolutions of the Hertzian models. In fact, both multi-Hertzian and semi-Hertzian models can be applied to deal with non-elliptical, but still planar, contact patches. A survey on these models can be found in references [81,86,87]. Multi-Hertzian models [88] approximate the contact ellipse with multiple simple ellipses, while semi-Hertzian models [86,89] are based on the virtual penetration between the wheel and rail profiles, but they still assume that the contact pressure distribution has an ellipsoidal shape in the rolling direction. While classical semi-Hertzian methods neglect the elastic deformations of the wheel and the rail in the determination of the contact patch, by virtually penetrating the two profiles of a pre-determined quantity, researchers from Sweden recently developed the ANALYN algorithm, implemented in MATLAB,

which ensures bigger accuracy thanks to an approximate estimation of the total elastic deformation [90].

The wheel-rail interaction generates forces in both normal and tangential direction with respect to the contact patch plane. As shown in precious sections, a longitudinal force is produced only if a small longitudinal creepage ξ is generated, as a result of the difference between the wheel rolling speed and its circumferential speed. Similarly, lateral forces require the generation of a lateral creepage η. Furthermore, a third creepage contribution exists, which is the spin creepage φ, that is due to the rotation of the contact patch around the normal direction. Linearized creepage values for lateral and spin creepage can be related to the wheel geometry and to the wheelset state according to the expression provided by Ayasse et al. [91], see equations (3.10) and (3.11). Please note that in these equations, $\dot{Y}_w$ is the wheelset lateral speed, v_0 is the wheelset rolling speed, ψ is the yaw angle, γ is the wheel conicity and r_0 is the wheel rolling radius at the contact point.

$$\eta = \left(\frac{\dot{Y}_w}{v_0} - \psi\right) \cdot \frac{1}{\cos\gamma} \tag{3.10}$$

$$\varphi = -\frac{\sin\gamma}{r_0} + \frac{\dot{\psi}}{v_0}\cos\gamma \tag{3.11}$$

3.4.2 Adhesion models for dry conditions

Solving the tangential problem means determining the values of the tangential stresses, displacements and forces over the wheel-rail contact patch. These forces are derived from the integration of the tangential stresses generated at the contact patch. The exact solution to the rolling contact problem for half-elastic bodies was found by Kalker and implemented in the CONTACT algorithm [92], which however is computationally too slow for online application in MB simulations. Nonetheless, being the CONTACT algorithm the exact solution to the rolling contact problem, able to take into account the mutual influence between the normal and tangential stresses, it is widely adopted as a benchmark for the validation of simpler (and faster!) models.

A simple model for the calculation of the tangential forces was proposed by Carter [93], who considered the wheel-rail contact as an Hertzian contact between a cylinder and a plane. Carter was able to calculate the slip and adhesion zones inside the contact patch, with the latter being a function of the longitudinal creepage. Figure 53(a), which is extracted from the original Carter's paper,

qualitatively plots the shear stress distribution along the rolling direction. The contact patch length between A (leading edge) and C is the adhesion zone, while the length between points C and A' (trailing edge) is the slip zone. In the adhesion zone, the tangential pressure p_x is less than the friction limit, sketched as a dashed curve, while in the slip zone, pressure is saturated to the friction limit, see equation (3.12), where f is the friction coefficient and p_z is the normal contact pressure. According to Carter, the transmitted longitudinal force F_x could be estimated according to equation (3.13), where K_C is a constant value, r_w is the wheel radius and N is the applied normal load.

$$p_x(x) \begin{cases} = & fp_z(x), \quad Slip\ zone \\ \leq & fp_z(x), \quad Adhesion\ zone \end{cases} \tag{3.12}$$

$$F_x = K_C\sqrt{r_w N} \tag{3.13}$$

Carter's theory was limited to one-dimensional problems, as it only considered the longitudinal creepage. The extension to elliptical contact patches in contact conditions with both longitudinal and lateral creepages was provided by Vermeulen and Johnson [94]. Their theory calculated the adhesion zone as an elliptical area, with the same aspect ratio as the contact ellipse, and tangent to the contact ellipse at the leading edge, see Figure 53(b). The contact forces in longitudinal (F_x) and lateral (F_y) direction can be calculated according to Johnson and Veremeluen's theory as stated by equations (3.14) and (3.15), where the term corresponding to $|s_{tot}|>3$ ensures that the friction limit is not overcome. Please note that in equations (3.14) and (3.15), f is the friction coefficient, N is the normal load, **i** and **j** are unit vectors in longitudinal and lateral directions, respectively, while a and b are the semi-axis of the contact ellipse, G is the tangent modulus, and finally C_{11} and C_{22} are normalised coefficients that are calculated as elliptic integrals from the Hertzian theory. Tables storing the values of the Hertzian coefficients for different values of ellipse aspect ratio and Poisson's coefficient were later provided by Kalker [95].

$$\left(F_x, F_y\right) = \begin{cases} \dfrac{fN}{s_{tot}}\left[\left(1 - {}^{s_{tot}}/_{3}\right)^3 - 1\right] \cdot (\zeta \boldsymbol{i} + \vartheta \boldsymbol{j}), & |s_{tot}| < 3 \\ -\dfrac{fN}{s_{tot}} \cdot (\zeta \boldsymbol{i} + \vartheta \boldsymbol{j}), & |s_{tot}| \geq 3 \end{cases} \tag{3.14}$$

$$\zeta = \frac{\pi abG\xi}{fNC_{11}}, \qquad \vartheta = \frac{\pi abG\eta}{fNC_{22}}, \qquad s_{tot} = \sqrt{\xi^2 + \eta^2} \tag{3.15}$$

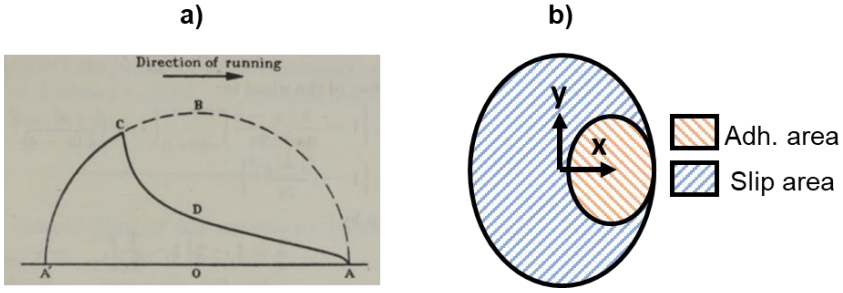

Figure 53: (a) Tangential pressure according to Carter's theory [93] and (b) contact patch division into adhesion and slip area according to Johnson and Vermeulen.

The solution for the rolling contact problem considering all three contributions of creepage was given by Kalker, who developed a linear theory [95] for elliptical contact patches, considering conditions of small creepage, whereby the size of the slip area is limited. Therefore, Kalker's linear theory can be used to compute the tangential forces in the liner region of the adhesion curve. According to the linear theory, wheel-rail contact forces are related to the creepage values as stated by equation (3.16), where M_z is the spin moment and coefficients C_{ij} are referred to as Kalker's coefficients, depending on the value of the Poisson's ratio and on the contact ellipse aspect ratio. The non-zero out-of-diagonal terms consider the coupling between the lateral and spin creepages.

$$\begin{Bmatrix} F_x \\ F_y \\ M_z \end{Bmatrix} = Gab \begin{bmatrix} C_{11} & 0 & 0 \\ 0 & C_{22} & -\sqrt{ab}C_{23} \\ 0 & \sqrt{ab}C_{23} & abC_{33} \end{bmatrix} \begin{Bmatrix} \xi \\ \eta \\ \varphi \end{Bmatrix} \tag{3.16}$$

As mentioned above, Kalker eventually provided the *exact* solution for the rolling-contact problem in the CONTACT algorithm [92], considering non-Hertzian contact patches and the influence of tangential stresses on the normal stress distribution. Since the computational speed of the CONTACT algorithm is not compatible with the requirements of dynamic simulations, much effort was dedicated by researchers to develop accurate algorithms, able to guarantee a high efficiency. Shen et al. [96] developed a heuristic model to expand the validity of Kalker's linear theory for larger creepage values, when the friction limit is reached. The developed heuristic method starts from the linear forces in lateral and longitudinal direction calculated from equation (3.16), with neglection of the spin moment. The effective nonlinear forces in longitudinal ($F_{x,NL}$) and lateral ($F_{y,NL}$) directions are then computed according to equations (3.17)-(3.19). The heuristic model by Shen et al. is in good agreement with more accurate algorithms

for low values of the spin creepage, while in conditions characterized by large spin creepage, larger deviations are observed.

$$F_{x,NL} = F_x\epsilon, \qquad F_{y,NL} = F_y\epsilon \tag{3.17}$$

$$\epsilon = \begin{cases} \dfrac{fN}{F_T}\left[\dfrac{F_T}{fN} - \dfrac{1}{3}\left(\dfrac{F_T}{fN}\right)^2 + \dfrac{1}{27}\left(\dfrac{F_T}{fN}\right)^3\right], & F_T < 3fN \\ \dfrac{fN}{F_T}, & F_T \geq 3fN \end{cases} \tag{3.18}$$

$$F_T = \sqrt{{F_x}^2 + {F_y}^2} \tag{3.19}$$

The most used algorithm for the calculation of the wheel-rail contact forces in MB codes is the FASTSIM code, developed by Kalker as the *simplified* rolling-contact theory [97]. According to Kalker, the *true* slip vector at the contact interface **w** can be expressed in vector form as the sum of a rigid slip **s** and an elastic slip **u** according to equation (3.20). The latter is related to the deformation of wheel and rail due to contact, see equation (3.21), in which x and y are longitudinal and lateral coordinates on the contact patch. The FASTSIM algorithm relies on the approximation that the elastic slip is linearly related to the tangential contact pressure $\mathbf{p_t}$ through a compliance parameter, representing the contact *flexibility*. Therefore, equation (3.20) can be rewritten in the form of equation (3.22), whereby w_x and w_y are longitudinal and lateral components of the true slip, p_x and p_y are longitudinal and lateral components of the tangential pressure, v_0 is the rolling speed and three different contact compliances L_1, L_2 and L_3 are used for the three creepage contributions. Kalker calculated the values of the three contact compliances for an elliptical contact patch starting from the results of the linear theory, see equation (3.23), however he also proposed the replacement of the three contact flexibilities with a single compliance parameter L_{eq}, calculated according to equation (3.24). Debate is still on going about the best expression for the calculation of the equivalent flexibility [98]. The FASTSIM code is not restricted to elliptical contact patches since the linear relationship between tangential pressure and elastic slip can be regarded as a constitutive law. Nonetheless, the values of the contact flexibility were given by Kalker for Hertzian patches, so the extension to non-Hertzian patches implies the determination of proper values of compliances. Details about the strategies that can be adopted to extend FASTSIM to non-elliptical contact patches can be found in the work by Sichani et al. [87].

$$\boldsymbol{w} = \boldsymbol{s} + \boldsymbol{u} \tag{3.20}$$

$$\boldsymbol{s} = v_0[(\xi - \varphi y)\boldsymbol{i} + (\eta + \varphi x)\boldsymbol{j}] \tag{3.21}$$

$$\begin{aligned} \frac{w_x}{v_0 L_{eq}} &= \frac{\xi}{L_1} - \frac{\varphi y}{L_3} - \frac{\delta p_x}{\delta x} \\ \frac{w_y}{v_0 L_{eq}} &= \frac{\eta}{L_2} + \frac{\varphi x}{L_3} - \frac{\delta p_y}{\delta x} \end{aligned} \tag{3.22}$$

$$L_1 = \frac{8a}{3GC_{11}}, \qquad L_2 = \frac{8a}{3GC_{22}}, \qquad L_3 = \frac{\pi a\sqrt{a/b}}{4GC_{23}} \tag{3.23}$$

$$L_{eq} = \frac{|\xi|L_1 + |\eta|L_2 + \sqrt{ab}|\varphi|L_3}{\sqrt{\xi^2 + \eta^2 + ab\varphi^2}} \tag{3.24}$$

Regardless of the expressions adopted to evaluate the contact flexibilities or the equivalent parameter, equation (3.22) is solved in the FASTSIM algorithm by dividing the contact patch into a number of longitudinal slices, and then numerically integrating equation (3.22) along each slice, by setting full adhesion conditions at the leading edge, where the normal contact pressure is assumed to be zero. Therefore, for the numerical integration, the contact patch is divided into a number of cells defining a computational grid, see Figure 54(a). During the numerical integration process, the value of the tangential pressure is compared to the friction limit, and when the friction limit is overcome, the tangential pressure is saturated. The region whereby the tangential pressure is saturated is the slip zone of the contact patch. On the other hand, in the adhesion zone, the pressure is below the friction limit, and the true slip is set to zero. Finally, after calculating the distribution of the longitudinal and lateral pressure on the contact area, the longitudinal and lateral forces can be obtained with a second step of numerical integration, as the integral of the tangential pressures over the contact area.

Kalker's FASTSIM algorithm is definitely faster compared to the exact solution implemented in the CONTACT code, and it can be easily used in the frame of MB simulations. Nonetheless, the FASTSIM code requires the calculation of the slip velocity and tangential pressure in each element of the contact patch grid for the determination of the contact forces, thus demanding a numerical integration scheme. To avoid the numerical integration, Polach [99] proposed an analytical method for Hertzian contact patches, assuming that in the adhesion area the tangential pressure has a linear growth from the leading edge,

until the friction limit is reached, see Figure 54(b). This hypothesis is identical to the basic assumption of Kalker's FASTSIM code, however Polach also proposed that once the total tangential force F_t is obtained, the components along the longitudinal and lateral directions are calculated as weighted on the creepage value, see equation (3.25), where η_c is a corrected lateral creepage, accounting for the effect of spin, and $s_{tot,c}$ is the total creepage value, calculated according to equation (3.26). The value of the total resulting tangential force F_T is estimated as a function of the gradient of the tangential stresses in the adhesion area ε, see equations (3.27) and (3.28), where f is the constant value of friction coefficient, N is the normal load, and C_{el} is a parameter related to the contact stiffness, which can be derived from Kalker's linear theory or numerically tuned.

$$F_x = F_T \frac{\xi}{s_{tot,c}}, \qquad F_y = F_T \frac{\eta_c}{s_{tot,c}} \tag{3.25}$$

$$s_{tot,c} = \sqrt{\xi^2 + {\eta_c}^2} \tag{3.26}$$

$$F_T = \frac{2Nf}{\pi}\left(\frac{\varepsilon}{1+\varepsilon^2} + \tan^{-1}\varepsilon\right) \tag{3.27}$$

$$\varepsilon = \frac{2}{3} \cdot \frac{C_{el}\pi a^2 b}{Nf} \cdot s_{tot,c} \tag{3.28}$$

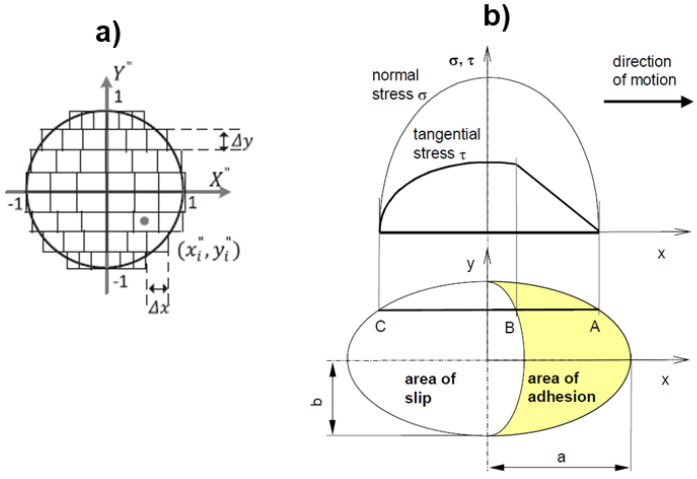

Figure 54: (a) Contact patch grid [81] and (b) tangential pressure distribution according to Polach's method [99].

3.4.3 Adhesion models for degraded conditions

The adhesion models shown in the previous section consider a constant friction coefficient at the contact interface. Therefore, the adhesion curves predicted by these models features the shape plotted in Figure 43, with saturation of the adhesion coefficient to the static friction coefficient. Nonetheless, it is well known from experimental evidence that the friction coefficient is not constant, and it is strongly dependent on the sliding speed value. More in detail, the friction coefficient decreases as the slip speed increases, because of the *falling friction* phenomenon. Typically, the falling friction phenomenon is modelled with piece-wise linear, rational or exponential equations, as reviewed by Yuan et al. [7]. Furthermore, the contamination at the wheel-rail interface can change the slope of the linear part of the adhesion curve. A reduced slope with respect to the theoretical one calculated according to Kalker's linear theory is observed for dry conditions, too, because of the effect of roughness and third body materials, such as wear particles. Therefore, these two effects must be taken into account when modelling adhesion, especially in degraded conditions.

Back in 2005, Polach modified his original model to take into consideration both aforementioned phenomena [100]. Instead of assuming a constant friction coefficient, the advanced Polach's model relies on the exponential falling friction law as stated by equation (3.29), whereby v_s is the slip speed, A is the ratio of the friction coefficient for infinite relative speed f_∞ to the static friction coefficient f_s, see equation (3.30), and B is a parameter that modifies the falling friction rate. Moreover, Polach defined two reduction factors for the adhesion and slip zones, so that in the end, the total tangential force according to the modified Polach's theory is calculated according to equation (3.31), whereby k_A and k_S are the two reduction coefficients and $f(v_s)$ is the speed-dependent friction coefficient as stated by equation (3.29). Polach performed many experimental traction tests on different locomotives in both dry and wet conditions, numerically tuning the model parameters. Furthermore, Polach provided the typical values of the main model parameters for dry and wet conditions, which are given in Table 14. Figure 55 shows the adhesion curve calculated with the Polach's model for dry and contaminated conditions, also plotting the reference curve for the original model.

$$f(v_s) = f_s[(1 - A)e^{-Bv_s} + A] \tag{3.29}$$

$$A = \frac{f_\infty}{f_s} \tag{3.30}$$

$$F_T = \frac{2Nf(v_s)}{\pi}\left(\frac{k_A\varepsilon}{1+\varepsilon^2} + \tan^{-1} k_S\varepsilon\right) \tag{3.31}$$

Table 14: Parameters of Polach's model for dry and wet conditions.

Parameter	Dry	Wet
k_A	1	0.3
k_S	0.4	0.1
f_s	0.55	0.3
A	0.4	0.4
B (s/m)	0.6	0.2

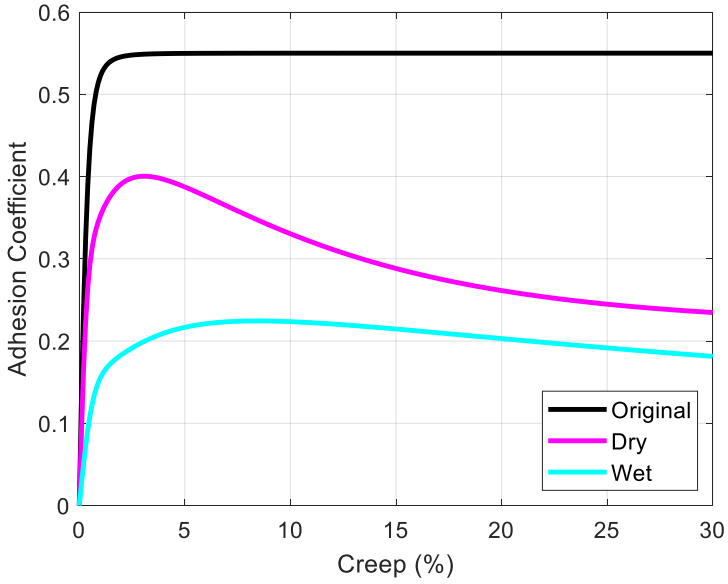

Figure 55: Adhesion curves according to Polach's model (vehicle speed of 60 km/h and axle-load of 22.5 tonnes).

In a collaboration between Polach and the CQU research group, the falling friction exponential expression as stated in equation (3.29) was introduced in a modified version of FASTSIM, able to consider the reduction of friction with slip speed [101]. The proposed modified FASTSIM algorithm relies on a variable correction factor k_{red} that is used to reduce the contact flexibility, calculated according to equation (3.32), where k_0, α_{inf}, β and k_{inf} are model parameters

identified from experimental data and numerical tests. The reduction factor becomes lower as the ratio of the slip area to the adhesion area increases, i.e., as creepage becomes higher. The variable reduction factor ensures a better agreement with experimental results, compared to methods that apply a constant value for the reduction factor. In fact, the latter kind of methods [102] requires a too high reduction of the flexibility to obtain the adhesion peak for large creepage values typical of degraded conditions.

$$k_{red} = k_0 \left(\alpha_{inf} + \frac{1 - k_{inf}}{1 + \beta\varepsilon} \right) \tag{3.32}$$

Vollebregt [103] recently improved the CONTACT algorithm by taking into account both the slope reduction in the linear part of the adhesion curve as well as the falling friction phenomenon. The upgraded CONTACT version relies on the exponential falling friction law as stated in equation (3.33), whereby f_s is the static friction coefficient, f_∞ is the friction coefficient for infinite relative speed, v_s is the sliding speed and finally v_{hlf} is the sliding speed that corresponds to halving of the difference between static and dynamic friction coefficients. Nonetheless, Vollebregt found that the application of equation (3.33) in CONTACT could lead to numerical instabilities, therefore he introduced a friction memory contribution, to smooth the variation of the friction coefficient. By identifying the position of an element in the contact patch with vector **x** and time with t, the friction memory contribution is described by the differential equation given in (3.34), where f^* is the friction coefficient calculated with equation (3.33), f is the effective friction coefficient value, and finally d_c and $v_{s,min}$ are model parameters. More in detail, d_c is the slip distance, on which the friction smoothing is applied, while $v_{s,min}$ is a minimum value of the slip speed. Therefore, the friction memory assumes that the friction coefficient calculated according to equation (3.33) is a steady-state value of the friction coefficient, which is attained only after a certain sliding distance d_s at sliding speed v_s is run. On the other hand, for what concerns the reduction of the initial slope of the adhesion curve, Vollebregt modelled the contact between wheel and rail by introducing an elastic interface layer between the two contacting bodies, acting as a series stiffness.

$$f(v_s) = f_\infty + (f_s - f_\infty) e^{-\log_2 {}^{v_s}/_{v_{hlf}}} \tag{3.33}$$

$$\dot{f}(\boldsymbol{x}, t) = -\frac{\max\{v_s(\boldsymbol{x}, t), v_{s,min}\}}{d_s} \left[f(\boldsymbol{x}, t) - f^*(\boldsymbol{x}, t) \right] \tag{3.34}$$

Prior to the activities shown in the present thesis, the Politecnico di Torino research group developed its own contact model, which calculates the longitudinal and lateral contact forces starting from the linear forces obtained from Kalker's linear theory, see equations (3.35) and (3.36), where d, δ and k are model parameters that are obtained as a function of the model exponents n_i [104]. The model relies on a strongly nonlinear power function, and the falling friction phenomenon is described by adjusting the model exponents rather than adopting a falling friction law, so that the computational speed of the algorithm is unchanged. The model exponents were tuned by Bosso and Zampieri to obtain a good agreement between the model outputs and the results of FASTSIM and Polach's method. Furthermore, the model exponents were tuned on the adhesion curves obtained from experimental tests carried out on a scaled roller-rig.

$$F_x = \frac{f_{11}\xi}{\sqrt[n]{d + \frac{|f_{11}\xi|^{n_1} + |f_{22}\eta|^{n_1} + |f_{23}\cdot[\delta\varphi + k(\delta\varphi)^{n_2}]|^{n_1}}{(fN)^{n_1}}}}$$

$$F_y = \frac{(f_{22}\eta + f_{23}\varphi)}{\sqrt[n]{d + \frac{|f_{11}\xi|^{n_1} + |f_{22}\eta|^{n_1} + |f_{23}\cdot[\delta\varphi + k(\delta\varphi)^{n_2}]|^{n_1}}{(fN)^{n_1}}}} \tag{3.35}$$

$$f_{11} = GabC_{11}, \qquad f_{22} = GabC_{22}, \qquad f_{23} = G(ab)^{3/2}C_{23} \tag{3.36}$$

Although the previous models are able to deal with the falling friction phenomenon and with the slope reduction of the linear part of the adhesion curve, thus being suitable for degraded adhesion conditions, they do not consider the possible adhesion recovery related to an improvement of the adhesion conditions thanks to the work of the friction forces generated for large slip values.

Ridolfi et al. [105] developed a model for degraded adhesion conditions able to deal with adhesion recovery, which was tuned against experimental data in the simulation of braking operations of a vehicle equipped with an active WSP system. The proposed algorithm relies on the heuristic method developed by Shen et al. [96], and it models the hysteresis of the adhesion coefficient by introducing different corrective coefficients according to whether the creep is increasing or decreasing during the simulation. Therefore, the adhesion coefficient becomes a function of not only creepage, but also a function of the creepage derivative. The main novelty of the proposed approach however is that during the simulation, the adhesion coefficient is related to the amount of specific dissipated energy W_{sp}

(J/m), calculated according to equation (3.37), where s_{tot} is the total creepage and μ is the adhesion coefficient. In fact, the core hypothesis of the model is that when a large amount of energy is dissipated at the contact, the cleaning action of the friction forces is able to remove a big amount of the contaminant sticking to the rolling surfaces. Therefore, in each time step of the simulation t, the adhesion coefficient is calculated according to equations (3.38) and (3.39), where Δt is the time step, μ^* is the estimated adhesion coefficient, calculated according to the modified Shen's theory with hysteresis of adhesion coefficient, μ_r is the maximum adhesion coefficient after full removal of the contaminant, H(z) is a discrete transfer function that filters the change of adhesion coefficient, μ_f is the final value of adhesion coefficient, and finally W_{lim} and W_{max} are model parameters that manage the adhesion recovery. As stated by equation (3.38), when the dissipated energy is less than the limit value W_{lim}, the model does not consider any adhesion recovery, and the adhesion coefficient is considered equal to the one obtained with the modified Shen's theory. On the other hand, if the dissipated energy is larger than a maximum value W_{max}, that the authors set equal to 7.8 kJ/m according to the indications of international rules, then dry adhesion conditions are restored, and the adhesion coefficient is set equal to the value that would be obtained without the contaminant. For all intermediate values of dissipated energy, the model performs a linear interpolation between the adhesion coefficient for degraded conditions and the adhesion coefficient for restored dry conditions. To account for the effect of the rail adhesion recovery phenomenon, which leads to higher friction levels on the rear wheelsets of a vehicle, Ridolfi et al. reduced the value of the friction coefficient on the wheelsets of the rear bogie of the simulated vehicle by a 10% factor. Therefore, the proposed model is able to deal with both wheel and rail adhesion recovery phenomena, although the rail adhesion recovery is simply considered as an a priori assumed reduction of the friction coefficient.

$$W_{sp}(t) = \mu(t) N s_{tot} \tag{3.37}$$

$$\mu(t+\Delta t) = \begin{cases} \mu^*(t), & W_{sp}(t) < W_{lim} \\ \mu_r, & W_{sp}(t) > W_{max} \\ \dfrac{W_{sp}(t) - W_{lim}}{W_{max} - W_{lim}} [\mu_r - \mu^*(t)] + \mu^*(t), & otherwise \end{cases} \tag{3.38}$$

$$\mu_f(t+\Delta t) = H(z)\mu(t+\Delta t) \tag{3.39}$$

The research team from UniFi kept on working on modelling of adhesion recovery phenomena and proposed a new model in 2014 [106]. The upgraded model still relates the amount of adhesion recovery to the dissipated specific energy, but it does not address the problem of the rail adhesion recovery. According to this model, the adhesion coefficient is assumed to be variable between two limit curves, one corresponding to fully degraded conditions, and the other one referring to restored dry conditions, see Figure 56. The adhesion coefficient is thus calculated as an intermediate value lying in between the two limit curves according to equation (3.40), where μ_r and μ_d refer to the adhesion coefficient for restored dry and degraded conditions, respectively, while λ is a function that manages the transition between the two curves as a function of the dissipated specific energy W_{sp}, calculated with equation (3.37). At the initial stage of the development of the model, the authors proposed to set the function λ equal to the exponential function described by equation (3.41), where τ_w is a tuning parameter that modifies the rate of the transition between the two curves. The limit curves are described as two adhesion curves derived from the modified Polach's theory for degraded conditions, accounting for falling friction and linear slope reduction effects, see equations (3.29)-(3.31).

$$\mu = \left[1 - \lambda\left(W_{sp}\right)\right]\mu_d + \lambda(W_{sp})\mu_s \tag{3.40}$$

$$\lambda\left(W_{sp}\right) = 1 - e^{-\tau_w W_{sp}} \tag{3.41}$$

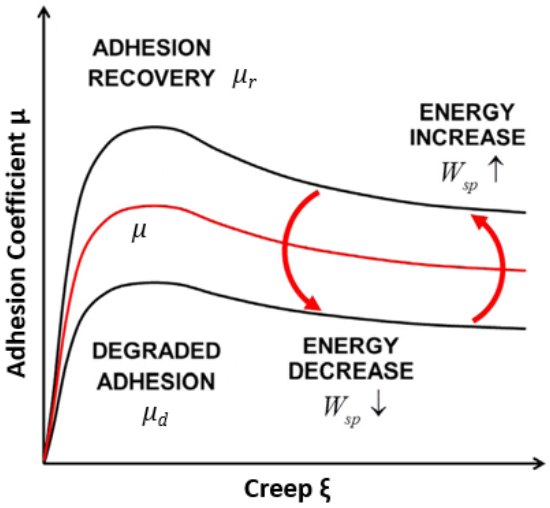

Figure 56: UniFi adhesion recovery model [106].

Recently, Zhu et al. [107] slightly modified the approach proposed by UniFi researchers, by assuming that the limit adhesion curves for degraded and recovered adhesion are not constant, but they change as a function of the total cumulated dissipated energy, see Figure 57.

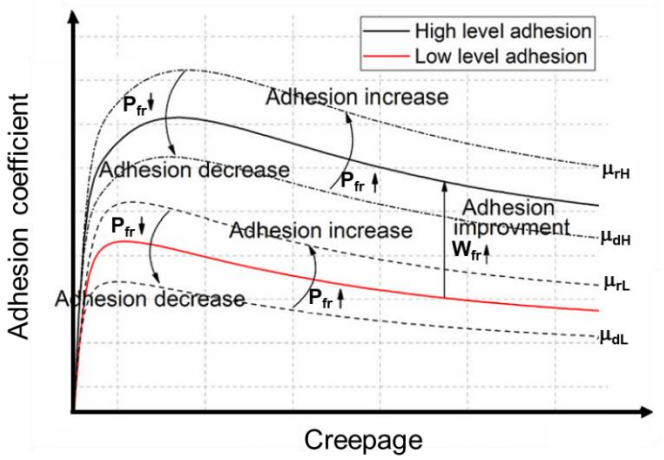

Figure 57: Adhesion recovery model proposed by Zhu et al., modified from [107].

According to this model, the adhesion coefficient in each time step is calculated as an in-between value between the two curves corresponding to degraded and recovered adhesion μ_d and μ_r, by managing the transition as a function of the dissipated power P_{fr} (W), see equations (3.42) and (3.43), where λ_1 is the smoothing transition function. The curves describing the degraded and improved adhesion μ_d and μ_r are not fixed, but they vary between two limit curves, corresponding to the minimum and maximum adhesion levels for both degraded and improved adhesion conditions. The transition between the two curves is managed with a second smoothing transition function λ_2, as a function of the total specific dissipated energy W_{fr}, see equations (3.44) and (3.45), where t is time, subscripts d and r refer to degraded and improved conditions, while subscripts L and H correspond to the lower and upper bounds for the adhesion curves. The four limit curves are defined with four Polach's equations, see equations (3.29)-(3.31), while the smoothing transition functions are in the form of the equation adopted by UniFi researchers, see equation (3.46), where $\tau_{w,1}$ and $\tau_{w,2}$ are model parameters that the authors tuned from experimental data.

$$\mu = \left[1 - \lambda_1(P_{fr})\right]\mu_d + \lambda_1(P_{fr})\mu_r \tag{3.42}$$

$$P_{fr} = \mu N v_s \tag{3.43}$$

$$\begin{aligned}\mu_d &= \left[1-\lambda_2\left(W_{fr}\right)\right]\mu_{dL} + \lambda_2\left(W_{fr}\right)\mu_{dH} \\ \mu_r &= \left[1-\lambda_2\left(W_{fr}\right)\right]\mu_{rL} + \lambda_2\left(W_{fr}\right)\mu_{rH}\end{aligned} \tag{3.44}$$

$$W_{fr} = \int_0^t P_{fr}(t')\,dt' \tag{3.45}$$

$$\begin{aligned}\lambda_1\left(P_{fr}\right) &= 1 - e^{-\tau_{w,1}P_{fr}} \\ \lambda_2\left(W_{fr}\right) &= 1 - e^{-\tau_{w,2}W_{fr}}\end{aligned} \tag{3.46}$$

A great contribution to the experimental investigation and the numerical modelling of adhesion recovery phenomena was given by researchers from Czech Republic, who performed a big amount of tests by means of a dedicated single-wheel roller-rig [108]. The full-scale roller-rig, shown in Figure 58, includes a tram wheel pressed against a rail roller by means of a swing arm, with an adjustable normal force provided by an air spring. Both the wheel and the rail roller are independently powered, and experimental tests were carried out by setting a constant speed of the rail roller, and then increasing the traction torque on the wheel shaft, to obtain sliding at the contact interface. Voltr and Lata found that the shape of the adhesion characteristic in degraded conditions was strongly dependent on the maximum achieved value of slip: when the slip value was allowed to increase even above 100%, an approximately full adhesion recovery was observed. Therefore, Voltr and Lata assumed that for large values of slip, the adhesion coefficient lays on a Polach's adhesion curve featuring a static friction coefficient value in between the values corresponding to initial (fully degraded) and final (improved) conditions. Voltr and Lata provided an empirical model to describe the phenomenon, relating the increase of the static friction coefficient value Δf_s to the energy dissipated in a certain time window t_d, thus introducing a memory effect [109]. The static friction coefficient can therefore be calculated in each time step as stated by equation (3.47) and (3.48), where subscript d and r refer to degraded and improved conditions, respectively, t_d is the time window length for the memory term and C_1 is a model parameter. To reproduce the adhesion hysteresis loops observed during the experimental tests, the friction coefficient in each time step is calculated according to equation (3.49), where f_{th} is the friction coefficient calculated according to Polach's exponential falling friction law, see equation (3.29), and C_2 is a second model parameter.

$$f_s(t) = f_{s,d} + \min\left\{\Delta f_s(t), f_{s,r} - f_{s,d}\right\} \tag{3.47}$$

$$\Delta f_s(t) = C_1[E_d(t) - E_d(t - t_d)] \tag{3.48}$$

$$f(t) = f_{th}(t) + C_2 \frac{dv_s}{dt} \tag{3.49}$$

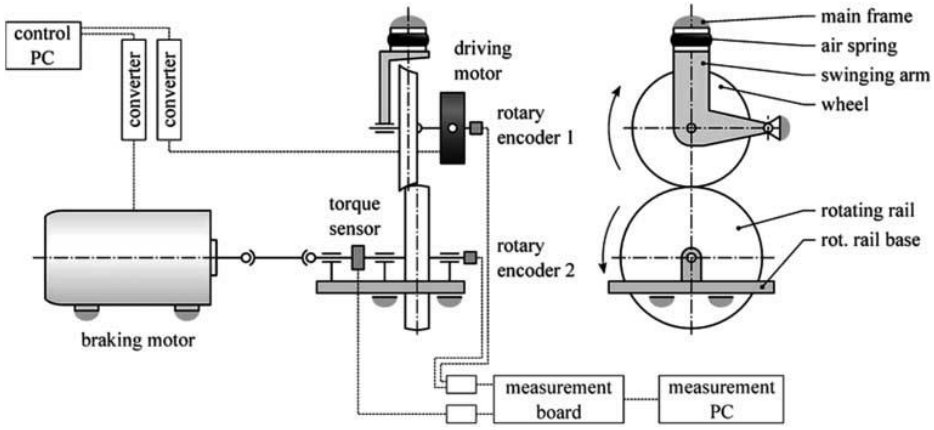

Figure 58: Full-scale roller-rig used by Czech researchers [109].

The models based on the transition of the adhesion curve between limit curves described using Polach's method calculate the adhesion coefficient with a global approach, as Polach's model does not compute the distribution of the tangential pressure and sliding speed on the contact patch. In the last years, the UniFi research group proposed an upgrade to the original FASTSIM code, in which the friction coefficient is not constant on the whole contact patch, but it is calculated in each element of the contact patch grid as a function of the slip speed, using the exponential function in the form of equation (3.29) [110]. The friction coefficient value depends on the amount of specific dissipated power per unit area $\dot{w}_{sp}$ (W/m^2), which is calculated in each element of the computational grid with equation (3.50), where x and y are the coordinates of the contact patch element, $\mathbf{p_t}$ is the tangential pressure and **w** is the true slip, calculated according to equation (3.20). The friction coefficient value takes an intermediate value between the limit values corresponding to fully degraded (f_d) and fully improved (f_r) conditions, with a smoothing transition function λ_{xy} depending on the value of the specific dissipated power, see equations (3.51) and (3.52), where τ_{FS} is the main model parameter. The greatest difference compared to the original model by UniFi researchers is that in this case, it is the friction coefficient, rather than the adhesion coefficient, that varies between two limit curves. The limit curves are in exponential falling friction functions instead of Polach's adhesion curves.

$$\dot{w}_{sp}(x,y) = \boldsymbol{p_t}(x,y) \cdot \boldsymbol{w}(x,y) \tag{3.50}$$

$$f = \left[1 - \lambda_{xy}(\dot{w}_{sp})\right] f_d + \lambda_{xy}(\dot{w}_{sp}) f_r \tag{3.51}$$

$$\lambda_{xy}(\dot{w}_{sp}) = 1 - e^{-\tau_{FS}\dot{w}_{sp}(x,y)} \tag{3.52}$$

3.5 The new multi-axle roller-rig

As shown in the previous sections, several experimental devices can be used in a laboratory environment for the investigation of degraded adhesion, and some experimental tests have already been carried out to gain further insights into the adhesion recovery phenomena, with the work by Voltr and Lata [109] being a milestone in the field. Furthermore, adhesion models able to consider the effect of improved conditions due to the cleaning action performed by the sliding forces have been proposed, however they mainly deal with an "isolated" wheel, and they are not able to consider the adhesion recovery on the following wheelsets of a vehicle (rail adhesion recovery). The reason is that the typical configurations of the laboratory devices used for adhesion investigation, surveyed in §3.3, cannot easily reproduce the real condition of the passage of multiple wheelsets over the same surface.

Prior to the beginning of the activities shown in this thesis, the Politecnico di Torino railway research group tried to simulate the rail adhesion recovery phenomenon with a single-wheelset scaled roller-rig [111]. To simulate the passage of multiple wheelsets over the same surface, the roller-rig included a contaminating system, for the application of a contaminant on a small angular sector of the roller, and a cleaning system for the removal of the contaminant from the wheel surface, see Figure 59. Cleaning the wheelset after each contact with the contaminated roller section should, in theory, ensure that at each revolution, a clean wheel faces a contaminated roller. Nonetheless, the difficulties in obtaining an effective cleaning of the wheel surface did not allow an easy execution of the tests and a simple data analysis. Therefore, for a good simulation of the rail adhesion recover phenomenon, a test bench including many wheelsets running over the same surface should be developed. For this reason, the Politecnico di Torino research group designed a new innovative scaled roller-rig with four wheelsets running over the same pair of rollers, which is called *multi-axle roller-rig*. The innovative configuration of the bench was designed by the research group with the ambitious long-term goal of building a reliable laboratory device that may replace on-track tests at the initial stages of development of WSP and

monitoring systems, with significant benefits in terms of cost reduction and speed of execution of the tests.

Although the multi-axle roller-rig was designed and built by the research group in past activities, prior to the beginning of the present thesis, for the sake of readability, this section starts with an overview on the bench hardware configuration. Then, focus is shifted to the activities performed in the frame of the present thesis, dealing with the calibration and connection of the sensors, and with the development of the bench control software and data processing routines. Finally, a last subsection shows the preliminary experimental tests performed while drafting this thesis for the assessment of the validity of the bench setup.

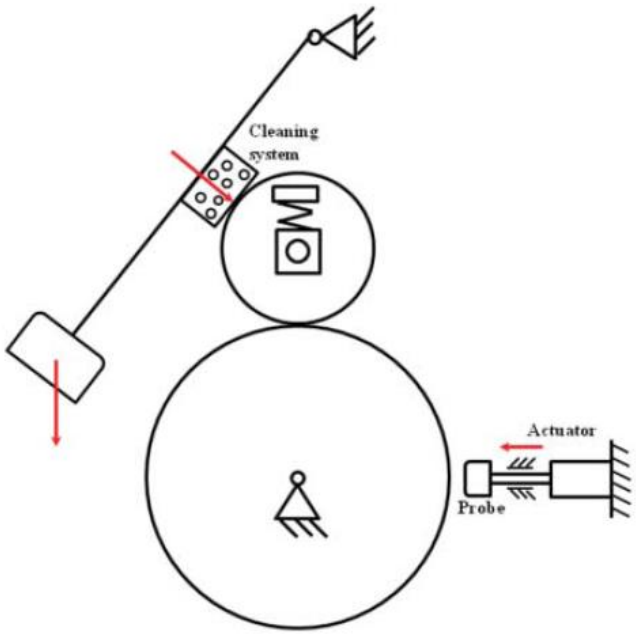

Figure 59: Single-wheelset roller-rig for rail adhesion recovery studies [111].

3.5.1 Mechanical design and working principle

The layout of the new multi-axle roller-rig is shown in Figure 60, which highlights the bench configuration, including four wheelsets mounted above the same pair of rollers. To reduce the size of the bench, the two outer wheelsets are mounted with an inclination of 72° with respect to the vertical axis, while the inclination of the two inner wheelsets is equal to 24°. The strategy adopted to obtain slip between each wheelset and the rollers is based on the application of a braking torque, which can be independently adjusted on each wheelset, while

powering the rollers. The similitude rule followed on the bench is the one proposed by Jaschinski [112], with a length scaling factor equal to 5 and a density scaling factor equal to 1, see Table 13. Nonetheless, because of the layout of the bench, other scaling factors and similitude strategies could be easily implemented with few changes to the basic rig configuration.

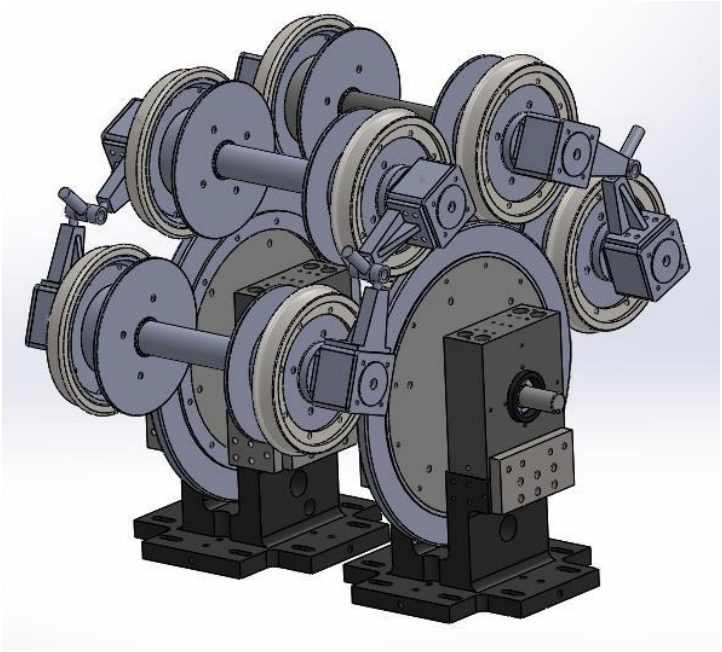

Figure 60: Multi-axle roller-rig (CAD model) [113].

To reduce costs and simplify the layout of the bench, the new multi-axle roller-rig is realized with a modular design. The main modules on the bench are:

- One frame.
- Two rollers.
- Four scaled wheelsets with axle-boxes for connection to the bench frame.
- A braking system installed on each wheelset, for the independent adjustment of the braking torque on each wheelset.
- A spring suspension system on each axle-box for the adjustment of the wheel-roller normal contact force.

The bench frame is realized with S235 cold-rolled steel profiles that are fixed to the bench base, see Figure 61, where also the two rollers can be observed. The two rollers are mounted on separate supports, see Figure 62, so that they can be either independently powered with two motors or they can be connected with a mechanical joint and powered by a single motor. Furthermore, mounting the two

rollers on two separate supports allows to change the distance of the two rollers, in order to modify the reproduced track gauge. Each roller is realized with a hub (5), fixed to the roller shaft (3), and a rim (4), which is machined to reproduce a desired rail profile. In the tests shown in the present thesis, the rollers have a nominal diameter of 368 mm with profiles machined to the UIC60 rail profile canted 1:20 and scaled 1:5. Furthermore, this design allows to only replace the roller rim in case of profile wear, with a big reduction of costs compared to the replacement of the whole roller. Finally, the holes on the outer axle-boxes (1) are designed for a connection to an external motor, to allow an independent powering of the two rollers. Nonetheless, in this thesis, the two rollers were connected with a joint and powered by a single ACM BRL 220 6 brushless motor, controlled with a dedicated drive.

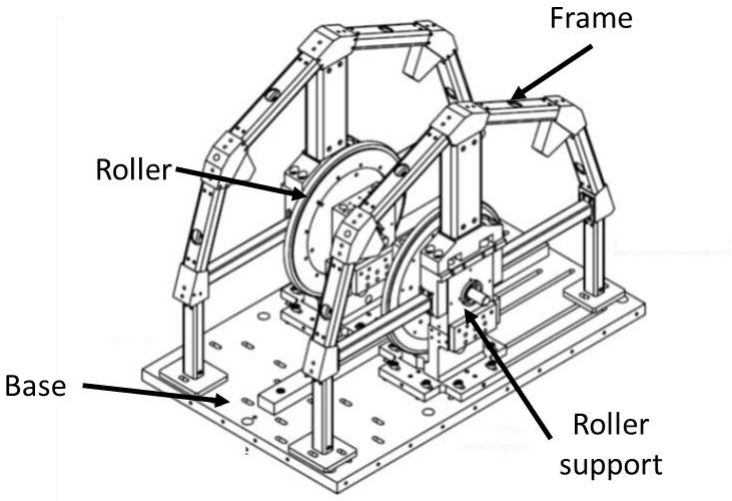

Figure 61: Multi-axle roller-rig with frame (CAD drawing), modified from [114].

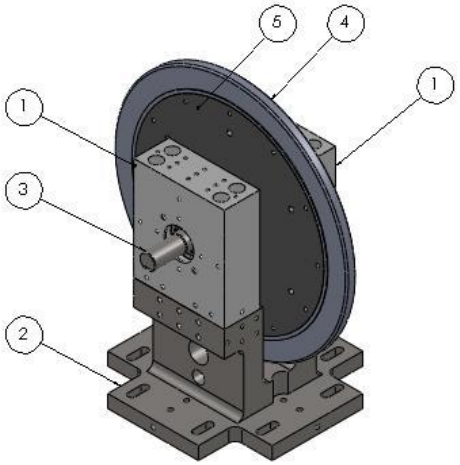

Number	Component
1	Axle-box
2	Support
3	Shaft
4	Rim
5	Hub

Figure 62: Roller with support, redrawn from [115].

Each wheelset, sketched in Figure 63, includes two wheels, two brake discs (6) and two axle-boxes (4) for the connection to the rig frame. As for the rollers, the wheels are realized with a hub (3) and a rim (2). This solution enables the simulation of different wheel profiles as well as a fast and easy replacement of the rim in case of wear. In the tests shown in this thesis, the wheels had a diameter of 184 mm and were machined to the S1002 wheel profile, scaled 1:5. The hub (3) is connected to the shaft (1) with a key joint (7), while the rim (2) is mounted on the hub with bolts (10). Each brake disc (6) is connected to the corresponding wheel with bolts passing through a brake drum (8). The axial position of the elements mounted on the shaft (1) is adjusted by two nuts (5). Finally, the longitudinal position of the wheelset on the bench is adjusted by means of mechanical brackets (9), paired to a fitting in the bench frame via a threaded connection.

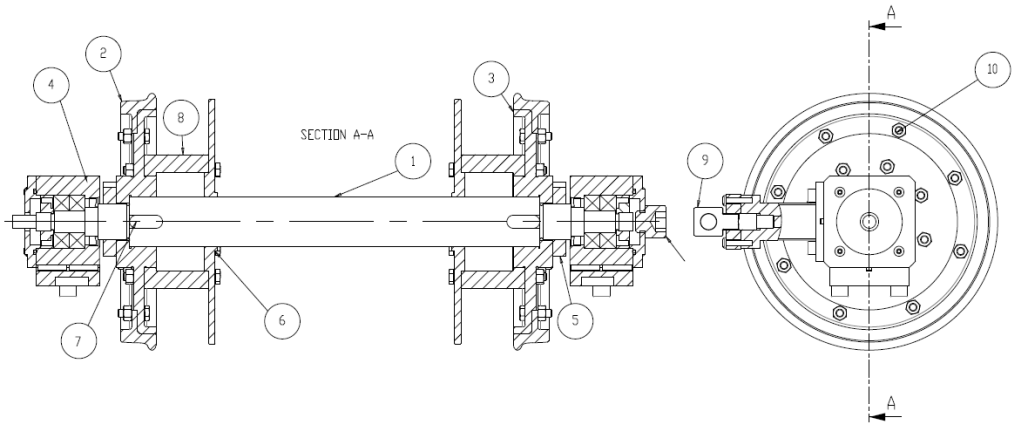

Number	Component	Number	Component
1	Shaft	**6**	Brake disc
2	Wheel rim	**7**	Key joint
3	Wheel hub	**8**	Brake drum
4	Axle-box	**9**	Bracket
5	Nut	**10**	Bolt

Figure 63: Wheelset module, redrawn from [115].

As already mentioned, the creepage at each wheel-roller interface is obtained by braking the wheelsets while keeping the rollers at a constant speed through a proper control of the motor drive. To achieve different creepage values, the braking system installed on the bench ensures an independent adjustment of the braking torque acting on each wheelset. Each brake disc installed on the wheelsets, is paired with a motorcycle Brembo P32G brake calliper, which is supplied with compressed air instead of oil. The braking module installed on each wheelset is shown in Figure 64.

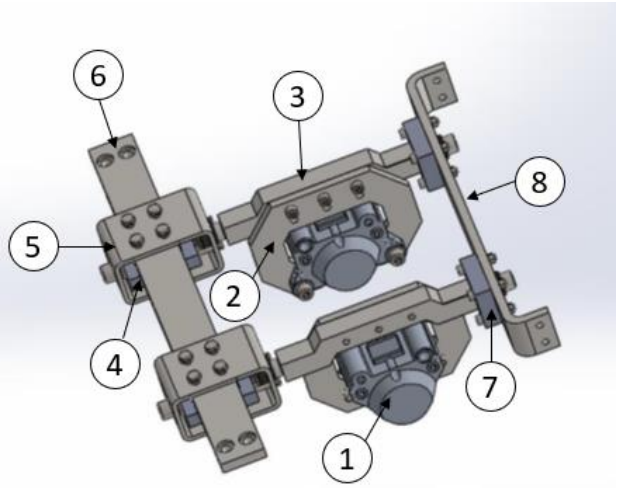

Number	Component	Number	Component
1	Brake calliper	**5**	Load cell support
2	Calliper plate	**6**	Mounting bar
3	Horizontal bracket	**7**	Anti-rotation device
4	S-beam load cell	**8**	Bent mounting bar

Figure 64: Braking module, redrawn from [115].

The braking module includes two brake callipers (1), and it is connected to the bench frame via the mounting bars (6) and (8). The braking module also comprises the components required for the measurement of the tangential braking force. In fact, each calliper is fixed to a plate (2) which is tightened to a horizontal bracket (3), whose rotation is prevented by the anti-rotation device (7). At the end of each horizontal bracket is a FUTEK LSB 302 FSH 02089 S-beam cell (4), which indeed measures the tangential force resulting from braking. The pressure of the compressed air flowing to the two brake callipers is adjusted by means of an ITV-0050 3BS electro-pneumatic regulator. Since the bench includes four wheelsets, a total of four electro-pneumatic regulators is required for the independent adjustment of the braking pressure on each wheelset.

Finally, to simulate different axle-loads acting at the wheel-rail contact interface, each-axle-box is provided with a helical spring suspension system, see

Figure 65. The normal contact preload is adjusted by compressing the spring (4), i.e., by tightening the threaded pin (1). As a consequence, the pin (1) translates and compresses the spacer (2), which eventually compresses the spring (4) and applies the preload on the spring suspension system. Fastened to the threaded pin (1) is a load button cell (6), for the measurement of the applied preload. The position of the spring suspension system on the frame is adjusted by means of the threaded support (7) and the nut (8). The normal contact load is not equal to the load applied with the spring suspension system, because a fraction of the weight of the wheelset gives a contribution to the contact load, too, see Figure 66. Since the inner wheelsets (2 and 3) have a lower inclination with respect to the outer wheelsets (1 and 4), the radial component of the weight force for the inner wheelsets is larger. Therefore, if the same axle-load is desired on the four wheelsets, the preload on the springs installed on wheelsets 1 and 4 must be larger. In fact, the normal contact load N at the interface between wheel ij and the roller can be calculated according to equation (3.53), where F_s is the spring force, measured by the load button cell, m_w is the wheelset mass, equal to approximately 15.16 kg, g is gravity and α is the wheelset angle with the vertical direction, which is equal to 24° on wheelsets 2 and 3, and equal to 72° on wheelsets 1 and 4. Please note that subscript i refers to the wheelset number (1-4), while subscript j refers to the wheel side, which can either be left (2) or right (1). The left side is the one where the brushless motor, powering the rollers, is mounted.

$$N_{ij} = \frac{m_w g \cos \alpha_i}{2} + F_{s,ij} \tag{3.53}$$

Photographs of the bench after setup are given in Figure 67, which shows the detail of a wheelset with the braking module on the right, while Table 15 highlights the main operating conditions that can be simulated with the new multi-axle roller-rig.

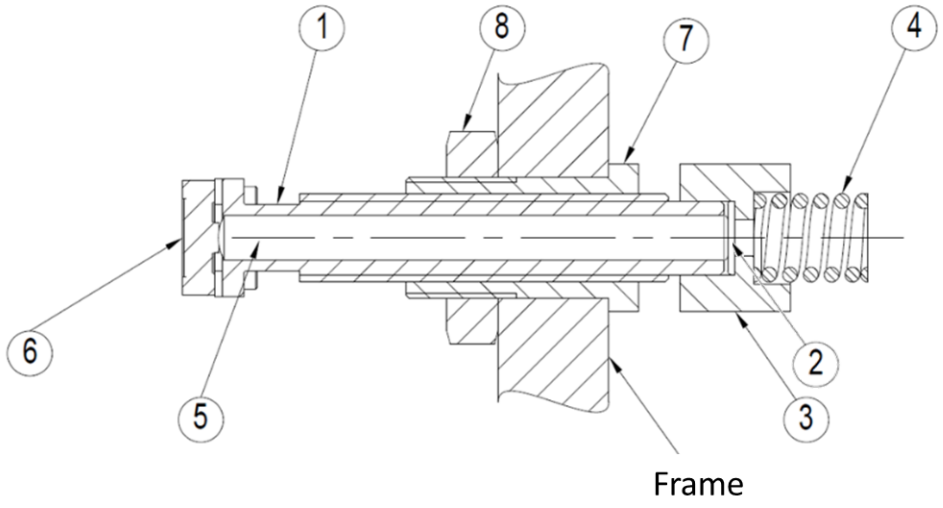

Number	Component	Number	Component
1	Threaded pin	**5**	Pin
2	Spacer	**6**	Load button cell
3	Spring holder	**7**	Threaded support
4	Spring	**8**	Nut

Figure 65: Spring suspension system, redrawn from [115].

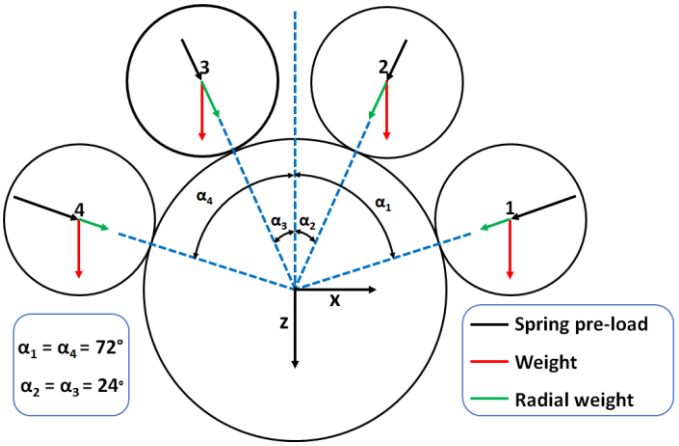

Figure 66: Bench configuration and radial forces [115].

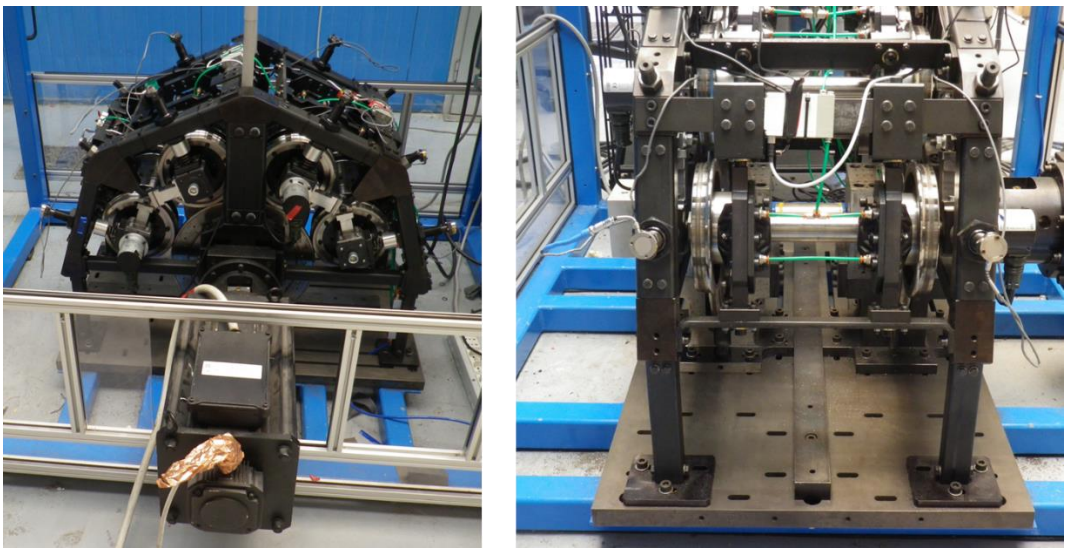

Figure 67: Photographs of the multi-axle roller-rig [115].

Table 15: Main bench parameters.

Parameter	Value
Wheel radius (full-scale)	460-520 mm
Roller radius	184-208 mm
Axle-load	2-25 tonnes
Railway gauge	1435/1524/1667 mm
Scaling factor	1:5 or 1:4

The new multi-axle roller-rig was designed with the primary goal of performing adhesion experiments, therefore it is equipped with dedicated sensors for the estimation of adhesion coefficient and creepage. When the two rollers are connected with a joint, the creepage ξ on each wheelset, identified by subscript i, can be calculated with equation (3.54), where subscripts w and r refer to wheelset and roller, respectively, and τ_{wr} is the transmission ratio, which is theoretically equal to 2, because the wheel radius is half of the roller radius. Nonetheless, the transmission ratio was identified from experimental tests run without application of a braking torque, and a value of 2.006 was identified, which is indeed very

close to the theoretical one. The speed of each wheelset is measured with magnetic incremental encoders (ELAP REM470–1024-8/24-R-10-PP2), while the speed of the rollers is acquired from the motor drive. Nonetheless, in future upgrades of the activity, the roller speed could be acquired with an additional encoder mounted on the roller shaft. Since the encoders measure the angular position of the wheelset shaft, speed is obtained with a numerical differentiation of the acquired signal.

$$\xi_i = \frac{\omega_r - \frac{\omega_w}{\tau_{wr}}}{\omega_r} \tag{3.54}$$

To understand the strategy for the estimation of the adhesion coefficient, it is useful to consider the forces acting on a wheelset when a braking torque T_b is applied, see Figure 68. For the rotational equilibrium of the wheelset equation (3.55) holds, where $\dot{\omega}_{w,i}$ is the wheelset angular deceleration, $I_{w,yy}$ is the wheelset rotational inertia, N is the normal contact load and F_x is the transmitted tangential force. If the tangential and normal loads are known, the adhesion coefficient μ can be finally evaluated according to equation (3.56), where subscript i refers to the wheelset number.

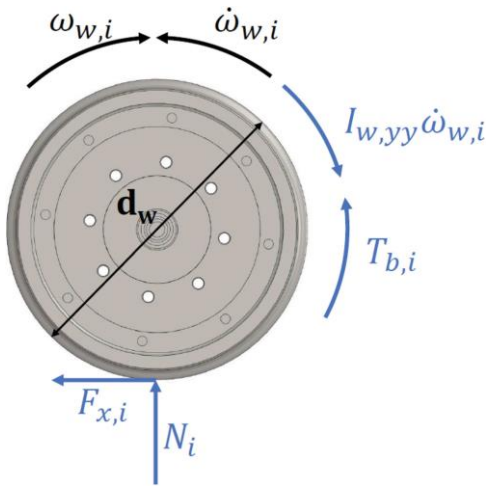

Figure 68: Forces on the braked wheelset [51].

$$F_{x,i} = \frac{T_{b,i} - I_{w,yy}\dot{\omega}_w}{r_w} \tag{3.55}$$

$$\mu_i = \frac{F_{x,i}}{N_i} \tag{3.56}$$

The tangential force F_x cannot be directly measured, however, it can be estimated if the parameters that appear in the right side of equation (3.55) are known. The wheel radius is approximately equal to 92 mm, while the wheelset inertia was estimated from a CAD model, and it is equal to 0.051 kg·m^2. The wheelset deceleration can be estimated with a numerical differentiation of the encoder speed signal, while the braking torque can be estimated from the signals of the S-beam cells installed on the braking system modules, which measure the tangential force between each brake disc-brake pad pair. Therefore, the total braking torque on wheelset i can be evaluated according to equation (3.57), where F_{tb} is the tangential braking force, measured by the S-beam cell, subscripts 1 and 2 refer to the bench side and r_b is the wheelset braking radius, which was properly calibrated on each wheelset during the bench setup, as shown in the following subsection. To apply the braking torque on each wheelset, four electro-pneumatic regulators are used, that allow to set the desired value of downstream pressure and provide the feedback (f\b) value. Finally, the normal load N on each wheelset can be estimated from the measurements of the two load button cells installed on the two axle-boxes of the wheelset i ($F_{s,i1}$ and $F_{s,i2}$), and from the knowledge of the wheelset mass m_w (15.16 kg according to the CAD model of the bench), as stated by equation (3.58).

$$T_{b,i} = (F_{tb,i1} + F_{tb,i2}) r_{b,i} \tag{3.57}$$

$$N_i = \max\{F_{s,i1}, F_{s,i2}\} + m_w g \cos \alpha_i \tag{3.58}$$

Obviously, before the beginning of the experimental campaign run on the new multi-axle roller-rig, the bench required a setup, including i) the calibration of the sensors installed on the bench, ii) the definition of a strategy for the connection of the sensors to the data acquisition boards and finally iii) the development of a bench control software for the management of the experiments.

3.5.2 Calibration of the sensors

As previously stated, among the activities performed in the context of the present thesis was the calibration of the sensors which are needed to estimate the adhesion and creepage coefficient on each wheelset. Precisely, at a first stage of the bench setup, the load-button cells and the electro-pneumatic valves were calibrated, and then the braking radius of each wheelset was estimated by means of an experimental test.

The load button cells used for the experimental activity described in this thesis came with a documentation including a calibration law obtained by the manufacturer (FUTEK) as well as the results of a shunt calibration. The shunt calibration allows to simulate a loading condition by applying a known resistor in parallel with one of the branches of the Wheatstone bridge. In fact, the shunt resistance unbalances the bridge, and an output voltage is produced, as if an external load was effectively applied. To verify the reliability of the shunt calibration data, a new shunt calibration was performed on all eight load button cells, and the results were in perfect agreement with the datasheet provided by the manufacturer, except for two cells. Therefore, these two cells were recalibrated with the experimental device shown in Figure 69, which relies on a working principle similar to the one adopted on the spring suspension system installed on each axle-box of the bench. The load button cell under test (1) is fixed to the head of a hex-head hollow threaded pin (2), which is tightened to a housing (3). Known masses (4) are placed on a cylindrical element (5), lying on the top of the housing (3). When the known weights (4) are applied, the pin (6) translates inside the hole of the threaded pin (2) and presses the load button cell (1), which then outputs the measured signal. Two series of tests were run. In the first series, 5 known masses of 1 kg were consecutively applied, and then they were removed one after another. In the second test series, first a known weight of 10 kg was placed on the cylindrical element, and then masses of 1 kg were consecutively placed on top. In the end, all masses were removed one after each other to unload the system. Figure 70 shows the value of the measured loads during the test for one cell, to better highlight the strategy for the execution of the two series of calibration tests. Therefore, the calibration line obtained for the two tested cells was recreated based on the results of the experimental tests and used for the signal acquisition.

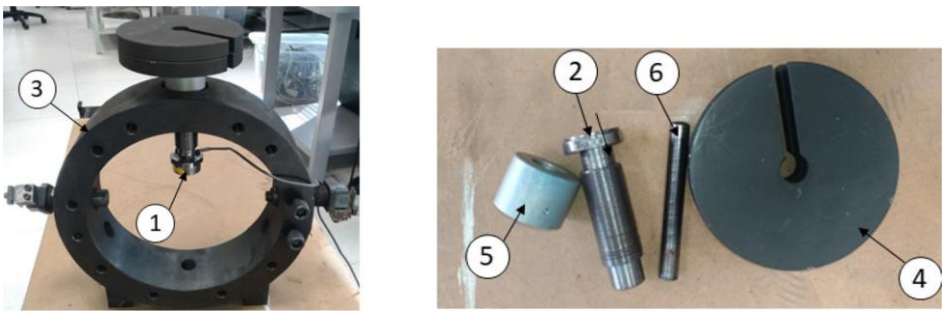

Figure 69: Experimental device for the calibration of the load button cells [115].

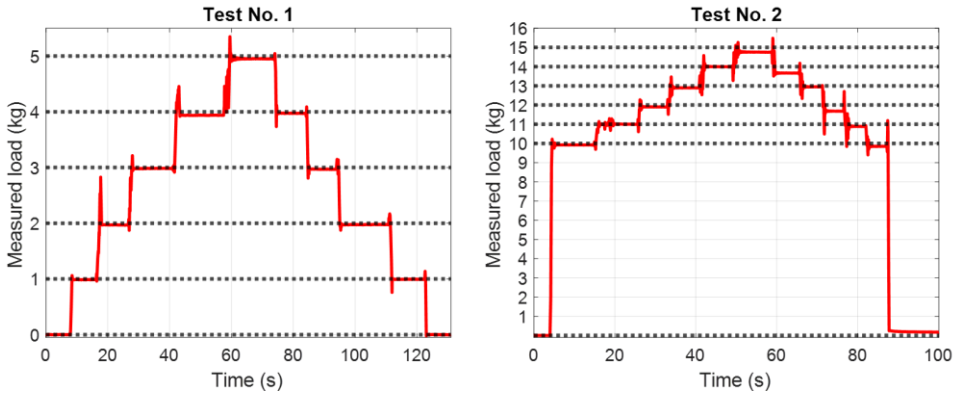

Figure 70: Time-history of recorded load during calibration of load button cells.

The four electro-pneumatic regulators installed on the bench allow to apply a braking pressure in the range 0.01-9 bar with a voltage command in the range 0-10 V, while the f\b value is provided with a voltage signal in the range 1-5 V. Therefore, the theoretical set and f\b calibration laws should be as stated by equation (3.59), where V is voltage, p is pressure, and subscripts set and f\b clearly refer to set and f\b values.

$$p_{set} = \frac{8.99}{10} \cdot V_{set} + 0.01, \qquad p_{f\backslash b} = \frac{8.99}{4} \cdot \left(V_{f\backslash b} - 1\right) + 0.01 \tag{3.59}$$

Nonetheless, to achieve a better accuracy of the experimental measurements, all four electro-pneumatic regulators were recalibrated, using the experimental device sketched in Figure 71. The tested valve (1) is supplied with compressed air flowing in the pneumatic plant of the laboratories of the research group, and the flow rate is adjusted by acting on the throttle (2), which is mounted upstream of valve (1) inlet. A known voltage set value is applied with an industrial PC (3) with a dedicated LabVIEW control code. The f\b voltage value is recorded in LabVIEW, while the pressure at the outlet of the tested valve is measured with a digital pressure switch (4), featuring a higher accuracy with respect to the electro-pneumatic regulators. Calibration tests were performed by increasing the set voltage in the range 0-10 V with steps of 0.5 V, and then voltage was gradually reduced from 10 V to 0 V, again with a step of 0.5 V. The calibration line for each valve was obtained using the least squares method to minimize the error between the experimental data and the predictions of the linear fitting function, by means of a dedicated MATLAB script. The calibration line was obtained considering the average value between the pressure values measured during loading (rising pressure) and unloading (decreasing pressure) stages of the calibration test. Figure

72 shows the experimental measurements and the theoretical and experimental calibration laws for one of the four valves, considering both the set and f\b lines. The theoretical and experimental calibration laws are clearly very close to each other, and similar results to the one plotted in Figure 72 were obtained on all four valves. Therefore, the pressure acquisitions with the new bench are performed considering the experimental characteristic law of each valve, while the set calibration lines of the valves are used to apply the desired braking pressure on each wheelset.

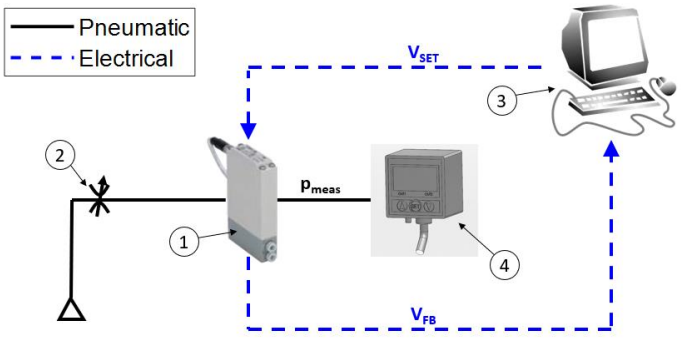

Figure 71: Experimental device for the calibration of the electro-pneumatic regulators [115].

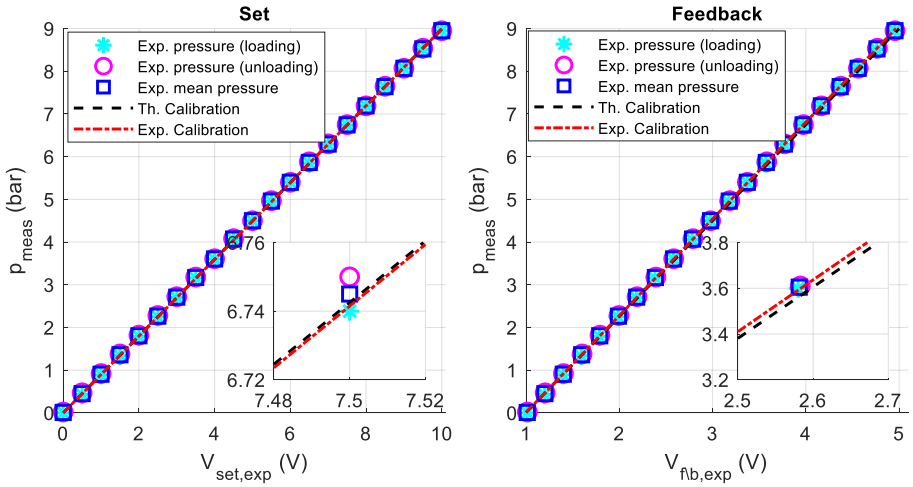

Figure 72: Results of the calibration of electro-pneumatic regulators.

Finally, because of the bench configuration, the braking torque is estimated starting from the measurement of the tangential load acting at each brake disc-

brake pad interface performed by the S-beam cells, as shown in the previous section. Therefore, to estimate the braking torque, the braking radius must be known, as stated by equation (3.57). The braking radius could be assumed equal to 75 mm for all brake pads starting from the CAD drawings of the bench, however, due to mounting errors and vibrations, and because of the high sensitivity of the estimated adhesion coefficient from this parameter, it was calibrated with a specifically designed experimental test, that allowed to obtain a specific value of braking radius for each wheelset. The test was carried out by setting reference values of applied pressure on the tested wheelset while keeping the rollers at a constant rotational speed. The applied braking pressure must ensure good adhesion conditions without generating a gross slip at the interface. In fact, when a braking pressure is set on a wheelset, the motor torque on the roller shaft must balance the inertia of the rollers and the resistant torque due to the wheelset. The latter can be considered as equal to the sum of two terms: a basic rolling resistance torque, only related to the rolling speed, and an additional resistant torque due to the application of the braking torque, which is a function of the braking pressure, see equation (3.60) and Figure 73. Please note that in equation (3.60) and Figure 73, ω_r is the roller speed, $\dot{\omega}_r$ is the roller rotational acceleration, T_M is the driving torque, T_R is the total resistant torque, $T_{R,0}$ is the basic rolling resistance torque, $T_{R,b}$ is the resistant torque due to the application of the braking pressure p_b and finally $I_{r,yy}$ is the rotational inertia of the roller shaft. Nonetheless, if good adhesion conditions still hold, a steady-state condition can be reached, and the inertial term in equation (3.60) can be neglected. The basic rolling resistance is equal to the motor torque produced when the rollers run at a constant speed without application of a braking torque on the wheelset, because in this condition the resistance torque $T_{R,b}$ is equal to 0. The driving torque can be read from the motor drive via the TCP\IP Mobdbus protocol. Since the resistant torque on the braking shaft is equal to the braking torque on the wheelset, multiplied by the wheel-roller transmission ratio, the braking radius r_b on wheelset i can be calculated according to equation (3.61).

$$T_M = T_R + I_{r,yy}\dot{\omega}_r = T_{R,0}(\omega_r) + T_{R,b}(p_b) + I_{r,yy}\dot{\omega}_r \tag{3.60}$$

$$r_{b,i} = \frac{T_M - T_{R,0}(\omega_r)}{\tau_{wr} \cdot \left(F_{tb,i1} + F_{tb,i2}\right)} \tag{3.61}$$

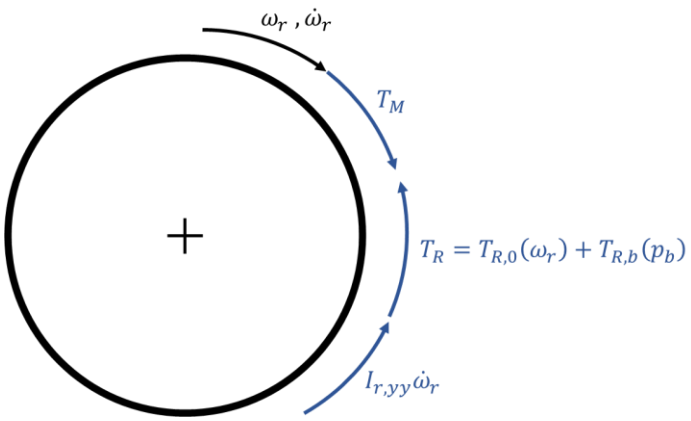

Figure 73: Free body diagram of rollers when braking a wheelset [115].

Therefore, calibration tests were carried out on each wheelset by setting the roller speed to 100 rpm and first determining the basic rolling resistance when no braking pressure is applied, considering a moving average of the driving torque with a time window of 20 s. Next, the braking radius was evaluated by setting the braking pressure to 1 and 1.5 bar, and then calculating moving averages of the motor torque and of the braking forces measured by the S-beam cells on the part of the signal corresponding to steady-state conditions. Finally, the effective braking radius on each wheelset was calculated as the mean value between the radii corresponding to the two tested braking pressures. Table 16 shows the value of braking radius, with standard deviation (Std. dev.) and coefficient of variance (CoV), for each wheelset.

Table 16: Calibration of the braking radius on each wheelset.

Wheelset No.	**Braking radius (mm)**	**Std. dev. (mm)**	**CoV**
1	81.90	2.08	2.54%
2	81.29	2.27	2.79%
3	79.73	2.01	2.52%
4	79.01	2.05	2.59%

3.5.3 Connection of the sensors

After performing the calibration of the sensors, the activities shown in the present thesis dealt with the determination of the strategy for the connection and communication among the sensors, the industrial PC managing the bench and the motor drive used to control the brushless motor powering the rollers. As already pointed out, the multi-axle roller-rig includes four incremental encoders, eight load button cells, eight S-beam cells and four electro-pneumatic valves. Furthermore, the motor speed and torque values can be adjusted and measured by establishing a communication with the motor drive. The strategy defined for wiring and connection of the sensors is briefly sketched in Figure 74, where the same symbols as in the previous sections are used. More in detail, F_s is the spring suspension force, measured by the load button cell, F_{tb} is the tangential braking force, measured by an S-beam cell, ω_w is the wheelset rotational speed, measured by an encoder, p_{set} and $p_{f\backslash b}$ are the set and feedback values of the applied braking pressure, managed by an electro-pneumatic valve, and finally subscripts i and j refer to wheelset number (1-4) and to the side of the bench (1-2). All signals coming from the sensors are acquired with a LabVIEW control software implemented in an industrial PC (NI PXIe-8840).

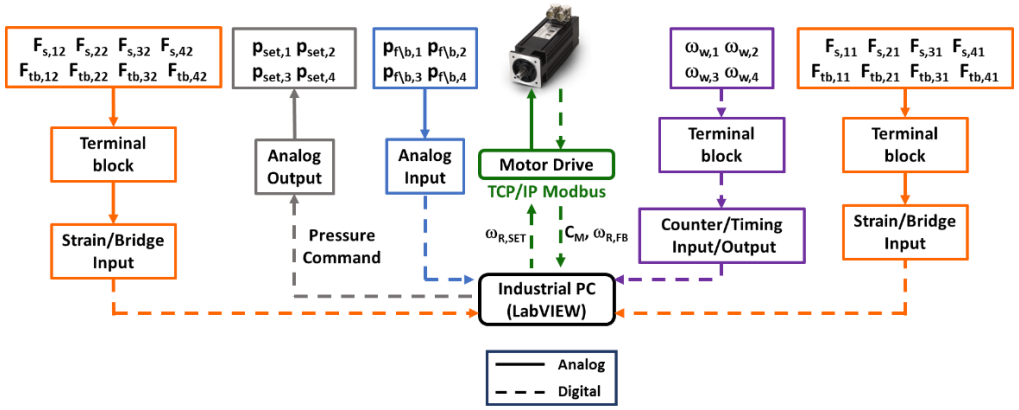

Figure 74: Cabling and connection strategy of the multi-axle roller-rig.

As noticeable from Figure 74, the signals coming from the eight S-beam load cells and from the eight load button cells are sent to two terminal blocks (NI TB-4330), connected to two strain/bridge input modules (NI PXIe-4330). Each terminal block receives the signals from the four load button cells and the four S-beam cells installed on the same side of the bench. In fact, each PXIe-4330 module is provided with eight channels for the acquisition of signals measured from strain gauge sensors. The voltage supply for each load cell is directly provided by the industrial PC through the data acquisition board.

Shifting focus to the four encoders, each sensor includes five wires, namely the positive and negative poles of the voltage supply and the three output counters (A, B and zero pulse), plus a shield. All wires of the four encoders are sent to a terminal block (NI SCB-68A), which is eventually connected with a 68-pin cable to a counter/timing input/output module (NI PXIe-6612). The digital input/output data acquisition board is provided with 40 PFI (programmable function interface) signals, that can work as input/output timing or digital signals. The 40 PFI signals can be arranged in order to obtain eight 32-bit counters, so that the data acquisition board can have eight channels for encoder acquisition. To reduce the electrical noise and to increase the accuracy of the acquisition, the NI PXIe-6612 module allows to set digital filters, which can be easily activated by the LabVIEW control software. The positive and negative poles of the voltage supply for each encoder are connected in parallel with two wires coming from a current generator, which is used to power all the encoders and the four electro-pneumatic regulators. Although the encoder manufacturer suggests keeping the shield cable as floating, the shields are connected to ground, as this connection experimentally proved to strongly reduce the electrical noise.

The four electro-pneumatic regulators require two different types of supply, namely an electrical and a pneumatic power supply. Compressed air is supplied to the valves thanks to the pneumatic plant installed in the laboratories of the research group, which includes a volumetric compressor able to produce compressed air up to a pressure of 10 bar. On the other hand, the electrical power supply is provided by the same current generator used to power the encoders. Since the encoders can be powered by a DC supply with voltage in the range 8-24 V and the nominal voltage for the valve DC power supply is 24 V, the current generator is set to provide an electrical DC power with a constant voltage of 24 V. The working principle of each valve is described in Figure 75, which is extracted from the datasheet of the device [116]. The electro-pneumatic regulator has three ports, connected to input chamber (SUP), output chamber (OUT) and open to atmosphere (EXH). The internal control circuit (4) allows to set a desired value of the output pressure as a voltage signal, and the f\b value is measured with the pressure sensor (3). If the f\b pressure is below the set value, the solenoid of the supply valve (1) is powered, so that air flows directly from the supply to the output port. On the other hand, if the output pressure is higher than the set value, the solenoid of the exhaust valve (2) is powered, and air flows from the output chamber to the atmosphere.

For installation on the new multi-axle roller-rig, the inlet port of each valve is connected to a pneumatic manifold, served by the volumetric compressor of the pneumatic plant, while the output chamber is connected to the two brake callipers installed on each wheelset. Focusing on the electrical connections, each valve has four wires, namely two wires for power supply (positive pole and ground), one wire for the set voltage and one wire for the f\b pressure signal. The four cables for the positive pole of the voltage supply are connected in parallel to a wire coming from the current generator, and a similar connection is performed for the four wires corresponding to the electrical ground. The desired pressure is set using a USB analog output module (NI USB-9263), which is able to manage four channels, while the feedback values are recorded using a four-channel USB analog input module (NI USB-9263).

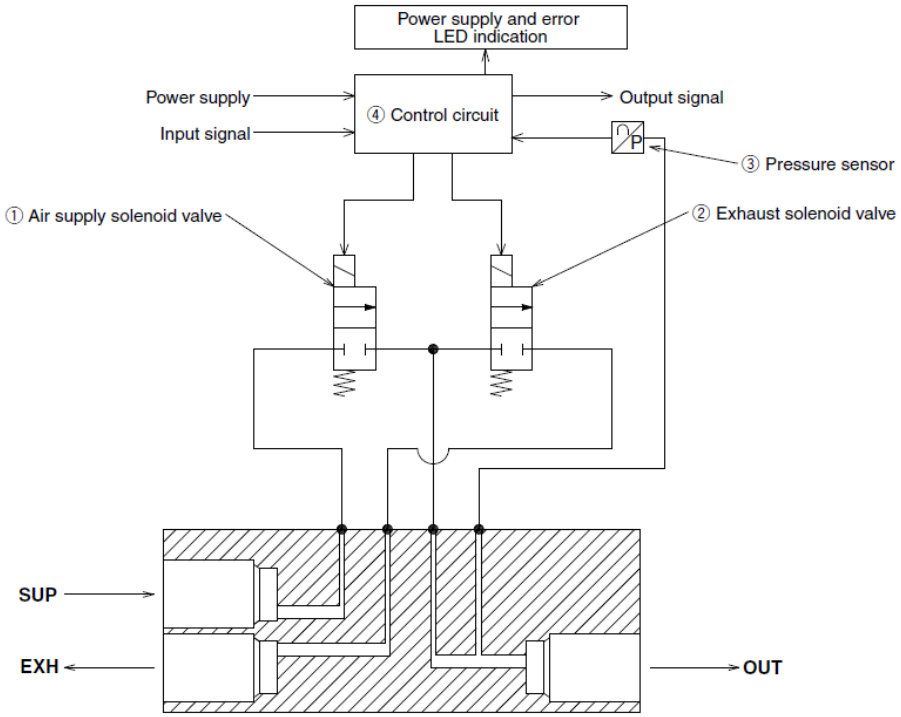

Figure 75: Working principle of the electro-pneumatic regulators [116].

Finally, the brushless motor installed on the roller shaft is managed using a NIDEC Unidrive SP4402. More in detail, two drives are installed in the drive cabinet of the laboratories of the research group, see Figure 76. Please note that Figure 76 shows the data transmission among the drives and the industrial PC, which will be described in the following lines. Drive 2 is used to control the

brushless motor of the new multi-axle roller-rig, while drive 1 was used in past activities to control the motor of the axle-box test bench installed in the laboratory of the research team. Each drive allows to perform read/write operations on the motor parameters of interest either via the CTSync software or manually using a SM-Keypad Plus. Data can be transmitted between the two drives thanks to a proprietary network communication (CTNet) developed by Control Techniques S.p.a. Each drive includes three slots for the installation of add-on modules. Drive 1 is provided with an Ethernet module and an Application Plus module, while drive 2 is provided with a Profibus module and an Application Plus module. The Application Plus module is widely used in the automation field, since it enables a faster update of the motor parameters, with variables featuring a larger number of bits compared to the default variables used by the drives.

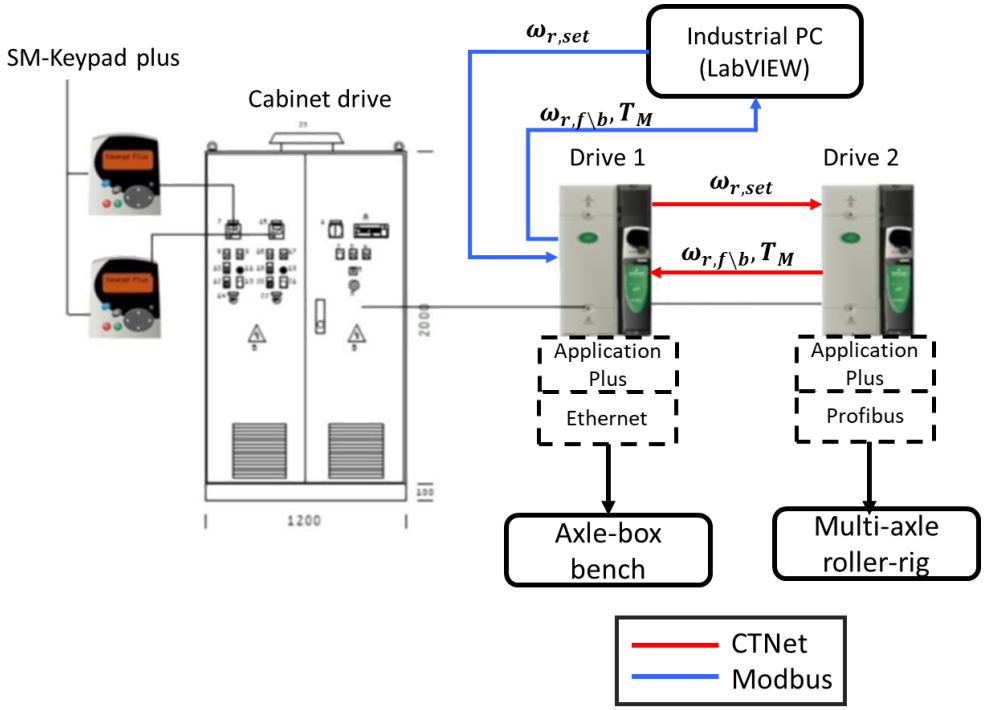

Figure 76: Data transmission among the motor drives and industrial PC.

In the experimental tests performed with the new multi-axle roller-rig, the roller motor is set servo mode, so that the motor can be controlled in either speed or torque modes, see Figure 77. The choice between speed and torque modes is made depending on the value of a variable that can be set by the user: when the variable is set to 0, the servo mode controls the motor with a speed reference, while when the value of the variable is set to 1, torque mode is activated. The

servo mode enables other control strategies, i.e., the variable for the control type selection can have values different from 0 or 1, however, in the tests performed with the new bench, only torque and speed reference signals were passed to the motor drive. When the speed control mode is activated, the drive receives a reference speed value, and a first PID controller (speed loop) calculates the reference torque that must be applied by the motor, compensating for the system inertia. On the other hand, if the torque mode is selected, the speed loop is bypassed, and the drive directly receives a torque reference value. Regardless of how the torque reference is obtained, the torque signal is then multiplied by a proportional gain to obtain a current reference signal, which is saturated and filtered by the motor drive. Finally, the motor current is calculated by a second PI control loop (current loop). In the preliminary experimental campaign performed with the new bench, both speed and torque control modes were tested. When the motor was controlled in torque, the reference torque was calculated with an external speed loop. Table 17 shows the values of the proportional, integral and derivative gains implemented in the control loops.

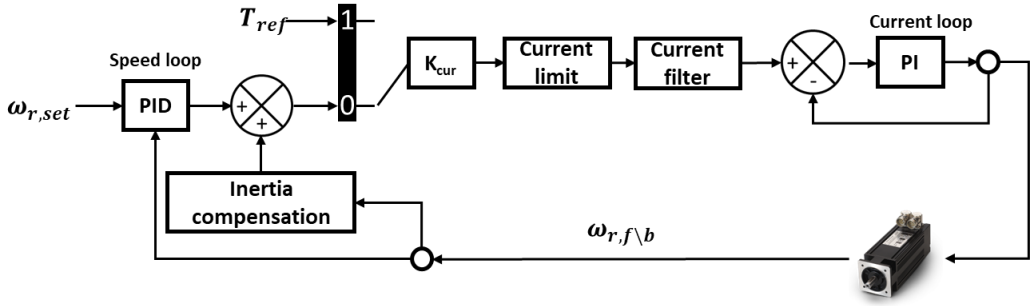

Figure 77: Servo mode control loop.

Table 17: Gains of the controller loops.

Gain*	Drive speed loop	External speed loop	Current loop
K_p	0.28	0.02	130
K_i	0.80	2e-5	225
K_d	0.04	1e-6	-

* Subscripts p, i and d refer to proportional, integral and derivative controller constants.

The gains of the drive speed loop and of the current loop were obtained with the default drive auto-tuning process. On the other hand, the gains of the external speed loop for the calculation of the reference torque were experimentally calibrated to ensure a good static accuracy without compromising the stability of the system. Regardless of the control mode, the reference signal must be transmitted from the industrial PC to the motor drive, and then the motor drive must send the values of feedback speed and torque to the industrial PC. The data transmission is managed using the strategy depicted in Figure 76. Since drive 1 of the drive cabinet includes an Ethernet module, data is transmitted between the industrial PC and drive 1 via the TCP/IP Modbus communication protocol, through dedicated libraries directly available in LabVIEW. Then, data is transferred between the two drives via the internal CTNet communication network. This strategy allows to control the software via an Ethernet protocol, even if drive 2 is not provided with an Ethernet module.

3.5.4 Data acquisition and processing

As previously stated, at the beginning of the activities described in this thesis, the bench control software and the routines for the analysis of the experimental data had to be conceived from scratch. The strategy that is currently adopted to control the bench, perform the experimental tests, acquire data from the sensors and compute the values of the adhesion and creepage coefficients was defined as the results of an intensive trail-and-error procedure. The paragraphs below describe in detail the final strategy, which can be considered a major contribution of the present thesis. To optimize the efficiency of the data acquisition, the bench control software now performs a limited number of data processing operations, thus demanding the post-processing operations to an external MATLAB routine.

Data acquisition and bench control operations are managed with a dedicated control software implemented in LabVIEW. Since the braking torque on the wheelsets is not obtained by means of a motor, but it is applied using the air brake system, the new multi-axle roller-rig allows to perform transient tests rather than to achieve steady-state creepage conditions. This feature makes the bench suitable for the simulation of real transient braking operations of railway vehicles. Nonetheless, as the experimental tests simulate transient conditions, the wheelsets tend to achieve locking conditions very quickly after exiting the linear stable part of the adhesion characteristic. Therefore, for an accurate measurement of the adhesion coefficient even in the nonlinear part of the adhesion curve, a large sampling rate is required. For this reason, the LabVIEW control software was developed paying great attention to the efficiency of the acquisition, in order to maximize the sampling rate. During the experimental campaign performed within the frame of the present thesis, the LabVIEW control software has been upgraded several times to increase the sampling rate and to achieve the highest stability of the acquisition. The final version of the newly built LabVIEW code only performs data acquisition and saving functions, with plotting and data processing operations kept to a minimum. In fact, these additional operations tend to drastically decrease the performances of the acquisition. For this reason, the LabVIEW control software only calculates and plots quantities that allow to promptly evaluate the safety of the bench operations, and most of the data processing operations are demanded to an external MATLAB routine. The MALAB post-processing routine loads the text files saved during the acquisition and processes data to calculate the creepage and adhesion coefficients.

The flow chart implemented in the final version of the multi-axle roller-rig LabVIEW control software is sketched in Figure 78. The routine comprises three major while loops:

1. *Loop 1*. Data acquisition from sensors and control of the roller brushless motor, with establishment of the connection with the motor drive through the TCP\IP Modbus communication protocol, by means of LabVIEW built-in blocks. Through this connection, the user can set the desired motor speed and control mode (speed or torque modes can be selected) and then the corresponding speed and torque feedback values are received. The signals coming from all the encoders and the S-beam and load button cells, as well as the pressure f\b values provided by the electro-pneumatic regulators, are acquired and filled in queues based on a *first-in-first-out* (FIFO) logic.

2. *Loop 2*. Application of desired pressure signal on each wheelset and estimation of creepage. Depending on the type of test to be performed, the pressure signal can be generated from a manual input, or it can be calculated as a function of the estimated creepage. The calculation of creepage directly within the LabVIEW control software allows to promptly detect locking conditions of the wheel and to immediately release the braking pressure, to avoid a catastrophic wear of the wheel surfaces.
3. *Loop 3*. Data dequeuing and writing on a text file storing the signals acquired during the experimental tests.

The definition of separated loops performing different tasks is essential to ensure that the acquisition loop can read data at the desired sampling rate, with no other additional operations that could act as a bottleneck of the whole acquisition. Furthermore, using queues is crucial to transfer data from the data acquisition loop (loop 1) to the data storage loop (loop 3), and to ensure that there is no missing data in the final text file.

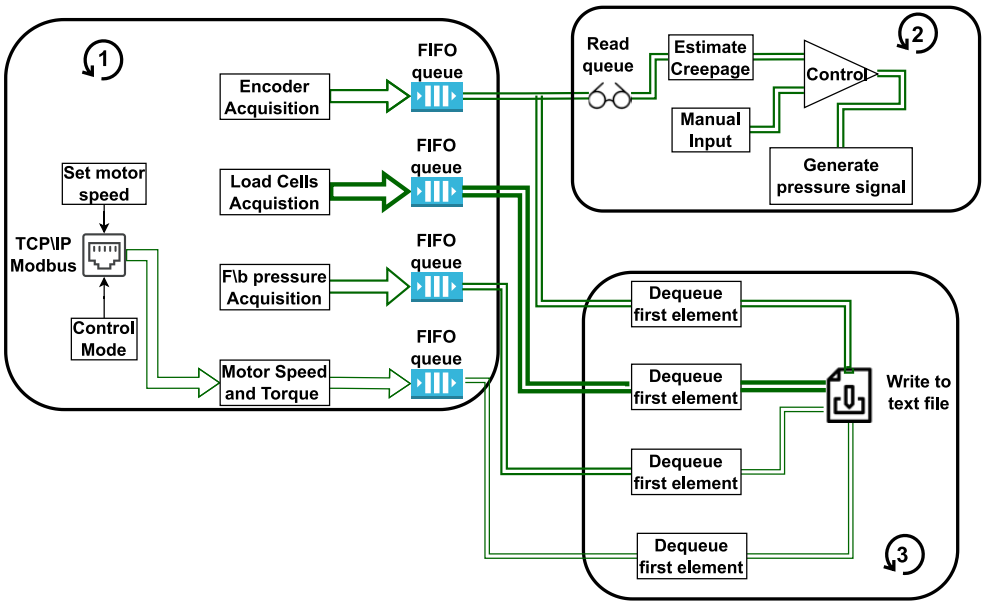

Figure 78: Flow chart of the LabVIEW data acquisition and bench control software (thicker lines refer to a larger number of elements) [51].

The current upgraded version of the LabVIEW control software allows to store data at a rate of 1 kHz, except for the motor torque and speed f\b values, which are read at a rate of 250 Hz, as the transfer rate between the motor drive and the industrial PC is limited by the communication via the TCP\IP Modbus

protocol. Nonetheless, the sampling rate is independently adjusted for each sensor, and it can differ from the rate of 1 kHz used to store data. In fact, the LabVIEW control software sets the sampling mode of each sensor to *continuous sampling* mode. This option means that when the acquisition is initiated, all sensors start to acquire data continuously at a defined rate, and data is stored in a temporary buffer. The buffers are then read in the LabVIEW control software and treated as a LabVIEW *waveform* datatype. The waveform datatype can be regarded as a special structure with three fields, namely i) a numerical array storing the values of the acquired signal, ii) a timestamp defining the beginning of the signal acquisition and iii) a numerical variable defining the time spacing between consecutive values in the numerical array. The length of each buffer can be independently set for each data acquisition board. To acquire all signals within the same loop, it is essential that the time required to fill the buffer is the same for all data acquisition boards. The time required to fill the buffer t_b is related to the sensor sampling frequency f_s and the buffer length s_b, as stated by equation (3.62).

$$t_b = \frac{s_b}{f_s} \tag{3.62}$$

Therefore, the acquisition of each sensor was carefully adjusted in terms of sampling frequency and buffer size to ensure that the buffer filling time is the same for all data acquisition boards and as close as possible to the time required to run the data acquisition loop (loop 1). In fact, the execution time for loop 1 is limited by the TCP\IP Modbus communication between the control software and the motor drive, which was experimentally evaluated equal to 4 ms. The sampling frequency and the buffer size set for each sensor is given in Table 18, which highlights that the buffer filling time is the same for all sensors.

Table 18: Buffer length and sampling rate for all sensors.

Sensor	Sampling rate (kHz)	Buffer length	Filling time (ms)
Encoder	100	400	4
Load button cell	1	4	4
S-beam cell	1	4	4
Electro-pneumatic valve	2	8	4

As noticeable from Table 18, the sampling rate of the encoders is quite higher compared to the sampling time of the other sensors. In fact, the NI PXIe-6612 digital input/output module allows to perform a continuous sampling only according to three internal clocks that generate a time base for the acquisition (100 MHz, 20 MHz and 100 kHz) unless an external clock signal is produced. Therefore, to acquire data using one of the clocks available on the digital input/output module, the lowest frequency of 100 kHz was selected. Nonetheless, since the encoder data acquisition is set in the LabVIEW control software to automatically output the angular position of the wheelset, it is clear that storing the encoder signal at a rate of 100 kHz would produce huge output files. Therefore, in the data storage loop (loop 3), most of the elements in the encoder buffer are discarded, so that data is saved at a rate of 1 kHz. The same operation is performed on the elements stored in the queue filled by the acquisition of the electro-pneumatic regulators, which sample data at a rate of 2 kHz. To improve the acquisition of the encoder signals, the LabVIEW control software applies digital filters on the encoder counters, chosen among the ones available in the NI PXIe-6612 board. More in detail, a 5.12 μs digital filter with 100 MHz clock is applied to counters A and B: this means that a high signal passes only if at least 512 rising edges of the clock are recorded and if the pulse width of the counter is larger than 5.12 μs. For the zero pulse counter, a 2.56 ms digital filter with 100 kHz clock is selected, so that a high signal is passed only if the pulse lasts for more than 2.56 ms and more than 256 rising edges of the reference clock are recorded.

The bench control algorithm is implemented in loop 2 of the LabVIEW control software. The control algorithm allows to independently adjust the braking pressure on each wheelset. Basically, the control algorithm allows to perform the three kinds of test sketched in Figure 79 and listed below:

- *Adhesion curve test*. This kind of test simply allows to obtain an adhesion curve, by braking one or more wheelsets with an increasing pressure ramp, see Figure 79(a) and(d). A quick release signal is applied if locking conditions are detected. The test can be performed under different contamination conditions at the interface.
- *Wheel adhesion recovery test*. This kind of test is performed to obtain adhesion loops, i.e., adhesion characteristics including a "forward" and a "backwards" curve, which correspond to increasing and decreasing creepage values, respectively. The test is carried out by first applying an increasing pressure ramp, thus increasing the wheel-roller creepage, and then applying a decreasing pressure ramp after a limit creepage value is detected, see Figure 79(b) and (d). The two ramps have the same gradient. The test can be performed both in dry and degraded conditions.
- *Rail adhesion recovery test*. This kind of test is performed to investigate the improvement of adhesion as a result of the cleaning action performed by the front wheelsets. The test is run by setting a constant braking pressure on all wheelsets, and then contaminating the roller surface, see Figure 79(c) and (d). The initial braking pressure must be low enough to ensure a good adhesion level under uncontaminated conditions.

The adhesion curve test and the rail adhesion recovery test are performed with an open loop control because the reference pressure is not calculated automatically from other quantities recorded on the bench. On the other hand, the wheel adhesion recovery test is performed with an automatically adjusted pressure signal, because the pressure ramp to be applied depends on the limit creepage value. In fact, when a limit creepage value is detected, the increasing pressure ramp signal is removed, and a decreasing ramp is applied. The selection of the test to be run is performed by means of Boolean variables that are available to the user in the GUI of the LabVIEW control software in the form of virtual buttons. To maximize the safety of operations, the motor can be stopped, and the pressure can be released at any moment in case of danger detection.

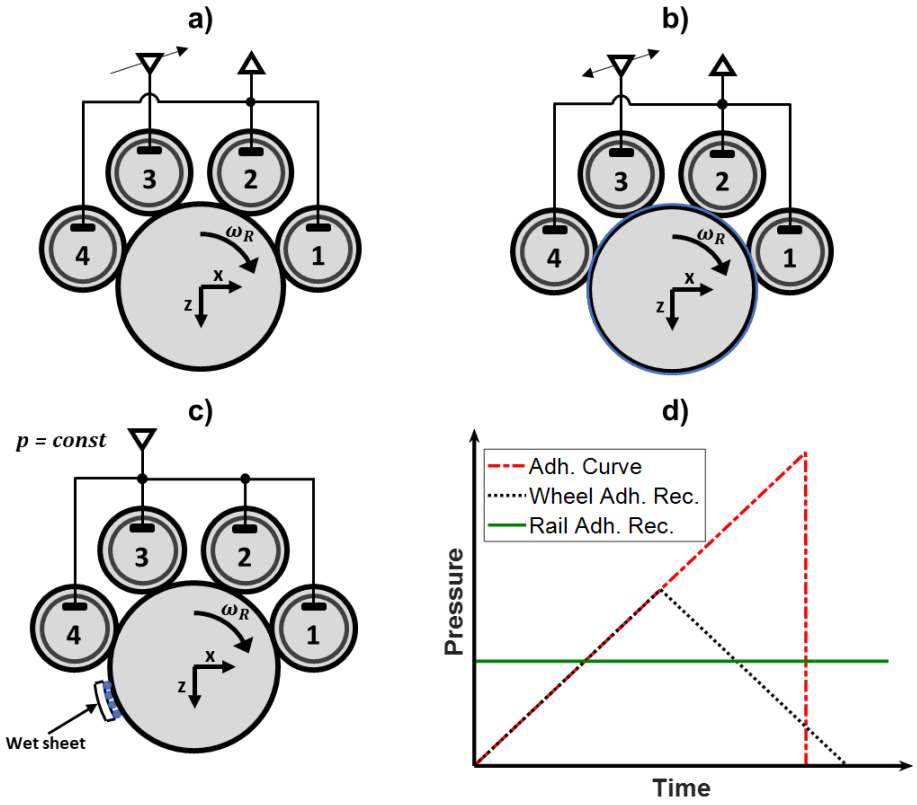

Figure 79: (a)-(c) Tests that can be performed on the new bench and (d) pressure signal in the three tests. More in detail: (a) adhesion curve test, (b) wheel adhesion recovery test, (c) rail adhesion recovery test.

Regardless of the specific test selected by the user, the LabVIEW control software outputs a text file in *.lvm* extension after each run, storing the data collected by the sensors installed on the bench. More in detail, the output text file includes 22 main channels:

- 4 channels storing the angular position of each wheelset, measured by the encoders.
- 8 channels storing the normal force measured by each load button cell.
- 8 channels storing the braking force measured by each S-beam cell.
- 4 channels storing the braking pressure f\b value recorded by each electro-pneumatic regulator.
- 2 channels storing the f\b values of motor speed and torque, respectively.

The output text file is loaded by a dedicated MATLAB script performing the main post-processing operations required for the calculation of creepage and

adhesion coefficient on each wheelset. Just like the LabVIEW bench control software, the MATLAB routine used to post-process the raw data acquired form the sensors was fully developed in the frame of the present thesis. Because of the large size of the output data, the MATLAB routine uses vectorization strategies to speed up the calculation on the loaded data, which is saved in the form of MATLAB matrixes. The first operation performed by the MATLAB post-processing routine is the synchronization of the signals coming from the four data acquisition boards installed on the bench. This can be easily done because the measurements of the sensors are treated in the LabVIEW control software as waveforms, which include a timestamp corresponding to the time when the acquisition is started by each data acquisition board. This information is stored in the output text file, so that a unique time vector can be defined in MATLAB, and the measurements are perfectly synchronized. Since the encoders measure the angular position of the wheelsets, the MATLAB routine also performs the calculation of the angular speed of each wheelset, by means of simple numerical differentiations. Nonetheless, to reduce the numerical noise in the differentiated signal, the angular position signal is smoothed with a combination of a low-pass filter and a moving average before differentiation. The adopted low-pass filter is a 4^{th} order Butterworth filter with cut-off frequency of 450 Hz, while the moving average filter spans a window of 52 ms. Figure 80 shows the speed signals calculated from the original (unfiltered) and smoothed angular position signals on a preliminary adhesion curve test performed on the new bench. The differentiation of the original signal produces a *discrete* speed signal because the encoder measurement is a discrete measurement, obtained by counting the rising and falling edges of the digital counters. Therefore, the filtering of the angular position signal is crucial to obtain a differentiated speed signal able to properly reproduce the dynamics of the braked wheelset during the test. Next, the acceleration of the wheelsets is calculated with a numerical differentiation of the speed signal and smoothed with a moving average calculated on a window of 15 ms. Since the encoder speed is stored at a rate of 1 kHz, while the roller motor speed provided via the Modbus protocol is available at a lower rate of 250 Hz, the latter signal is re-interpolated with a sampling frequency of 1 kHz. The re-interpolation is performed by means of a piecewise-cubic (spline) function, which interpolates the roller speed signal smoothed with a moving average featuring a window of 16 ms. A good agreement between the original and re-interpolated signals on a preliminary test performed on the bench can be observed in Figure 81. The zoomed view shows that the re-interpolated signal includes more points compared to the original one. At this point, the MATLAB routine is able to easily calculate

the creepage value on each wheelset, by applying equation (3.54) starting from the computed speed signals for both wheelsets and rollers. Please note that Figures 80 and 81 highlight the strategy adopted to run the adhesion curve tests on the multi-axle roller-rig. At the beginning of the test, the roller speed is increased from standstill to the desired value (200 rpm in the preliminary test shown in Figures 80 and 81). After reaching steady-state conditions, the braking pressure ramp is applied until full locking of the braked wheelset is detected, and the quick release signal is applied, so that the braked wheelset immediately recovers adhesion, and the test is stopped. Because of the robust control of the roller motor, the roller speed is approximately constant even during the application of the braking pressure on the wheelset.

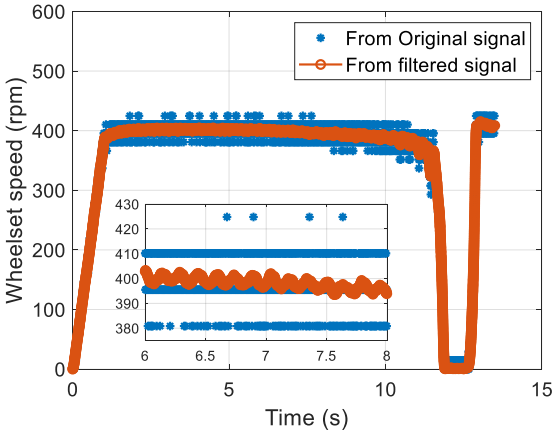

Figure 80: Wheelset speed calculated from encoder signals.

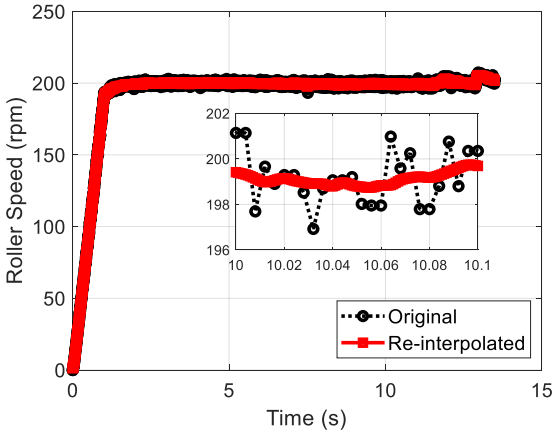

Figure 81: Re-interpolation of roller speed.

The MATLAB routine also processes data coming from the load button and S-beam cells. At the beginning of each test, the applied braking pressure is zero on all wheelset, so the signals coming from the S-beam cells should be equal to zero. Therefore, to obtain reliable outputs, the MATLAB routine offsets the measurements of the S-beam cells to ensure that the braking force on each brake disc-brake pad is zero when no braking torque is applied. Moreover, the signals of both the load button and S-beam cells are filtered with the same low-pass filter applied to the encoder signals and smoothed with a moving average featuring a window length of 21 ms. Finally, using the filtered data, the adhesion coefficient can be calculated by applying equations (3.55)-(3.58). The MATLAB routine calculates the adhesion coefficient by compensating for the inertia of the braked wheelset. In fact, as mentioned above, because of its configuration, the multi-axle roller-rig simulates transient braking operations instead of obtaining steady-state creepage conditions. Therefore, during the adhesion curve tests, the wheelset speed is not constant, but it decreases as the applied braking pressure increases. The wheelset inertia is not negligible, so the deceleration of the wheelset must be evaluated to obtain an accurate value of the adhesion coefficient. Figure 82 shows the influence of considering inertia on the adhesion curve. When the wheelset inertia is neglected, the adhesion coefficient in the nonlinear part of the adhesion curve is overestimated, as stated by equations (3.55) and (3.56). In fact, if the wheelset deceleration is not compensated for, the value of the wheel-rail tangential contact force becomes larger. The adhesion curves obtained when considering and neglecting inertia are similar only in the linear part of the characteristic. In fact, in the stable region of the adhesion curve, most of the contact patch is in the adhesion zone, so that from a macroscopic perspective, the peripheral speed of rollers and braked wheelset is the same, and it features an approximately constant value. On the other hand, when gross slip is generated at the contact interface, the peripheral speed of the wheelset becomes lower than the roller peripheral speed, and a larger deviation between the two curves plotted in Figure 82 can be observed.

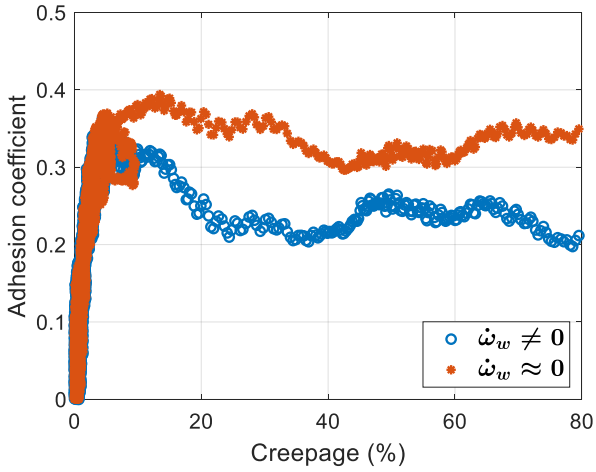

Figure 82: Effect of wheelset inertia on the estimation of the adhesion coefficient [51].

3.5.5 Results of adhesion tests

After the setup of the new multi-axle roller-rig, preliminary tests were performed to experimentally assess the reliability of the new bench in the investigation of degraded adhesion conditions. First, simple adhesion curve tests were carried out to verify the repeatability of the experimental results collected with the bench. The adhesion recovery tests are run by braking one or more wheelsets with an increasing pressure ramp, so it was necessary to verify that the adhesion curves are not affected by the ramp gradient. A preliminary test was run by applying a braking pressure on wheelset 1 of the bench for different values of the braking pressure ramp gradient. Precisely, three values of gradient were considered, equal to 0.96 bar/s, 1.92 bar/s and 0.48 bar/s, see the inner plot in Figure 83. Figure 83 shows that the adhesion curves obtained with the three ramps are very similar to each other, so the adhesion coefficient obtained on the bench can be considered as independent from the ramp chosen to carry out the test. The first ramp with gradient of 0.96 bar/s was selected as the reference ramp for the adhesion curve tests, since it ensures a good compromise between execution time and capability of acquiring the measurements of the sensors. In fact, very fast ramps would immediately lead to wheel locking conditions, thus requiring higher sampling rates in the LabVIEW bench control software, even for the estimation of the adhesion coefficient in the linear part of the adhesion curve. On the other hand, with slow ramps, the test time would become high, with a risk of thermal drift at the wheel-roller contact interface, which would make difficult to correctly understand the output results.

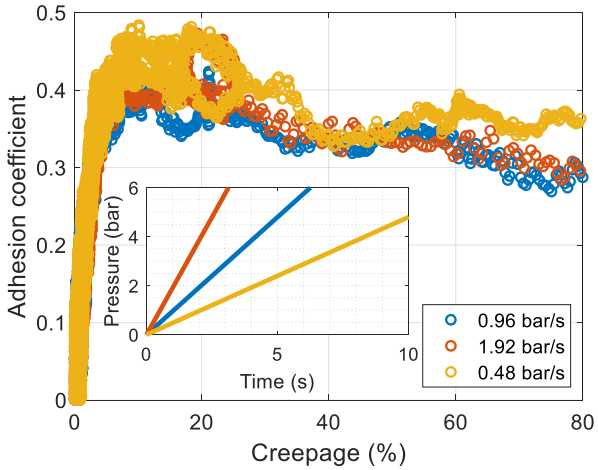

Figure 83: Effect of pressure ramp gradient on the measured adhesion curve.

As shown in §3.5.3, the roller brushless motor is set to servo mode, which allows to control the motor in either torque or speed modes, depending on the value of a Boolean variable which is transferred from the LabVIEW control software to the motor drive via the TCP\IP Modbus protocol. To assess the influence of the control mode on the estimated adhesion coefficient, an adhesion curve test was performed by braking one wheelset at a time while keeping the rollers shaft at a constant speed. Figure 84 shows the adhesion curves obtained with the two control modes on wheelset 4, with the rollers rotating at a speed of 200 rpm, which corresponds to a real vehicle speed of approximately 30 km/h. A good agreement between the two adhesion curves corresponding to the two control modes can be noticed. Since the torque control mode proved to be more robust during the preliminary experimental tests, it was selected to run all subsequent tests.

Finally, adhesion curve tests were performed by braking all four wheelsets at the same time, and similar adhesion curves were recorded, as shown in Figure 85, thus confirming that the bench ensures a good repeatability on all four wheelsets. The slight differences in the maximum adhesion coefficient on the four wheelsets can be related to a non uniform value of the applied normal load and to slight differences in the adhesion conditions at the contact interface that may be due to the generation of small wear debris in previous tests. In conclusion, the preliminary adhesion curve tests proved that the bench configuration allows to obtain reliable and repeatable adhesion data.

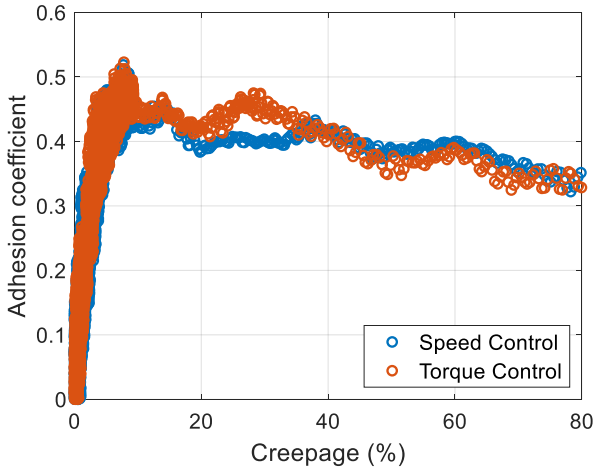

Figure 84: Effect of motor control mode on the measured adhesion curve [51].

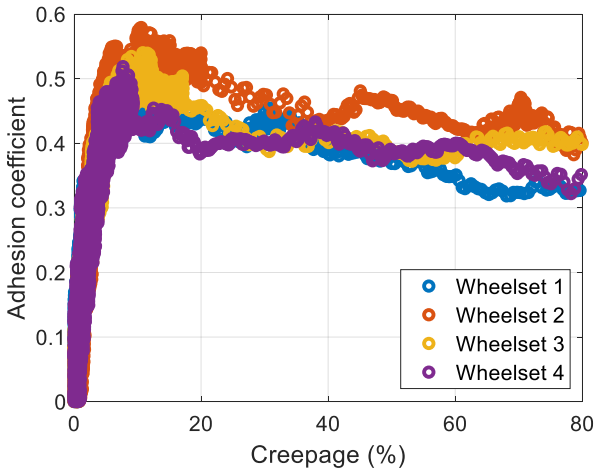

Figure 85: Repeatability of adhesion curves obtained on the four wheelsets.

After assessing the accuracy and the repeatability of the new bench in the execution of the basic adhesion curve tests, wheel adhesion recovery tests were run, to investigate the adhesion improvement on a single wheelset due to the work of the friction forces in the unstable region of the adhesion curve. These tests were run by applying the braking pressure ramp only on wheelset 3 of the bench, while leaving the other wheelsets as unbraked. This strategy allows to relate the adhesion recovery only to the sliding forces generated between wheelsets 3 and the rollers, because the other wheelsets are in good adhesion conditions. Therefore, a big point of merit of the configuration of the new bench is that it allows to easily simulate the pure wheel adhesion recovery phenomenon, even if

all four wheelsets roll over the same pair of rollers. To investigate in detail the wheel adhesion recovery phenomenon, an experimental campaign was planned to consider different values of the roller speed as well as both dry and wet conditions. To simulate wet conditions, the roller surface was contaminated with wet sheets before the beginning of the tests.

Figure 86 and Figure 87 show the results for three values of roller speed in dry and wet conditions, respectively, for a normal load adjusted to simulate an axle-load of 10 tonnes on a real vehicle. The tested roller speeds of 100, 200 and 300 rpm roughly correspond to real vehicle speeds of 15, 30 and 45 km/h. Relatively low values of speed and axle-load were selected to limit the wear of the profiles of wheels and rollers when gross slip conditions are achieved. In each plot shown in the two figures, two adhesion curves can be observed, which are referred to as *forward* (FW) and *backwards* (BW) curves. The former is the adhesion curve recorded with an increasing pressure ramp, i.e., with an increasing creepage at the contact interface, while the latter is the adhesion curve corresponding to the decreasing pressure ramp, which is applied to reduce creepage.

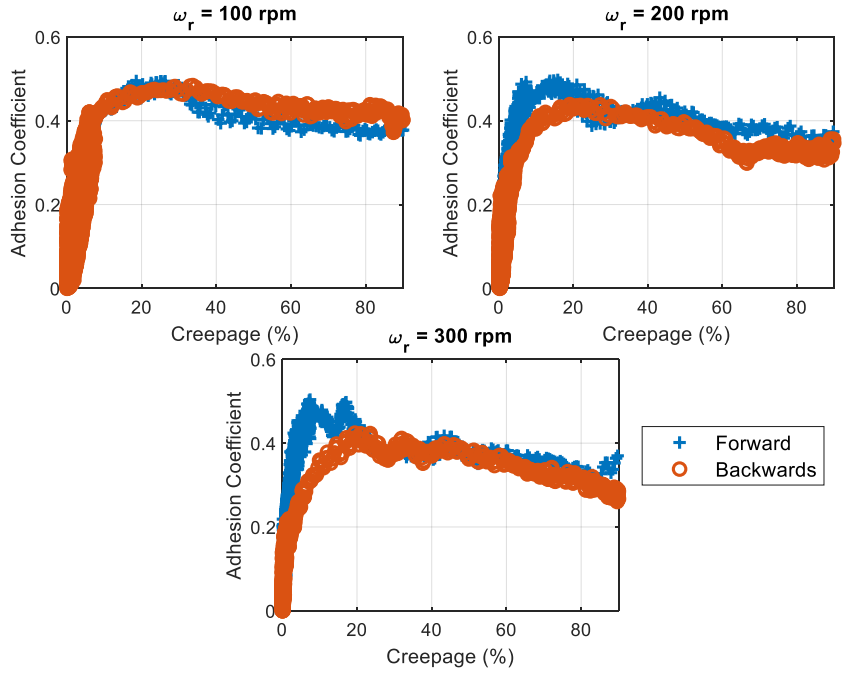

Figure 86: Results of wheel adhesion recovery tests for dry conditions.

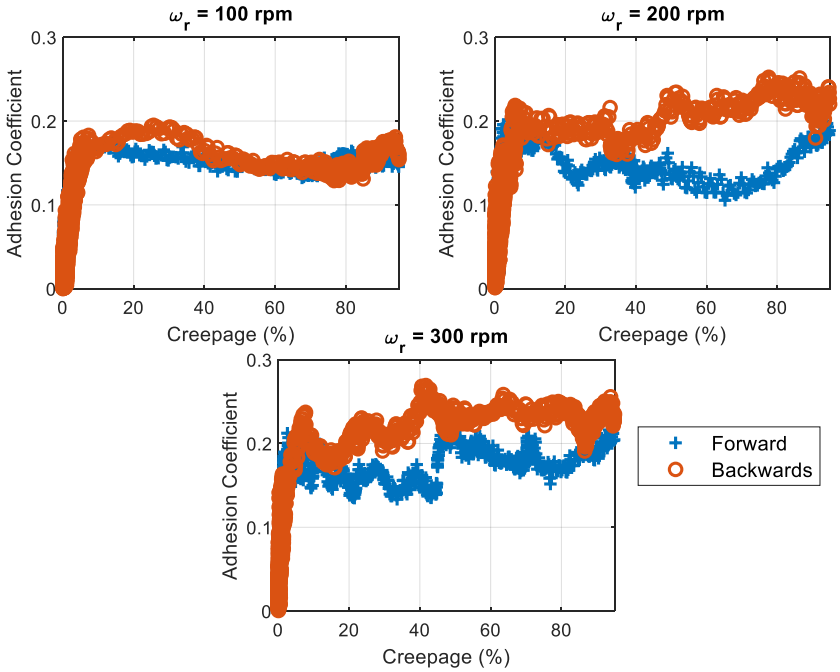

Figure 87: Results of wheel adhesion recovery tests for wet conditions.

A first comparison between Figure 86 and Figure 87 highlights that the adhesion coefficient recorded at the transition point between the linear and nonlinear parts of the FW adhesion curves drops from a value in the range 0.44-0.5 to a value between 0.18 and 0.22 when the surface conditions change from dry to wet. In fact, the major effect of a water contamination is a reduction of the available friction. Nonetheless, the most interesting phenomenon that can be observed by comparing the two figures is related to the adhesion improvement that can be observed in the two cases. For dry conditions, see Figure 86, the FW and BW curves roughly overlap in both the linear and nonlinear regions of the adhesion characteristics, with deviations limited to the transition zone between the two regions. However, for all three values of roller speed, there is no noticeable adhesion recovery when the decreasing pressure ramp is applied. This is in line with the expectations, as in dry conditions there is no contaminant layer to be removed, except for possible very small wear debris. On the other hand, when the wheel-roller interface is wet, see Figure 87, an adhesion recovery can be noticed for all roller speed values, and a hysteresis loop in the adhesion curves is clearly observed, as the BW curve is always above the FW curve in the nonlinear region. In fact, in wet contamination, a water layer is present at the wheel-roller contact interface, which is partially removed when gross slip conditions are achieved, due

to the energy dissipated at the contact patch. The experimental tests carried out in wet conditions clearly suggested that the shape of the adhesion recovery hysteresis loop is strongly dependent on the roller speed. In fact, in the test run at 100 rpm, the hysteresis loop is slender, and the adhesion improvement in the BW curve is limited. On the other hand, when the roller speed is equal to 200 rpm, the hysteresis loop becomes wider. An interesting phenomenon was observed in the test run with the roller speed set to 300 rpm, see the lower plot in Figure 87. In fact, in this test, an abrupt adhesion improvement was recorded in the FW curve at a creepage value of approximately 45%, thus suggesting that a sufficiently large amount of energy was dissipated to remove a noticeable portion of the contaminant. Nonetheless, the adhesion coefficient value did not get back to values close to the ones observed in dry conditions. The dependency of the hysteresis loop shape on the roller speed can be related to the amount of dissipated power at the contact interface. In fact, for a fixed value of creepage, if the roller speed increases, the sliding speed increases, too, and a larger amount of power is dissipated at the contact. Furthermore, with higher roller speeds and consequent larger dissipated power, the contact temperature is expected to rise, and this may give an additional contribution to the removal of the contaminant layer. Nonetheless, temperature data were not recorded on the bench, as the initial configuration of the bench did not include temperature sensors. In future works, the bench could be provided with laser temperature sensors to estimate the temperature at the contact interface and to correlate this quantity to the adhesion improvement.

To quantitatively analyse the adhesion improvement recorded in wet conditions, a fitting operation was carried out on the FW and BW adhesion curves recorded for the three values of tested roller speed, to identify the values of the parameters of Polach's model for degraded adhesion, see equations (3.29)-(3.31). The Polach's model was selected as some of the innovative models that tried to consider the effects of adhesion recovery surveyed in §3.4.3 were developed starting from Polach's equations. The fitting operation was implemented in a dedicated MATLAB routine developed in the frame of the present thesis. The MATLAB routine relies on MATLAB built-in functions with the aim to minimize the sum of squared errors (SSE) between the experimental measurements and model predictions, see equation (3.63), where $F_{x,exp}$ and $F_{x,model}$ are the experimental and model values of the tangential contact forces, n_{meas} is the number of experimental observations and k is the summation counter. The minimization was carried out using the default interior-point algorithm [117], and

further details about the implementation of the fitting routine can be found in [118].

$$SSE = \sum_{k=1}^{n_{meas}} \left(F_{x,exp,k} - F_{x,model,k}\right)^2 \tag{3.63}$$

The results of the fitting operation are shown in Figure 88, where each plot includes the experimental values of adhesion coefficient for FW and BW curves, the theoretical adhesion curve for wet conditions according to Polach, and the fitting curves for FW and BW characteristics. Please note that the FW curve obtained in the test run with the roller speed set to 300 rpm was fitted only for creepage values below 42%, because the Polach's model is not able to account for the abrupt adhesion recovery observed in the test. The values of the Polach's coefficients for the fitting curves are given in Table 19.

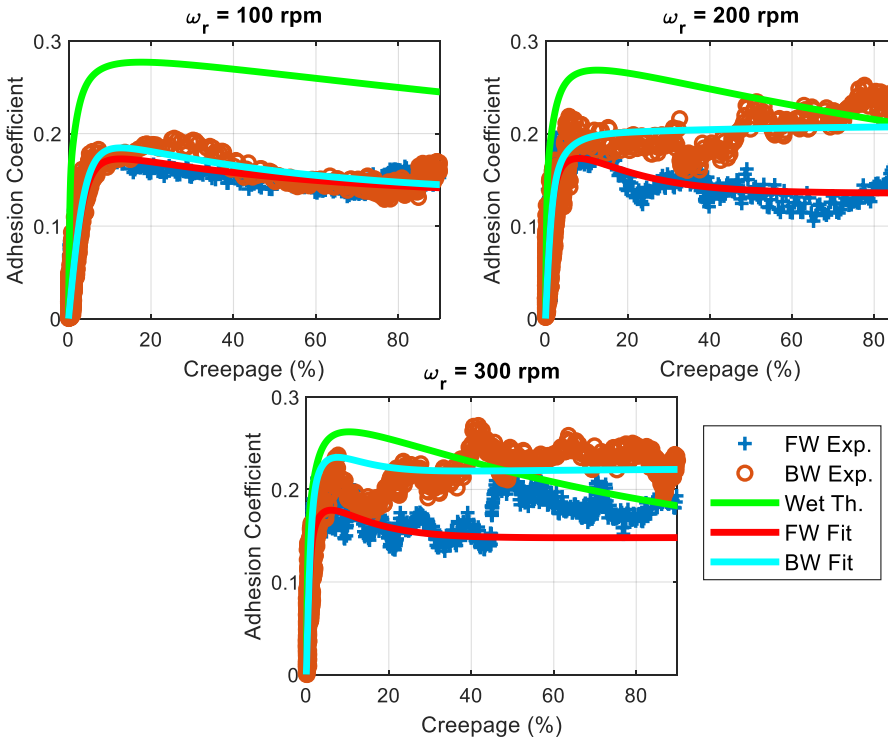

Figure 88: Fitting of adhesion curves with Polach's model.

Table 19: Parameters of Polach's model obtained from fitting operation.

Parameter	100 rpm		200 rpm		300 rpm	
	FW	**BW**	**FW**	**BW**	**FW**	**BW**
k_A	0.02	0.02	0.05	0.05	0.09	0.09
k_S	0.02	0.02	0.03	0.03	0.05	0.05
f_s	0.19	0.21	0.25	0.25	0.24	0.34
A	0.69	0.64	0.56	0.85	0.62	0.67
B (s/m)	1	1	1.64	2.5	1.55	2

Focusing on the 100-rpm test, the BW curve features a slightly higher value of the static friction coefficient f_s, while the A and B coefficients, related to the falling friction coefficient, are similar for the FW and BW curves, as the hysteresis loop is indeed very slender. On the other hand, in the 200-rpm test, the static friction coefficient has a limited variation, while the A and B parameters of the BW curve are larger than the corresponding ones obtained on the FW curve. This is clearly related to the contaminant removal and to the consequent change of the friction conditions, which modifies the falling friction behaviour. In fact, as a result of the contaminant removal, two opposite phenomena are acting in the nonlinear part of the BW curves. Due to the falling friction effect, the adhesion coefficient would tend to decrease, but the work of the friction forces is removing the contaminant, thus leading to an increase of the adhesion coefficient. The Polach's model is clearly not able to separate the two phenomena, so the global effect is reflected as a change in the falling friction parameters. The same result is obtained for the 300-rpm test, where also a larger increase in the maximum adhesion coefficient is achieved compared to the other tests, because at 300 rpm, the largest amount of power is dissipated at the contact interface. As noticeable from a comparison between Table 19 and Table 14, the A, B, k_A and k_S parameters obtained from the fitting operations are quite different compared to the theoretical values for wet conditions suggested by Polach. These differences can be related to the large values of spin coefficient that are generate on roller-rigs, while Polach performed experimental traction tests on real locomotives in

conditions of pure longitudinal creepage. Nonetheless, despite these differences, the fitting operations allowed to compare form a quantitative point of view the FW and BW curves obtained in the wheel adhesion recovery tests.

Finally, the last experimental test carried out on the new bench was a rail adhesion recovery test, which is performed by applying the same constant braking pressure on all four wheelsets and then contaminating the roller surface. The contamination was applied by pushing wet sheets against the roller surface at discrete times. The results of the test are shown in Figure 89, which plots the creepage value recorded on each wheelset as a function of time. The zoomed views on the right side of Figure 89 correspond to the three separate applications of the wet sheets during the test. In all four applications, the highest values of creepage are recorded on wheelset 1, which is the first one to face the contaminant, while wheelset 4 is always the least affected by the contamination. The rail adhesion recovery can be clearly noticed in the plots, as after a certain amount of time, the initial creepage values are restored on all wheelsets, because of the cleaning action operated by the friction forces. However, some discrepancies arose during the test, as wheelset 3 reached larger values of creepage compared to wheelset 2, and this is clearly unexpected. Probably, these deviations from the expected results could be related to a non uniform value of the normal load applied by the spring suspension system and to slightly different initial adhesion conditions. Unfortunately, it is not easy to investigate a possible dependency of this behaviour on the amount of the contaminant lying at the contact interface, as the wet sheets were pushed manually against the roller surface, because the bench in its current configuration does not allow to control the amount of applied contaminant. Nonetheless, despite these discrepancies arising at the initial stages of the surface contamination, the wheelsets always got back to their initial creepage value in the sequence 4-3-2-1 after removing the water layer, which is opposite to the sequence of contaminant facing, and this is in good agreement with the preliminary expectations.

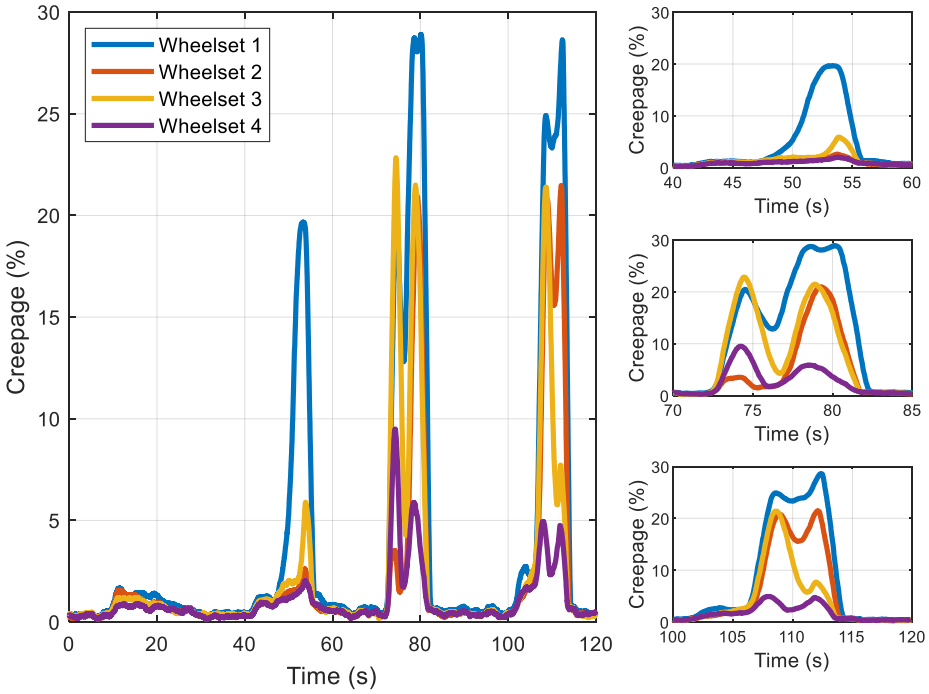

Figure 89: Results of rail adhesion recovery test.

In conclusion, the new multi-axle roller-rig proved to produce reliable and accurate results with a good repeatability, and the adhesion curves obtained on the bench are not affected by the motor control mode or by the gradient of the pressure ramp. Since the tests run on the bench simulate transient operations rather than steady-state conditions, after reaching the adhesion saturation points, the wheelset reach locking conditions abruptly, thus requiring a high sampling rate. Therefore, it is crucial to estimate the wheelset deceleration, to avoid an overestimation of the wheelset coefficient. To tackle these issues, two strategies were implemented. First, the LabVIEW control software was optimized to allow a data storage with a rate of 1 kHz, which ensures an adequate number of measurement points even in the unstable part of the adhesion curve. Moreover, since the data acquisition board for the counting of the encoder pulses cannot directly measure speed, the LabVIEW control software acquires the angular position of each wheelset, and the wheelset deceleration is estimated in the post-processing stage with two numerical differentiations of the original signal. An effective data filtering strategy was implemented in the MATLAB post-processing routine, which is able to compute stable values of acceleration starting from the original angular position signal.

The biggest point of merit of the new bench is that it allows to perform adhesion recovery tests with a good simulation of the real operating conditions, because the four wheelsets are all rolling over the same surface. The wheel adhesion recovery tests highlighted that for the case of dry contact, there is no generation of a considerable adhesion loop, regardless of the roller speed, because of the absence of a contaminant layer to be destroyed. On the other hand, the tests performed in wet conditions clearly produced a hysteresis loop with a shape strongly dependent on the roller speed. An interesting finding of this experimental campaign was that when the roller speed increases, an abrupt adhesion recovery can be already recorded in the forward adhesion curve, corresponding to increasing creepage. The fitting of the adhesion curves obtained in these tests according to Polach's model highlighted that because of the adhesion recovery phenomena, not only the static friction coefficient tends to increase, but also the coefficients of the falling friction law are modified. In fact, when gross slip is generated at the contact patch, if creepage increases, the work of the friction forces tends to destroy the contaminant layer, thus improving the adhesion conditions, but the falling friction phenomenon has an opposite effect, which tends to reduce the available friction.

Finally, the results of the rail adhesion recovery test showed that the new multi-axle roller-rig can properly simulate the mutual interaction among the following wheelsets of a vehicle, despite the very simple strategy adopted for the surface contamination, which is currently applied manually without the possibility of accurately control the amount of contaminant. Although some discrepancies were recorded in the tests, the highest creepage value was always recorded on the first wheelset facing the contaminant, and creepage was recorded to get back to the initial values prior to the application of the contaminant, because the friction forces remove the water layer. Furthermore, the adhesion recovery always occurred in the opposite sequence of contaminant facing, which means that the front wheelset is the last one to get back to the initial creepage values. In fact, the front wheelset is the one which starts the removal of the contaminant, and hence it is the one that faces the largest amount of contamination at the contact interface.

3.6 Testing of air brake monitoring systems

The original configuration of the multi-axle roller-rig, shown in §3.5, was modified after the conclusion of the experimental campaign for the investigation of adhesion phenomena, in order to obtain a new bench layout allowing to perform testing and validation of air brake monitoring systems and algorithms, on

which the research group has been working for over a decade. The bench configuration was modified to reproduce the typical freight train air brake system in laboratory conditions. In the frame of the present thesis, a monitoring board, developed by the group in past activities, was used for the purposes of analysing the outputs of the air brake system. This task had not been performed by the group before. The contribution of this thesis mainly concerns the development of a new LabVIEW control software, managing the communication with a monitoring unit, and of a new motor control strategy allowing the bench to simulate stop braking operations considering the inertia of the whole vehicle.

3.6.1 Brief overview on monitoring systems

The adoption of on-board monitoring systems able to detect the conditions of the most critical subsystem of the vehicle is essential to improve the safety and the reliability of the railway system as a whole. The development of monitoring systems can lead the way to the introduction of predictive maintenance strategies, to improve the maintenance schedule with considerable benefits in terms of life-costs of the vehicles. Moreover, monitoring systems can allow a prompt detection of failure of the critical vehicle components during operation, with a strong improvement of the vehicle safety. The widespread diffusion of monitoring systems onboard freight wagons was traditionally prevented by the lack of electrification of wagons. Nonetheless, the growing availability of low-power sensors and controllers, as well as the recent advancements in the field of energy harvesting solutions [119], is boosting the development of monitoring systems even for installation onboard non electrified vehicles. A comprehensive survey on recent concepts and established monitoring systems for freight wagons can be found in the work by Bernal et al. [120]. The reference surveys different issues that must be faced to obtain reliable monitoring systems, such as the generation of electrical power, the hardware layout of the monitoring system, the data transmission and communication strategies and the development of efficient algorithms to post-process data in order to identify possible faults or to evaluate the health state of the monitored components. Because of the big role played by the air brake system for what concerns the safety of railway vehicles, the air brake plant is a key vehicle system to be carefully monitored, as indeed Aimar and Somà [121] reported that on intermodal freight wagons, the failure rate for the braking system was higher compared to axle-boxes and wheels. Examples of solutions for monitoring of the air brake systems on freight wagons can be found in the works by Hartley et al. [122] and by Aimar and Somà [121]. Moreover, prior to the activities shown in the previous thesis, the research group developed and tested several configurations of a comprehensive monitoring unit able to perform diagnostic operations on many critical vehicle components, including axle-boxes, wheels and of course the air brake system [123-126].

A reliable monitoring system must typically include the following main components.

- A variable number of sensors, for the measurement of the major quantities of interest. Acceleration, pressure and temperature are the typical signals to be acquired for reliable diagnostic operations on the critical vehicle components.
- A variable number of signal conditioning and acquisition modules, to acquire data measured by the monitoring sensors.
- An electric power generator, often coupled with a storage system (e.g., batteries).
- A data transmission system, able to send data from the monitoring system installed on-board the vehicle to a hub in the locomotive or even to a remote server.
- Possibly a memory element for data storage.
- A micro-controller, for the management of the components included in the monitoring unit. The micro-controller can implement basic algorithms for the processing of the sensor measurements.

The complexity of the hardware and software configurations of monitoring systems requires intensive testing campaigns to ensure a high reliability onboard the vehicles in all conditions, including unsafe operating scenarios. Despite being the more realistic ones, on-field tests are not the best option in the first stages of product development. In fact, beyond all reasons listed in the previous sections focusing on adhesion tests, such as high costs, traffic interruption and poor repeatability of testing conditions, another issue arises when dealing with on-track tests of monitoring units. In fact, testing of new monitoring systems should inevitably consider fault conditions, however the simulation of such scenarios on a real vehicle could be unsafe and dangerous. Therefore, even in the field of monitoring systems, experimental testing in laboratory conditions can be the best compromise solution, especially in the first stages of design, when a large number of tests must be performed in the shortest time.

3.6.2 New configuration of the multi-axle roller-rig

The original configuration of the multi-axle roller-rig was not directly suitable for the investigation of the performances of monitoring systems and changes were required to allow the execution of the new activity. Nonetheless, since the aim of the new work was to prove the possibility of using the new bench as a test rig for

the validation of monitoring systems, the research group decided to make the minimum number of changes with respect to the original layout, to contain costs. The new configuration of the multi-axle roller-rig, described in the following paragraphs, was conceived in the frame of the present thesis, and changes were made to replicate the real freight train air brake system in laboratory conditions.

The bench configuration was modified in order to reproduce the typical UIC freight train air brake system, see §1.2 and Figure 1, on the multi-axle roller-rig. To reduce the costs related to these changes, the electro-pneumatic regulators already installed on the bench were used to control the pressure in different parts of the simulated brake plant. Figure 90(a) sketches the pneumatic circuit developed to replicate the freight train air brake system on the new multi-axle roller-rig. The compressed air produced by the volumetric compressor in the laboratory of the research group is stored in a main reservoir at a pressure of 8 bar, and a pressure reducer (PR) sets the downstream pressure at a value of 5 bar, which is the nominal pressure in the air brake pipe in running conditions when no braking effort is generated. One of the electro-pneumatic regulators installed on the bench (EPR 1) adjusts the outlet pressure to simulate a pressure drop in the brake pipe. For a *physical* simulation of the braking delays on a vehicle in the train composition, the air brake pipe is reproduced by means of a long pipe. In future developments of the activity, the length of the tube and the bench control algorithm could be tuned to reproduce different delays, depending on the position of the simulated vehicle and on the braking regime. A second electro-pneumatic regulator (EPR 2), acting as the distributor installed on real vehicles, is used to set the pressure in a reservoir, simulating the auxiliary reservoir, to a value of 3.8 bar when no braking action is commanded. The air stored in the auxiliary reservoir is fed to the brake callipers installed on wheelset 1 of the bench, to reproduce the braking operation of a freight wagon. The pressure sent to the brake callipers is adjusted by means of the electro-pneumatic regulator mounted on the first wheelset of the bench (EPR 3). Different values of vehicle axle-load can be simulated by adjusting the normal force exerted by the spring suspension system, while the braking force at each brake pad-brake disc contact interface is measure by the two S-beam cells mounted on wheelset 1. Figure 90(b) shows the new pneumatic devices installed on the bench, namely the main reservoir (1), the auxiliary reservoir (2) and the long pipe (3), used to simulate the delays in the braking signal transmission.

Since some of the electro-pneumatic regulators available on the bench were used to adjust the pressure in the simulated air brake system, to reduce the cost of the bench changes, the braking operation of the vehicle is simulated by applying a

braking pressure on just one wheelset of the bench. The underlying assumption is that the braking operation of the wheelset is representative of the braking operation of the whole vehicle. In future works, the bench configuration could include additional pneumatic valves, to apply a braking torque on all four wheelsets. Furthermore, the original braking system was not modified, so the braking action is still applied by means of brake pad-disc pairs, while commonly freight wagons are equipped with tread braking. Nonetheless, this activity was carried out just to show the feasibility of the new strategy, so the braking system was left unchanged to reduce the number of changes and to minimize costs. A new braking system could be developed in future upgrades, to reproduce block brakes and to even simulate the real brake cylinder and brake rigging installed on a real vehicle.

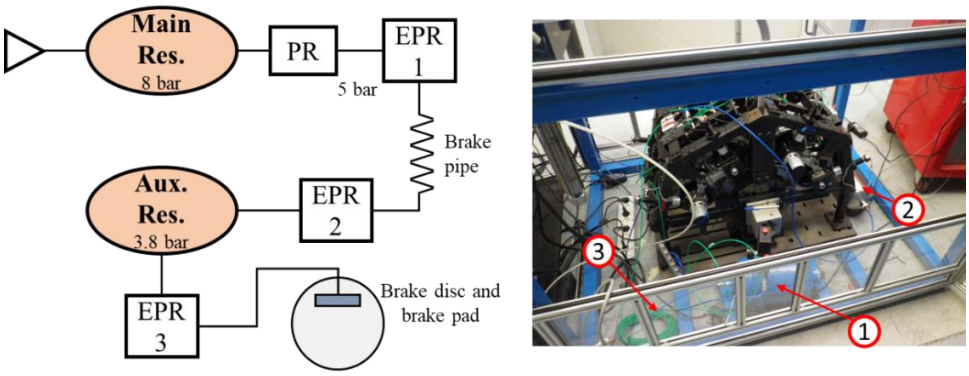

Figure 90: Braking system reproduced on the multi-axle roller-rig: (a) pneumatic circuit [126] and (b) photo of the bench.

In the preliminary tests shown in this thesis, the new bench configuration was used to test the latest version of the monitoring unit developed by the research group, which is the result of research activities that have been going on for over a decade. The monitoring unit was developed outside the frame of this thesis, however the following lines give an overview on its design for the sake of readability. The upgraded version of the monitoring unit is integrated in a single electronic board, shown in Figure 91, including a multi-channel data acquisition, with proper signal conditioning depending on the input signal. The board is controlled by a 32-bit ARM7 processor, whereby an editable in-house code for data acquisition and transmission runs. Data can be transmitted either via Modbus protocol or via a CAN network. The board includes an SD memory, for data storage, and data coming from different monitoring units installed on several wagons in the train composition can be processed by an embedded PC. Each

monitoring unit is intended to acquire data for a single bogie and can manage signals coming from different sensors installed on the vehicle. The goal of the activity shown in this section was to assess the capability of the latest version of the unit to acquire signals that could be needed by a generic air brake diagnostic system, namely:

- Pressure in brake pipe, brake cylinder and auxiliary reservoir.
- Output of a weighing cell for the estimation of the vehicle weight on rails.
- Wheelset speed.
- Brake pad temperature.

The required pressure signals were collected from the pressure f\b values provided by the three electro-pneumatic regulators (EPR 1, EPR 2 and EPR 3) used to reproduce the air brake system. Although the bench does not include a real empty-loaded device, the signal of the weighing cell was simulated using the measurements of one of the load button cells installed on the axle-boxes of the brake wheelset. The wheelset speed was measured using the encoder already installed on the braked wheels. In the context of the activities carried out to investigate adhesion phenomena, shown in §3.5, the encoder signals were acquired by a digital input/output module (NI PXIe-6612), connected to the industrial PC and managed with the original LabVIEW control software. On the other hand, in this work, the encoder signals were directly acquired by a digital chip (HCTL-2032-SC), installed on the monitoring board, able to calculate the rotational speed thanks to a low-level counting of the encoder pulses. Finally, to obtain temperature data, two Pt1000 thermal resistance sensors were installed to measure the temperature of the brake callipers mounted on the braked wheelset, and their outputs were directly acquired by means of an analog/digital converter (ADS1148), installed on the monitoring unit.

Figure 91: Monitoring unit.

The new strategy adopted for data acquisition and bench control operations is shown in Figure 92. The development of a new bench control software, starting from the multi-axle roller-rig original control software, is one of the main contributions of this thesis. The new LabVIEW control software was developed to manage the new connection between the industrial PC and the monitoring unit, as well as to implement a new roller motor control strategy, enabling the simulation of the vehicle deceleration during braking. The desired pressure values downstream the three electro-pneumatic regulators, representing pressure values in brake pipe (EPR 1), at the outlet of the distributor (EPR 2) and at the brake cylinder (EPR 3), are set using the same USB analog output module (NI USB-9263) as used in the previous activity dealing with degraded adhesion studies. Similarly, the f\b values are recorded by means of the original analog input module (NI USB-9239) installed on the bench. The signal coming from one of the two load button cells mounted on the vehicle, simulating the weighing cell of a real vehicle, as well as the tangential forces measured by the two S-beam cells on the braked wheelset are acquired using the already available analog input strain-bridge module (NI PXIe-4330). The braking forces or the braking torque are commonly not measured by monitoring systems, however in this work measuring the applied braking forces was essential to properly control the motor, according to the strategy described below. The pressure f\b values provided by the three electro-pneumatic regulators and the measurement of the load button cell, simulating the weighing cell, must be available to the monitoring unit, as on a real-vehicle, the wires coming from the sensors would be directly connected to the

monitoring board. To simulate this condition, these signals are read in LabVIEW and written to an additional analog output module (NI PXIe-4322), connected to the industrial PC, which eventually transmits data to an ADS1148 analog/digital converter installed on the monitoring board.

The new LabVIEW control software still manages the communication between the industrial PC and the roller motor drive. The first LabVIEW control software, developed for the adhesion investigation tests, relied on a TCP\IP communication between the motor drive and the industrial PC, via dedicated LabVIEW libraries. Nonetheless, because of the new motor control strategy, this solution was discarded, and the reference speed signal, calculated by the algorithm in the modified LabVIEW bench control code, is sent from the industrial PC to the motor drive as an analog signal, via the same analog output module (NI PXIe-4322) used for data transmission from the industrial PC to the monitoring board.

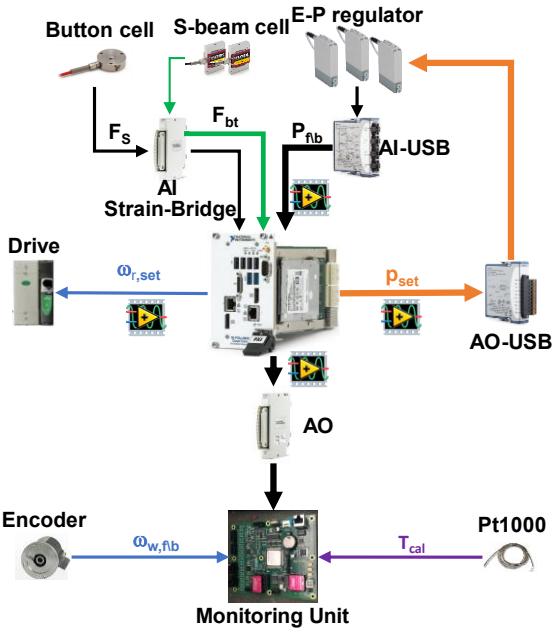

Figure 92: Strategy for the control of the modified bench configuration [127].

The greatest novelty implemented in the new LabVIEW control software for testing of air brake diagnostic systems lies in the strategy developed for the roller motor control, which must simulate the deceleration of a real vehicle during braking. The algorithm is described in the following lines, and it is based on longitudinal train dynamics. The new motor control strategy can be regarded as

one of the main contributions of the present thesis, since it combines the experimental activity dealing with the setup of the multi-axle roller-rig, see §3.5, and the numerical activity related to longitudinal train dynamics simulation, shown in chapter 2. The braking operation is simulated by applying a pressure drop signal downstream of the first electro-pneumatic regulator (EPR 1), thus reproducing the pressure drop in the brake pipe. In the preliminary stages of the activity, the applied signal was a pressure ramp until a desired pressure drop saturation value, see Figure 93(a). In future upgrades, the generated signal could feature any desired trend and it could be obtained from data collected on real vehicles. According to the f\b pressure measured by EPR 1, the value of theoretical braking pressure at the brake cylinder is calculated from the look-up-table shown in Figure 93(b), which was determined based on the prescriptions of the UIC 540 leaflet [12] and on an experimental tuning of the bench, which highlighted that the braking action on the wheelset is produced when the braking pressure at the brake calliper is above 0.6 bar.

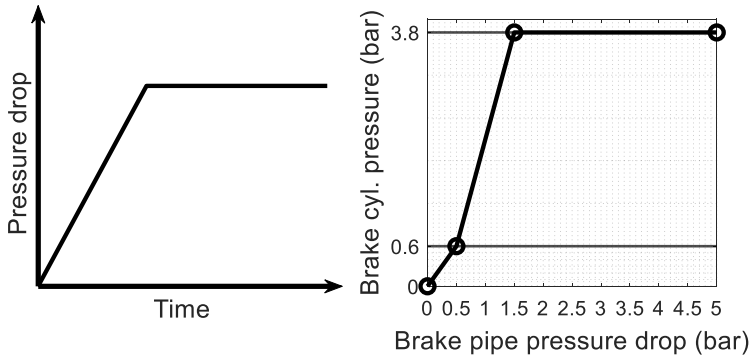

Figure 93: (a) Pressure drop signal and (b) Pressure drop-brake cylinder pressure LUT.

To control the motor and adjust the roller speed according to the applied braking effort, it is essential to estimate the applied braking torque. The braking torque on the braked wheelset is indeed calculated from the measurements of the S-beam cells installed on the braked wheelset, according to equation (3.57). The next step is the determination of the new value of roller speed starting from the estimated braking torque. The basic idea is to determine the updated value of the roller speed starting from the longitudinal train dynamics equation, see equation (2.1). To simplify the algorithm, the effects of both ordinary and accidental resistant forces, as well as the elasticity of the coupling systems, were all

neglected. Furthermore, a unitary inertia factor was assumed, as indeed the inertia factor on wagons is close to 1. Therefore, based on the introduced simplifying assumptions, equation (2.1) can be re-written in the form of equation (3.64) for a generic wagon, where m is the wagon mass, n_{ax} is the number of axles, $\ddot{x}$ is the wagon deceleration and $F_{x,i}$ is the longitudinal contact force acting on each wheelset, due to the application of the braking effort. Please note that in equation (3.64) the wheelset longitudinal forces are positive for braking operations. Assuming that the tangential forces on the four wheelsets are equal to a constant value F_x, equation (3.65) holds.

$$m\ddot{x} = \sum_{i=1}^{n} F_{x,i} \tag{3.64}$$

$$\frac{m}{n_{ax}}\ddot{x} = F_x \tag{3.65}$$

Considering the rotational equilibrium of the scaled wheelset, see Figure 68, the longitudinal contact force between the wheelset and the rollers is calculated by applying equation (3.55) on the braked wheelset. Assuming that good adhesion conditions hold during the braking operation, the wheelset rotational deceleration $\dot{\omega}_w$ is related to the peripheral deceleration $\ddot{x}_w$ as stated by equation (3.66), where r_w is once again the wheel radius.

$$\dot{\omega}_w = \frac{\ddot{x}_w}{r_w} \tag{3.66}$$

By combining equations (3.66) and equation (3.55), a relationship between the measured braking torque and the corresponding wheelset deceleration is obtained, as stated by equation (3.67). As the bench follows the similitude rule suggested by Jaschinski, the deceleration estimated on the bench with equation (3.67) corresponds to the deceleration of a full-scale system.

$$\ddot{x}_w = \frac{T_b r_w}{m_w r_w^2 + I_{w,yy}} \tag{3.67}$$

If the wheel and the roller are in good adhesion conditions, the peripheral deceleration of the roller is equal to the peripheral deceleration of the wheelset, hence the roller rotational deceleration can be simply evaluated with equation (3.68).

$$\dot{\omega}_r = \frac{\ddot{x}_w}{r_r} \tag{3.68}$$

Therefore, if the above calculations are performed at a certain time instant t_k during the test, the new roller reference speed for the next time instant $\omega_{r,set,k+1}$ can be calculated according to equation (3.69), where k is the index related to time discretization and Δt_k is the execution time required by the LabVIEW loop performing data acquisition and motor control, which is accurately measured at each iteration and it has a roughly constant value of 10 ms.

$$\omega_{r,set,k+1} = \omega_{r,set,k} - \dot{\omega}_{r,k}\Delta t_k \tag{3.69}$$

On the multi-axle roller-rig, the roller rotational speed corresponds to a vehicle speed in km/h V as stated by equation (3.70), where n_r is the roller speed in rpm.

$$V = 3.6\sqrt{5}\omega_r r_r = 3.6\sqrt{5}n_r \frac{\pi}{30} r_r \tag{3.70}$$

At the end of each test, two text files are generated. The first file stores data acquired in the LabVIEW control software, namely, the f\b pressure at the outlet of each electro-pneumatic regulator, the normal force measured by the load button cell and the sum of the tangential forces measured by the S-beam cells. The second file is generated by the code running in the monitoring unit, and it stores data sent from the industrial PC to the monitoring board (pressures and weighing cell signal), as well as the measurements of the Pt1000 thermal sensors and of the encoder. Data is post-processed with an external MATLAB routine, similar to the function developed for adhesion investigations.

3.6.3 Results

Experimental tests were carried out on the new bench configuration with the primary aim of testing the new motor control strategy and the effectiveness of the data transmission from the industrial PC to the monitoring board.

Table 20 shows the main parameters of three preliminary tests carried out on the bench with the new control software, in terms of maximum pressure drop in the brake pipe, maximum pressure at the brake cylinder and gradient of the pressure ramp in the linear part of the input ramp signal. As noticeable from Table 20, tests 1 and 3 were run with the same maximum pressure drop in the brake pipe, but the ramp gradient was faster on test 3. On the other hand, test 2 was run

with the same ramp gradient as for test 1, but the limit value of the pressure drop was lower. All tests were run from an initial roller speed of 260 rpm, which corresponds to a speed of 40 km/h on a full-scale vehicle.

Table 20: Tests for the validation of the new bench configuration.

Test No.	Max. pressure drop (bar)	Max brake cyl. pressure (bar)	Gradient (bar/s)
1	0.71	1.16	0.186
2	0.66	1	0.186
2	0.71	1.16	0.231

Figure 94 shows the values of the main quantities recorded during the third test, highlighting the strategy adopted to replicate the braking operation. The test starts with the roller motor at zero speed, then speed is increased until the nominal value is reached. After steady-state conditions are achieved, the pressure drop signal is activated, by applying a pressure ramp saturated at a pre-set value (equal to 0.71 bar for the third test). It is interesting to notice that after achieving the constant value of pressure drop, the brake cylinder pressure stops rising, as the brake cylinder pressure is calculated from the LUT in Figure 93(a). As the brake cylinder pressure increases, the applied braking torque on the braked wheelset increases, too, and the roller speed decreases, because the new control strategy calculates a new reference speed for the roller motor according to the theoretical deceleration estimated starting from the measurements of the S-beam cells, see §3.6.2. Finally, when the roller speed is zero, the brake cylinder pressure is released, and the pressure in the brake pipe is restored to the initial value of 5 bar. From the upper plot in Figure 94, it is interesting to observe that the braking torque increases even after the saturation of the brake cylinder pressure. This is related to a dependency of the brake pad-brake disc friction coefficient on speed, as indeed the friction coefficient is higher at low speed. The same aforementioned considerations hold for the other tests performed on the bench, which are not shown here for the sake of brevity.

When a braking test is run with the new bench, the pressure signals provided by the three electro-pneumatic regulators and the weighing signal given by the load button cell are acquired in LabVIEW and transferred to the monitoring unit

as analog signals via the NI PXIe-4322 analog output module. Figure 95 confirms the good agreement between the brake cylinder pressure obtained in LabVIEW and the one available in the monitoring unit. The difference in the frequency content of the two signals plotted in Figure 95 is related to the different sampling rates of the LabVIEW control software and of the monitoring unit. The LabVIEW control software acquires the pressure data at a rate of 2 kHz, while the monitoring unit can store data at a maximum frequency of 1 kHz. However, the frequency of 1 kHz is enough to capture the dynamic behaviour of the pressure in the brake cylinder.

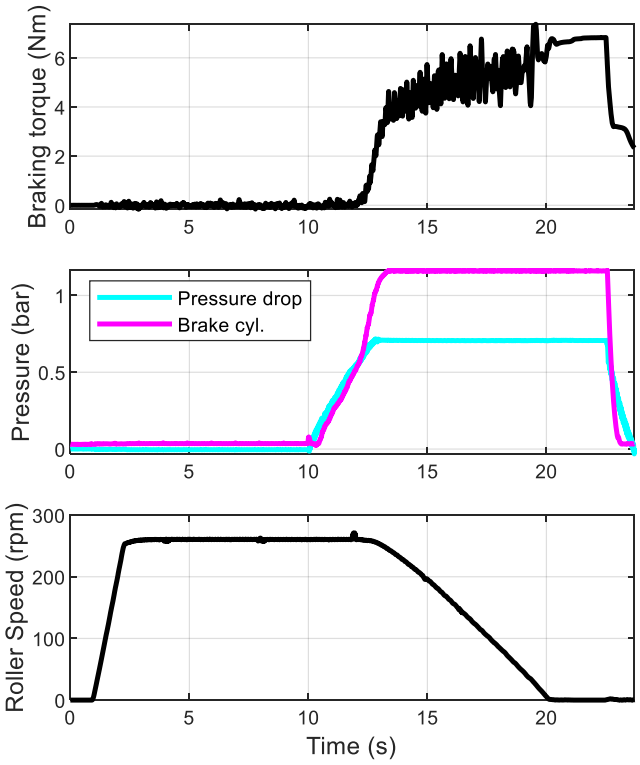

Figure 94: Simulation of braking operations with vehicle inertia on the new bench configuration (test 3).

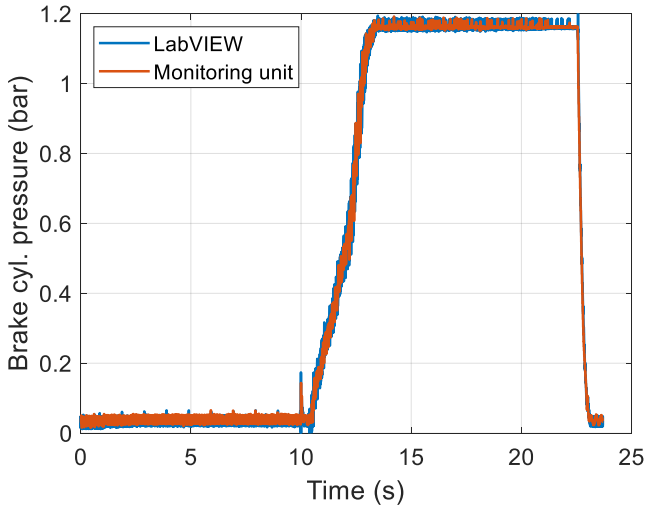

Figure 95: Brake cylinder pressure acquired in LabVIEW and by monitoring unit (test 3).

Finally, the results of the braking tests in terms of braking distance and speed as a function of time are plotted in Figure 96, which shows the quantities for a full-scale vehicle, only considering the part of the experimental acquisition after the beginning of the application of the brake pipe pressure drop ramp signal. The full-scale quantities can be easily calculated from the quantities measured on the multi-axle roller-rig, by adopting the scaling factors for the Jaschinski's model with a unitary scaling of density and a length scaling factor equal to 5, see Table 13. Figure 96 confirms the validity of the proposed motor control strategy, as test 2 features the longest braking distance, since it is the test with the lowest value of brake cylinder pressure. Furthermore, the upper plot highlights the good repeatability of the implemented control strategy. In fact, tests 1 and 3 feature the same maximum brake cylinder pressure, and they show a similar acceleration in the linear part of the speed curve, which corresponds to the braking action after the saturation of the brake cylinder pressure. However, since test 3 is performed with a faster rate of the brake pipe pressure drop, the braking distance is lower than the braking distance for test 1, as noticeable from the braking curve given in the lower plot in Figure 96.

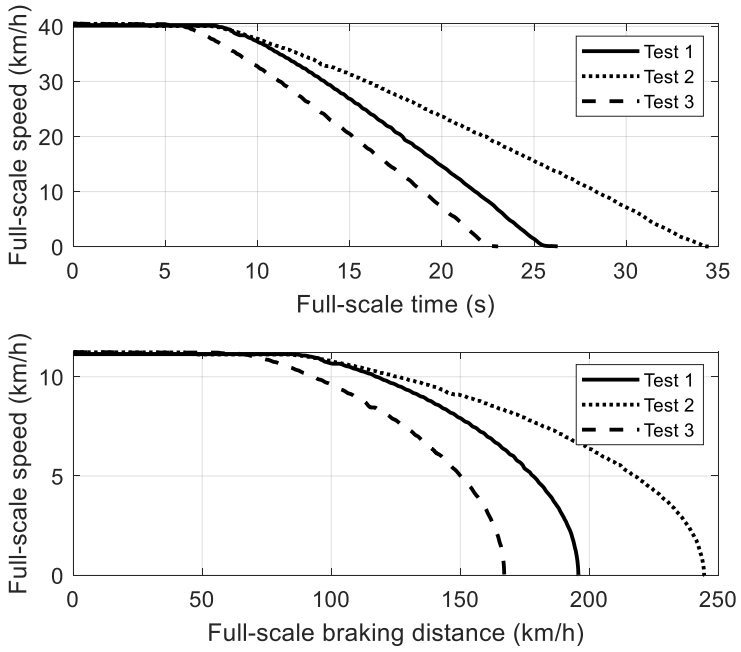

Figure 96: Braking curves reproduced on the multi-axle roller-rig.

In conclusion, the changes made to the bench mechanical layout and the development of the new LabVIEW control software allow to use the multi-axle roller-rig as a reliable device for testing and validation of air brake monitoring systems. Obviously, further work is needed to optimize the performances of the bench, however the activities performed in the frame of the present thesis were fundamental to ensure the proper working of the bench even in the new configuration, requiring the simulation of the vehicle inertia and data transfer from the industrial PC to the monitoring unit. More in detail, the new motor control strategy, based on the longitudinal train dynamics equations, ensures a good repeatability, and allows to reproduce braking operations characterized by different values of the maximum brake cylinder pressures and of the pressure rise gradient. The new bench control software specifically implemented for the new bench layout as a major contribution of this thesis allows to transfer data from the sensors to the monitoring unit by means of an additional analog output module installed on the bench, and a good agreement between the data measured by the sensors and the signals available to the monitoring unit is ensured.

Chapter 4

Damage of wheel rolling surface

The dynamics of railway vehicles ultimately depends on the forces acting at the wheel-rail contact interface, whereby a steel-to-steel rolling contact takes place. At the same time, on freight wagons with block brakes, the braking action is produced as a result of the sliding contact between the wheel tread and the shoes. The presence of friction in both aforementioned contact conditions inevitably leads to a damage of the wheel rolling surface. This chapter shows two topics that the research group has recently begun to investigate with numerical codes. The first topic is related to the wear of the wheel lateral profile, while the second activity deals with the thermo-mechanical simulation of the wheel-shoe contact. A strong relation exists between the two topics, as the integration of thermal models and wear models would theoretically allow to determine the wheel worn profile as a result of both the dynamic running and tread braking operations. As a matter of facts, an ambitious future target of the research group is the development of such a model, able to consider the effects of both phenomena. The activities performed while drafting the present thesis were intended to lay the foundations for the development of numerical codes that the research group can adopt in future works.

Prior to the beginning of this thesis, the research group worked on the topic of the numerical simulation of wear of wheel profiles both for research purposes as well as in the frame of collaborations with industrial partners, launching the calculations with the wear module of the Simpack commercial MB software. Nonetheless, the research group observed that the Simpack wear module features numerical instabilities, and alternative strategies for the profile update and smoothing were proposed in [104]. For this reason, one of the major goals of the activities carried out in the present thesis was the development of in-house wear

algorithms, to be initially validated against the outputs of the Simpack wear module. In fact, benchmarking the wear algorithms against the outputs calculated by Simpack allows to get a further insight into the algorithm implemented in the commercial code, and this can thrust the optimization of wear algorithms to avoid numerical instabilities. The starting point of this activity was a detailed state-of-the-art research focusing on the strategies shown in the literature for the simulation of wear of transversal wheel profiles. The outcome of the literature review activity is the state-of-the-art review paper [128].

Concerning the simulation of the wheel-shoe contact, the research group had not worked on the topic previously, so among the activities of the present thesis was a state-of-the-art review on the existing numerical models presented in the literature. At this early stage of development of the activity, the research group aimed at building reliable models that can be integrated in more complex frameworks in future developments. As an example, wheel-shoe thermal models could be integrated into MB models or LTD codes to compute the wheel/shoe temperature during air brake operations. Therefore, the present thesis dealt with the design of a numerical framework for the simulation of the wheel-shoe thermo-mechanical behaviour, which had to be conceived from scratch. As shown in this chapter, the new computational framework includes the simulation of the longitudinal train dynamics of reference vehicles, for the calculation of the main input quantities of a finite-element (FE) model for the calculation of the wheel-shoe contact pressure and wheel temperature. More in detail, a huge contribution to the implementation of the FE model in the ANSYS FE code was given by students working on their master's degree thesis under the supervision of the research group.

The chapter is organized as follows. Section 4.1 deals with the numerical modelling of wear of wheel profiles. The section includes an overview on the tribology of wear in the railway field and the main findings of the state-of-the-art activity carried out in the frame of the present thesis. Next, focus is given to a comparison between different wear algorithms for the calculation of the wear depth distribution in a reference simulation scenario, with a benchmarking against the outputs of the Simpack wear module. Section 4.2 concerns the numerical modelling of the wheel-shoe contact, with a brief overview on the numerical models that can be found in the literature. Then, attention is given to the new computational framework developed in the frame of the present thesis and to the preliminary results obtained with the newly conceived tool.

4.1 Wear of wheel lateral profiles

4.1.1 Background on wheel wear tribology and wear laws

The transversal profile of railway wheels is designed to ensure a smooth transition when the contact point shifts from the tread towards the flange zone during curve negotiation, see Figure 46. Due to the large contact stresses acting at the wheel-rail contact interface, the wheel profile is subjected to wear, which can eventually modify the dynamic behaviour of the railway vehicles. Apart from wear of the wheel profile, the wheel-rail contact is responsible for the generation of other damage phenomena, such as the rolling contact fatigue (RCF) and changes of the wheel profile shape in the circumferential direction. The latter damage type includes the generation of wheel flats, that arise when the wheel slides over the rail during braking operations under poor adhesion conditions, and the wheel polygonization, or wheel out-of-roundness. However, these phenomena are outside the scope of this chapter, and the interested reader can refer to works in the literature for further details [129,130]. In the rest of the section, focus will be given only to the *uniform* wear of the wheel profile, i.e., to a wear phenomenon that only modifies the lateral shape of the wheel profile, which is assumed to maintain an axisymmetric shape in the longitudinal direction.

Figure 97 highlights that as the wheel transversal profile is worn out, when the wheelset features a little lateral shift, the contact point tends to “jump” further and further away from its original position [131]. In such conditions, the local curvature of the profile in the contact point can drastically change, and this eventually affects the values of the contact patch size and of the contact forces. Similarly, as the wear phenomenon leads to a higher conformity of the wheel-rail contact, the wheel profile shape can become hollow, and this is known to cause limited bogie steering capabilities, higher rolling resistance, higher contact stresses, higher rolling noise and higher impact damage to the infrastructure [132].

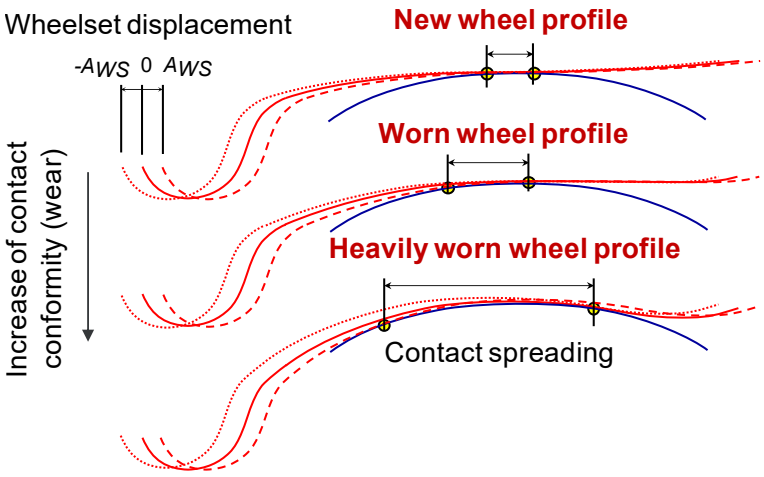

Figure 97: Contact point spreading, redrawn from [131].

To tackle the critical drawbacks related to wear of railway wheels, a deep knowledge of the wear phenomenon occurring at the wheel-rail contact interface is essential. In 1990, Lim and Ashby [133] mapped the wear mechanisms for sliding contact scenarios as a function of sliding speed and normal contact pressure, also highlighting a correlation with the temperature at the contact interface, see Figure 98. According to Lim and Ashby, when the contact pressure is above a threshold limit, the predominant wear mechanism is seizure of the contact surfaces. At high values of sliding speed and hence of contact temperature, wear is dominated by *hot* mechanisms. If the temperature of one contacting body is above the melting point, wear is the result of melting. On the other hand, if the bulk temperature rises but stays below the melting point, a severe oxidation takes place, with changes of the material properties. For lower values of contact pressure and sliding speed, the bulk temperature of the contacting bodies does not increase significantly, however local temperature peaks can lead to a mild oxidation. Finally, for very low values of sliding speed, wear is the result of *cold* mechanisms, namely plastic phenomena.

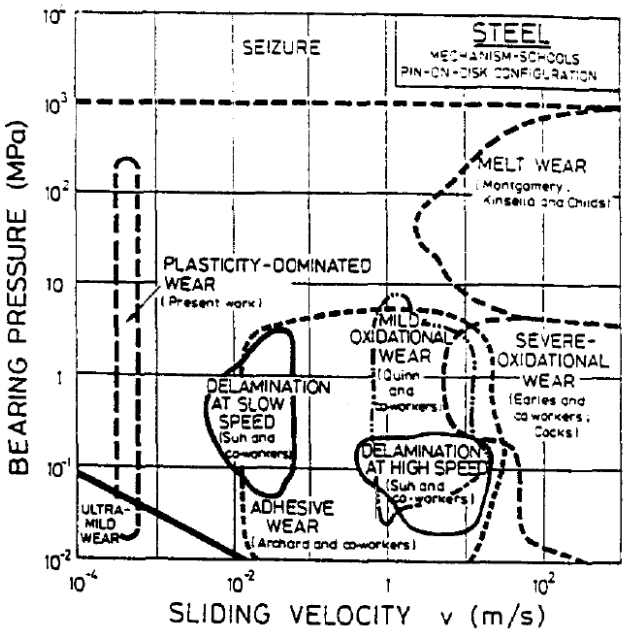

Figure 98: Lim and Ashby's wear mechanism map [133].

Although the contribution by Ashby and Lim is a milestone in the field, it mainly concerned pure sliding contact conditions, which differ from the rolling-sliding contact that characterizes the wheel-rail interface. Moreover, Ashby and Lim considered a large number of mechanisms, that can be absent in the wheel-rail contact. Many experimental studies have been performed over the years to deeply investigate the wear phenomena that take place at the wheel-rail interface. Pioneering works date bake to the early 50s, when the British Railways Technical Centre (BRR) promoted an experimental investigation of the phenomenon, as Dearden [134] highlighted the economic cost and the performance loss due to wear, suggesting simple countermeasures. Beagley [135] ran wear tests using an Amsler's machine installed in the laboratories of the BRR, with the rail and wheel discs both made of the BS11 rail steel. Beagley identified two wear regimes, namely a *mild* regime, dominated by oxidative phenomena, and a *severe* regime, where the predominant wear mechanism was a mechanical delamination. Beagley suggested that the transition between the two regimes occurs when the maximum shear stress exceeds a threshold limit. Bolton et al. [136] extended the work by Beagley to consider a wheel disc made of the class D rail wheel steel and confirmed the observation of mild and severe regimes. The results collected by Bolton et al. suggested that in the mild regime, the wear rate is a function of contact pressure only, unless the creepage value is below 1%. On the other hand,

the wear rate proved to be a function of both creepage and pressure in the severe regime, and the BRR researchers found a linear relationship with respect to the wear number Tγ, normalized by the contact area A. The Tγ index is related to the amount of specific dissipated energy at the contact interface per unit of contact length (J/m), and it can be calculated from the knowledge of contact forces and creepages. In a general case, the wear number Tγ is obtained with equation (4.1), where F_x is the longitudinal force, F_y is the lateral force, M_z is the spin moment, and finally ξ, η and φ are longitudinal, lateral and spin creepage coefficients, respectively.

$$T\gamma = |F_x\xi| + |F_y\eta| + |M_z\varphi| \tag{4.1}$$

A new experimental campaign carried out by Bolton and Clayton at BRR in 1984, considering a larger number of wheel and rail steels, highlighted a third wear regime [137]. The authors referred to the three wear modes as modes I, II and III, to avoid misleading considerations with respect to the original nomenclature of mild and severe wear. Whilst modes I and II approximately corresponded to the mild and severe regimes identified in previous research, mode III featured an extreme wear rate, and it was characterized by ploughing and scoring of the contact surfaces. Based on the observation of side-worn rails, Bolton and Clayton declared that wear at the rail gauge corner is mainly related to wear mode II, while mode III is predominant on the gauge face.

Zakharov et al. [138] identified a fourth wear regime when performing experimental tests with a twin-disc machine able to simulate conditions of combined lateral and longitudinal creepage. The fourth model was referred to as a *heavy* regime, and it was found in-between the wear modes II and III previously defined by BRR researchers. The Russian researchers related the experimentally estimated wear rate to the parameter $p_z\gamma$, which in case of a gross sliding and pure longitudinal or lateral contact conditions is related to the Tγ/A index by a proportionality factor equal to πf/4, where f is the friction coefficient. The heavy wear regime featured a decreasing wear rate with increasing $p_z\gamma$ parameter, and the authors suggested that this wear mode could coexist with severe wear on the wheel flange and rail gauge.

Further insights into the understanding of wear transitions were given in a more recent work by Lewis et al. [139], in the context of a collaboration among Sheffield University (USFD), Swedish Royal Institute of Technology (KTH), technical university of Lisbon and the ALSTOM Ferroviaria company. According

to this work, the transition from mild to severe regime is related to the development of full slip conditions on the contact patch, while the second transition from severe to catastrophic mode is linked to a reduction of the mechanical properties of the steel materials at high temperature.

Because of the complexity of wear mechanisms, the calculation of the removed material based on an accurate modelling of the physical phenomena involved in the wear process is practically impossible. Therefore, the strategy followed in the literature is the development of wear laws tuned on data obtained from experimental test campaigns. Wear laws can be classified depending on the quantity correlated to the worn material. Laws that compute the worn material as a function of either the normal load or the dissipated energy exist. Furthermore, wear laws can be applied globally or locally. In the first case, the worn material is calculated from contact parameters, such as forces and creepages. Conversely, local approaches require the determination of the distribution of contact tangential and normal pressures, as well as of the sliding speed, over the contact patch. Obviously, global applications ensure simpler and faster computations, but they are less accurate compared to local approaches. The next subsection will show a comparison between the two approaches on a reference vehicle-track scenario, carried out by the research group in the preliminary stage of this activity.

The main wear law based on the contact normal load is the Archard's wear law [140,141], that calculates the worn volume V_{worn} as a function of the normal load N and of the sliding distance d_s, according to equation (4.2), where H_s is the Brinell hardness of the softer body at the contact, expressed in Pa, while k_{Arch} is a proportionality coefficient. The proportionality coefficient is usually not a constant, and it is obtained from experimental wear maps, as a function of the slip speed and of the normal contact pressure p_z, thus relating wear to the same quantities considered by Lim and Ashby to map the wear mechanisms. The wear map commonly adopted in the railway field is the one suggested by researchers from KTH [142], who collected data from twin-disc and pin-on-disc tests for different wheel and rail steel materials. The map, shown in Figure 99, identifies four wear zones, although zones I and III are both considered as "mild" and feature a similar value of the wear coefficient. It is interesting to notice that as for the wear mechanism map by Ashby and Lim, the KTH wear map predicts a catastrophic wear regime, dominated by seizure, for contact pressure values above a pre-defined threshold p_{lim}, that is commonly assumed equal to 80% of the Brinell hardness of the softer material. Although the KTH wear map can be considered as material-independent, since it was obtained from data collected for

various rail and wheel steels, works can be found in the literature dealing with the determination of wear coefficients for specific pairs of wheel and rail steels [139,143].

$$V_{worn} = k_{Arch} \frac{N d_s}{H_s} \tag{4.2}$$

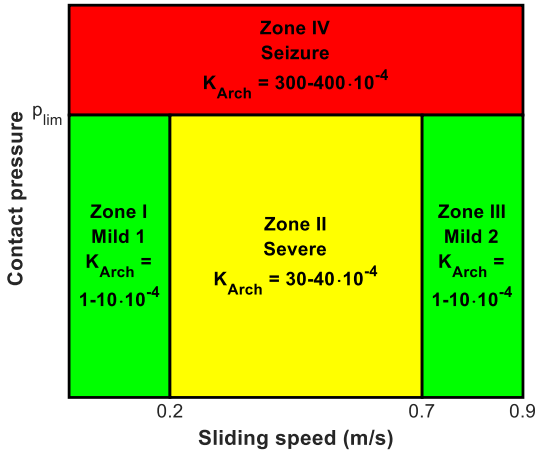

Figure 99: KTH wear map.

The Archard's wear law can be applied in local form to directly estimate the wear depth Δz_n normal to the contact patch in each element of the contact patch gird, defined by co-ordinates x and y, as stated by equation (4.3), where v_s is the sliding speed, v_0 is the rolling speed, and Δx is the contact patch discretization step in longitudinal direction.

$$\Delta z_n(x,y) = k_{Arch} \frac{p_z(x,y)}{H_s} \cdot \frac{v_s(x,y)\Delta x}{v_0} \tag{4.3}$$

Concerning the wear laws based on the friction energy loss, BRR researchers proposed two global wear laws to estimate the amount of worn material for wheel and rail steels, starting from the Tγ index [144]. More in detail, the wheel wear rate for a British class D wheel according to BRR ΔS_w can be calculated in terms of cross-sectional area loss per km of travelled distance (mm^2/km) according to equation (4.4), where d_w is the wheel diameter (mm). On the other hand, the wear rate of a rail made of a BS11 rail steel ΔS_r can be obtained in terms of cross-sectional area loss (mm^2) per thousands of axle passages according to equation (4.5). Although both expressions consider three different ranges of Tγ values, they

still account for only two types of wear regimes, namely severe and mild. In fact, the first two conditions in each equation correspond to different behaviours observed in the mild wear zone, as Harvey and McEwen predicted a constant wear rate in the mild regime for Tγ values above 100 N. Therefore, the laws proposed by Harvey and McEwen relied on the findings of the first experimental campaigns by Beagley and Bolton, before the identification of the third wear regime.

$$\Delta S_w = \begin{cases} 0.25\dfrac{T\gamma}{d_w}, & T\gamma \leq 100\ N \\ \dfrac{25}{d_w}, & 100 < T\gamma < 200\ N \\ \dfrac{1.19T\gamma - 154}{d_w}, & T\gamma \geq 200\ N \end{cases} \tag{4.4}$$

$$\Delta S_r = \begin{cases} 5 \cdot 10^{-4} T\gamma, & T\gamma \leq 100\ N \\ 5 \cdot 10^{-2}, & 100 < T\gamma < 200\ N \\ (2.5T\gamma - 322) \cdot 10^{-3}, & T\gamma \geq 200\ N \end{cases} \tag{4.5}$$

A wear law accounting for the three wear regimes identified at BRR in 1986 was proposed by the scholars from USFD. The USFD wear law estimates a wear rate Δm_{USFD}, expressed in terms of lost mass per unit of contact area and unit of rolled distance ($\mu g/mm^2/m$) as a function of the Tγ/A index, which is the wear number normalized by the contact area. This index is believed to give a better description of the wear conditions at the contact patch, since for fixed values of dissipated energy, if the contact area is lower in size, a more severe wear can be expected. The expression for the calculation of the wear rate according to a global application of the USFD law is given in equation (4.6), from which the three wear regimes can be immediately identified.

$$\Delta m_{USFD} = \begin{cases} 5.3\dfrac{T\gamma}{A}, & T\gamma/A \leq 10.4\ N/mm^2 \\ 55, & 10.4 < T\gamma/A < 77.2\ N/mm^2 \\ 61.9\left(\dfrac{T\gamma}{A} - 77.26\right) + 55, & T\gamma/A \geq 77.2\ N/mm^2 \end{cases} \tag{4.6}$$

The USFD wear law can be applied in a local form by calculating the dissipated index Tγ/A in each element of the contact patch, thus obtaining a τγ local parameter calculated as stated by equation (4.7), whereby $\mathbf{p_t}$ is the tangential pressure vector, **w** is the true slip vector, v_0 is the rolling speed and $\dot{w}_{sp}$ is the normalized dissipated energy per unit area, calculated according to equation

(3.50). Please note that according to Peng et al. [145], the local τγ index can be calculated as stated by equation (4.8), as the product of the norm of the tangential stress vector and of the norm of the local creepage vector. Equation (4.8) uses the same notation as in equation (4.7), with subscripts x and y simply referring to the vector components in longitudinal (x) and lateral (y) direction. Therefore, the local wear rate $\Delta m_{USFD}(x,y)$ can be calculated by replacing the index Tγ/A in equation (4.6) with the locally evaluated τγ index, determined according to equation (4.7) or (4.8). Finally, the normal wear depth in each cell of the contact patch grid can be obtained with equation (4.9), where ρ is density and Δx is the discretization step in longitudinal direction.

$$\tau\gamma(x,y) = \frac{\dot{w}_{sp}(x,y)}{v_0} = \frac{\boldsymbol{p_t}(x,y) \cdot \boldsymbol{w}(x,y)}{v_0} \tag{4.7}$$

$$\tau\gamma(x,y) = \sqrt{p_x^2(x,y) + p_y^2(x,y)} \cdot \frac{\sqrt{w_x^2(x,y) + w_y^2(x,y)}}{v_0} \tag{4.8}$$

$$\Delta z_n(x,y) = \Delta m_{USFD}(x,y) \cdot \frac{\Delta x}{\rho} \tag{4.9}$$

Another energetic wear law is the one by Zobory [146], who suggested a local method to calculate the flow rate of wear debris mass per unit of contact area in each element of the contact patch $\dot{m}_d$ (kg/s/m^2) as proportional to the specific dissipated power $\dot{w}_{sp}$, see equation (4.10), where k_{zob} is a wear coefficient. Zobory's model was developed to consider two wear zones, namely mild and severe wear, hence the wear coefficient assumed different values in the two zones. The transition between the two zones depended on the value of specific dissipated power. Zobory's model was developed for a local application, thus requiring the identification of the distribution of sliding speed and tangential pressure on the contact patch. However, to speed up the calculation, Zobory suggested a quick strategy to evaluate the dissipated power over the contact grid. Zobory's fast model suggested to calculate the specific power as proportional to the local value of the normal contact pressure, see equation (4.11), where $p_{z,avg}$ is the average normal contact pressure and the wear number Tγ is calculated from the global contact parameters using equation (4.1).

$$\dot{m}_d(x,y) = k_{zob}\left(\dot{w}_{sp}\right)\dot{w}_{sp}(x,y) \tag{4.10}$$

$$\dot{w}_{sp}(x,y) = v_0 \, \frac{T\gamma}{A} \cdot \frac{p_z(x,y)}{p_{z,avg}} \tag{4.11}$$

Finally, it is worth mentioning another energetic wear law, which was proposed by Krause and Poll [147] and it is now currently available in the wear module of the Simpack commercial MB code, alongside with the Archard's law. The Krause-Poll law is extremely similar to Zobory's law, as it predicts two wear regimes, depending on the value of the dissipated power. The implementation of the Krause-Poll law in Simpack is stated by equations (4.12) and (4.13), where V_{worn} is the worn volume, W_{fr} is the dissipated energy, P_{fr} is the dissipated power per contact area A, Δt is the integration time step, C is the wear coefficient and subscripts m and s refer to mild and severe wear zones.

$$V_{worn} = \begin{cases} C_m W_{fr}, & P_{fr}/A \leq 4 \ W/mm^2 \\ C_s W_{fr}, & P_{fr}/A > 4 \ W/mm^2 \end{cases} \tag{4.12}$$

$$W_{fr} = P_{fr} \Delta t, \qquad P_{fr} = v_0 \, T\gamma \tag{4.13}$$

Examples of implementation of the Krause-Poll law in a local form were not found in the literature. Nonetheless, with similar considerations as for the other wear laws shown above, a local implementation is possible if the dissipated friction work and power are calculated locally in each element of the contact patch, as stated by equations (4.14) and (4.15). Please note that once again, the specific dissipated energy can be calculated according to either equation (3.50) or equation (4.8).

$$\Delta z_n(x,y) = \begin{cases} C_m W_{fr}(x,y), & \dot{w}_{sp}(x,y) \leq 4 \ W/mm^2 \\ C_s W_{fr}(x,y), & \dot{w}_{sp}(x,y) > 4 \ W/mm^2 \end{cases} \tag{4.14}$$

$$W_{fr}(x,y) = \dot{w}_{sp}(x,y) \Delta t \Delta x \Delta y, \tag{4.15}$$

The brief overview of wear laws adopted in the railway field given above is not exhaustive, and other expressions for the calculation of wear can be found in the literature. Nonetheless, a state-of-the-art review activity highlighted that the wear laws surveyed in the previous lines are among the most common in the simulation of the wear of railway wheel profiles.

It is interesting to remark that the wear laws commonly adopted for the calculation of the removed material were tuned on several datasets, coming from

different experimental tests, run under various conditions. Peng et al. [145] showed that the BRR, KTH, USFD and Zobory's laws can be analytically manipulated to obtain equivalent expressions for the calculation of the wear depth as a function of a common wear index, but the agreement of the model outputs is far from close. Similarly, De Arizon et al. [148] proved that the KTH wear law, based on Archard's equation, gives results in good agreement with Zobory's model, while the BRR law tends to compute higher wear rates. Therefore, the selection of a proper wear law and of the correct wear coefficient is not an easy task, because different wear laws can unfortunately lead to significantly different outputs.

4.1.2 Wear numerical modelling

Because of the key role played by the wheel lateral profile shape and of its influence on the railway vehicle dynamics, wheels are periodically subjected to re-turning operations, with the aim to restore their original shape. Commonly, these operations are planned based on a pre-determined kilometric schedule, i.e., maintenance is performed after a certain amount of kilometres is travelled. Since present-day computers can achieve high computational power, it is possible to implement numerical tools to estimate the wear of wheel profiles. These numerical models can enable the simulation of the running behaviour of railway vehicles in operating conditions characterized by worn wheel profiles, thus allowing to assess the running safety during the whole life of the wheels. At the same time, numerical codes for wheel profile wear estimation can be used to better plan the maintenance operations throughout the expected life of the wheels. In fact, the EN 15313 standard [149] defines the main geometrical requirements for the transversal profile of railway wheels, hence launching wear simulations can be a great support to accurately identify the time interval between subsequent maintenance interventions.

A recent collaboration of the research group with an industrial partner highlighted that many key points regarding the implementation of wear models deserve a further understanding. Therefore, as a part of the activities carried out during the development of the present thesis, a comprehensive state-of-the-art research was carried out to survey the typical strategies for numerical modelling of wear of wheel and rail transversal profiles [128]. The state-of-the-art review highlighted that nowadays, the simulation of the wheel profile wear is carried out by means of numerical tools with a module for the dynamic simulation of the vehicle running behaviour and a module for the implementation of the wear law. However, different solutions can be adopted to update the profiles after the wear computation, which can be summarized in the four flow charts provided in Figure

100. The simplest strategy is the one corresponding to case (a), whereby a dynamic simulation is launched, typically in a commercial MB code, and then wear is computed without subsequent iterations. This approach does not allow to model the mutual influence between wear and vehicle dynamics, but it can be adopted if the goal of the simulation is to assess the dependency of wear on some vehicle/track parameters, at the initial stages of vehicle design. Moreover, this first strategy allows to easily run the computation with wear modules available in commercial MB codes, with obvious benefits in terms of implementation easiness. Nonetheless, to obtain reliable results, it is essential to simulate short travelled distances. A step forward can be taken with the approach sketched in case (b), whereby the numerical code still launches a single MB simulation, but wear is computed at discrete steps, with an update of the wheel profile at the end of each iteration of the wear computation module. Because of the advances in the field of co-simulation and parallel computing, this approach currently has a limited application, but it was used in the past to trade-off accuracy and speed of the computation [150,151] and to implement advanced contact models, even relying on the FE method, in the wear module [152,153]. The typical approach followed nowadays, see Figure 100(c), is based on an iteration of dynamic simulations followed by a wear calculation. Each dynamic simulation is run with fixed profiles, under the reasonable hypothesis that due to the large-time scale involved in the wear evolution, the vehicle dynamics can be considered unaffected by wear, as long as the simulated travelled distance is not too large. Finally, a recent advance in the field is the online update of the profiles during the dynamic simulation, with a continuous update of the profiles for the subsequent step of the dynamic simulation [154,155], as depicted Figure 100(d). Nonetheless, this strategy can be critical in terms of computational stability, and the wheel-rail contact algorithm implemented in the dynamic module must be able to deal with profiles changing at each time step.

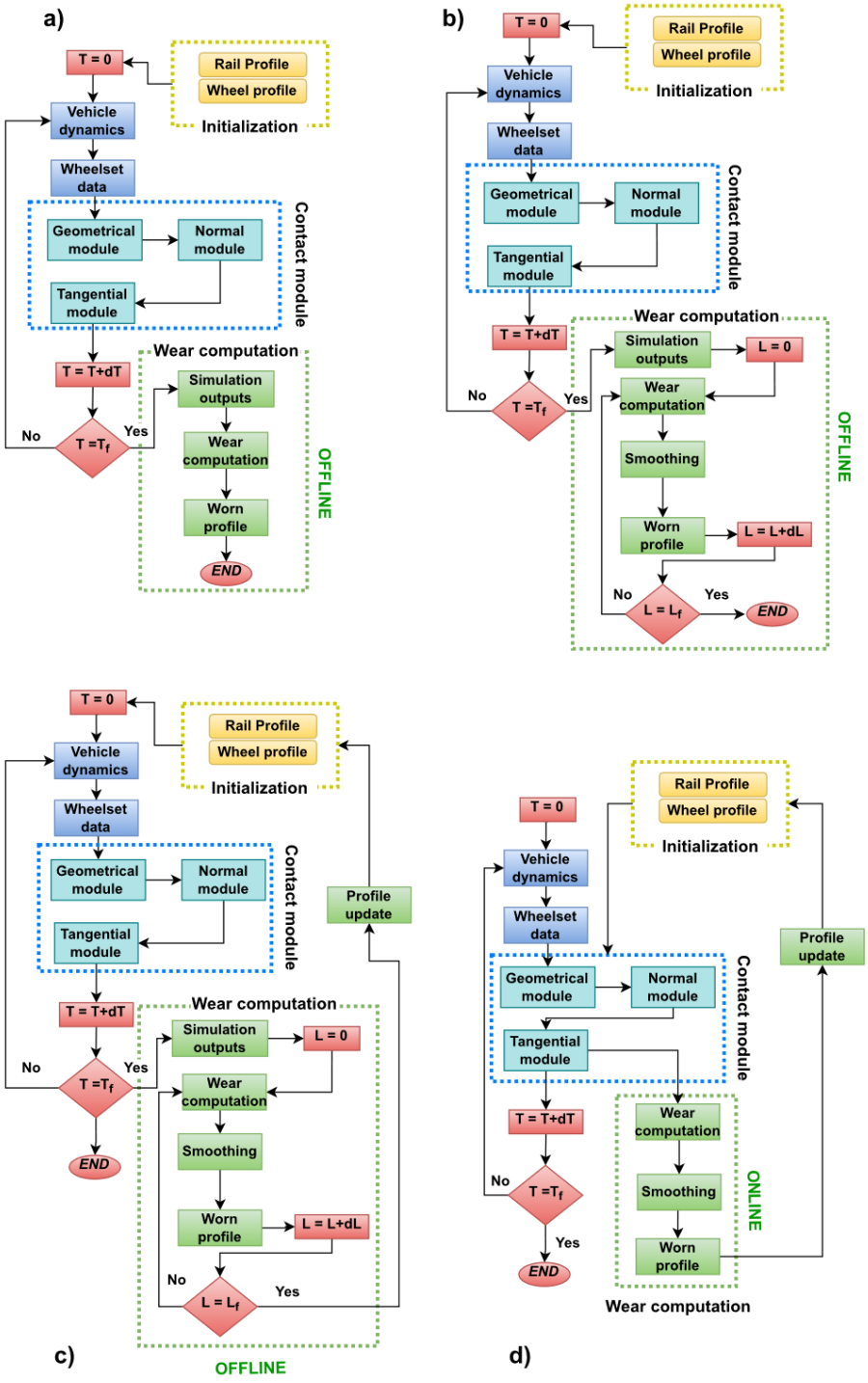

Figure 100: Strategies for the update of wheel worn profiles [128].

The state-of-the-art review activity highlighted that among the key points in wear modelling deserving further investigation is an assessment of the modelling accuracy of built-in modules available in MB codes. More in detail, since the collaboration with the industrial partner was carried out using Simpack as the reference MB code for vehicle dynamics simulations, which relies on a global approach for the implementation of Archard and Krause-Poll wear law, it seems worthwhile to study the difference that can be expected between local and global approaches. Some works in the literature previously dealt with the topic, however knowledge is still far from a last answer. In fact, a collaboration between university scholars and ALSTOM Ferroviaria investigated the differences between local and global approaches, but only considering the USFD wear law [156], and without benchmarking the results against the outputs of a commercial module. On the other hand, Ignesti et al. [157] benchmarked the results of an in-house wear code, implementing a local approach, with the results of the Simpack wear module. Nonetheless, whilst the local approach used the USFD wear law, the worn profile calculated by Simpack was obtained with the global implementation of the Krause-Poll equation.

Therefore, one of the activities performed in the frame of the present thesis concerned a preliminary comparison between the local and global application of the KTH Archard's wear law, with a benchmarking against the outputs of the Simpack wear module. In fact, it is of great interest to better understand the validity and the reliability of the wear algorithm implemented in a commercial multibody code, as previous works of the research group proved that the numerical simulation of wear can be numerically unstable [158]. The comparison of the two approaches is essential to develop new in-house wear algorithm that the research group could use in future upgrades of its activities dealing with railway vehicle dynamics modelling and numerical simulation of the wheel-shoe mechanical and thermal behaviour. The differences between the global and local applications of wear laws are shown in Figure 101. The starting point of the computation is always the forces and creepages at the wheel-rail contact patch, which are commonly obtained from the outputs of a MB dynamic simulation. If a global approach is chosen, the total worn volume can be estimated. However, as the computation typically aims to identify the shape of the worn wheel profile, the wear depth distribution along the profile must be identified. Therefore, global algorithms rely on a priori assumptions to spread the total worn volume along the profile and obtain a distribution of wear depths. On the other hand, when a local approach is selected, the first step of the computation is the calculation of the

distribution of sliding speed and tangential pressure over the contact patch, by means of local contact models, such as FASTSIM. The main advantage of the local approach over the global one is that once the distributions of the tangential pressure and slip speed are known, the calculation of the wear depth in each cell of the contact patch grid is straightforward, and no a priori assumption is to be formulated. For both approaches, the final output is the shape of the worn profiles, which can be then used in a new iteration of the dynamic simulation.

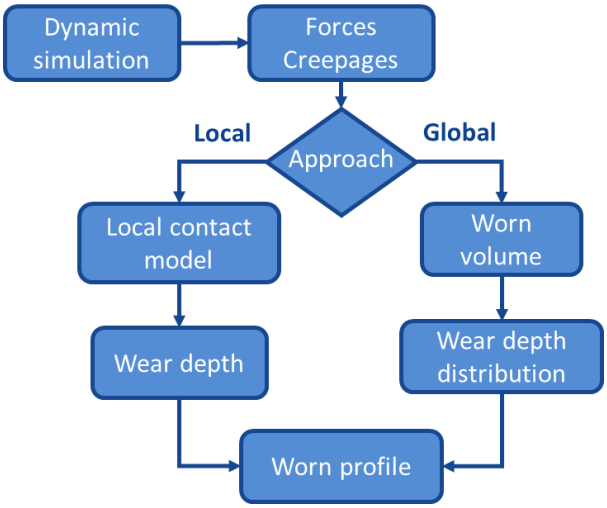

Figure 101: Implementation of global and local approaches for wear computation.

The computational framework built to evaluate the differences between the local and global applications of the KTH wear law is depicted in Figure 102. The first step is the dynamic simulation of a reference railway vehicle modelled in the Simpack MB code. The reference vehicle chosen to carry out this activity is the Aln663 diesel railcar, which operates on lines featuring high tortuosity levels. The MB model of the Aln663 diesel railcar was had already been implemented by the research group before the beginning of the present thesis. Nonetheless, to perform the comparison between the outputs of the Simpack wear module and the results computed by in-house local and global application of wear laws, a Simpack output project file (with *.spf* extension) was specifically built, in order to extract the main output results at the end of the dynamic simulation. The generation of the *.spf* project file is essential for the future upgrades of the activities, as a cascade of dynamic simulations followed by wear calculation and profile replacement is going to be launched. The outputs collected at the end of the dynamic simulation include the states of all bodies in the model, the values of contact forces and creepages in each contact patch for each time step, as well as

the wheel worn profile calculated by the Simpack wear module. These outputs are available from the *.spf* file and stored in a text file which is then loaded by a dedicated MATLAB routine, performing both global and local wear calculations. In this preliminary stage, since the activity aimed to compare the two approaches and to benchmark the results with the worn profile computed by the Simpack wear module, a single dynamic simulation with a single wear calculation was run, thus following the flow chart in Figure 100(a).

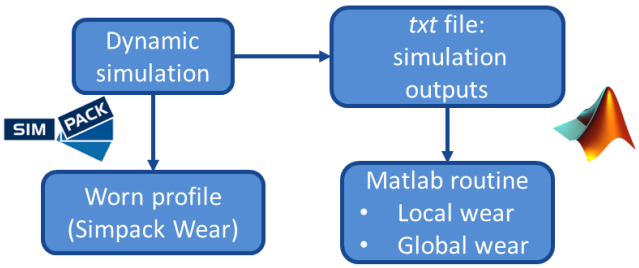

Figure 102: Computational framework built for the comparison of global and local approaches in wear calculation.

The Simpack model includes the model of both the Aln663 diesel railcar and of the track. To run a fast simulation, allowing to easily compare the outputs of the local and global approaches, a simple track with four curves was defined in the present thesis, see Figure 103, which shows the curve radius, the superelevation and the reference vehicle speed along the track. The curves have decreasing radii of 1000, 800, 600 and 400 m, and they are faced in both left and right-hand directions. The curves with radius of 1000 and 800 m have a superelevation of 150 mm, while curves with radius of 600 and 400 m have superelevation of 400 m. The speed profile decreases as the curve radius increases, and speed is constant in each track section with constant curve radius. The maximum speed at the beginning of the simulation is set to 120 km/h, which is the maximum speed allowed for the Aln663 railcar.

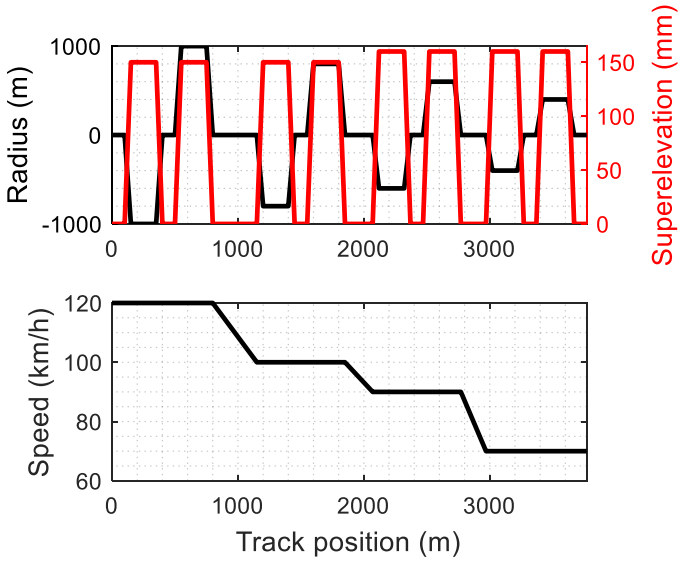

Figure 103: Track layout and speed profile (values of curve radius equal to zero refer to straight sections).

Focusing on the vehicle model, the Aln663 diesel railcar is a passenger vehicle equipped with two FIAT bogies. The inner wheelset of each bogie is powered, while the outer one is trailed. The primary and secondary suspensions of the FIAT bogie are both realized with helical springs, and the suspension forces in lateral and lateral directions are given by the shear stiffness of the springs. Moreover, the primary suspension includes a rubber element for the connection of the axle-box control arm to the bogie frame. The helical springs on the secondary suspensions are flexicoil springs, with a rubber element for the calibration of the shear stiffness. The Simpack model is sketched in Figure 104, where all model bodies are highlighted. More in detail, the model includes one coach, two bolsters, two bogies, four wheelsets and eight axle-boxes. Each body in the model has six degrees of freedom (dofs), set via the Simpack *general rail track joint*, except for the axle-boxes, which are only allowed to spin along the lateral axis with respect to the wheelsets. On each bogie, the helical springs of the primary suspension are modelled as Simpack flexicoil spring elements, with definition of stiffness in axial and shear directions. The rubber joint for the connection of the axle-box control arm to the bogie frame is simulated by means of a Simpack bushing force element. On the other hand, the flexicoil springs of the secondary suspension are modelled with Simpack shear spring elements. The coach is connected to the two bolsters with bushing elements with large values of stiffness, to simulate a rigid joint. The Simpack models also simulates the lateral bump stops of the secondary

suspensions, the dampers of both suspension stages and the anti-roll bars. The wheel-rail tangential forces are calculated in the model using Kalker's FASTSIM algorithm, which is directly implemented in Simpack. The speed profile shown in Figure 103 is followed by applying proper torque values on the powered wheelsets (coloured in grey in Figure 104), which are calculated with a proportional controller. Further details about the implementation of the model can be found in [158].

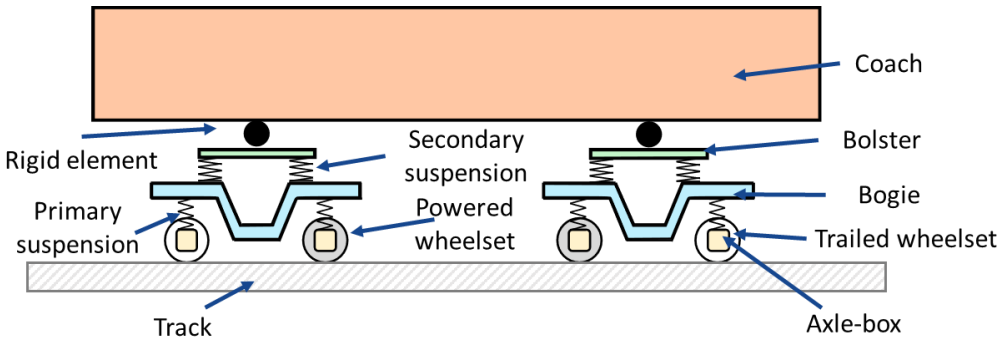

Figure 104: Sketch of the Aln663 diesel railcar MB model [159].

As previously outlined, the implemented numerical tool calculates wear using the KTH implementation of Archard's wear law. Based on the indications provided by Jendel [142], the theoretical wear coefficients given by the experimental KTH wear map, see Figure 99, should be reduced to account for the effects of natural and artificial lubrication on the track. Therefore, the wear coefficients given in Table 21 are applied in the four wear zones identified by the KTH wear map, see Figure 99. The activity aims to not only compare the outputs of global and local approaches, but also to investigate the modelling accuracy of the Simpack wear module. The Simpack wear module calculates the worn profile using a global approach, however the strategy adopted to spread the worn volume along the profile is not declared, due to intellectual property reasons. For this reason, a global method was developed and implemented in the MATLAB routine, with the goal to better understand the strategy adopted by Simpack.

Table 21: Wear coefficients adopted in the numerical wear calculation.

Wear zone.	Wear regime	Wear coefficient
I	Mild	0.7E-4
II	Severe	5E-4
III	Mild	0.7E-4
IV	Catastrophic (seizure)	50E-4

The MATLAB global algorithm implemented in the frame of the present thesis calculates the worn volume for each contact point in each time step with equation (4.2), starting from the outputs of the MB simulation, which are stored in a text file. The Archard coefficient is extracted from the KTH wear map plotted in Figure 99, but using the coefficients given in Table 21. The limit pressure identifying the seizure zone is set to 80% of the Brinnel hardness of the wheel steel, considered equal to 300 HB. Once the total worn volume is known, the normal wear depth along the lateral coordinate of the contact patch y is calculated under the assumption of a semi-elliptical distribution of the worn volume, as stated by equation (4.16), where b is the lateral semi-axis of the contact ellipse, R_{cp} is the wheel radius at the contact point and δ is the contact angle. Equation (4.16) states that wear is uniformly spread along the circumferential direction, as indeed the wear model only focuses on the wheel profile wear, assuming that the wheel shape is still axisymmetric along the circumferential direction.

$$\Delta z_n(y) = \frac{2}{\pi b} \frac{V_{worn}}{2\pi R_{cp} \cos\delta} \sqrt{1 - \left(\frac{y}{b}\right)^2} \tag{4.16}$$

On the other hand, the local model implements the FASTSIM algorithm to calculate the distribution of stresses and sliding speeds on the contact patch. The FASTSIM method implemented in the MATLAB routine proved to ensure a perfect agreement in terms of force values with respect to the outputs of the MB simulation. The normal wear depth is calculated in each element of the contact patch grid with the local implementation of Archard's law, as stated by equation (4.3). To obtain a uniform profile, the wear depth along each longitudinal strip is

summed and averaged along the wheel circumference, to obtain a distribution of wear depths along the lateral contact patch coordinate y, as stated by equation (4.17), where n_x is the number of elements along the longitudinal contact patch grid, depending on the discretization step, v_0 is the rolling speed and Δt is the sampling step of the dynamic simulation outputs.

$$\Delta z_n(y) = \sum_{k=1}^{n_x} \frac{\Delta z_n(x_k, y)}{2\pi R_{cp}} \cdot v_0 \Delta t \tag{4.17}$$

Both global and local methods allow to compute the distribution of the normal wear depth along the lateral coordinate defined over the contact patch grid. Nonetheless, to obtain the worn profile, the material loss along the lateral (Y) and vertical (Z) coordinates of the wheel profile must be evaluated. For each contact point position and time step, the removed material is calculated according to equation (4.18), where γ is the local profile gradient, which depends on the lateral position on the profile, and ΔY and ΔZ are the wear depths along lateral and vertical directions. The wear depths are cumulated for each time step and each contact point position, and finally the worn profile is obtained by removing the material from the original profile. Please note that in equation (4.18), the normal wear depth is expressed as a function of the lateral profile coordinate, instead that as a function of the local coordinate on the contact patch. In fact, the distribution of the normal wear depth must be re-interpolated on the wheel profile coordinates.

$$\begin{aligned} \Delta Y(Y) &= \Delta z_n(Y) \frac{1}{\sqrt{1+\gamma(Y)^2}} \\ \Delta Y(Y) &= \Delta z_n(Y) \frac{\gamma(Y)}{\sqrt{1+\gamma(Y)^2}} \end{aligned} \tag{4.18}$$

The results of the comparison between the two approaches are given in Figure 105, which plots the wear depth along the transversal profile coordinate for the three wear algorithms, namely the global method used by the Simpack wear module, the MATLAB global model and the MATLAB local implementation of Archard's law. Because of the short simulated travelled distance, the wear depth calculated by each model is multiplied by a scaling factor equal to 20, which is usually referred to as a *wear multiplier*. The wear multiplier is often used in wear simulations to magnify the amount of worn material, in order to reduce the computational effort. In fact, in the present case study, the track has a total length

of 3770 m. The wear multiplier equal to 20 virtually amplifies the wear depth, as if the simulated distance was equal to 75.40 km.

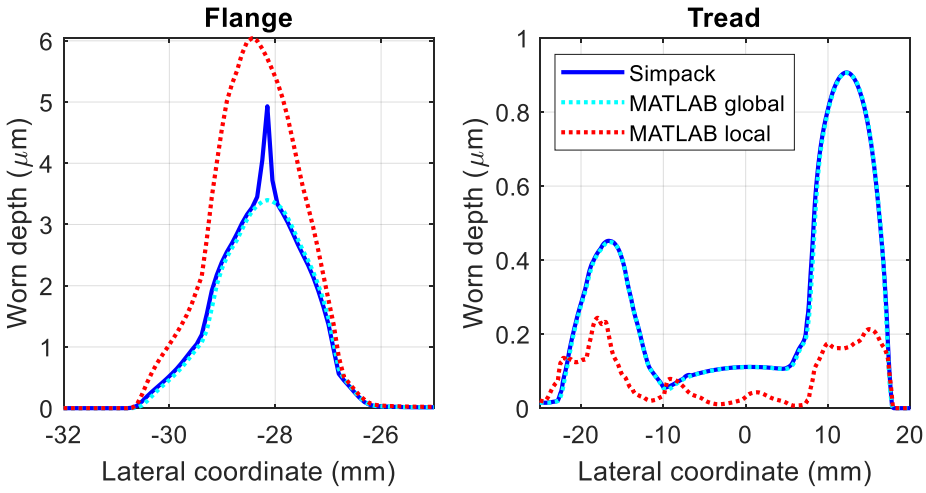

Figure 105: Results of wear computation with local and global approaches.

As shown in Figure 105, a good agreement exists between the outputs of the Simpack wear module and the wear depth predicted by the MATLAB global function. The total worn volume according to the Simpack wear module is equal to 57.9 mm^3, while the MATLAB global routine predicts a worn volume of 56.3 mm^3, with an error below 3%. The Simpack model predicts a wear depth peak on the flange, at a lateral position of approximately -28 mm, but this localized difference can be tolerated, as because of the aforementioned intellectual property reason, there is no chance to know which strategy Simpack applies to spread the worn volume along the profile. Moreover, differences could be also related to different interpolation methods used by the two global routines. Nonetheless, the result that immediately stands out from the plot is that the local method predicts larger wear on the flange, and lower wear depths on the tread. Concerning the total worn volume, the local approach predicts a total removed volume equal to 47 mm^3, which is quite lower compared with the one calculated by the global methods. The explanation to this behaviour can be easily given by identifying the wear regimes on reference contact positions on the flange and on the tread, see Figure 106. When the contact point lies on the tread, most of the contact patch elements are in the adhesion zone, whereby wear is zero. Nonetheless, the global approach tends to compute wear on all lateral positions, thus the estimated wear depth increases. Conversely, when the contact point is on the flange, although the

average wear regime is the mild regime, there are few elements that can fall into the catastrophic regime. As the wear coefficient of the seizure zone is definitely higher compared to wear coefficient for the mild zones, the wear computed by the local method increases, as the global algorithm adopts the wear coefficient for the mild regime, even in the zones where the local regime is catastrophic. Concerning the computational effort, the local method is 1.5 times slower than the global method in the implementation of the MATLAB routine, while no data is available for the Simpack wear module computation.

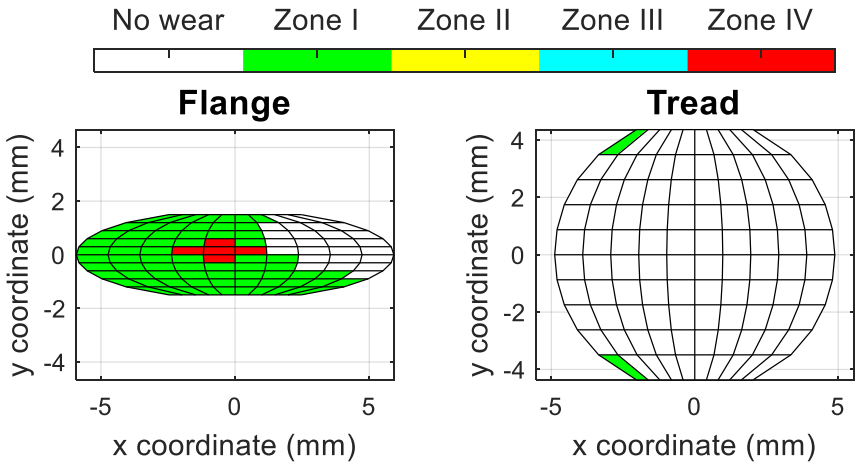

Figure 106: Wear regimes over the contact patch (tread and flange contact).

The activity shown in this section is clearly at an early stage, and much work needs to be carried out to obtain a further understanding of the differences between the local and global approaches. Nonetheless, a first outcome is that the global implementation of Archard's wear law should be avoided when the goal is the accurate determination of the worn profile shape, because the global method is not capable of capturing the local behaviour of the wear phenomenon. As larger differences between the two methods are expected in case of simulations with longer travelled distances, work is already going on to perform loop of dynamic iterations with profile updates, as shown in Figure 100(c). Moreover, the MATLAB global routine leads to outputs close to the ones of the Simpack module on the presented case study, but a further validation shall be carried out on different track layouts, considering different values of curve radius, superelevation and running speed. Furthermore, the comparison performed on the KTH wear law should be extended to consider other wear laws, especially the Krause-Poll law, which is the other expression available in Simpack.

In conclusion, the main outcome of the activity carried out in the frame of the present thesis is the implementation and validation of in-house MATLAB routines for the calculation of the worn profile based on the main outputs of MB dynamic simulations. The development of in-house algorithms is essential to overcome the main limits of the Simpack wear module, which features numerical instabilities. The preliminary validation of the newly built routines against the outputs of the Simpack wear module is encouraging, so future efforts must be made to optimize the algorithms to ensure a high computational efficiency and a high numerical stability of the computation, especially in simulation scenarios requiring the update of the worn profile for a next iteration of dynamic simulation.

4.2 Wheel-shoe thermo-mechanical interaction

4.2.1 Brief overview on tread braked wheel thermal models

As shown in the chapter 1, tread braking is the most common braking system adopted on freight wagons, because of its low cost and simple design. Nonetheless, since the braking torque is obtained by the friction between the wheel and the shoes, a friction heat flux flows into the wheel, thus leading to a wheel surface temperature rise. Thermal stresses and strains can eventually damage the wheel tread surface, with possible generation of shelling, spalling, fatigue cracks and wheel warping [160,161]. Furthermore, local steel microstructure changes can arise if fast cooling occurs after reaching high temperature peaks during the braking action, with possible formation of brittle martensite. Local formation of martensite has been witnessed near wheel flats produced in braking operations after reaching full sliding conditions [162-164]. At the same time, the adoption of new composite and sinter brake shoe materials must be safely investigated, as new materials must not cause excessive temperature rises during braking operations, which may eventually be another possible source of steel microstructural changes. In fact, despite reducing rolling noise and avoiding the formation of hot spots, new composite and sinter shoe materials are known to cause higher thermal stresses on the wheel surface [165]. Due to the aforementioned reasons, the numerical simulation of the wheel-shoe thermo-mechanical behaviour is essential to evaluate the thermal stresses generated on tread braked wheels. Furthermore, the development of proper codes can thrust the implementation of more reliable monitoring algorithms, able to detect anomalies of the braking system in real time, based on temperature measurements.

Nowadays, the simulation of the wheel-shoe contact in terms of both mechanical and thermal behaviour is performed via finite element (FE) models. Over the last decades, Swedish researchers have been implementing a FE model

for the computation of the temperature of tread braked wheels [166]. The model is axisymmetric, so it is not able to directly compute local temperature peaks in circumferential direction, as the friction heat flux is assumed to be uniform along the circumferential direction. Another method witnessed in the literature is the development of FE models considering the real three-dimensional (3D) geometry of wheels and shoes [167-169], but because of the large computational effort required by this modelling approach, the simplifying assumption of uniform contact pressure over the wheel-shoe contact patch is typically formulated, thus avoiding the solution of the wheel-shoe contact problem. To compute the distribution of the wheel-shoe contact pressure along the circumferential direction, Suresh Babu and Siva Prasad [161] developed a FE bi-dimensional (2D) model, only considering the wheel thermo-mechanical behaviour in a plane normal to the wheel axis. This kind of models can detect the generation of hot spots in the circumferential direction, and the plane stress condition can be considered as reasonable, since the axial thickness of brake shoes is quite smaller compared to the wheel radius. Nonetheless, the FE model proposed by Suresh Babu and Siva Prasad relied on ANSYS elements performing a weak coupling of the thermal and mechanical dofs, thus solving the contact problem in each time step of the computation. However, the results of their simulation highlighted that the contact pressure distribution has limited changes during the braking operation, hence it is slightly affected by the temperature rise.

Based on the brief overview of the modelling strategies for the simulation of the temperature of tread braked wheels given in the previous lines, the research group has recently started working on the development of a plane FE model, with the aim to achieve a high computational efficiency together with an accurate modelling of the main thermal fluxes involved in braking operations. Compared to the model proposed by Babu and Prasad, the new model developed by the research group completely decouples the thermal and contact problems, to ensure a higher computational efficiency.

4.2.2 Wheel temperature calculation tool

The flow chart of new tool for the computation of the temperature of tread braked wheels in sketched in Figure 107. The design of the computational framework is one of the major contributions of the present thesis to the works of the research group dealing with the simulation of the wheel-shoe thermo-mechanical behaviour. The tool includes a structural module, for the static solution of the wheel-shoe contact problem, and a thermal module for the calculation of the

wheel temperature via a transient simulation. Both the contact and the thermal modules are implemented in the ANSYS Mechanical APDL commercial FE code. The inputs for the FE model are calculated with a simplified version of the LTDPoliTo code, which simulates the braking operations of an isolated wagon. The simplified version of the LTDPoliTo code computes speed, friction coefficient and normal force on the blocks during a braking operation, which then become the main inputs for the contact module. The contact module calculates the distributions of normal and tangential pressure on the wheel-shoe contact patch. The distribution of the tangential pressure is then adopted to estimate the heat flux flowing into the wheel, which becomes the main input for the thermal module. The latter is run to evaluate the temperature of the tread braked wheels, considering three main heat fluxes, namely:

- *Friction heat flux*. Friction heat generated at the wheel-shoe contact patch due to friction and sliding.
- *Convection*. Cooling from the surrounding air.
- *Rail chill effect*. Wheel surface cooling due to the contact with the *fresh* rail.

The tool can simulate drag braking operations at constant speed on a downhill section as well as stop braking operations. Furthermore, the contact module can deal with both 1Bg and 2Bg block configurations. The 1Bg configuration features 1 brake block per wheel, while the 2Bg configuration includes two brake blocks per wheel. The acronym Bg is from German language, and it indicates that each block holder has only one brake shoe, with typical length of 320 mm.

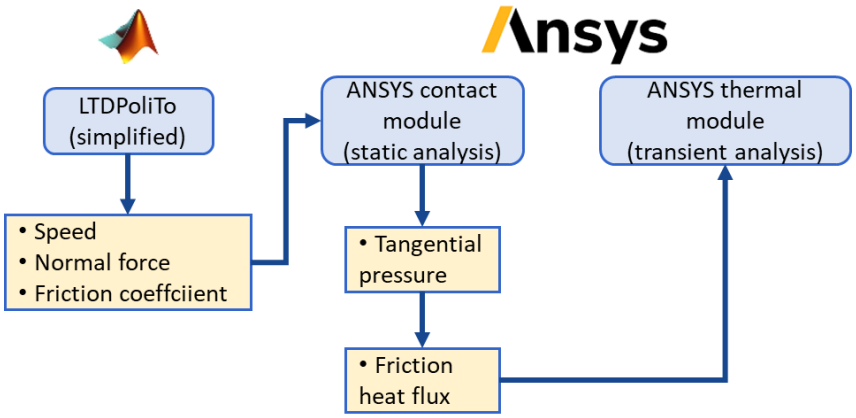

Figure 107: Flow chart of the tool for the tread braked wheel temperature calculation.

The MATLAB routine implementing the simplified version of the LTDPoliTo code was totally developed in the frame of the present thesis. It considers the LTD

equation, see equation (2.1), written for an isolated vehicle, as well as the rotational equilibrium of a wheelset. The latter equation would allow theoretically to evaluate degraded adhesion conditions, but in the preliminary simulations performed at this initial stage of the code development, only dry contact conditions were considered. To simplify the model, straight track sections are simulated, so that the curving resistance can be neglected, and the braking effort is assumed to be uniform on all wheelsets of the wagon. Therefore, with an approach similar to the one adopted in §3.6.2, the LTD equation for the isolated wagon can be written as stated by equation (4.19), while the rotational equilibrium of the braked wheelset is stated by equation (4.20). In equations (4.19) and (4.20) the same symbols as in chapter 2 and §3.6.2 are used, and. positive values refer to downhill sections and deceleration. The ordinary resistant forces in equation (4.19) are calculated using the expression suggested by the international benchmark, see equation (2.5).

$$m\ddot{x} + mgi_g - F_{ord} - n_{ax}F_x = 0 \tag{4.19}$$

$$T_b = I_{w,yy}\dot{\omega}_w + F_x r_w \tag{4.20}$$

The braking torque T_b can be related to the normal force on each brake block $F_{b,N}$ according to equation (4.21), where n_{bw} is the number of blocks per wheel and μ_b is the wheel-shoe friction coefficient, which for cast iron brake blocks can be calculated with the Karwazki's expression as a function of speed and force on the brake block, as stated by equation (2.29).

$$T_b = 2n_{bw}F_{b,N}\mu_b(V, F_{b,N})r_w \tag{4.21}$$

In case of a drag braking operation, equations (4.19) and (4.20) can be regarded as algebraic equations, and their solution is straightforward. In fact, if the track grade and running speed are known, the wheelset longitudinal force F_x can be calculated from equation (4.19), setting the deceleration to zero, as speed is constant during drag braking operations. Therefore, the force on the brake block is constant and it can be found by solving equation (4.21). Please note that if the wheel-shoe friction coefficient is modelled as a function of the normal force, an iterative scheme is required to calculate both the friction coefficient and the normal force. Conversely, concerning stop braking operations, the input of the simulation is the pressure rise in the brake cylinder, which can be modelled according to a heuristic exponential pressure similar to the one introduced in §2.3.2, see equation (2.25). The brake cylinder pressure is assumed to rise

according to the expression given in equation (4.22), where $p_{cyl,max}$ is the maximum brake cylinder pressure, t_{app} is the brake application delay and the parameter τ is calculated as shown in §2.3.2, as a function of the brake cylinder filling time. Please note that equation (4.22) could be replaced by the approach shown in §2.3.2, which allows to calculate the normal force as a function of the braked weight only. Nonetheless, in this work, a reference wagon as suggested in annex O of the UIC 544-1 leaflet was considered, for which all main parameters of the braking system are known, see Table 22.

$$p_{cyl}(t) = p_{cyl,max}\left[1 - e^{-(t-t_{app})/\tau}\right] \tag{4.22}$$

Table 22: Parameters of the reference wagon

Quantity	Value
Central rigging ratio	1.47
Ratio after central rigging	8
Brake cylinder return spring force	1.5 kN
Slack adjuster force	2 kN
Brake rigging efficiency	0.83
Block configuration	2Bg
Changeover weight	44 tonnes
Maximum brake cylinder pressure	Empty: 1.3 bar, Loaded: 3.8 bar
Weight on rails	Tare: 20 tonnes, Fully loaded: 80 tonnes

Once the brake cylinder pressure is determined according to equation (4.22), the normal force on the brake blocks can be calculated according to the equations provided in the UIC 544-1 leaflet, see equations (1.9) and (1.10). At this point,

equations (4.19) and (4.20) represent a system of ordinary differential equations, because speed varies during a stop braking operation, but in each time step, three unknowns must be identified, namely linear and rotational deceleration, and the wheelset longitudinal force. To solve this issue, the heuristic contact model developed by the research group in past activities is introduced, to relate the longitudinal force to the creepage at the wheel-rail interface [104].

As already stated, the main outputs of the simplified version of LTDPoliTo, simulating an isolated vehicle, include the speed of the wagon, the force on each brake block and the friction coefficient during the simulation. In drag braking operations, such quantities are constant, while for stop braking operations, they are calculated as time histories. Nonetheless, to avoid launching a huge number of FE analyses, a single value of friction coefficient and normal contact force is considered in the static module. More in detail, the maximum value of brake block force and the average value of friction coefficient are selected as constant parameters to be used in the structural module for the solution of the wheel-shoe contact problem.

The contact model implemented in ANSYS Mechanical APDL is sketched in Figure 108, for the 2Bg configuration. Nonetheless, the model can be easily adapted to a block configuration with a single brake block, by simply excluding one of the two brake blocks. The model considers plain stress conditions, and the axial thickness of the wheel and shoe is set equal to 80 mm. The wheel is meshed with PLANE183 elements, with 2 dofs per node, corresponding to translations in radial and circumferential directions, and quadratic shape functions. The circumferential dof of the elements on the inner radius of the wheel, corresponding to the wheelset hole, is suppressed, but the rotation is modelled by applying the ANSYS CMROTATE command. The external radius of the wheelset is set equal to 460 mm, while the inner radius is assumed equal to 80 mm. The brake shoe has a circumferential length of 320 mm, and it is meshed with the same elements used for the wheel. A layer of CONTA172 is applied to the nodes on the wheel outer periphery that are in contact with the shoes, while a layer of TARGE169 elements is defined over the brake shoe inner surface. These ANSYS built-in elements allow to deal with the conformal contact between the wheel and the shoe, which is solved by means of a default ANSYS algorithm, able to adjust the contact stiffness automatically at each iteration. The contact algorithm computes the tangential and normal contact pressure distributions, optionally considering the effects of sliding and friction and the dependency of the normal contact pressure on the tangential stresses. The normal load acting on each shoe is

applied in radial direction on an external node, which is connected to the outer periphery of the shoe by means of MPC184 elements, acting as rigid links, thus assuming that the stiffness of the brake block holder is much larger compared to the one of the shoe material.

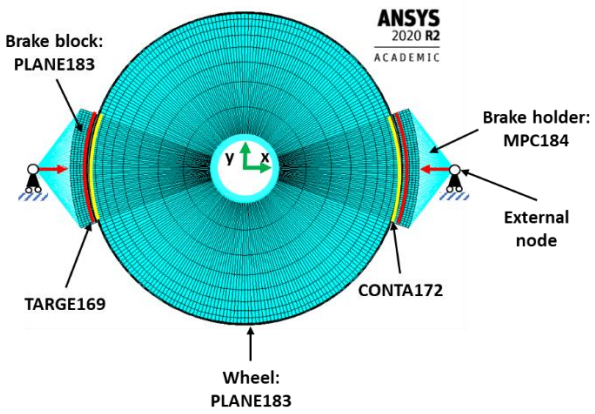

Figure 108: Sketch of the ANSYS contact module [170].

Preliminary results of the normal contact pressure calculated by the contact module can be observed in Figure 109, which plots the pressure distribution along the angular position on the brake shoe for two values of normal load, namely 28.3 kN and 40 kN. Since full sliding conditions exist at the wheel-shoe contact interface, the tangential contact pressure can be calculated as proportional to the normal contact pressure distribution, through the wheel-shoe friction coefficient. The curves with a star marker in Figure 109 correspond to a simulation with no friction and no sliding at the contact interface, while curves with a square marker consider the effect of the previously neglected phenomena. When the contact algorithm accounts for friction and sliding, the pressure distribution becomes asymmetric and a pressure peak arises at the leading edge, corresponding to a block jamming effect. When friction is present at the contact interface, the pressure distribution must indeed be asymmetric to ensure the rotational equilibrium of the brake shoe. It is interesting to point out that because of the conformity between the wheel and shoe surfaces, the contact patch area is slightly affected by the value of the normal load. As a consequence, the maximum contact pressure tends to be proportional to the applied load. This consideration is exploited in the simulation of stop braking operations, to calculate a value of contact pressure proportional to the value of normal load during the initial stage of the braking operation, when the pressure in the brake cylinder is rising.

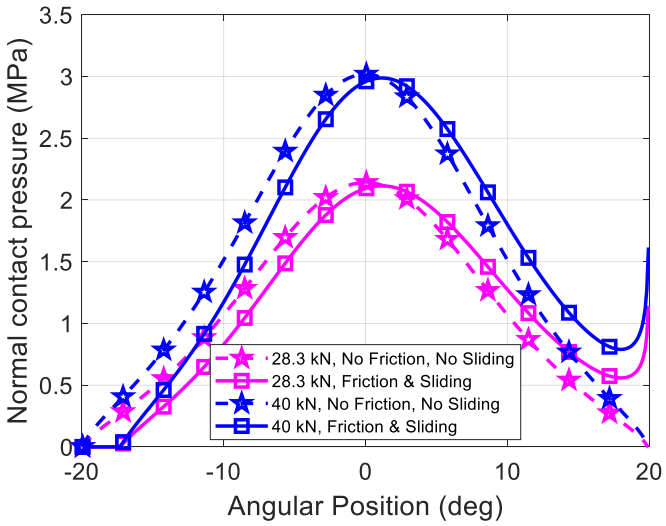

Figure 109: Effect of friction and siding on the contact pressure distribution .

The distribution of the tangential contact pressure along the circumferential direction is proportional to the distribution of the friction heat flux, as stated by equation (4.23), whereby q_{tot} is the friction heat flux, p_θ is the tangential pressure, θ is the circumferential position and v_{ws} is the wheel-shoe sliding speed, which can be considered equal to the wheel rolling speed, as a first approximation. The total heat flux is partitioned between the wheel and the shoe, according to a partitioning factor α, see equation (4.24), where q_w is the friction heat flux flowing into the wheel and q_b is the heat flux entering the shoe. The partitioning factor α is a function of the wheel and shoe thermal and mechanical properties, and it can be calculated according to the expression suggested by Pradhan and Samantaray [171], see equation (4.25), where κ is the thermal diffusivity, λ is the thermal conductivity, S is the contact surface and finally subscripts b and w refer to wheel and shoe. The thermal diffusivity κ is related to other thermal properties according to equation (4.26), where c_p is the specific heat and ρ is density. Figure 110 shows the partitioning factor for cast iron and composite brake shoes, considering both 1Bg and 2Bg block configurations. The properties of wheel steel, as well as of cast iron and composite shoes, are summarized in Table 23. Properties for composite shoes are extracted from a reference literature paper [172].

$$q_{tot}(\vartheta) = p_\vartheta(\vartheta) v_{ws} \tag{4.23}$$

$$q_w(\vartheta) = \alpha q_{tot}(\vartheta), \qquad q_b(\vartheta) = (1-\alpha) q_{tot}(\vartheta) \tag{4.24}$$

$$\alpha = \left(1 + \sqrt{\frac{\kappa_w}{\kappa_b}\frac{\lambda_b}{\lambda_w}\frac{S_b}{S_w}}\right)^{-1} \tag{4.25}$$

$$\kappa = \frac{\lambda}{\rho c_p} \tag{4.26}$$

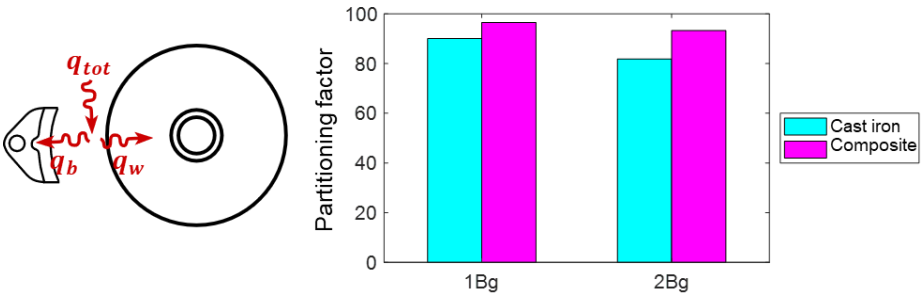

Figure 110: Partitioning factor for cast iron and composite shoes.

Table 23: Thermal and mechanical properties (wheel steel, cast iron and composite shoes)

Quantity	Wheel	Cast iron shoe	Composite shoe
Specific heat (J/kg/K)	487	560	1500
Thermal conductivity (W/m/K)	50	48	5
Density (kg/m^3)	7818	7100	2670
Young's modulus (GPa)	210	103	10
Poisson's ratio	0.283	0.25	0.25

The friction heat flux flowing into the wheel, calculated according to equations (4.23)-(4.26) is the main input for the thermal module, implemented in ANSYS Mechanical APDL and performing a transient analysis, to determine the

evolution of the wheel temperature during braking operations. The thermal module accounts for the effects of rail chill and air convection. The heat fluxes in the different zones of the wheel outer periphery are shown in Figure 111 for both 1Bg and 2Bg configurations. Each sector in contact with the shoe receives a certain amount of the friction heat flux, which is generated by the sliding contact with the shoe. This heat flux eventually leads to the temperature rise on the wheel tread surface. The rest of the wheel periphery is cooled down by the surrounding air, via a convective heat exchange. Finally, while the vehicle is running, the wheel always faces a new *fresh* rail, which tends to cool down the contacting wheel sector, via conductive phenomena. Figure 111 highlights that for the 1Bg configuration, only one sector of the wheel periphery is in contact with the shoe, and the remaining portion is cooled down by air convection and rail chill. Nonetheless, to obtain the same braking torque, a larger contact force is required in the 1Bg configuration case, which means that a larger amount of friction heat is produced.

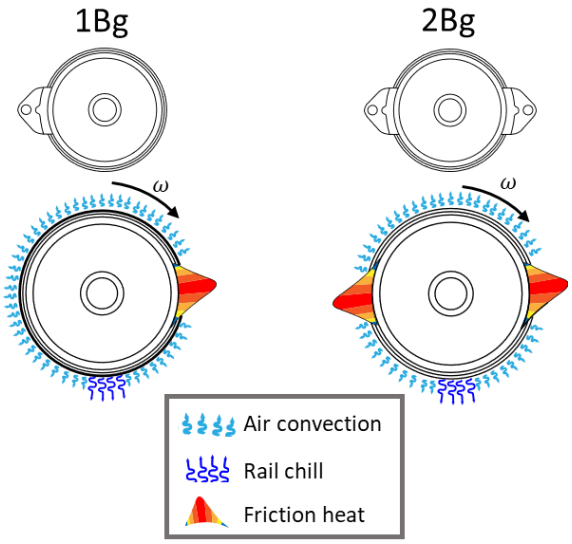

Figure 111: Heat fluxes on the wheel surface for 1Bg and 2Bg configurations.

The FE thermal model implemented in ANSYS Mechanical APDL is sketched in Figure 112. To reduce the computational load, only $1/8^{th}$ of the wheel is modelled, and adiabatic boundary conditions are applied on the lateral edges, thus assuming that the heat flux inside the wheel in circumferential direction is negligible with respect to the heat flux in radial direction. This assumption is confirmed by experimental data that Trenitalia kindly shared with the research group, highlighting that the temperature inside a tread braked wheel has a radial

layer-like pattern. The 45° sector of the wheel modelled in ANSYS is meshed with PLANE77 elements, featuring a single dof per node, corresponding to the node temperature. The boundary conditions are applied via the definition of layers of SURF151 elements, that are ANSYS built-in elements allowing to define different kinds of boundary conditions and external loads. The inner periphery and the lateral edges are covered with layers of SURF151 for the application of adiabatic boundary conditions. On the other hand, two different layers of SURF151 are applied on the outer periphery of the meshed wheel. One layer is used to define the friction heat flux, while the other one is used for the definition of convective heat fluxes. In fact, although the rail chill is a conductive phenomenon from a merely physical point of view, it is modelled in the thermal module as an equivalent convective load, following the approach developed by Vakkalagadda et al [165]. The air convection coefficient is calculated as a function of the wheel peripheral speed according to a literature correlation suggested by Churchill and Bernstein [173]. The cooling effect produced by air convection increases with increasing speed, as shown in Figure 113, which plots the air convection coefficient as a function of the wheel peripheral speed. Both the friction heat flux and the convective loads are applied by means of ANSYS tables, which are ANSYS built-in variable types specifically provided to deal with time and space varying loads. In fact, to reproduce the wheel rotation, the wheel mesh is fixed, and the thermal fluxes are rotated during the simulation. The numerical scheme adopted to solve the thermal differential equations of the transient analysis is the Crank-Nicolson's integration method [174], selected among the built-in solvers in ANSYS. Further details about the module implementation and about the calculation of the air convection and rail chill equivalent convection coefficient can be found in the works published by the research group [170,175].

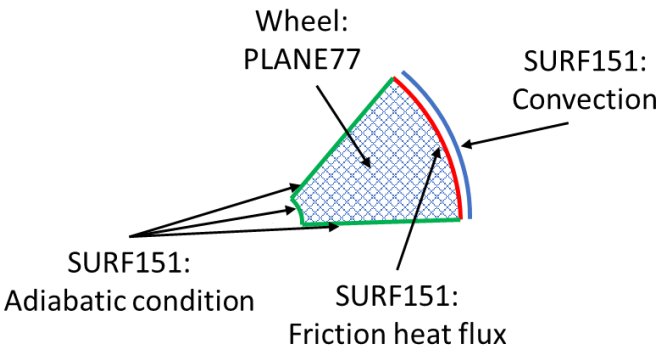

Figure 112: Mesh built in the thermal module.

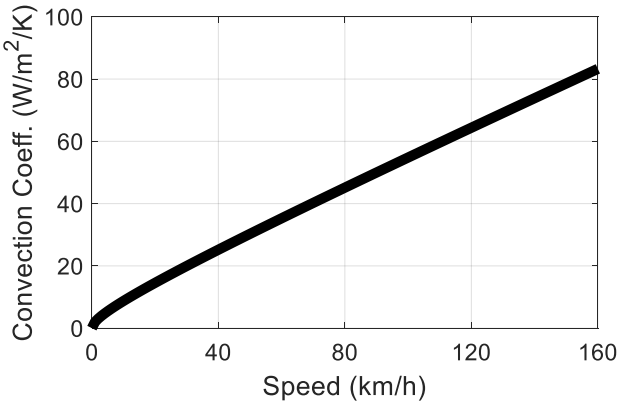

Figure 113: Air convection coefficient as a function of wheel speed.

4.2.3 Preliminary results

After building the computational framework described in the previous subsection, some preliminary simulations were run to assess the modelling capability of the new tool.

A first validation of the code was obtained by running a simulation under the same operating scenario as in the experimental tests carried out by Vernersson and Lundén by means of a full-scale brake test rig [172]. The simulated operation is a drag braking operation with P10 cast iron brake shoess in 1Bg configuration, constant speed of 100 km/h, axle-load of 10 tonnes and a braking power of 31.5 kW, which corresponds to a simulated track slope of about 11.6‰. In these conditions, the simplified version of the LTDPoliTo code estimates a wheel-shoe friction coefficient of 0.135 and a normal load on the shoe equal to 8.4 kN. Figure 114 shows the wheel temperature on a node close to the wheel outer periphery for a simulated time of 15 minutes. The average temperature of the last wheel revolution is equal to 246.8 °C, corresponding to a temperature increase from ambient temperature of 20°C equal to 226.8°C, which is in excellent agreement with the temperature increase of 225 °C extracted from Vernersson and Lundén's work. Please note the local sharp temperature drop in the zoomed views in Figure 114, which corresponds to the cooling action due to the rail chill effect.

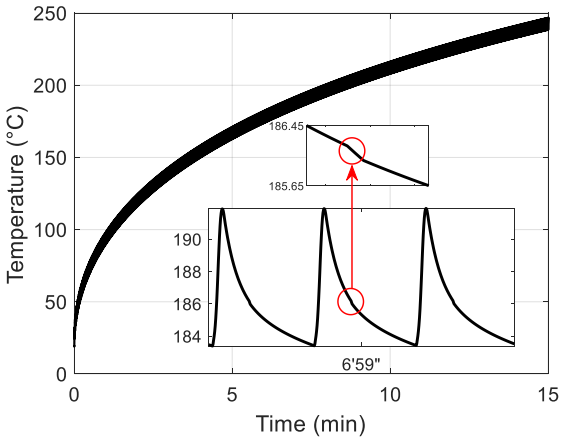

Figure 114: Wheel temperature calculated for the operating conditions suggested by Vernersson [172].

After validating the code against the experimental data provided by Vernersson, a simulation was launched to evaluate the differences in the temperature evolution related to the block configuration, thus comparing the 1Bg and 2Bg configurations. The simulation was run for a drag braking operation at 100 km/h on a slope of 21‰, which correspond to the operating condition suggested in the EN 13979 standard [176]. Since the 1Bg block configuration produces the braking torque on a single interface with the wheel, a larger pressing force is required with respect to the 2Bg configuration. The simplified LTDPoliTo routine for drag braking operation calculates a pressing force of 13.8 kN with a friction coefficient of 0.14, while for the 2Bg configuration, the normal force on each shoe is equal to 5.24 kN with a friction coefficient of 0.18. It is interesting to point out that since the 2Bg configuration splits the production of the braking torque on two separate interfaces, the normal force is more than halved compared to the 1Bg configuration, because for cast iron shoes, the friction coefficient calculated with Karwatzki's equation increases for larger values of the normal force on the shoe, see equation (2.29) and Figure 34. Figure 115 shows the distribution of the friction heat flux along the circumferential direction for 1Bg and 2Bg configurations, which is proportional to the tangential pressure distribution, as stated by equation (4.23).

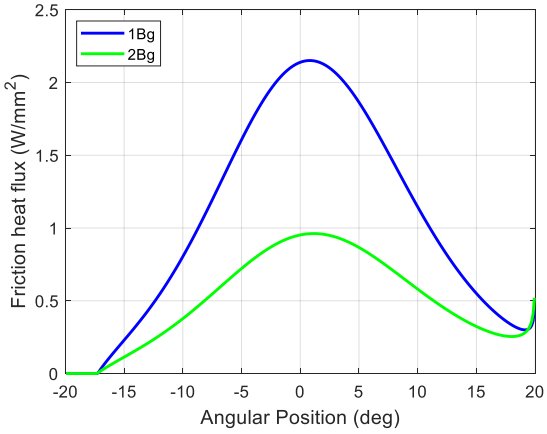

Figure 115: Heat flux flowing into the wheel for 1Bg and 2Bg configurations (operating conditions suggested by EN 13979 standard).

The results in terms of temperature evolution on a wheel surface node is given in Figure 116. The zoomed view in the lower part of Figure 116 shows that for each revolution of the wheel, two temperature peaks are recorded for a 2Bg configuration, while a single peak is obtained with the 1Bg configuration. As a consequence, the wheel braked with the 1Bg configuration features a larger temperature variation over a single revolution, thus confirming that the 1Bg configuration is much more harmful for the wheel compared to the 2Bg configuration, in terms of thermal stresses. The zoomed view in the upper left corner of Figure 116 shows the cooling due to the rail chill effect. It is worth mentioning that the simulation of the rail chill effect must be carefully evaluated. In fact, to correctly capture the rail chill in the simulation, the integration time step Δt must be lower than the time spent in the contact, which is equal to the ratio between the running speed v_0 and the longitudinal length of the contact patch 2a, i.e., $\Delta t < \frac{2a}{v_0}$. The latter inequality states that the time step must be reduced if the wheel-rail contact patch size decreases. Nonetheless, the cooling action due to the rail chill effect is reduced if the contact patch size is small. Therefore, the amount of heat flux due to the rail chill effect should be evaluated prior to each simulation, so as to possibly neglect the simulation of the rail chill and to increase the time step, with considerable benefits in terms of the computational efficiency of the simulation.

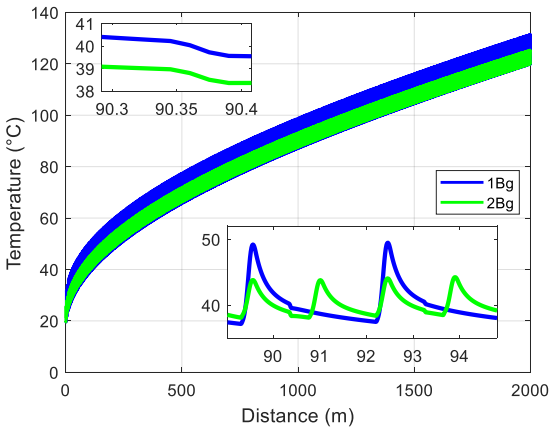

Figure 116: Temperature on the wheel surface for 1Bg and 2Bg configurations (operating conditions suggested by EN 13979 standard).

To assess the influence of air cooling on the wheel temperature, a new set of simulations was run, considering a constant braking power of 31.88 kW, which is the braking power corresponding to the operating conditions extracted from the EN 13979 standard. The simulations were launched on the reference wagon described in Table 22 for an axle-load value equal to 20 tonnes and block configuration with cast iron shoes featuring a 2Bg arrangement. Table 24 shows the main operating conditions in the three simulations run at constant braking power, highlighting that when speed is higher, the normal force on each block and the friction coefficient decrease. In fact, according to Karwatzki's formula, the friction coefficient increases at decreasing speed, because it tends to get closer to the value of static friction.

Table 24: Drag braking simulations at constant braking power.

Speed (km/h)	Grade (‰)	Friction coefficient	Normal force (kN)	Braking power (kW)
60	21	0.18	5.24	31.88
80	16.6	0.17	4.17	31.88
100	14.3	0.16	3.39	31.88

Figure 117 highlights that the friction heat flux distribution in the three simulations is approximately the same, because the braking power is constant, while the temperature evolution plotted in Figure 118 shows that if speed increases, the wheel surface temperature decreases, because of the larger amount of heat transferred from the wheel surface to the surrounding air via convective phenomena.

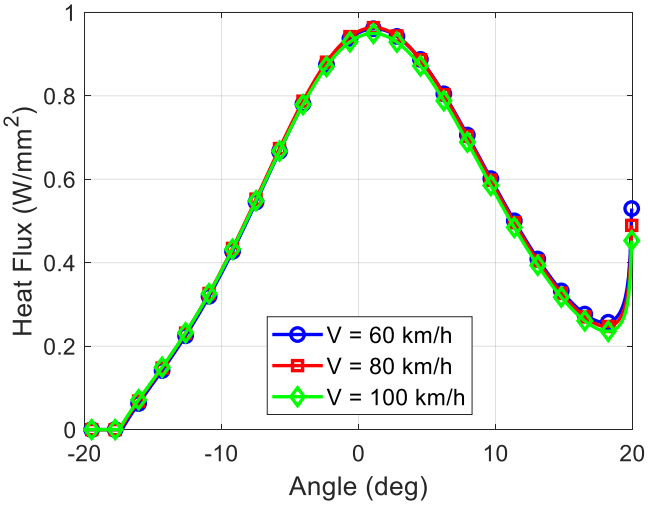

Figure 117: Heat flux calculated in simulations at constant braking power.

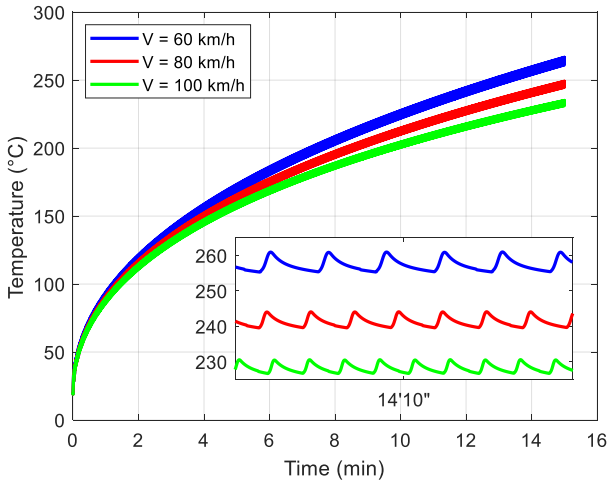

Figure 118: Temperature evolution for simulations at constant braking power.

As mentioned in the previous subsection, the new tool for the calculation of tread brake wheel temperature can deal with not only drag braking operations, but

also with stop braking operations. Therefore, a stop braking operation was simulated considering two different brake shoe materials, namely P10 cast iron shoes and LL composite shoes. The latter have frictional properties similar to cast iron shoes, but they feature different values of thermal and mechanical properties, see Table 23. The comparison is not extended to K shoes, characterized by a higher value of the friction coefficient, which is approximately constant with speed. In fact, K shoes commonly require changes in the braking system installed on the wagon, such as reduction of the brake cylinder diameter and/or adjustments to the rigging ratio, otherwise wheel locking conditions would be achieved easily. Since the frictional behaviour of cast iron and LL shoes is similar, this preliminary simulation was run under the assumption that the friction coefficient for LL shoes can be calculated with Karwatzki's formula. As a consequence, a single LTD simulation can be run with the simplified version of the LTDPoliTo code. Nonetheless, for future upgrades of this activity, a more accurate simulation shall be run, considering the real frictional behaviour of LL shoes, thus taking into account the different dynamic behaviour of the vehicle during the braking operation with cast iron and composite shoes. The stop braking simulation was run on the reference wagon featuring the main properties given in Table 22, considering an axle-load of 20 tonnes and an initial speed of 100 km/h. The temperature evolution for the two simulation scenarios, with cast iron and composite shoes, is shown in Figure 119, where two different trends can be observed for both curves. First, when the simulation time is below 40 s, the temperature evolution has a continuous pattern of rise and decrease, because the vehicle is being braked, so a temperature peak is followed by the cooling action of air convection and rail chill. After 40 s, the vehicle is completely stopped, so the braking action is over, and the temperature decreases because of the action of the air convection only. As expected, the wheel temperature is higher when a composite shoe is adopted, because the composite material leads to a larger amount of the total heat flux to flow into the wheel. Therefore, the preliminary simulation suggests that when replacing cast iron shoes with composite organic or sintered ones, the thermal stresses on the wheel become higher.

In conclusion, the results shown in this section confirm the validity of the proposed model and of the computational framework conceived in the frame of the present thesis, which includes the simplified version of the LTDPoliTo code. Therefore, the research group can now count on a reliable numerical tool that is going to be used in planned future works dealing with the integration of the wheel-shoe thermal model directly within the LTDPoliTo code or within a MB

model of a reference vehicle, thus allowing to calculate the wheel/shoe temperature as an additional output of the dynamic simulation.

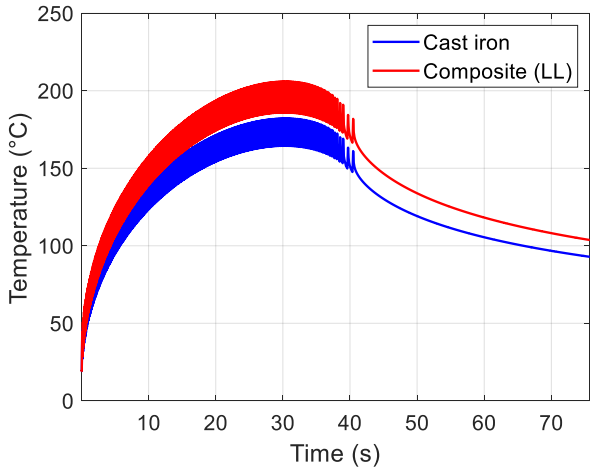

Figure 119: Temperature evolution for stop braking operation (comparison of cast iron and composite shoe materials).

Chapter 5

Conclusions

The activities carried out in the context of this thesis dealt with the simulation of critical issues of railway braking operations, by means of specifically built numerical and experimental tools.

Concerning the dynamic behaviour of whole trains and the calculation of in-train forces, this thesis led to the development of the new LTDPoliTo in-house numerical code for longitudinal train dynamics simulations. Prior to the beginning of this thesis, the research group needed to develop its own LTD code since LTD simulators are typically not available as commercial software packages. The need for an efficient and reliable in-house code arose as LTD simulations are required for the investigation of many different topics that the research group is currently facing, such as the experimental simulation of braking operations and the calculation of the temperature of tread braked wheels. The newly built code calculates outputs in good agreement with the results of the simulators joining an international benchmarking activity (the international benchmark of longitudinal train dynamics simulators). The biggest point of merit of the new LTDPoliTo code is its high numerical stability and accuracy. In fact, in comparison with a previous code implemented in the Simpack commercial multibody code, the new LTDPoliTo code is free of numerical divergences on train compositions with a big number of vehicles. Concerning the computational efficiency, the use of vectorization strategies and the a priori definition of the Jacobian sparsity pattern of the system allowed to obtain up to 40x speed-up compared to an original MATLAB code, written with conditional loops and Boolean statements.

A first work performed using the new LTDPoliTo code highlighted that the outputs of the longitudinal train dynamics simulations are slightly affected by the expressions used for the estimation of the curving resistances, while larger discrepancies in the results are given by different expression for the calculation of the ordinary resistant forces. The investigation on the outputs produced by different laws for ordinary and curving resistances suggested that as a general rule, the driving control signal should always be provided as a function of position instead of time. Furthermore, the simulations should be launched using proper expressions for the evaluation of the rolling resistances, tuned on the specific vehicles included in the simulated train composition. When such laws are not available, the best option is the adoption of literature expressions that explicitly consider the dependency of the ordinary resistances on the main vehicle parameters, like axle-load and number of axles.

To enhance the modelling capabilities of the LTDPoliTo code, a new module for the estimation of the air brake forces acting on wagons fitted with the UIC air brake system was developed as a major contribution of the present thesis. The module can calculate the air brake forces on European wagons based on the knowledge of the braked weight only, and the time delays of the braking action are simulated by means of a heuristic exponential function. The method used to estimate the air brake forces on the wagons is new and the literature review does not show evidence of the application of a similar strategy in other LTD codes. The biggest benefit of the proposed approach is that it allows to maintain the high computational efficiency of the original LTDPoliTo code, that had initially been implemented for the simulations suggested in the international benchmark. The new method was tuned to minimize the discrepancies between the simulated braking distances and the theoretical values provided by the UIC 544-1 leaflet. Simulations of emergency braking operations of typical freight train compositions running on European lines were launched, and the error between the simulated and theoretical braking distance was always below 5%, thus confirming the validity of the proposed approach. Nonetheless, further work shall be carried out soon to extend the model capabilities, in order to simulate different kinds of braking operations, especially braking operations in G position.

Finally, the LTDPoliTo code was included in a computational framework for the derivation of surrogate models of multibody models of freight wagons. The surrogate models are derived via machine learning techniques to compute the main safety indexes defined by the international standards (derailment coefficient Y/Q, wheel unloading ratio DQ/Q and the sum of the wheelset lateral forces ΣY)

directly from the outputs of longitudinal train dynamics simulations, with no need for long-lasting multibody simulations. The results of the activity proved that 344 training samples are a reasonable amount of samples to build accurate metamodels in terms of the R^2 score, especially for the prediction of the Y/Q and DQ/Q indexes. In fact, the 8 surrogate models built via the least squares support vector machine technique for the estimation of the Y/Q coefficient on all wheels of the reference wagon achieved an average value of the R^2 score equal to 0.901, while the average R^2 score for the 8 models computing the DQ/Q parameter was 0.804. A lower value of the average R^2 score, equal to 0.737, was obtained for the 4 models predicting the ΣY index, but the results of the activity proved that the proposed approach is promising, especially considering that the metamodels allow to reduce the computational times by up to four orders of magnitude compared to launching multibody simulations. This activity shall be soon extended to consider stop braking operations of a larger number of train configurations, including wagons with variable axle-load, so that a reliable add-on module can be added to the LTDPoliTo code for the prediction of the safety indexes. The strategy proposed in this thesis, based on the replacement of computationally expensive MB simulations with fast-to-evaluate surrogate models to be integrated within LTD codes is clearly not limited to the LTDPoliTo code only. Therefore, it is believed that this approach, based on modern methods such as machine learning techniques, can extend the scope of common LTD simulators allowing to evaluate the running safety indexes despite not directly calculating the wheel-rail contact forces. This strategy would hence ensure a quick evaluation of the safety of a long train composition with LTD simulations only, with no need for MB dynamic simulations. For instance, the derived surrogate models could be integrated into optimization schemes aiming at finding the best train composition for the minimization of the derailment risk.

As a result of the work performed in the context of the present thesis, the research group can now count on a reliable and computationally efficient new in-house LTD code. As a matter of facts, the group is currently adopting the LTDPoliTo code for many activities, including the experimental simulation of air brake operations on the multi-axle roller-rig and the numerical prediction of the temperature of tread braked wheels.

Shifting focus to the experimental simulation of braking operations, the activities carried out in the frame of this thesis included the experimental setup of the new multi-axle roller-rig installed at the laboratories of Politecnico di Torino. The bench had been specifically designed by the research group prior to the

beginning of the present thesis, in order to investigate adhesion recovery phenomena, related to the cleaning effect of the tangential forces in full sliding conditions. The bench setup, performed as a major contribution of this PhD thesis, required the calibration of the main sensors installed on the bench, such as load-cells and electro-pneumatic valves, and the development of a LabVIEW data acquisition and bench control software. The control software allows to perform three main kinds of tests, namely tests to obtain adhesion curves, tests for the simulation of the wheel adhesion recovery phenomenon and tests for the investigation of the rail adhesion recovery phenomenon. A campaign of adhesion curve tests proved the high repeatability of the bench for different values of the braking pressure ramp gradient, of the motor control mode and of the tested wheelset. The results of the wheel adhesion recovery tests highlighted that in wet conditions, the adhesion characteristic features a hysteretic behaviour with a *forward* curve, corresponding to increasing creepage, and a *backwards* curve, related to decreasing creepage. The backwards curve is characterized by larger values of the adhesion coefficient, because of the polishing action performed by the friction forces, that partially removes the contaminant layer between the wheels and the rollers. On the other hand, in dry conditions, there is no appreciable hysteresis loop in the adhesion characteristic, because the sliding forces have no contaminant layer to remove, and the backwards and forward curves are approximately overlying each other, with slight differences that can be related to thermal effects. The hysteresis loop obtained in wet conditions proved to be strongly dependent on the roller speed. In fact, if the roller speed increases, the hysteresis loop becomes larger, and a sharp adhesion recovery may be even detected in the forward curve. In fact, the cleaning action is related to the energy dissipated at the contact interface, which becomes larger for higher values of the roller speed. Moreover, the increase of the roller speed may activate thermal effects that give a contribution to the removal of the contaminant. Finally, the rail adhesion recovery tests highlighted that the application of a contaminant leads to a sudden increase of creepage on all wheelsets, but after a certain time the initial creepage value is restored, because the sliding forces remove the contaminant. However, the maximum creepage increase is recorded on the first wheelset facing the contaminant, while the last one benefits of the best adhesion level, because of the cleaning action performed by the front wheelsets. Further investigations and a better understanding of this phenomenon are needed, since they may result in a radical improvement of the braking torque mechatronic control systems.

The original bench configuration was then modified to reproduce the air brake system installed on European freight wagons in the laboratory of the research group. The new configuration includes the experimental simulation of the main and auxiliary reservoirs as well as of the brake pipe, so that the bench can be adopted for the laboratory testing and validation of air brake monitoring systems. The new bench configuration required the development of a new bench control software, for the transmission of the acquired data to a monitoring unit and for the implementation of a new motor control strategy, able to simulate the vehicle inertia on the bench, with no need for the installation of flywheels and gearboxes. The new motor control strategy is able to modify the roller speed according to the measured values of braking torque, and the calculation of the vehicle deceleration is performed using a simplified version of the longitudinal train dynamics equations. Simple tests with application of a ramp signal for the pressure drop in the brake pipe suggested that the new strategy can accurately simulate realistic braking operations, and future upgrades shall concern the reproduction of braking operations starting from the collection of real on-field data.

Now that the bench configuration has been established and calibrated, the next steps of the activity shall deal with the execution of a comprehensive test campaign, dealing with the simulation of a larger number of braking scenarios, in terms of axle-load, running speed and type of operation (drag braking, stop braking, emergency braking, etc.). Furthermore, the bench should be provided with additional valves, with PWM control, to test, validate and develop new braking torque control systems and algorithms. The long-term goal for the activities of the research group involving the multi-axle roller-rig is the use of the new bench at the early stage of development of WSP/monitoring systems, when many tests are required with high reproducibility, short duration and low costs. In fact, the configuration of the bench with four wheelsets over the same pair of rollers, is one of a kind, and can effectively enable the simulation of the mutual influence among the wheelsets of a railway vehicle, which is not accounted for by traditional rigs described in the literature.

Obviously, further investigations shall be performed to compare the results obtained on the multi-axle roller-rig with results that are collected on-track. In fact, the current layout of the bench allows to easily simulate conditions of *continuous* track contamination, whereby the contamination is extended to a large portion of the track. On the other hand, the multi-axle roller-rig cannot easily simulate a *local* track contamination, whereby the contamination is limited to a small, short section of the rails. The simulation of the vehicle running on a short,

contaminated section would require the development of an effective system able to quickly clean the surface of the rollers. Furthermore, the bench layout configuration is such that when the rollers are contaminated, the centrifugal forces tend to push the contaminant away from the contact interface, but this phenomenon obviously does not occur on a real vehicle. Finally, since the multi-axle roller-rig is a scaled rig, similitude strategies must be applied to ensure the correspondence with the full-scale system. Nonetheless, similitude models typically do not guarantee a perfect scaling of all quantities, and a scaling factor for nonlinear phenomena is almost impossible to determine. The similitude models adopted on railway roller-rigs typically do not consider the similitude of thermal quantities. Nonetheless, adhesion recovery phenomena strongly depend on the power dissipated at the contact interface, which leads to an increase of the surface temperature of the wheel and rail/roller. Therefore, the results obtained with the multi-axle roller-rig might differ from results obtained on the real vehicle, due to the differences in the thermal inertia and in the cooling/heating conditions compared to the real wheel-rail contact conditions. Because of the aforementioned reasons, further investigations, based on both experimental measurements and numerical simulations, are needed to improve the reliability of the multi-axle roller-rig and the correspondence with the real condition of a real vehicle running over a railway track.

Finally, the thesis shows two new activities that the research group has recently started to set up for the simulation of the damage of wheel surfaces, dealing with the numerical simulation of wear of wheel lateral profiles and of the wheel-shoe thermal and mechanical behaviour. In-house wear algorithms were implemented in MATLAB in the frame of the present thesis, and a comparison between local and global applications of Archard's wear law was performed. The global algorithm was specifically implemented with the aim to mimic the calculation implemented in the Simpack wear module, which is not totally clear due to intellectual property reasons. The results highlighted that global applications of the wear law compute higher wear depths on the tread and lower values on the flange, compared to local approaches. The availability for the research group of new in-house routines for the computation of wear of wheel profiles is the key to overcome the shortcomings of the wear module implemented in the Simpack commercial MB code. In fact, with the Simpack wear module, the user has a limited control on the strategies used to smooth and update the worn profile, and this can seriously compromise the numerical stability of the computation. At the same time, the Simpack MB code does not allow to set

different values of the wear coefficients along the track, while this can be easily done with in-house dedicated routines. Therefore, based on the activities performed in the present thesis, it is believed that the best option to ensure a good numerical stability is the development of external routines for the computation of the worn material and the profile smoothing and update, with the commercial software package only demanded to run the dynamic simulation.

Shifting focus to the simulation of the wheel-shoe thermo-mechanical interaction, this thesis contributed with the design of a new computational framework, including a simplified version of the LTDPoliTo code and FE models. The FE models are demanded to compute the wheel-shoe contact pressure distribution and of the wheel temperature evolution. The outputs of preliminary simulations confirmed that the 1Bg block configuration produces higher thermal stresses on the wheel surface, so configurations with 2 blocks on each wheel should be preferred. Since the air convection coefficient increases with speed, the wheel surface temperature is lower at higher speed values for constant values of braking power. Finally, simulations of stop braking operations suggested that much attention must be paid when replacing traditional cast iron shoes with composite materials, because the thermal and mechanical properties of composite shoes are such that a larger amount of the total friction heat flux flows into the wheel.

These last two numerical activities dealing with the simulation of the damage of wheel surfaces will require further upgrades. The comparison between local and global approaches shall be extended to consider different wear laws and a wider range of curves and speeds, as well as different types of vehicles. On the other hand, the tool for the calculation of the wheel temperature shall be further validated against experimental data, so that the model outcomes can be adopted in reliable and accurate monitoring systems. It is important to highlight that the goal of the research group at this preliminary stage was the development and initial validation of reliable numerical models, that can be used in future works within more complex frameworks. For instance, the wear model and the wheel-shoe FE models could be combined to develop wheel damage prediction tools able to consider wear due to the wheel-rail contact and wear related to tread braking operations altogether. At the same time, as an extension of this thesis, the research group is working on the development of simplified models for the calculation of the shoe temperature during braking. In fact, one of the final goals of the activity is the integration of the thermal models in the LTDPoliTo code and even in MB

models, thus allowing to compute the wheel/shoe temperature directly from LTD or MB simulations.

References

[1] Günay, M., Korkmaz, M.E. & Özmen, R., An investigation on braking systems used in railway vehicles. *Engineering Science and Technology, an International Journal,* **23**(2), pp. 421-431, 2020. https://doi.org/10.1016/j.jestch.2020.01.009.

[2] González-Gil, A., Palacin, R. & Batty, P., Sustainable urban rail systems: Strategies and technologies for optimal management of regenerative braking energy. *Energy Conversion and Management,* **75**, pp. 374-388, 2013. https://doi.org/10.1016/j.enconman.2013.06.039.

[3] Wu, Q., Luo, S. & Cole, C., Longitudinal dynamics and energy analysis for heavy haul trains. *Journal of Modern Transportation,* **22**(3), pp. 127-136, 2014. https://doi.org/10.1007/s40534-014-0055-x.

[4] Lu, Q., He, B., Wu, M., Zhang, Z., Luo, J., Zhang, Y., et al., Establishment and Analysis of Energy Consumption Model of Heavy-Haul Train on Large Long Slope. *Energies,* **11**(4), 2018. https://doi.org/10.3390/en11040965.

[5] UIC 540:2016. *Brakes - Air Brakes for freight trains and passenger trains*.

[6] Cătălin, C., Train Braking. *Train Braking, Reliability and Safety in Railway*, ed. X. Perpinya, InTech, 2012. https://doi.org/10.5772/37552.

[7] Yuan, Z., Wu, M., Tian, C., Zhou, J. & Chen, C., A Review on the Application of Friction Models in Wheel-Rail Adhesion Calculation. *Urban Rail Transit,* **7**(1), pp. 1-11, 2021. https://doi.org/10.1007/s40864-021-00141-y.

[8] EN 15625:2021. *Railway applications - Braking - Automatic variable load sensing devices*.

[9] EN 15624:2021. *Railway applications - Braking - Empty-loaded changeover devices*.

[10] Nakazawa, S.-i. & Hijikata, D., Wheel Slide Protection System by the Use of the Tangential Force in the Macro Slip Area. *Quarterly Report of RTRI,* **58**(3), pp. 196-203, 2017. https://doi.org/10.2219/rtriqr.58.3_196.

[11] Pugi, L., Rindi, A., Ercole, A.G., Palazzolo, A., Auciello, J., Fioravanti, D., et al., Research activity for the introduction of the "long locomotive" braking arrangement. *Ingegneria Ferroviaria,* **64**(10), pp. 833-852, 2009.

[12] UIC 544-1:2014. *Brakes - Braking performance*.

[13] Paukert, H. Train braking performance determination. *Global Railway Review* [Online article], (2), 2005. Available from: https://www.globalrailwayreview.com/article/2618/train-braking-performance-determination/.

[14] El-Sibaie, M., Recent advancements in buff and draft testing techniques. In: *Proceedings of the 1993 IEEE/ASME Joint Railroad Conference*, pp. 115-119, 1993. https://doi.org/10.1109/RRCON.1993.292955.

[15] Cantone, L., Negretti, D. & Vullo, V., Evaluation of the Admissible Longitudinal Compressive Forces by Means of Multibody Train Simulations. In: *Proceedings of the First International Conference on Railway Technology: Research, Development and Maintenance*, ed. J. Pombo, Civil-Comp Press: Stirlingshire (Scotland), 2012. https://doi.org/10.4203/ccp.98.26

[16] Krishna, V.V., Berg, M. & Stichel, S., Longitudinal Train Dynamics for Freight Wagons passing through an S-curve. In: *Proceedings of the First International Railway Symposium Aachen (IRSA)* ed. R.W. De Doncker, N. Niessen, C. Schindler, pp. 193-203, 2017.

[17] Krishna, V.V., Jobstfinke, D., Melzi, S. & Berg, M., An integrated numerical framework to investigate the running safety of overlong freight trains. *Proceedings of the Institution of Mechanical Engineers, Part F: Journal of Rail and Rapid Transit,* **235**(1), pp. 47-60, 2021. https://doi.org/10.1177/0954409720905203.

[18] Cole, C., Longitudinal Train Dynamics and Vehicle Stability in Train Operations. *Handbook of Railway Vehicle Dynamics*, ed. S. Iwnicki, M. Spiryagin, C. Cole, T. McSweeney, CRC Press: Boca Raton (FL, USA), pp. 452-519, 2019.

[19] Wu, Q., Spiryagin, M. & Cole, C., Longitudinal train dynamics: an overview. *Vehicle System Dynamics,* **54**(12), pp. 1688-1714, 2016. https://doi.org/10.1080/00423114.2016.1228988.

[20] Rochard, B.P. & Schmid, F., A review of methods to measure and calculate train resistances. *Proceedings of the Institution of Mechanical Engineers, Part F: Journal of Rail and Rapid Transit,* **214**(4), pp. 185-199, 2000. https://doi.org/10.1243/0954409001531306.

[21] Maksym Spiryagin, Colin Cole, Yan Quan Sun, Mitchell McClanachan, Valentyn Spiryagin & McSweeney, T., Longitudinal Train Dynamics. *Design and Simulation of Rail Vehicles*, CRC Press: Boca Raton (FL, USA), pp. 129-197, 2014.

[22] Wu, Q., Wang, B., Spiryagin, M. & Cole, C., Curving resistance from wheel-rail interface. *Vehicle System Dynamics,* **60**(3), pp. 1018-1036, 2022. https://doi.org/10.1080/00423114.2020.1843689.

[23] Sapronova, S.Y., Tkachenko, V.P., Fomin, O.V., Kulbovskiy, I.I. & Zub, O.V., *Rail Vehicles: The Resistance to the Movement and the Controllability: Monograph*: Dnipro, 2017.

[24] Cole, C., Spiryagin, M., Wu, Q. & Sun, Y.Q., Modelling, simulation and applications of longitudinal train dynamics. *Vehicle System Dynamics,* **55**(10), pp. 1498-1571, 2017. https://doi.org/10.1080/00423114.2017.1330484.

[25] Wu, Q., Cole, C., Spiryagin, M., Chang, C., Wei, W., Ursulyak, L., et al., Freight train air brake models. *International Journal of Rail Transportation*, pp. 1-49, 2021. https://doi.org/10.1080/23248378.2021.2006808.

[26] Cantone, L., TrainDy: The New Union Internationale Des Chemins de Fer Software for Freight Train Interoperability. *Proceedings of the Institution of Mechanical Engineers, Part F: Journal of Rail and Rapid Transit,* **225**(1), pp. 57-70, 2011. https://doi.org/10.1243/09544097jrrt347.

[27] Cole, C. & Sun, Y.Q., Simulated comparisons of wagon coupler systems in heavy haul trains. *Proceedings of the Institution of Mechanical Engineers, Part F: Journal of Rail and Rapid Transit,* **220**(3), pp. 247-256, 2006. https://doi.org/10.1243/09544097jrrt35.

[28] EN 15566:2016. *Railway applications - Railway rolling stock - Draw gear and screw coupling*.

[29] EN 15551:2017. *Railway applications - Railway rolling stock - Buffers*.

[30] Craciun, C., Mitu, A.M., Cruceanu, C. & Siretanu, T., Modeling the buffers hysteretic behavior for evaluation of longitudinal dynamic in-train forces. Presented at: *SISOM 2012 and Session of the Commission of Acoustics*, Bucharest (Romania), 30-31 May, 2012.

[31] Wu, Q., Yang, X., Cole, C. & Luo, S., Modelling polymer draft gears. *Vehicle System Dynamics,* **54**(9), pp. 1208-1225, 2016. https://doi.org/10.1080/00423114.2016.1196822.

[32] Cole, C., Improvements to wagon connection modelling for longitudinal train simulation. Presented at: *CORE 1998: Engineering innovation for a competitive edge: Conference on railway engineering*, Capricorn International Resort (Queensland, Australia), 7-9 September, 1998.

[33] Wu, Q., Cole, C., Luo, S. & Spiryagin, M., A review of dynamics modelling of friction draft gear. *Vehicle System Dynamics,* **52**(6), pp. 733-758, 2014. https://doi.org/10.1080/00423114.2014.894199.

[34] Spiryagin, M., Wu, Q. & Cole, C., International benchmarking of longitudinal train dynamics simulators: benchmarking questions. *Vehicle System Dynamics,* **55**(4), pp. 450-463, 2017. https://doi.org/10.1080/00423114.2016.1270457.

[35] Wu, Q., Spiryagin, M., Cole, C., Chang, C., Guo, G., Sakalo, A., et al., International benchmarking of longitudinal train dynamics simulators: results. *Vehicle System Dynamics,* **56**(3), pp. 343-365, 2018. https://doi.org/10.1080/00423114.2017.1377840.

[36] Bosso, N., Magelli, M. & Zampieri, N., Development and validation of a new code for longitudinal train dynamics simulation. *Proceedings of the Institution of Mechanical Engineers, Part F: Journal of Rail and Rapid Transit,* **235**(3), pp. 286-299, 2021. https://doi.org/10.1177/0954409720923497.

[37] Shampine, L.F. & Reichelt, M.W., The MATLAB ode suite. *SIAM Journal of Scientific Computing,* **18**(1), pp. 1-22, 1997. https://doi.org/10.1137/S1064827594276424.

[38] Shampine, L.F., Gladwell, I., Shampine, L. & Thompson, S., *Solving ODEs with MATLAB*, Cambridge university press: Cambridge (UK), 2003.

[39] Zhang, Z., Li, G., Chu, G., Zu, H. & Kennedy, D., Compressed stability analysis of the coupler and buffer system of heavy-haul locomotives. *Vehicle System Dynamics,* **53**(6), pp. 833-855, 2015. https://doi.org/10.1080/00423114.2015.1023318.

[40] Bosso, N., Magelli, M., Rossi Bartoli, L. & Zampieri, N., The influence of resistant force equations and coupling system on long train dynamics simulations. *Proceedings of the Institution of Mechanical Engineers, Part F: Journal of Rail and Rapid Transit,* **236**(1), pp. 35-47, 2022. https://doi.org/10.1177/09544097211001149.

[41] Bosso, N., Magelli, M. & Zampieri, N., A numerical method for the simulation of freight train emergency braking operations based on the UIC braked weight percentage. *Railway Engineering Science*, 2023. https://doi.org/10.1007/s40534-022-00296-9.

[42] EN 14363:2016. *Railway applications - Testing and Simulation for the acceptance of running characteristics of railway vehicles - Running Behaviour and stationary tests*.

[43] Bosso, N., Magelli, M. & Zampieri, N., Application of machine learning techniques to build digital twins for long train dynamics simulations. *Vehicle System Dynamics*, 2023. https://doi.org/10.1080/00423114.2023.2174885.

[44] Wu, Q. & Cole, C., Computing Schemes for Longitudinal Train Dynamics: Sequential, Parallel and Hybrid. *Journal of Computational and Nonlinear Dynamics,* **10**(6), 2015. https://doi.org/10.1115/1.4029716.

[45] Pugi, L., Rindi, A., Ercole, A.G., Palazzolo, A., Auciello, J., Fioravanti, D., et al., Preliminary studies concerning the application of different braking arrangements on Italian freight trains. *Vehicle System Dynamics,* **49**(8), pp. 1339-1365, 2011. https://doi.org/10.1080/00423114.2010.505291.

[46] Krishna, V.V., Wu, Q., Hossein-Nia, S., Spiryagin, M. & Stichel, S., Long freight trains & long-term rail surface damage – a systems perspective. *Vehicle System Dynamics*, pp. 1-24, 2022. https://doi.org/10.1080/00423114.2022.2085584.

[47] Vapnik, V.N., *Statistical Learning Theory*, Wiley: New York (NY, USA), 1998.

[48] Suykens, J.A.K., Van Gestel, T., De Brabanter, J., De Moor, B. & Vandewalle, J., *Least Squares Support Vector Machines*, World Scientific, 2002. https://doi.org/doi:10.1142/5089.

[49] Olofsson, U., Adhesion and friction modification. *Wheel-rail interface handbook*, ed. R. Lewis, U. Olofsson, Woodhead Publishing Limited: Cambridge (UK), pp. 510-527, 2009.

[50] Mayer, R. & Rasel, T. Reproducible braking distance: Wheel slide protection. Knorr-Bremse. Available from: https://rail.knorr-bremse.com/en/de/stories/technical-articles/content-page-57.json.

[51] Bosso, N., Magelli, M. & Zampieri, N., Investigation of adhesion recovery phenomenon using a scaled roller-rig. *Vehicle System Dynamics,* **59**(2), pp. 295-312, 2021. https://doi.org/10.1080/00423114.2019.1677922.

[52] Malvezzi, M., Pugi, L., Papini, S., Rindi, A. & Toni, P., Identification of a wheel–rail adhesion coefficient from experimental data during braking tests. *Proceedings of the Institution of Mechanical Engineers, Part F: Journal of Rail and Rapid Transit,* **227**(2), pp. 128-139, 2013. https://doi.org/10.1177/0954409712458490.

[53] Logston, C.F., Jr. & Itami, G.S., Locomotive Friction-Creep Studies. *Journal of Engineering for Industry,* **102**(3), pp. 275-281, 1980. https://doi.org/10.1115/1.3183865.

[54] Zhang, W., Chen, J., Wu, X. & Jin, X., Wheel/rail adhesion and analysis by using full scale roller rig. *Wear,* **253**(1), pp. 82-88, 2002. https://doi.org/10.1016/S0043-1648(02)00086-8.

[55] Zhou, J., Wu, M., Tian, C., Yuan, Z. & Chen, C., Experimental investigation on wheel–rail adhesion characteristics under water and large sliding conditions. *Industrial Lubrication and Tribology,* **73**(2), pp. 366-372, 2021. https://doi.org/10.1108/ILT-07-2020-0236.

[56] Vollebregt, E., Six, K. & Polach, O., Challenges and progress in the understanding and modelling of the wheel–rail creep forces. *Vehicle System Dynamics,* **59**(7), pp. 1026-1068, 2021. https://doi.org/10.1080/00423114.2021.1912367.

[57] Bosso, N., Gugliotta, A., Magelli, M., Oresta, I.F. & Zampieri, N., Study of wheel-rail adhesion during braking maneuvers. In: *Procedia Structural Integrity* **24**, pp. 680-691, 2019. https://doi.org/10.1016/j.prostr.2020.02.060.

[58] Shrestha, S., Wu, Q. & Spiryagin, M., Review of adhesion estimation approaches for rail vehicles. *International Journal of Rail Transportation,* **7**(2), pp. 79-102, 2019. https://doi.org/10.1080/23248378.2018.1513344.

[59] Harrison, H., McCanney, T. & Cotter, J., Recent developments in coefficient of friction measurements at the rail/wheel interface. *Wear,* **253**(1), pp. 114-123, 2002. https://doi.org/10.1016/S0043-1648(02)00090-X.

[60] Areiza, Y.A., Garcés, S.I., Santa, J.F., Vargas, G. & Toro, A., Field measurement of coefficient of friction in rails using a hand-pushed tribometer. *Tribology International,* **82**, pp. 274-279, 2015. https://doi.org/10.1016/j.triboint.2014.08.009.

[61] Lewis, S.R., Lewis, R. & Olofsson, U., An alternative method for the assessment of railhead traction. *Wear,* **271**(1), pp. 62-70, 2011. https://doi.org/10.1016/j.wear.2010.10.035.

[62] Stolarski, T.A., Friction in a pin-on-disc configuration. *Mechanism and Machine Theory,* **24**(5), pp. 373-381, 1989. https://doi.org/10.1016/0094-114X(89)90067-0.

[63] Olofsson, U. & Sundvall, K., Influence of leaf, humidity and applied lubrication on friction in the wheel-rail contact: Pin-on-disc experiments. *Proceedings of the Institution of*

Mechanical Engineers, Part F: Journal of Rail and Rapid Transit, **218**(3), pp. 235-242, 2004. https://doi.org/10.1243/0954409042389364.

[64] Abbasi, S., Olofsson, U., Zhu, Y. & Sellgren, U., Pin-on-disc study of the effects of railway friction modifiers on airborne wear particles from wheel–rail contacts. *Tribology International,* **60**, pp. 136-139, 2013. https://doi.org/10.1016/j.triboint.2012.11.013.

[65] Cann, P.M., The "leaves on the line" problem—a study of leaf residue film formation and lubricity under laboratory test conditions. *Tribology Letters,* **24**(2), pp. 151-158, 2006. https://doi.org/10.1007/s11249-006-9152-2.

[66] Zhu, Y., Olofsson, U. & Persson, K., Investigation of factors influencing wheel–rail adhesion using a mini-traction machine. *Wear,* **292-293**, pp. 218-231, 2012. https://doi.org/10.1016/j.wear.2012.05.006.

[67] Galas, R., Omasta, M., Krupka, I. & Hartl, M., Laboratory investigation of ability of oil-based friction modifiers to control adhesion at wheel-rail interface. *Wear,* **368-369**, pp. 230-238, 2016. https://doi.org/10.1016/j.wear.2016.09.015.

[68] Fletcher, D.I. & Beynon, J.H., Development of a Machine for Closely Controlled Rolling Contact Fatigue and Wear Testing. *Journal of Testing and Evaluation,* **28**(4), pp. 267-275, 2000. https://doi.org/10.1520/JTE12104J.

[69] Lewis, R. & Dwyer-Joyce, R.S., Wear at the wheel/rail interface when sanding is used to increase adhesion. *Proceedings of the Institution of Mechanical Engineers, Part F: Journal of Rail and Rapid Transit,* **220**(1), pp. 29-41, 2006. https://doi.org/10.1624/105812406X10779.

[70] Gallardo-Hernandez, E.A. & Lewis, R., Twin disc assessment of wheel/rail adhesion. *Wear,* **265**(9-10), pp. 1309-1316, 2008. https://doi.org/10.1016/j.wear.2008.03.020.

[71] Arias-Cuevas, O., Li, Z., Lewis, R. & Gallardo-Hernández, E.A., Rolling-sliding laboratory tests of friction modifiers in dry and wet wheel-rail contacts. *Wear,* **268**(3-4), pp. 543-551, 2010. https://doi.org/10.1016/j.wear.2009.09.015.

[72] Arias-Cuevas, O., Li, Z. & Lewis, R., A laboratory investigation on the influence of the particle size and slip during sanding on the adhesion and wear in the wheel-rail contact. *Wear,* **271**(1-2), pp. 14-24, 2011. https://doi.org/10.1016/j.wear.2010.10.050.

[73] Omasta, M., Machatka, M., Smejkal, D., Hartl, M. & Křupka, I., Influence of sanding parameters on adhesion recovery in contaminated wheel-rail contact. *Wear,* **322-323**, pp. 218-225, 2015. https://doi.org/10.1016/j.wear.2014.11.017.

[74] Chen, H., Ban, T., Ishida, M. & Nakahara, T., Experimental investigation of influential factors on adhesion between wheel and rail under wet conditions. *Wear,* **265**(9-10), pp. 1504-1511, 2008. https://doi.org/10.1016/j.wear.2008.02.034.

[75] Allen, P., Zhang, W., Liang, Y., Zeng, J., Jung, H., Meli, E., et al., Roller Rigs. *Handbook of Railway Vehicle Dynamics*, ed. S. Iwnicki, M. Spiryagin, C. Cole, T. McSweeney, CRC Press: Boca Raton (FL, USA), pp. 761-823, 2019.

[76] Myamlin, S., Kalivoda, J. & Neduzha, L., Testing of Railway Vehicles Using Roller Rigs. *Procedia Engineering,* **187**, pp. 688-695, 2017. https://doi.org/10.1016/j.proeng.2017.04.439.

[77] Bosso, N., Allen, P. & Zampieri, N., Scale Testing Theory and Approaches. *Handbook of Railway Vehicle Dynamics*, ed. S. Iwnicki, M. Spiryagin, C. Cole, T. McSweeney, CRC Press: Boca Raton (FL, USA), pp. 825-867, 2019.

[78] Bosso, N., Gugliotta, A. & Zampieri, N., RTCONTACT: An efficient wheel-rail contact algorithm for real-time dynamic simulations. Presented at: *2012 Joint Rail Conference, JRC 2012*, Philadelphia (PA, USA), 17-19 April, 2012. https://doi.org/10.1115/JRC2012-74044.

[79] Jaschinski, A., Chollet, H., Iwnicki, S., Wickens, A. & Von Würzen, J., The application of roller rigs to railway vehicle dynamics. *Vehicle System Dynamics,* **31**(5-6), pp. 345-392, 1999. https://doi.org/10.1076/vesd.31.5.345.8360.

[80] Liu, B. & Bruni, S., Analysis of Wheel-Roller Contact and Comparison with the Wheel-Rail Case. *Urban Rail Transit,* **1**(4), pp. 215-226, 2015. https://doi.org/10.1007/s40864-015-0028-3.

[81] Meymand, S.Z., Keylin, A. & Ahmadian, M., A survey of wheel–rail contact models for rail vehicles. *Vehicle System Dynamics,* **54**(3), pp. 386-428, 2016. https://doi.org/10.1080/00423114.2015.1137956.

[82] Elkins, J.A., Prediction of wheel/rail interaction: The state-of-the-art. *Vehicle System Dynamics: International Journal of Vehicle Mechanics and Mobility,* **20**(1), pp. 1-27, 1992. https://doi.org/10.1080/00423119208969385.

[83] Blanco-Lorenzo, J., Santamaria, J., Vadillo, E.G. & Correa, N., On the influence of conformity on wheel–rail rolling contact mechanics. *Tribology International,* **103**, pp. 647-667, 2016. https://doi.org/10.1016/j.triboint.2016.07.017.

[84] Vollebregt, E., Detailed wheel/rail geometry processing with the conformal contact approach. *Multibody System Dynamics,* **52**(2), pp. 135-167, 2021. https://doi.org/10.1007/s11044-020-09762-w.

[85] Johnson, K.L., Normal contact of elastic solids - Hertz theory. *Contact Mechanics*, Press Syndicate of the University of Cambridge: Cambridge (UK), pp. 84-106, 1985.

[86] Piotrowski, J. & Chollet, H., Wheel–rail contact models for vehicle system dynamics including multi-point contact. *Vehicle System Dynamics,* **43**(6-7), pp. 455-483, 2005. https://doi.org/10.1080/00423110500141144.

[87] Sichani, M.S., Enblom, R. & Berg, M., Comparison of non-elliptic contact models: Towards fast and accurate modelling of wheel–rail contact. *Wear,* **314**(1), pp. 111-117, 2014. https://doi.org/10.1016/j.wear.2013.11.047.

[88] Pascal, J.P. & Sauvage, G., The Available Methods to Calculate the Wheel/Rail Forces in Non Hertzian Contact Patches and Rail Damaging. *Vehicle System Dynamics,* **22**(3-4), pp. 263-275, 1993. https://doi.org/10.1080/00423119308969028.

[89] Ayasse, J.B. & Chollet, H., Determination of the wheel rail contact patch in semi-Hertzian conditions. *Vehicle System Dynamics,* **43**(3), pp. 161-172, 2005. https://doi.org/10.1080/00423110412331327193.

[90] Sh. Sichani, M., Enblom, R. & Berg, M., A novel method to model wheel–rail normal contact in vehicle dynamics simulation. *Vehicle System Dynamics,* **52**(12), pp. 1752-1764, 2014. https://doi.org/10.1080/00423114.2014.961932.

[91] Allen, P., Zhang, W., Liang, Y., Zeng, J., Jung, H., Meli, E., et al., Wheel-Rail Contact Mechanics. *Handbook of Railway Vehicle Dynamics*, ed. J.-B. Ayasse, H. Chollet, M. Sebès, CRC Press: Boca Raton (FL, USA), pp. 241-280, 2019.

[92] Kalker, J.J., *Three-Dimensional Elastic Bodies in Rolling Contact*, Springer: Dordrecht (The Netherlands), 1990. https://doi.org/10.1007/978-94-015-7889-9.

[93] Frederick William Carter & Love, A.E.H., On the action of a locomotive driving wheel. *Proceedings of the Royal Society of London Series A, Containing Papers of a Mathematical and Physical Character,* **112**, pp. 151-157, 1926. https://doi.org/10.1098/rspa.1926.0100.

[94] Vermeulen, P.J. & Johnson, K.L., Contact of Nonspherical Elastic Bodies Transmitting Tangential Forces. *Journal of Applied Mechanics,* **31**(2), pp. 338-340, 1964. https://doi.org/10.1115/1.3629610.

[95] Kalker, J.J. *On the Rolling Contact of Two Elastic Bodies in the Presence of Dry Friction* (PhD Thesis): TU Delft, 1967.

[96] Shen, Z.Y., Hedrick, J.K. & Elkins, J.A., A Comparison of Alternative Creep Force Models for Rail Vehicle Dynamic Analysis. *Vehicle System Dynamics,* **12**(1-3), pp. 79-83, 1983. https://doi.org/10.1080/00423118308968725.

[97] Kalker, J.J., A Fast Algorithm for the Simplified Theory of Rolling Contact. *Vehicle System Dynamics,* **11**(1), pp. 1-13, 1982. https://doi.org/10.1080/00423118208968684.

[98] Vollebregt, E. & Voltr, P., Improved accuracy for FASTSIM using one or three flexibility values. *Vehicle System Dynamics,* **61**(1), pp. 309-317, 2023. https://doi.org/10.1080/00423114.2022.2042331.

[99] Polach, O., A fast wheel-rail forces calculation computer code. *Vehicle System Dynamics,* **33**(sup1), pp. 728-739, 2000. https://doi.org/10.1080/00423114.1999.12063125.

[100] Polach, O., Creep forces in simulations of traction vehicles running on adhesion limit. *Wear,* **258**(7-8), pp. 992-1000, 2005. https://doi.org/10.1016/j.wear.2004.03.046.

[101] Spiryagin, M., Polach, O. & Cole, C., Creep force modelling for rail traction vehicles based on the Fastsim algorithm. *Vehicle System Dynamics,* **51**(11), pp. 1765-1783, 2013. https://doi.org/10.1080/00423114.2013.826370.

[102] Rovira, A., Roda, A., Lewis, R. & Marshall, M.B., Application of Fastsim with variable coefficient of friction using twin disc experimental measurements. *Wear,* **274-275**, pp. 109-126, 2012. https://doi.org/10.1016/j.wear.2011.08.019.

[103] Vollebregt, E.A.H., Numerical modeling of measured railway creep versus creep-force curves with CONTACT. *Wear,* **314**(1-2), pp. 87-95, 2014. https://doi.org/10.1016/j.wear.2013.11.030.

[104] Bosso, N. & Zampieri, N., A Novel Analytical Method to Calculate Wheel-Rail Tangential Forces and Validation on a Scaled Roller-Rig. *Advances in Tribology,* **2018**, 2018. https://doi.org/10.1155/2018/7298236.

[105] Allotta, B., Meli, E., Pugi, L., Ridolfi, A., Rindi, A. & Vettori, G., Simulation of railway braking tests under degraded adhesion conditions. Presented at: *The 2nd Joint International Conference on Multibody System Dynamics (IMSD 2012)*, Stuttgart (Germany), 29 May - 1 June, 2012.

[106] Allotta, B., Meli, E., Ridolfi, A. & Rindi, A., Development of an innovative wheel–rail contact model for the analysis of degraded adhesion in railway systems. *Tribology International,* **69**, pp. 128-140, 2014. https://doi.org/10.1016/j.triboint.2013.09.013.

[107] Zhu, W., Zhu, W., Zheng, S. & Wu, N., An improved degraded adhesion model for wheel–rail under braking conditions. *Industrial Lubrication and Tribology,* **73**(3), pp. 450-456, 2021. https://doi.org/10.1108/ILT-07-2020-0244.

[108] Voltr, P., Lata, M. & Černy, O., Measuring of wheel–rail adhesion characteristics at a test stand. Presented at: *18th International Conference Engineering Mechanics 2012*, Svratka (Czech Republic), 14-17 May, 2012.

[109] Voltr, P. & Lata, M., Transient wheel-rail adhesion characteristics under the cleaning effect of sliding. *Vehicle System Dynamics,* **53**(5), pp. 605-618, 2015. https://doi.org/10.1080/00423114.2014.961488.

[110] Meacci, M., Shi, Z., Butini, E., Marini, L., Meli, E. & Rindi, A., A railway local degraded adhesion model including variable friction, energy dissipation and adhesion recovery. *Vehicle System Dynamics,* **59**(11), pp. 1697-1718, 2021. https://doi.org/10.1080/00423114.2020.1775266.

[111] Bosso, N., Gugliotta, A. & Zampieri, N., Strategies to simulate wheel-rail adhesion in degraded conditions using a roller-rig. *Vehicle System Dynamics,* **53**(5), pp. 619-634, 2015. https://doi.org/10.1080/00423114.2014.981194.

[112] Jaschinski, A. *On the application of similarity laws to a scaled railway bogie model* (PhD Thesis): TU Delft, 1991.

[113] Re, G. *Progetto e realizzazione di un banco prova multiassiale per lo studio del sistema frenante dei veicoli ferroviari* (Master's degree Thesis): Politecnico di Torino, 2015.

[114] De Fusco, A. *Studio dell'adesione ruota-rotaia in condizioni degradate mediante simulazione numerica e tecniche sperimentali innovative* (Master's degree Thesis): Politecnico di Torino, 2016.

[115] Bosso, N., Gugliotta, A., Magelli, M. & Zampieri, N., Experimental Setup of an Innovative Multi-Axle Roller Rig for the Investigation of the Adhesion Recovery Phenomenon. *Experimental Techniques,* **43**(6), pp. 695-706, 2019. https://doi.org/10.1007/s40799-019-00327-x.

[116] SMC: ITV Electro-pneumatic Regulator/Electronic Vacuum Regulator. No.: CAT.EUS60-15F-UK. Available from: https://docs.rs-online.com/c26a/0900766b813c6fe9.pdf.

[117] Byrd, R.H., Gilbert, J.C. & Nocedal, J., A trust region method based on interior point techniques for nonlinear programming. *Mathematical Programming,* **89**(1), pp. 149-185, 2000. https://doi.org/10.1007/PL00011391.

[118] Magelli, M., Study of Adhesion Recovery phenomenon using a Multi-axle Roller-rig. In: *IOP Conference Series: Materials Science and Engineering* **1038**, IOP Publishing, 2021. https://doi.org/10.1088/1757-899X/1038/1/012001.

[119] Bosso, N., Magelli, M. & Zampieri, N., Application of low-power energy harvesting solutions in the railway field: a review. *Vehicle System Dynamics,* **59**(6), pp. 841-871, 2021. https://doi.org/10.1080/00423114.2020.1726973.

[120] Bernal, E., Spiryagin, M. & Cole, C., Onboard Condition Monitoring Sensors, Systems and Techniques for Freight Railway Vehicles: A Review. *IEEE Sensors Journal,* **19**(1), pp. 4-24, 2019. https://doi.org/10.1109/JSEN.2018.2875160.

[121] Aimar, M. & Somà, A., Study and results of an onboard brake monitoring system for freight wagons. *Proceedings of the Institution of Mechanical Engineers, Part F: Journal of Rail and Rapid Transit,* **232**(5), pp. 1277-1294, 2018. https://doi.org/10.1177/0954409717720348.

[122] Hattley, R.S., Swart, L. & Mulder, M., Development of an Instrumented Measuring Wagon to Monitor the Performance of Electronically Controlled Pneumatic Brakes. Presented at: *10th International Heavy Haul Association Conference*, New Delhi (India), 4-6 February, 2013.

[123] Bosso, N., Gugliotta, A. & Zampieri, N., Design and testing of an innovative monitoring system for railway vehicles. *Proceedings of the Institution of Mechanical Engineers, Part F: Journal of Rail and Rapid Transit,* **232**(2), pp. 445-460, 2018. https://doi.org/10.1177/0954409716675005.

[124] Bosso, N., Gugliotta, A., Magelli, M. & Zampieri, N., Monitoring of railway freight vehicles using onboard systems. In: *Procedia Structural Integrity* **24**, pp. 692-705, 2019. https://doi.org/10.1016/j.prostr.2020.02.061.

[125] Bosso, N., Gugliotta, A. & Zampieri, N., Wheel flat detection algorithm for onboard diagnostic. *Measurement,* **123**, pp. 193-202, 2018. https://doi.org/10.1016/j.measurement.2018.03.072.

[126] Bosso, N., Magelli, M. & Zampieri, N., Monitoring systems for railways freight vehicles. *International Journal of Computational Methods and Experimental Measurements,* **10**(4), pp. 359-371, 2022. https://doi.org/10.2495/CMEM-V10-N4-359-371.

[127] Bosso, N., Magelli, M. & Zampieri, N., Calibration and development of a multi-axis roller bench for monitoring the braking system of a railway vehicle. *Ingegneria Ferroviaria,* **75**(7-8), pp. 501-523, 2020.

[128] Bosso, N., Magelli, M. & Zampieri, N., Simulation of wheel and rail profile wear: a review of numerical models. *Railway Engineering Science,* **30**(4), pp. 403-436, 2022. https://doi.org/10.1007/s40534-022-00279-w.

[129] Tunna, J., Sinclair, J. & Perez, J., A Review of wheel wear and rolling contact fatigue. *Proceedings of the Institution of Mechanical Engineers, Part F: Journal of Rail and Rapid Transit,* **221**(2), pp. 271-289, 2007. https://doi.org/10.1243/0954409JRRT72.

[130] Tao, G., Wen, Z., Jin, X. & Yang, X., Polygonisation of railway wheels: a critical review. *Railway Engineering Science,* **28**(4), pp. 317-345, 2020. https://doi.org/10.1007/s40534-020-00222-x.

[131] Polach, O. & Nicklisch, D., Wheel/rail contact geometry parameters in regard to vehicle behaviour and their alteration with wear. *Wear,* **366-367**, pp. 200-208, 2016. https://doi.org/10.1016/j.wear.2016.03.029.

[132] Sawley, K. & Wu, H., The formation of hollow-worn wheels and their effect on wheel/rail interaction. *Wear,* **258**(7), pp. 1179-1186, 2005. https://doi.org/10.1016/j.wear.2004.03.029.

[133] Ashby, M.F. & Lim, S.C., Wear-mechanism maps. *Scripta Metallurgica et Materialia,* **24**(5), pp. 805-810, 1990. https://doi.org/10.1016/0956-716X(90)90116-X.

[134] Dearden, J., The Wear of Steel Rails: A Review of the factors involved. *Proceedings of the Institution of Civil Engineers,* **3**(5), pp. 456-481, 1954. https://doi.org/10.1680/ipeds.1954.11670.

[135] Beagley, T.M., Severe wear of rolling/sliding contacts. *Wear,* **36**(3), pp. 317-335, 1976. https://doi.org/10.1016/0043-1648(76)90110-1.

[136] Bolton, P.J., Clayton, P. & McEwen, I.J., Wear of Rail and Tire Steels Under Rolling/Sliding Conditions. *A S L E Transactions,* **25**(1), pp. 17-24, 1982. https://doi.org/10.1080/05698198208983059.

[137] Bolton, P.J. & Clayton, P., Rolling-sliding wear damage in rail and tyre steels. *Wear,* **93**(2), pp. 145-165, 1984. https://doi.org/10.1016/0043-1648(84)90066-8.

[138] Zakharov, S., Komarovsky, I. & Zharov, I., Wheel flange/rail head wear simulation. *Wear,* **215**(1), pp. 18-24, 1998. https://doi.org/10.1016/S0043-1648(97)00293-7.

[139] Lewis, R., Dwyer-Joyce, R.S., Olofsson, U., Pombo, J., Ambrósio, J., Pereira, M., et al., Mapping railway wheel material wear mechanisms and transitions. *Proceedings of the Institution of Mechanical Engineers, Part F: Journal of Rail and Rapid Transit,* **224**(3), pp. 125-137, 2010. https://doi.org/10.1243/09544097jrrt328.

[140] Archard, J.F., Contact and Rubbing of Flat Surfaces. *Journal of Applied Physics,* **24**(8), pp. 981-988, 1953. https://doi.org/10.1063/1.1721448.

[141] Archard, J.F., Hirst, W. & Allibone, T.E., The wear of metals under unlubricated conditions. *Proceedings of the Royal Society of London Series A: Mathematical and Physical Sciences,* **236**(1206), pp. 397-410, 1956. https://doi.org/10.1098/rspa.1956.0144.

[142] Jendel, T., Prediction of wheel profile wear—comparisons with field measurements. *Wear,* **253**(1), pp. 89-99, 2002. https://doi.org/10.1016/S0043-1648(02)00087-X.

[143] Bosso, N. & Zampieri, N., Experimental and Numerical Simulation of Wheel-Rail Adhesion and Wear Using a Scaled Roller Rig and a Real-Time Contact Code. *Shock and Vibration,* **2014**, 2014. https://doi.org/10.1155/2014/385018.

[144] McEwen, I.J. & Harvey, R.F. Interpretation of Wheel/Rail Wear Numbers. Derby (UK): Railway Technical Centre; 1986. Report No.: TM VDY 004.

[145] Peng, B., Iwnicki, S., Shackleton, P. & Crosbee, D., Comparison of wear models for simulation of railway wheel polygonization. *Wear,* **436-437**, 2019. https://doi.org/10.1016/j.wear.2019.203010.

[146] Zobory, I., Prediction of Wheel/Rail Profile Wear. *Vehicle System Dynamics,* **28**(2-3), pp. 221-259, 1997. https://doi.org/10.1080/00423119708969355.

[147] Krause, H. & Poll, G., Wear of wheel-rail surfaces. *Wear,* **113**(1), pp. 103-122, 1986. https://doi.org/10.1016/0043-1648(86)90060-8.

[148] De Arizon, J., Verlinden, O. & Dehombreux, P., Prediction of wheel wear in urban railway transport: comparison of existing models. *Vehicle System Dynamics,* **45**(9), pp. 849-866, 2007. https://doi.org/10.1080/00423110601149335.

[149] EN 15313:2016. *Railway applications - In-service wheelset operation requirements - In-service and off-vehicle wheelset maintenance*.

[150] Abeidi, A.S., Bosso, N., Gugliotta, A. & Soma`, A., Numerical Simulation of Wear in Railway Wheel Profiles. In: *Proceedings of 8th Biennial ASME Conference on Engineering Systems Design and Analysis, ESDA2006* **3**, pp. 963-977, 2006. https://doi.org/10.1115/ESDA2006-95571.

[151] Bosso, N., Gugliotta, A. & Abeidi, A.S., Influence of Vehicle Dynamics on Wear of Railway Wheel Profiles. *International Journal of Applied Engineering Research,* **13**(6), pp. 3540-3549, 2018.

[152] Chang, C., Wang, C., Chen, B. & Li, L., Study on numerical analysis method to wheel/rail wear of heavy haul train. In: *Proceedings, 9th International Heavy Haul Conference*, China Railway Publishing Home, pp. 837-845, 2009.

[153] Chang, C., Wang, C., Chen, B. & Li, L., A Study of a Numerical Analysis Method for the Wheel-Rail Wear of a Heavy-Haul Train. *Proceedings of the Institution of Mechanical Engineers, Part F: Journal of Rail and Rapid Transit,* **224**(5), pp. 473-482, 2010. https://doi.org/10.1243/09544097jrrt341.

[154] Tao, G., Ren, D., Wang, L., Wen, Z. & Jin, X., Online prediction model for wheel wear considering track flexibility. *Multibody System Dynamics,* **44**(3), pp. 313-334, 2018. https://doi.org/10.1007/s11044-018-09633-5.

[155] Tao, G., Wen, Z., Guan, Q., Zhao, X., Luo, Y. & Jin, X., Locomotive wheel wear simulation in complex environment of wheel-rail interface. *Wear,* **430-431**, pp. 214-221, 2019. https://doi.org/10.1016/j.wear.2019.05.012.

[156] Lewis, R., Kuka, N., Ariaudo, C., Dwyer-Joyce, R., Tassini, N. & Quost, X., Predicting Railway Wheel Wear Starting From Multi-Body Analysis: A Preliminary Study. Presented at:

IEEE/ASME/ASCE 2008 Joint Rail Conference, Wilmington (DE) 22-24 April, 2008. https://doi.org/10.1115/JRC2008-63021.

[157] Ignesti, M., Innocenti, A., Marini, L., Meli, E. & Rindi, A., Development of a model for the simultaneous analysis of wheel and rail wear in railway systems. *Multibody System Dynamics,* **31**(2), pp. 191-240, 2014. https://doi.org/10.1007/s11044-013-9360-0.

[158] Bosso, N. & Zampieri, N., Numerical stability of co-simulation approaches to evaluate wheel profile evolution due to wear. *International Journal of Rail Transportation,* **8**(2), pp. 159-179, 2020. https://doi.org/10.1080/23248378.2019.1672588.

[159] Bosso, N., Magelli, M. & Zampieri, N., Study on the influence of the modelling strategy in the calculation of the worn profile of railway wheels. In: *WIT Transactions on The Built Environment* **213**, ed. G. Passerini, J.M. Mera, WIT Press: Southampton (UK), pp. 65-76, 2022. https://doi.org/10.2495/CR220061.

[160] Srivastava, J.P., Sarkar, P.K. & Ranjan, V., Effects of thermal load on wheel–rail contacts: A review. *Journal of Thermal Stresses,* **39**(11), pp. 1389-1418, 2016. https://doi.org/10.1080/01495739.2016.1216060.

[161] Teimourimanesh, S., Lundén, R. & Vernersson, T., Braking capacity of railway wheels—state-of-the-art survey. Presented at: *16th International Wheelset Congress (IWC16)*, Cape Town (South Africa), 14-19 March, 2010.

[162] Ahlström, J. & Karlsson, B., Microstructural evaluation and interpretation of the mechanically and thermally affected zone under railway wheel flats. *Wear,* **232**(1), pp. 1-14, 1999. https://doi.org/10.1016/S0043-1648(99)00166-0.

[163] Ostash, O.P., Andreiko, I.M., Kulyk, V.V. & Vavrukh, V.I., Influence of braking on the microstructure and mechanical behavior of railroad wheel steels. *Materials Science,* **48**(5), pp. 569-574, 2013. https://doi.org/10.1007/s11003-013-9539-9.

[164] Chen, Y.Z., He, C.G., Zhao, X.J., Shi, L.B., Liu, Q.Y. & Wang, W.J., The influence of wheel flats formed from different braking conditions on rolling contact fatigue of railway wheel. *Engineering Failure Analysis,* **93**, pp. 183-199, 2018. https://doi.org/10.1016/j.engfailanal.2018.07.006.

[165] Vakkalagadda, M.R.K., Vineesh, K.P. & Racherla, V., Estimation of railway wheel running temperatures using a hybrid approach. *Wear,* **328-329**, pp. 537-551, 2015. https://doi.org/10.1016/j.wear.2015.03.026.

[166] Vernersson, T., Temperatures at railway tread braking. Part 1: Modelling. *Proceedings of the Institution of Mechanical Engineers, Part F: Journal of Rail and Rapid Transit,* **221**(2), pp. 167-182, 2007. https://doi.org/10.1243/0954409JRRT57.

[167] Milošević, M., Stamenković, D., Tomić, M., Milojević, A. & Mijajlović, M., Modeling thermal effects in braking systems of railway vehicles. *Thermal Science,* **16**(2), pp. 515-526, 2012. https://doi.org/10.2298/TSCI120503188M.

[168] Haidari, A. & Hosseini-Tehrani, P., Fatigue Analysis of Railway Wheels Under Combined Thermal and Mechanical Loads. *Journal of Thermal Stresses,* **37**(1), pp. 34-50, 2014. https://doi.org/10.1080/01495739.2013.850967.

[169] Haidari, A. & Tehrani, P.H., Thermal load effects on fatigue life of a cracked railway wheel. *Latin American Journal of Solids and Structures,* **12**, pp. 1144-1157, 2015. https://doi.org/10.1590/1679-78251658.

[170] Magelli, M., Development of a 2D finite element model for the investigation of the tread braked railway wheels thermo-mechanical behaviour. In: *IOP Conference Series: Materials*

Science and Engineering **1214**, IOP Publishing, 2022. https://doi.org/10.1088/1757-899X/1214/1/012041.

[171] Pradhan, S. & Samantaray, A.K., A Recursive Wheel Wear and Vehicle Dynamic Performance Evolution Computational Model for Rail Vehicles with Tread Brakes. *Vehicles,* **1**(1), pp. 88-115, 2019. https://doi.org/10.3390/vehicles1010006.

[172] Vernersson, T. & Lundén, R., Temperatures at railway tread braking. Part 3: wheel and block temperatures and the influence of rail chill. *Proceedings of the Institution of Mechanical Engineers, Part F: Journal of Rail and Rapid Transit,* **221**(4), pp. 443-454, 2007. https://doi.org/10.1243/09544097jrrt91.

[173] Churchill, S.W. & Bernstein, M., A Correlating Equation for Forced Convection From Gases and Liquids to a Circular Cylinder in Crossflow. *Journal of Heat Transfer,* **99**(2), pp. 300-306, 1977. https://doi.org/10.1115/1.3450685.

[174] Crank, J. & Nicolson, P., A practical method for numerical evaluation of solutions of partial differential equations of the heat-conduction type. *Mathematical Proceedings of the Cambridge Philosophical Society,* **43**(1), pp. 50-67, 2008. https://doi.org/10.1017/S0305004100023197.

[175] Bosso, N., Cantone, L., Falcitelli, G., Gjini, R., Magelli, M., Nigro, F.M., et al., Simulation of the thermo-mechanical behaviour of tread braked railway wheels by means of a 2D finite element model. *Tribology International,* **178**, 2023. https://doi.org/10.1016/j.triboint.2022.108074.

[176] EN 13979:2020. *Railway applications - Wheelsets and bogies - Monobloc Wheels - Technical approval procedure - Part 1: Forged and rolled wheels*.

Annex

Annex A: LTDPoliTo validation

This annex includes tables showing the results of all the simulators joining the activity for the international benchmarking of LTD codes [34,35] as well as the outputs of the new MATLAB LTDPoliTo code, developed in the frame of the present thesis and described in detail in chapter 2. The main outputs shown in the following tables for simulations scenarios 1, 2 and 4 are those considered in the results paper of the international benchmark [35] and already adopted in Table 5. The reader can refer to §2.2.3 for a description of the major outputs summarizing the results of the simulation. Please remind that in all tables showing the results of the simulations proposed in the international benchmark, couplers are numbered in ascending order starting from the first coupler behind the leading locomotive.

Table 25: Results of the simulators joining the international benchmark of LTD simulators in the first simulation scenario.

Code	Speed (km/h)		Largest in-train force* (kN)		Mean in-train force* (kN)		Max. deflection on coupler 10	
	Max.	Mean	Draft	Buff	Draft	Buff	Draft	Buff
TABLDSS	87.19	65.41	549@2	339@2	342	207	55.12	37.17
UM	88.19	65.73	592@2	355@2	376	219	50.49	33
CRE-LTS	85.92	65.12	559@2	351@2	343	251	15.67	11.8
TDEAS	87.41	65.56	549@2	339@2	334	218	33.54	17.56
PoliTO Simpack	87.21	65.41	561@2	339@2	340	199	56.41	48.71
TsDyn	85.09	65.01	563@2	343@2	370	195	60.97	34.98
CARS	84.99	65.36	611@2	346@2	371	226	56.03	35.03
BODYSIM	85.5	64.93	734@2	443@10	406	245	42.45	33.5
VOCO	86.16	63.91	678@2	144@20	482	79	43.58	9.64
LTDPoliTo	87.30	65.97	565@2	338@2	336	195	64.56	45.07

* Couplers numbered in ascending order from train head to tail, starting from the first coupler behind leading locomotive

** VOCO only joined the first simulation scenario.

Table 26: Results of the simulators joining the international benchmark of LTD simulators in the second simulation scenario.

Code	Speed (km/h)		Largest in-train force* (kN)		Mean in-train force* (kN)		Max. deflection on coupler 61	
	Max.	Mean	Draft	Buff	Draft	Buff	Draft	Buff
TABLDSS	89.47	64.12	759@54	404@54	457	265	81.99	38.70
UM	90.56	64.44	779@54	400@54	475	252	74.83	30.03
CRE-LTS	87.52	63.70	1004@54	419@54	631	297	17.15	7.62
TDEAS	89.59	64.26	730@54	415@54	459	280	42.25	24.34
PoliTO Simpack	88.45	63.24	1302@4	410@54	623	274	92.69	49.34
TsDyn	88.05	63.83	675@54	392@54	421	231	63.07	35.54
CARS	86.07	63.62	772@55	580@16	557	348	81.67	34.92
BODYSIM	88.84	63.83	720@54	479@62	462	261	45.58	29.38
LTDPoliTo	89.40	64.55	769@54	407@54	444	263	89.22	45.07

* Couplers numbered in ascending order from train head to tail, starting from the first coupler behind leading locomotive

Table 27: Results of the simulators joining the international benchmark of LTD simulators in the fourth simulation scenario.

Code	Speed (km/h)		Largest in-train force* (kN)		Mean in-train force* (kN)		Max. deflection on coupler 146	
	Max.	Mean	Draft	Buff	Draft	Buff	Draft	Buff
TABLDSS	81.53	44.45	1319@123	906@122	945	521	141.28	76.54
UM	82.35	44.75	1297@123	825@122	961	498	129.18	73.87
CRE-LTS	81.58	44.48	1411@124	869@118	983	501	28.81	14.39
TDEAS	81.83	44.63	1321@123	822@122	947	485	120.73	27.18
PoliTO Simpack	81.30	44.46	2114@89	2114@96	1765	819	227.68	84.07
TsDyn	80.73	44.57	1346@123	722@122	954	407	143.06	62.88
CARS	80.62	44.63	1308@123	866@122	957	547	142.62	89.79
BODYSIM	81.32	44.62	1420@123	848@122	934	440	82.53	48.50
LTDPoliTo	81.80	44.99	1309@123	867@122	932	501	161.71	96.35

* Couplers numbered in ascending order from train head to tail, starting from the first coupler behind leading locomotive